THE WAKE OF AN EXHAUST STACK IN A CROSSFLOW

A Thesis Submitted to the College of Graduate Studies and Research in Partial Fulfillment of the Requirements for the Degree of Doctor of Philosophy in the Division of Environmental Engineering at the
University of Saskatchewan
Saskatoon

By

Muyiwa Samuel Adaramola

PERMISSION TO USE

In presenting this thesis in partial fulfillment of the requirements for a Postgraduate degree from the University of Saskatchewan, I agree that the Libraries of this University may make it freely available for inspection. I further agree that the permission for copying this thesis in any manner, in whole or in part for scholarly purposes, may be granted by the professors who supervised my thesis work or, in their absence, by the Chair of the Division or Dean of the College in which my thesis work was conducted. It is understood that any copying or publication or use of this thesis or parts thereof for financial gain shall not be allowed without my written permission. It is also understood that due recognition shall be given to me and to the University of Saskatchewan in any scholarly use which may be made of any material in my thesis.

Requests for permission to copy or to make other use of material in this thesis in whole or in part should be addressed to:

Chair of the Division of Environmental Engineering
University of Saskatchewan
57 Campus Drive
Saskatoon, Saskatchewan S7N 5A9
Canada

ABSTRACT

Relatively few studies have been carried out on the turbulent wake structure of a finite circular cylinder and a stack partially immersed in a flat-plate turbulent boundary layer. There is a need to develop a better understanding of the wakes of these structures, since they have many important engineering applications. This thesis investigates the influence of the aspect ratio on the wake of a finite circular cylinder and the effects of the ratio of jet flow velocity to crossflow velocity (velocity ratio, R) on the wake of a stack in a cross-flow.

The wake characteristics of flows over a finite circular cylinder at four different aspect ratios (AR = 3, 5, 7 and 9) were investigated experimentally at a Reynolds number of $\mathrm{Re}_D = 6\times10^4$ using two-component thermal anemometry. Each cylinder was mounted normal to a ground plane and was either completely or partially immersed in a flat-plate turbulent boundary layer. The ratio of boundary layer thickness to the cylinder diameter was 3.

A similar turbulent wake structure (time-averaged velocity, turbulence intensity, and Reynolds shear stress distributions) was found for the cylinders with AR = 5, 7, and 9, while a distinctly different turbulent wake structure was found for the cylinder with AR = 3. This was consistent with the results of a previous study that focused on the time-averaged streamwise vortex structures in the wake. In addition, irrespective of the value of AR, high values were observed for the skewness and flatness factors around the free end of the cylinders, which may be attributed to the interaction of the tip vortex structures and downwash flow that dominates this region of the cylinder.

The wake characteristics of a stack of aspect ratio AR = 9 were investigated using both the seven-hole pressure probe and thermal anemometry. The seven-hole probe was used to measure the three components of the time-averaged velocity field, while the thermal anemometry was used to measure two components of the turbulent velocity field at various downstream locations from the stack. The stack was mounted normal to the ground plane and was partially immersed in a flat-plate turbulent boundary layer, for which the ratio of boundary layer thickness to the stack diameter was 4.5. In addition,

measurements of the vortex shedding frequency were made with a single-component hot-wire probe. The cross-flow Reynolds number was $Re_D = 2.3 \times 10^4$, the jet Reynolds number ranged from $Re_d = 7.6 \times 10^3$ to 4.7×10^4, and R was varied from 0 to 3.

In the stack study, three flow regimes were identified depending on the value of R: the downwash ($R < 0.7$), cross-wind-dominated ($0.7 < R < 1.5$), and jet-dominated ($R \geq 1.5$) flow regimes. Each flow regime had a distinct structure for the time-averaged velocity and streamwise vorticity fields, and turbulence characteristics, as well as the variation of the Strouhal number and the power spectrum of the streamwise velocity fluctuations along the stack height. The turbulence structure is complex and changes in the streamwise and wall-normal directions within the near and intermediate stack and jet wakes. In the downwash and crosswind-dominated flow regimes, two pairs of counter-rotating streamwise vortex structures were identified within the stack wake. The tip-vortex pair and base-vortex pair were similar to those found in the wake of a finite circular cylinder, located close to the free end and the base of the stack (ground plane), respectively. In the jet-dominated flow regime, a third pair of streamwise vortex structures was observed, referred to as the jet-wake vortex pair, which occurred within the jet-wake region above the free end of the stack. The jet-wake vortex pair has the same orientation as the base vortex pair and is associated with the jet rise.

ACKNOWLEDGEMENTS

I would like to express my sincere appreciation and gratitude to my supervisors, Dr. D. Sumner and Dr. D. J. Bergstrom, for their guidance, patience, encouragement and suggestions throughout the course of this program. You are more than supervisors to me.

My appreciation also goes to every member of my advisory committee, Dr. J. Bugg, Dr. C. Simonson, and Dr. H. Guo, as well as Dr. Y-H. Lin and Dr. H. Wang, for all their assistance and useful feedback in the course of this work. The technical assistance provided by Dave Deutscher is also appreciated.

I sincerely thank my wife Margaret, for her understanding and time, in taking care of our boys (Ebunoluwa and Inumidun), in my absence, in order to purse this degree. My thanks also go to my siblings (Ayodele, Folasade, Adenike and Temitope) for their support.

A special thanks to Jide Akinlade and his family; Dr. Ike Oguocha; Gbadebo Owolabi; and Lanre Oyewola. I sincerely appreciate your contributions to the successful completion of this program. I also thank Ebenezer Enninful, Femi Farinu, Femi Akosile, Sonne Udemgba and family, and Seraphine Kogo for their support.

The financial support of the Natural Sciences and Engineering Research Council (NSERC) of Canada, the Canada Foundation for Innovation (CFI), the Innovation and Science Fund of Saskatchewan, and the Division of Environmental Engineering is appreciated.

Finally, I thank God for his protection, wisdom and for the successful completion of this program.

DEDICATION

This thesis is dedicated to my late parents:

Gabriel and Kehinde Adaramola, and my boys: Ebunoluwa and Inumidun

TABLE OF CONTENTS

LIST OF FIGURES

LIST OF TABLES

NOMENCLATURE

English Symbols

AR	Aspect ratio, H/D
B	Logarithmic law constant
B_s	Smaller of upwind building height or width
B_L	Larger of upwind building height or width
C_D	Mean drag force coefficient, $2F_D / \rho U_\infty^2 \, DL$
C_{pr}	Pitch angle coefficient
C_{pt}	Yaw angle coefficient
C_{Ptotal}	Total pressure coefficient
C_q	Dynamic pressure coefficient
D	Cylinder diameter or stack external diameter [m]
d	Stack internal diameter [m]
E	Voltage [V]
E_N	Enhancement factor
F_b	Buoyancy flux
F_D	Drag force [N]
F_u	Streamwise flatness factor, $\frac{< u^4 >}{(u')^4}$
F_w	Wall-normal flatness factor, $\frac{< w^4 >}{(w')^4}$
f_s	Vortex shedding frequency [Hz]
g	Acceleration due to gravity [m/s^2]
H	Cylinder or stack height [m]
H_c	Maximum height of the roof recirculation region [m]
H_δ	Shape factor, δ^* / θ
h_b	Jet rise due to buoyancy flux [m]
h_d	Reduction in jet height [m]
h_m	Jet rise due to momentum flux [m]
Δh	Plume rise [m]

$h(x)$	Jet rise [m]
L_c	Length of the roof recirculation region [m]
L_r	Distance reattachment point on the wall from the building [m]
L_f	Vortex formation length [m]
N	Number of plumes
P	Centre-to-centre spacing or pitch [m]
$P_{()}$	Seven hole port pressure [N/m^2]
$\overline{P}$	Averaged pressure [N/m^2]
P/D	Pitch ratio
P_∞	Absolute pressure [N/m^2]
Q	Volume (flow) rate [m^3/s],
q	Dynamic pressure [N/m^2]
R	Velocity ratio, U_e/U_∞
R_g	Gas constant for air, [J/kgK]
Re_D	Cross-flow Reynolds number (based on external diameter, D), $\rho_\infty U_\infty D/\mu_\infty$
Re_d	Jet exit Reynolds number (based on internal diameter, d), $\rho_e U_e d/\mu_\infty$
R_m	Momentum flux ratio, $\left(R_\rho\right)R^2$
Re_x	Length Reynolds number (based on streamwise distance from the origin of the boundary layer), $\rho U_\infty x/\mu_\infty$
Re_θ	Ground plane Reynolds number (based on external diameter, θ), $\rho U_\infty \theta/\mu_\infty$
R_ρ	Density ratio, ρ_e/ρ
$\boldsymbol{R}$	Building dimension scale length [m]
r	Stack radius [m]
S_u	Streamwise skewness factor, $\frac{<u^3>}{(u')^3}$
S_w	Wall-normal skewness factor, $\frac{<w^3>}{(w')^3}$
St	Strouhal number, $f_s D/U_\infty$
T	Temperature [K]

U	Local velocity vector [m/s]
U_c	Jet exit centre ($r = 0$) velocity, [m/s]
U_z	Jet exit axial velocity, [m/s]
U_r	Jet exit radial velocity, [m/s]
U_θ	Jet exit tangential velocity, [m/s]
U_e	Exhaust exit velocity [m/s]
U_∞	Freestream (or cross-flow) velocity [m/s]
u^*	Friction velocity [m/s]
$U(z)$	Ground plane boundary layer velocity profile [m/s]
u, v, w	Local velocity [m/s]
$\overline{U}, \overline{V}, \overline{W}$	Time-averaged velocity [m/s]
u', v', w'	Root-mean square velocity [m/s]
V	Resultant velocity [m/s]
$-\langle uw \rangle$	Reynolds shear stress components [N/m^2]
X_c	Distance from the leading edge to H_c [m]
x	Distance from leading edge [m]
y	Cross-stream distance [m]
z	Vertical distance above the ground plane [m]

Greek Symbols

Γ	Circulation [m^2/s]
$\Delta\rho$	Difference between the ambient density and exhaust density, $\lvert\rho_e - \rho_\infty\rvert$
α, ψ	Yaw angle [Degrees]
β	Stack capping factor
δ	Boundary layer thickness [m]
δ^*	Boundary layer displacement thickness [m]
θ	Boundary layer momentum thickness [m] or pitch angle [Degrees]
κ	Logarithmic law constant (von Kármán constant = 0.41)
μ_e	Jet flow dynamic viscosity [Ns/m^2]
μ_∞	Cross-flow dynamic viscosity [Ns/m^2]

ν_∞	Freestream kinematic viscosity [m^2/s]
ρ_e	Jet flow density [kg/m^3]
ρ_∞	Freestream (or cross-flow) density [kg/m^3]
τ_w	Wall shear stress [Pa]
ω_x	Streamwise component of vorticity [s^{-1}]
ω_x^*	Non-dimensional streamwise component of vorticity

CHAPTER 1

INTRODUCTION

1.1 Background

This research considers the complex flow field associated with a stack in a cross-flow. Stacks are used to reduce the ground-level concentration of an exhaust gas by emission of the gas at greater heights. The flow over a stack (see Figure 1.1) in a cross-flow has many engineering applications such as chimney stacks mounted on residential, laboratory, and industrial buildings. For a stack mounted on a building rooftop, the local velocity field, the proximity of other buildings and structures, the stack exit flow temperature and velocity, the wind velocity and direction, and the stack height and shape are major factors that affect the rise and dispersion of the stack jet or plume (Wilson, 1979; Schulman and Scire, 1991; ASHRAE, 1999). These factors, especially the stack height and the ratio of the jet flow (or plume) momentum to crosswind momentum, also influence the local flow field around the stack itself. The purpose of a stack design is to increase the jet flow and disperse the associated pollutants as high as possible so that these pollutants will be mixed (or diluted) within the atmosphere in order to reduce the ground-level concentration of pollutants.

The jet rise can increase the effective height (physical height of the stack plus the height of the jet flow above the stack free end) of the stack and thereby increase the residence time of the pollutants in the atmosphere. This can reduce the maximum ground

concentration of the pollutants from the stack by a factor of more than three (Briggs, 1984). Generally, the elevation of the jet flow increases with increasing ratio of the jet flow momentum to the crosswind momentum. This can primarily be achieved by increasing the jet flow velocity and temperature relative to the crosswind velocity and temperature. For a non-buoyant jet flow, the property of most interest is velocity.

Figure 1.1: Rooftop-mounted stacks.

Jet rise can also be increased through the manifolding and ganging of a group of stacks. Manifolding involves the combination of exhausts from different sources and their release through a single stack. The nature of the exhausts to be combined, recommended industrial hygiene practice, and safety make it sometimes difficult to combine exhausts from different sources (ASHRAE, 2001). Other disadvantages of manifolding include the wide range of velocities from different sources to be combined, as well as the possibility of reduction in the jet rise, if a single stack needs to be shut down for repair (König and Mokhtarzadeh-Dehghan, 2002).

When two or more stacks are grouped (ganged) together in an appropriate pattern, the jet flows from individual stacks may merge together above the stacks to create a single jet flow. In some cases, this may lead to higher jet rise compared to the jet rise from a single stack and, eventually, lower ground-level concentration of the exhaust from the stacks (Contini and Robins, 2001; Macdonald *et al.,* 2002; Contini and Robins, 2004). The orientation of the stacks to the cross-flow direction, the number of stacks as well as the stack arrangement all influence the mixing and extent of jet rise (see e.g., Briggs, 1984; Overcamp and Ku, 1988; Contini and Robins, 2001; Macdonald *et al.,* 2002; Contini and Robins, 2004). The merging process for two elevated buoyant plumes as an example of "ganging" of stacks is shown in Figure 1.2.

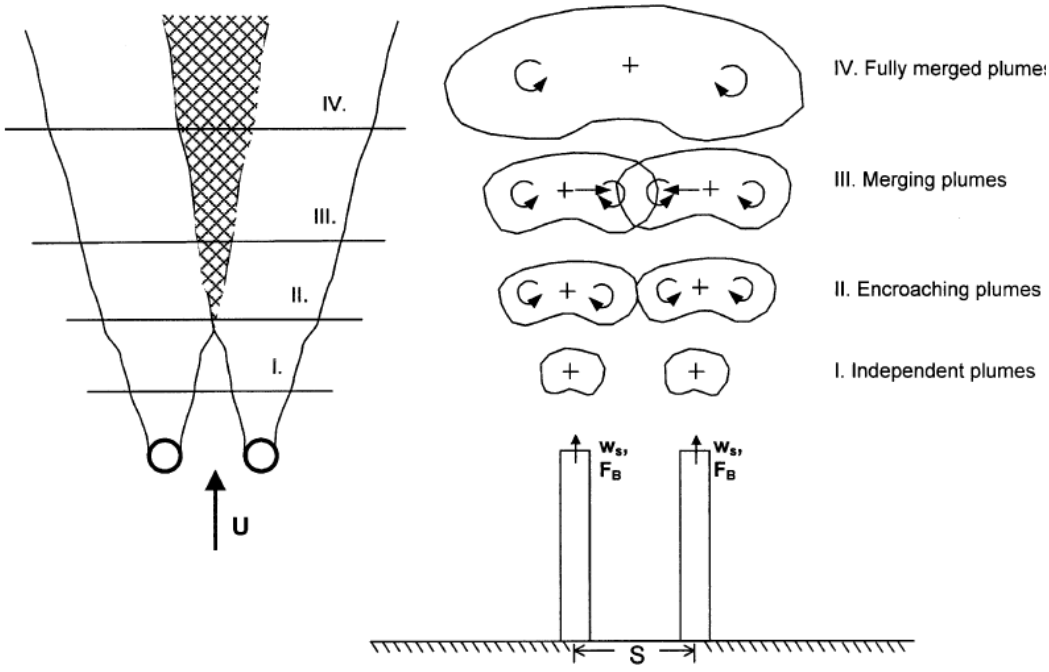

Figure 1.2: Schematic illustration of the merging process for two buoyant plumes released from a pair of stacks arranged in a line perpendicular to the wind. (Reprinted from Macdonald *et al*., 2002 with permission, see Appendix B, p. 226).

In practical applications, the behaviour of the jet flow (or plume) also depends on the stability of the atmosphere (see e.g. Slawson and Csanady, 1971). In a stable atmospheric condition, the ambient temperature decreases less rapidly with elevation than the jet temperature so the buoyancy of the jet decreases as it rises. In an unstable atmospheric condition, the jet flow cools less rapidly than the surroundings, so the buoyancy of the jet increases as it rises. In a neutral atmospheric condition, the jet and the environment temperature decrease at the same rate, so the relative different between the jet and the ambient temperatures are always the same. The jet flow is in equilibrium with respect to the surrounding wherever it is moved (vertically). For an effective jet rise as well as proper mixing of the jet flow with the atmosphere, an unstable atmospheric condition is desired. In the case of a non-buoyant jet flow (where the jet flow density is equal to the crosswind density), the influence of the atmosphere's stability is typically not considered.

The flow pattern around a building is another factor that can influence the jet rise. Knowledge of this flow pattern can provide useful information in locating a stack on a rooftop. The wind speed, its turbulence and the nature of the atmospheric boundary layer as well as the building Reynolds number are some of the factors that can influence the flow pattern around the building. Wilson (1979) identified three flow regions on a rooftop, the recirculation region, the high turbulence region, and the roof wake region. A sketch of the flow around a rectangular flat-top building is shown in Figure 1.3. In the recirculation region, the separated flow from the upwind edge of the building roof reattaches to the roof at a downwind distance from this edge. The flow recirculates within the separation bubble, with high levels of turbulence. The roof wake comprises both the recirculation and high turbulence regions. Due to the adverse pressure gradients

upwind of the building as a result of the boundary layer, a horseshoe vortex is produced at the base of the building and this can generate dust and debris, which can contaminate the air around the base of the building. Also, the flow that separates at the edges of the

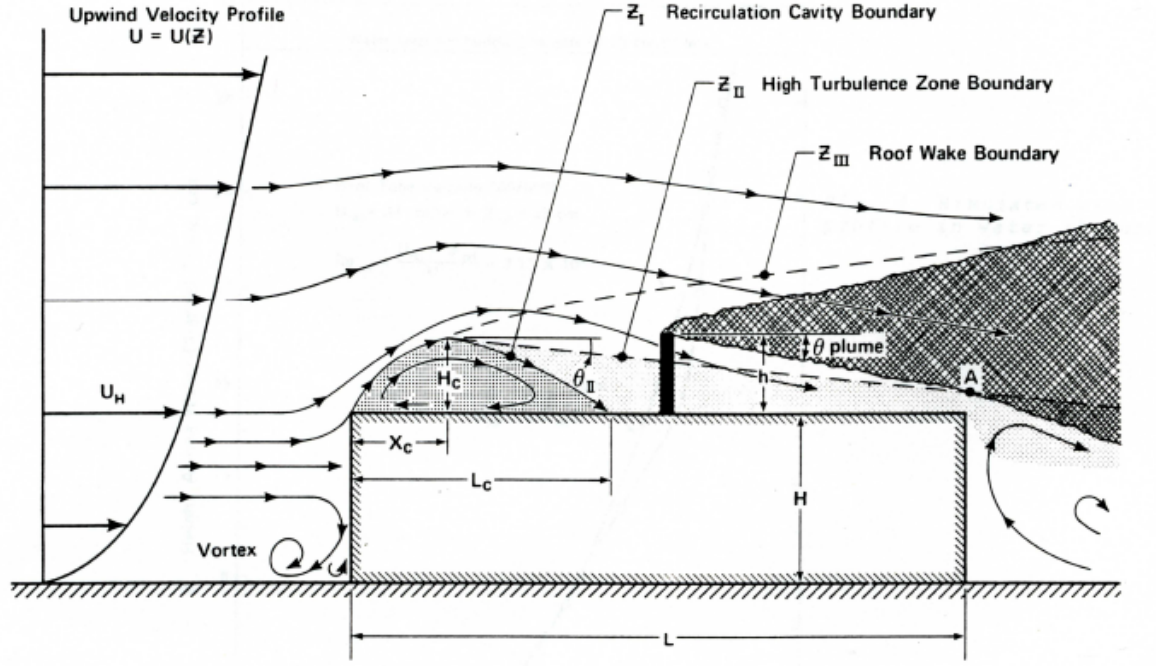

Figure 1.3: The flow pattern on the roof of a rectangular building (Reprinted from Wilson, 1979 and ASHRAE 1997 with permission, see Appendix B, p. 227). Where L = building length, H = building height, U_H = wind velocity at the building height, **R** = scale length, X_c = distance from the leading edge, L_c = length of the roof recirculation region, L_r = length of the building wake region, and h_s = stack height.

building creates a low-pressure wake behind the building. Flow recirculation can occur in this wake, and since a building has a finite height, downwash flow (a downward-directed local velocity field) can occur within the building wake. At very low jet velocity (compared to the wind velocity), stack-tip downwash flow could occur due to the region of low pressure that forms on the leeward side of the stack and the inability of the jet flow to penetrate the crosswind flow. If the plume or jet from the stack is caught in the wake of the building and within the flow regions on the building and in its vicinity, the

emissions will flow downward towards the rooftop and the ground level. This would adversely affect the air quality around the building, as well as create problems for the location of any intake vents on the top of the building. To reduce the effect of the plume on the rooftop and ground level, the stack effective height (which comprises the stack height and jet rise) should be sufficiently above the three flow regions shown in the Figure 1.3. Engineering design guidelines for rooftop-mounted stacks and the procedures for determining the dimensions shown in Figure 1.3 can be found, for example, in ASHRAE (1997 and 1999) and Stathopoulos *et al.* (2004) and are briefly discussed in the Appendix A of this thesis.

In the design of a stack, knowledge of the flow around the stack provides useful information about the forces that act on the stack. Information about the frequency of the vortex shedding, which can cause large fluctuating forces that can result in noise, vibration and possible structural failure, is also essential. Due to the possibility of a strong downwash flow within the near ($x/D < 5$) and intermediate wake ($5 < x/D < 50$) of the stack (where x is the streamwise distance from the stack and D is the external diameter of the stack) (Kiya and Matsumura, 1985; Matsumura and Antonia, 1993), the understanding of the flow dynamics within this region of the stack is crucial. This downwash flow, which may contain pollutants, is undesirable in engineering applications as a result of the likelihood of injury to the health of human beings, animals and plants or damage to any other equipment installed on the rooftop.

The flow around a finite circular cylinder represents the simplest possible stack geometry and the case of no jet flow issuing from the stack. In many practical applications involving the flow around a circular cylinder, e.g., chimney stacks and fuel-storage tanks, the length of the cylinder is finite and hence the free end effect strongly

influences the flow pattern around the cylinder, and the fluid forces acting on the cylinder. For a circular cylinder of finite height, H, and diameter, D, that is partially immersed in a boundary layer of thickness, δ, (see Figure 1.4), an adverse pressure gradient is formed within the region near the base of the cylinder, due to deflection of the flow by the cylinder, and vortices are created and stretched into a horseshoe shape. Also, the separated shear flow from the sides of the cylinder interacts with the downwash flow from the free end and with the upwash flow (upward-directed velocity) from the ground plane. These interactions make the flow field behind the finite cylinder complex and strongly three-dimensional. There are marked changes in the near-wake flow structure along the cylinder height, and these changes are strongly influenced by the cylinder's aspect ratio, AR (= H/D).

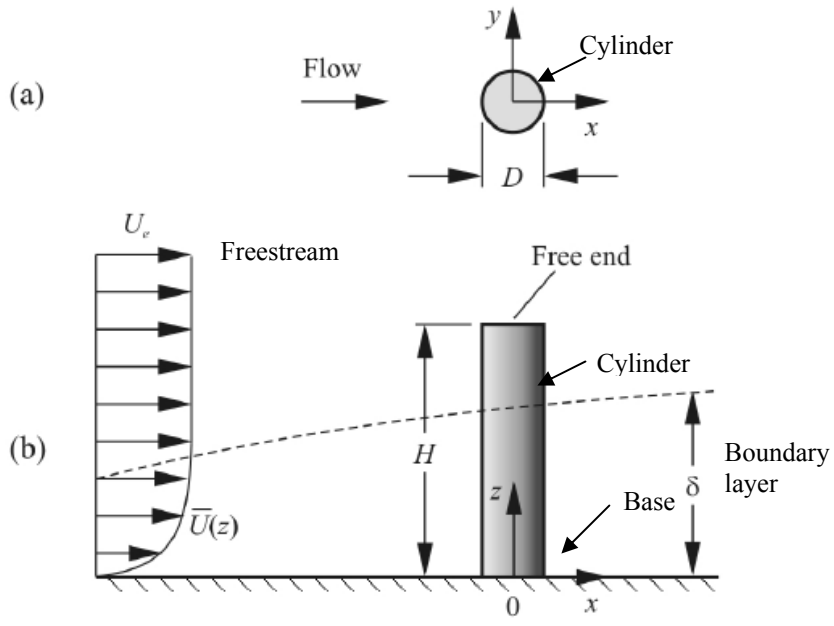

Figure 1.4: Circular cylinder of finite height mounted normal to a ground plane and partially immersed in a turbulent flat-plate boundary layer: (a) top view, and (b) side view. $U(z)$ is the boundary layer mean velocity profile, and x, y, z are the streamwise, cross-stream and wall-normal coordinates, respectively.

Despite the practical significance of this flow, the three-dimensional separated flow field of a finite cylinder remains much less understood than the classical case of the "infinite" cylinder (see e.g. Contanceau and Defaye, 1991 and Williamson, 1996), and there have been relatively few measurements of the turbulent wake of small-aspect-ratio circular cylinders reported in the literature. Several previous studies that have extensively measured the wake of a finite cylinder, e.g. Tanaka and Murata (1999), Park and Lee (2004), and Sumner *et al*. (2004), did not provide any information on the fluctuating velocity field, which is important for understanding the transport properties and diffusion in the wake. Okamoto and Sunabashiri (1992) measured the three turbulence intensity components in the wake of finite circular cylinders of AR = 1 to 7, but the measurements were restricted to spanwise profiles at the mid-height (z/H = 0.5) position. Leder (2003) measured the time-averaged streamwise vorticity field and the turbulent kinetic energy distribution in the wake of a short circular cylinder of AR = 2 using three-component laser Doppler velocimetry (LDV), but the measurements were mostly restricted to the recirculation zone close to the cylinder (x/D < 3.6). The flow around the finite cylinder is sufficiently complex that further study is needed to better understand the flow field. Further discussion of the finite circular cylinder is found in Section 2.3.

The presence of a jet flow issuing from the stack gives rise to an even more complicated flow structure compared with a finite circular cylinder, both around the stack and in its wake. The local flow field of the stack is characterized by complex interactions between the jet and stack wake regions, shear produced by the upward momentum of the jet, and downwash flow (Eiff *et al*., 1995; Johnston and Wilson, 1997; Eiff and Keffer, 1999; Huang and Hsieh, 2002; Huang and Hsieh, 2003; Mahjoub Säid

et al., 2005). The extent of this complexity depends on the jet-to-cross-flow momentum ratio, R_m ($= \rho_e U_e^2 / \rho_\infty U_\infty^2$, where ρ_∞ is cross-flow density, ρ_e is jet flow density, U_∞ is the freestream velocity and U_e is the jet exit velocity). For a non-buoyant jet flow, which is the focus of this study, this expression reduces to the jet-to-cross-flow velocity ratio, R ($= U_e/U_\infty$). Other factors that affect the flow around the stack and along its height include the stack Reynolds number, $\mathrm{Re}_D = \rho_\infty U_\infty D/\mu_\infty$ (where μ_∞ is the dynamic viscosity of the cross-flow fluid and D is the external diameter of the stack); the stack aspect ratio, AR; the relative thickness of the boundary layer at the location of the stack, δ/H; the jet Reynolds number, $\mathrm{Re}_d = \rho_e U_e d/\mu_e$ (where μ_e is the dynamic viscosity of the jet flow fluid and d is the internal diameter of the stack at the exit) and the diameter ratio, d/D. The flow field of a stack of uniform cylindrical shape, with external diameter, D, internal diameter, d, and height, H, is shown schematically in Figure 1.5.

In this figure, the stack is shown partially immersed in a turbulent boundary layer on the ground plane with freestream velocity, U_∞, boundary layer mean velocity profile, $U(z)$, and boundary layer thickness, δ. Also shown in this figure are the locations of the stack and jet wakes, as well as the rise, $h(x)$, of the elevated turbulent jet after it exits the stack.

The behaviour of a turbulent round jet issuing normally into a cross-flow also depends on how the jet is injected. The jet can be injected through either an orifice on the ground plane, which is referred to as ground-level source jet, or from an elevated source, as in the case of the stack (Figure 1.5). There is extensive work on the ground-level source jet in the literature and for the elevated jet in cross-flow, considerable

attention in the literature has focused on the jet rise (e.g., Briggs, 1984; Overcamp and Ku, 1988) with relatively fewer studies centred on the local flow field of the stack and

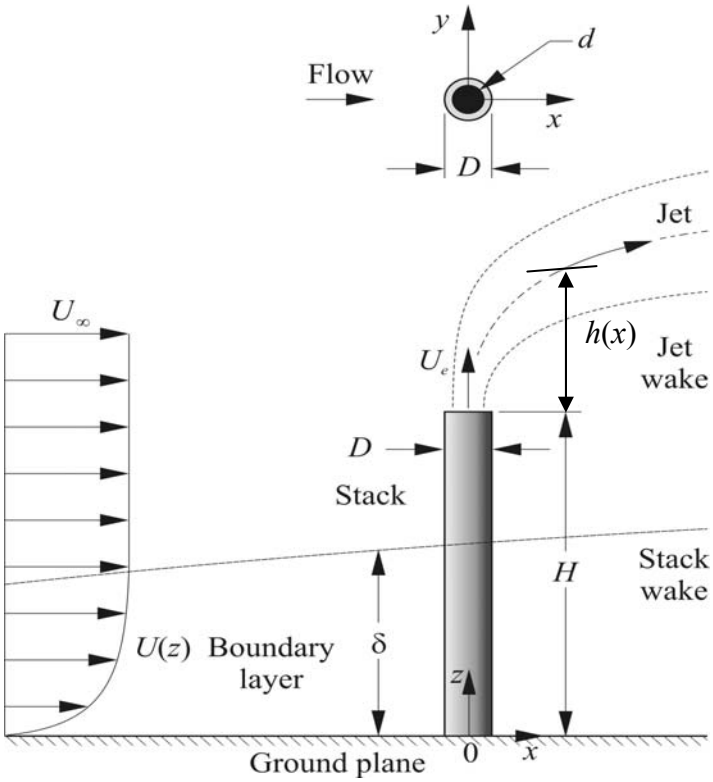

Figure 1.5: Schematic of a cylindrical stack mounted normal to a ground plane and partially immersed in a turbulent flat-plate boundary layer. *x*, *y*, z are the streamwise, cross-stream and wall-normal coordinates, respectively

jet. Some of the few studies devoted to the study of an elevated jet in cross-flow are the work of Moussa (1977), Eiff *et al*. (1995), Johnston and Wilson (1997), Eiff and Keffer (1997, 1999), Huang and Hsieh (2002, 2003), Huang and Lan (2005), and Mahjoub Säid *et al*. (2005, 2007). The inclination of the jet and associated wake structure of the combined jet and stack depends on the velocity ratio *R* (for a non-buoyant jet). The possibility of downwash flow (with pollutants) for low values of *R* can have an adverse environmental impact. Also, as a result of the complex nature of the near-wake structure

and limited information of an elevated jet flow in cross-flow, it is of interest to further study the effect of the jet flow on the flow dynamics within the stack wake.

1.2 Scope and Objectives

In most engineering applications, the exhaust jet flow from a stack is buoyant and the parameters of interest are likely to be the temperature and concentration of the pollutants. The focus of the present study is, however, on the measurement of the velocity field within the stack wake under the influence of a non-buoyant jet flow. This is a first step to understanding the effect of a buoyant jet on the wake characteristics of a stack. In real-life applications, the Reynolds numbers may be outside the subcritical flow regime, and the stack may be immersed within an atmospheric boundary layer and/or a rooftop boundary layer. The present study is limited to a short stack that is partially ($\delta/H < 1$) immersed in a zero-pressure gradient turbulent boundary layer. Due to the limitations of the wind tunnel test section and the likelihood of the test section walls to interfere with the stack flow structure for large external stack diameters (West and Apelt, 1982), the crosswind Reynolds number based on the stack external diameter is limited to the subcritical flow regime where $350 < Re_D < 2 \times 10^5$ (see Section 2.3).

As noted above, there are limited studies on the turbulent wake of a finite cylinder and a stack in cross-flow. Therefore, there is a need for further study that would provide more insight into the turbulent wake of these structures. The overall objective of the present study is to advance our fundamental understanding of these flows. More specifically, we will investigate:

1) the effect of aspect ratio, AR, on the turbulent wake of a finite circular cylinder in a cross-flow, and

2) the effect of the velocity ratio, R, on the time-averaged velocity and turbulence fields within the wake of a short stack subjected to a cross-flow.

For this study, a seven-hole probe will be used to measure the time-averaged velocity field (u, v, w) and a thermal anemometry probe will be used to measure the two-component turbulent velocity field (u, w) at various downstream locations from the stack. The outcomes of this study should improve our understanding of the wake of a finite cylinder and a stack in cross-flow.

1.3 Outline of the Thesis

In addition to Chapter 1, the main body of this thesis is made-up of seven other chapters. Reviews of the flow around a finite circular cylinder, ground source jet flow and elevated jet flow, both subjected to cross-flow, are presented in Chapter 2. The instrumentation and models used for this study as well as the experimental set-up are described in Chapter 3.

In Chapter 4, the effect of aspect ratio on the wake structure of a finite circular cylinder are presented and discussed. In addition to providing background information for the study of a stack in a cross-flow, the studies reported in Chapter 4 also provide further information that helps to improve the current level of understanding of the turbulent wake of a finite circular cylinder.

In Chapter 5, the effects of velocity ratio on the time-averaged properties within the stack wake are presented. In Chapter 6, the effect of the velocity ratio on the turbulent parameters within the stack wake and their relationship with the time-averaged parameters is discussed. The parameters considered are the Reynolds shear stress components, higher-order moments, and the skewness and flatness factors in both the

streamwise and wall-normal directions. The effect of the velocity ratio on the characteristics of the vortex shedding from the stack and the vortex formation length are given in Chapter 7. In Chapter 8, the summary of the findings of the study, the conclusions and contributions from this study, as well as recommendations for future work, are presented.

CHAPTER 2

LITERATURE REVIEW

2.1 Introduction

In this chapter, a detailed review of recent work on the finite circular cylinder and the stack (or elevated jet) in cross-flow is presented. The flow field of a stack of uniform cylindrical shape, with external diameter, D, internal diameter, d, and height, H, was shown schematically in Figure 1.6. The local flow field of a stack involves three fundamental yet complex flows: the boundary layer flow on the ground plane (Section 2.2), the separated flow field and the near wake of a finite circular cylinder (Section 2.3), and the development of an elevated round jet in cross-flow (Section 2.4). For a finite circular cylinder, the wake structure depends on the cross-flow (freestream) Reynolds number, the freestream turbulence, the aspect ratio of the cylinder, the relative thickness of the boundary layer at the location of the cylinder, the cylinder's surface roughness, etc. For a stack in cross-flow, in addition to these parameters, the momentum flux (or velocity) ratio, the jet Reynolds number, and the internal-to-external diameter ratio are the additional factors that can influence the flow around the stack and within its wake.

2.2 Ground Plane Boundary Layer

Whenever a viscous fluid flows over a solid surface, such as a flat-plate, frictional forces slow the motion of the fluid in a thin layer close to solid surface, known as a boundary layer. At any location along the surface, the streamwise velocity component

increases from zero at the wall to a maximum value in the freestream. When the shape of the time-averaged streamwise velocity and turbulence statistics profiles no longer changes with the increasing streamwise distance, x, from the leading edge, the flow is said to be fully developed.

The character of the boundary layer changes as it develops along the surface of the flat plate. Generally starting out as a laminar flow, the boundary layer thickens, undergoes transition to turbulent flow, and then continues to develop along the surface of the body. In laminar flow, the fluid moves in smooth layers. There is relatively little mixing and consequently the velocity gradients are small and shear stresses are low. The thickness of the laminar boundary layer increases with distance from the origin of the boundary layer and decreases with the Reynolds number, Re_x ($= \rho_\infty U_\infty x/\mu_\infty$, where x is the distance from the leading edge). As the velocity profile develops, instabilities occur and eventually the flow transitions into turbulent motion. The wall shear stress or skin friction coefficient is higher for a turbulent boundary layer than for a laminar boundary layer. This is because of the more effective mixing associated with turbulent flow.

For incompressible flow over a smooth flat-plate (zero-pressure gradient), in the absence of heat transfer, transition can be delayed up to a Reynolds number $\mathrm{Re}_x > 1 \times 10^6$ if external disturbances are minimized. But, under typical flow conditions, transition from a laminar to a turbulent boundary layer is considered to occur at a Reynolds number of $\mathrm{Re}_x = 500{,}000$ (Fox *et al.,* 2004). Turbulent boundary layer flow is characterized by unsteady mixing due to eddies of different sizes. The result is higher shear stress at the wall, a "fuller" velocity profile, and a greater boundary layer

thickness, δ. For a turbulent boundary layer, a typical velocity profile on a smooth flat plate can be approximated by a logarithmic law profile (White, 2003),

$$\frac{u}{u^*} \approx \frac{1}{\kappa} \ln\left(\frac{zu^*}{\nu}\right) + B \ , \tag{2.1}$$

where $$u^* = \left(\tau_w / \rho_\infty\right)^{0.5}, \tag{2.2}$$

u is the local streamwise velocity, u^* is the friction velocity, ν is the kinematic viscosity of the fluid, z is the distance above the flat plate, τ_w is the wall shear stress, ρ_∞ is the fluid density, κ = 0.41 and B = 5.0. The boundary layer thickness, δ, is defined as the distance above the surface at which the local velocity is within 1% of the freestream, $u = 0.99U_\infty$. The flat plate shape factor $H_\delta = \delta^* / \theta$, which is defined as the ratio of displacement thickness, δ^*, to momentum thickness θ, is H_δ = 1.3 for a fully-developed, zero-pressure gradient (ZPG) turbulent boundary layer (White, 2003).

The properties of the turbulent plane wall ZPG boundary layer depend primarily on the nature of the surface, whether it is smooth or rough. Krogstad and Antonia (1994) observed that the primary effect of surface roughness, which is usually encountered in both laboratory and atmospheric flows (Raupach *et al*., 1991), compared with a smooth surface, is to change the shape of the large-scale motion. These changes appear to be partly associated with the increased intensity of the wall-normal velocity fluctuations.

2.3 Flow Around a Finite Circular Cylinder

The turbulent wake of a two-dimensional or "infinite height" circular cylinder of diameter, D, is mainly characterized by the Kármán vortex street over a wide range of Reynolds number (see e.g. Contanceau and Defaye, 1991; Williamson, 1996;

Zdravkovich, 1997; Sumer and Fredsøe, 2002; Heseltine, 2003). At very low Reynolds numbers (Re < 1), inertial forces are negligibly small compared with viscous forces, the boundary layer separates from the surface at the rear stagnation point and no vortex shedding occurs from the cylinder. In addition, the flow is symmetrical around the cylinder and the flow downstream is almost a mirror image of the upstream flow. But, as the Reynolds number increases, the flow downstream no longer mirrors the flow upstream and the complexity of the flow increases.

For Reynolds numbers in the range of 5 to 40, the flow starts to separate from the surface of the cylinder and a pair of symmetrical attached vortices is formed at the rear of the cylinder. At a Reynolds number of about 40 to 70, the attached vortices, stretch, become unsteady and oscillate. At a Reynolds number between 90 and 350, these unsteady vortices are eventually shed in an alternating manner to create a regular vortex pattern, known as the Kármán vortex street, in the wake of the cylinder. As the Reynolds number is increased further, a critical flow regime is reached at a Reynolds number of about 2×10^5, at which the transition of the boundary layer from laminar to turbulent occurs. When the Reynolds number lies between 350 and 2×10^5, a flow regime called the subcritical flow regime is observed. In this flow regime, the flow is characterized by a laminar boundary layer prior to separation at about 80^o measured from the front stagnation point.

When the Reynolds number is greater than the critical value (2×10^5), the flow reattaches to the cylinder, the separation point shifts downstream and the wake becomes smaller. For Reynolds numbers in the range of 7×10^5 to 3.5×10^6, termed the supercritical flow regime, regular and organized vortex shedding ceases and the boundary layer flow becomes turbulent prior to separation from the surface of the

cylinder. When the Reynolds number is greater than 3.5 x 10^6, referred to as the postcritical flow regime, the boundary layer is fully turbulent before separation, and there is a slight increase in the cylinder's wake as well as resumption of vortex shedding from the cylinder. More detailed information about the various flow regimes and their characteristics can be found in, for example, Contanceau and Defaye (1991), Szepessy (1991), Williamson and Miller (1994), Williamson (1996), Zdravkovich (1997) and Heseltine (2003). In addition to Reynolds number, freestream conditions, cylinder end conditions and surface roughness can affect the flow regimes and eventually, the wake characteristics.

Given the above, it is not surprising that, the mean drag coefficient, C_D ($= 2F_D / \rho_\infty U_\infty^2 \, DH$, where F_D is the drag force) of the cylinder varies with the Reynolds number. The mean drag coefficient is inversely proportional to the Reynolds numbers for Reynolds number less than 100, approximately 1.2 when the Reynolds number lies between 100 and 10^5, suddenly drops at transition to a value of about 0.06 at Re = 4 x 10^5 and gradually increases thereafter and there is a second flat region for Re > 10^7 (see for examples, White, 2003 and Fox *et al*, 2004).

For a circular cylinder of finite height H and diameter D mounted normal to plane wall as presented in Figure 1.5, the turbulent wake is more complex and three-dimensional. The flow field of the finite cylinder is strongly influenced by the cylinder's aspect ratio, $AR = H/D$, and the thickness of the boundary layer, δ, developed on the wall relative to the cylinder height and diameter, i.e. the ratios δ/H and δ/D. The aspect ratio of the cylinder in particular has a major influence on the structure and characteristics of the wake (see Figure 2.1). For a circular cylinder of high aspect ratio, $AR >$ critical value

(see Figure 2.1(a)), there are three regions along the cylinder's height, namely the free end region, the middle region (characterized by a Kármán vortex street) which lies between the wall and free end regions (Kawamura *et al*., 1984; Zdravkovich, 2003; Donnert *et al*., 2007), and the base region. For $AR \leq$ critical value (depending on the study), (see Figure 2.1(b)), only the free end and base regions are present. Within the free end region of the cylinder, a pair of counter-rotating vortices, referred to as the tip vortex pair, is formed and it extends in the streamwise direction into the wake (Etzold and Fiedler, 1976; Kawamura *et al*., 1984; Lee, 1997; Park and Lee, 2000, 2002, 2004; Sumner *et al*., 2004). These tip vortex structures interact in a complex manner with the

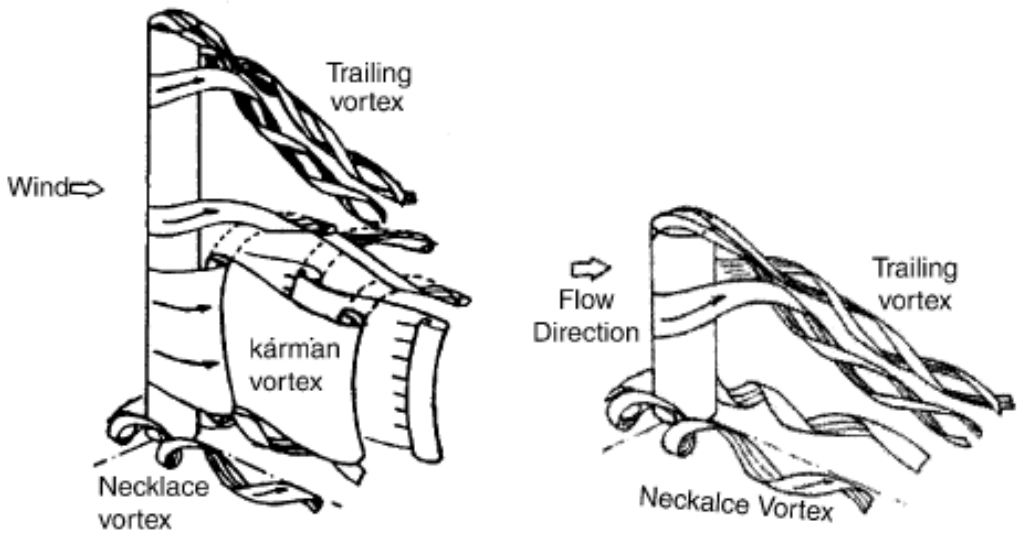

Figure 2.1: Flow around a finite length circular cylinder (a) $AR >$ critical AR, (b) $AR \leq$ critical AR (Reprinted from, Kawamura *et al*., 1984 with permission, see Appendix B, p. 227).

Kármán vortex shedding from the sides of the cylinder, and are thought to be responsible for the downwash flow near the free end (see e.g. Tanaka and Murata, 1999; Sumner *et al*., 2004 and Wang *et al*., 2006).

Within the base region, which is immersed in the plane wall boundary layer, the fluid near the wall has a lower velocity than the flow immediately above it, and because of the adverse pressure gradient, the fluid recirculates at the leading edge of the cylinder. The fluid is then swept around the cylinder's base, rotating and rolling up into a horseshoe vortex or necklace vortex (see Figure 2.3) (Agui and Andreopoulos, 1992; Graf and Yulistiyanto, 1998). The rotational direction of the horseshoe vortex is opposite to that of the base vortex structure discussed below (Sumner *et al*., 2004, Wang *et al*., 2006). The formation and size of the horseshoe vortex depends on the ground plane boundary layer thickness (δ/D and δ/H), the cross-flow Reynolds number based on the cylinder diameter (or the boundary layer thickness), and the height and geometry of the cylinder (Ballio *et al*., 1998; Baker, (1979 and 1980); Becker *et al*., 2002; Sumer and Fredsøe, 2002). Sumer and Fredsøe (2002) for example, noted that the smaller the values of δ/D, Reynolds number, and height of the cylinder, the smaller the size of the horseshoe vortex that will be formed.

In addition to the tip (or trailing) vortex structures, a pair of base vortex structures (distinct from the horseshoe vortex) may be found close to the cylinder-wall junction and within the boundary layer developed on the wall (Tanaka and Murata, 1999; Sumner *et al*., 2004, Wang *et al*., 2006). These base vortices induce upwash flow from the ground plane and are opposite in sense of rotation to the tip vortices (Sumner *et al*., 2004, Wang *et al*., 2006).

For higher aspect ratios (above the critical aspect ratio), the vortex shedding frequency (or Strouhal number, $St = f_s D/U_\infty$, where f_s is the vortex shedding frequency) may vary in a cellular fashion along the cylinder height, each cell having a different frequency for the case of a uniform approach flow (e.g., Fox and Apelt, 1993(a,b,c))

and for a shear flow (e.g., Maull and Young, 1974, and Griffin, 1985), with shedding being suppressed near the free end and the base. The number of cells along the cylinder height depends, among other factors, on the aspect ratio. For $AR > 7$, more than two cells have been observed (e.g., Lee and Wang, 1987; Fox and Apelt, 1993(a,b,c)), while the cellular structure disappears at lower aspect ratios, becoming a single cell of uniform frequency along the entire height for $AR < 7$ (Lee and Wang, 1987; Uematsu *et al*., 1990; Okamoto and Sunabashiri, 1992), particularly when δ/H is large (Sakamoto and Oiwake, 1984; Sumner *et al*., 2004).

For smaller aspect ratios (*AR* smaller than the critical aspect ratio, see Figure 2.1(b)), the flow around the free end may completely suppress antisymmetric Kármán vortex shedding from the cylinder. The critical aspect ratio below which antisymmetric vortex shedding is suppressed varies in the literature, from $AR = 1$ to 7. The different critical values observed for the aspect ratio are caused, in part, by the influence of the plane wall boundary layer (Luo 1993), which differs in relative thickness (δ/D and δ/H) between the various studies. For instance, Okamoto and Sunabashiri (1992) observed that the critical value may lie between $AR = 2$ and 4, that is there is a change from symmetrical vortex shedding for $AR \leq 2$ to antisymmetrical vortex shedding when $AR \geq 4$. Sakamoto and Arie (1983) reported a critical value of $AR = 2.5$, for which there is a change from the Kármán-type vortex shedding to the arch-type vortex shedding as the finite cylinder aspect ratio reduces. Based on their numerical study, Fröhlich and Rodi (2004) also observed arch-type vortex shedding for a finite cylinder of $AR = 2.5$. The same authors also observed a critical value of $AR = 2$ for a rectangular prism. Some other critical values identified in literatures are $AR = 1$ (Uematsu *et al.,* 1990), $AR = 2$ (Okamoto, 1991), $AR = 3$ (Lee and Wang, 1987), $AR = 4$ (Kawamura *et al.,* 1984), $AR =$

6 (Luo, 1993) and AR = 7 (Fox and West 1993a)). Generally, at and below the critical aspect ratio, antisymmetric Kármán vortex shedding may be replaced with symmetric arch vortex shedding at a definite frequency (Lee, 1997; Okamoto, 1991; Okamoto and Sunabashiri, 1992; Taniguchi *et al*., 1981; Sakamoto and Arie, 1983; Tanaka and Murata, 1999), and the longitudinal tip vortices may no longer form (Fox and West, 1993a,b,c).

Kármán vortex shedding from a finite circular cylinder is strongly influenced by the tip vortices and the downwash flow. The interaction between downwash flow and Kármán vortex shedding is strongly influenced by AR and δ/H. A general observation in many studies is that the dimensionless vortex shedding frequency, or Strouhal number, St, decreases as AR decreases, because of the increasing influence of downwash (e.g. Park and Lee, 2000). Park and Lee (2002) investigated the wake structure of a finite circular cylinder of AR = 6 embedded in an atmospheric boundary layer at $Re_D = 2 \times 10^4$. They observed that the vortex shedding frequency and vortex formation length (which represents the distance from the stack where the separated shear layers eventually detached from the stack) are lower than those for uniform flow. They also reported that the mean streamwise velocity of the wake behind the finite cylinder in an ABL has a larger velocity deficit as well as higher streamwise turbulence intensity in the central region than for a finite cylinder in a uniform flow.

Due to the downwash from the free end, the location of the separation line on the side of the circular cylinder shifts forward and the mean drag coefficient, C_D, decreases as the aspect ratio decreases (see for example Kawamura *et al*., 1984; Okamoto and Sunabashiri, 1992; Sumner *et al.*, 2004) and is generally lower than for an "infinite" circular cylinder. Sarode *et al.* (1981) reported that the overall drag coefficient, C_D, for a

finite circular cylinder increases rapidly with aspect ratio for $AR < 4$ but only gradually when $AR > 4$.

The study presented in this thesis is an extension on previous work carried out by Heseltine (2003) and reported by Sumner *et al*. (2004). Some of their findings are briefly described below. Further insight into the distinct wake structure for cylinders smaller than the critical aspect ratio was obtained by Sumner *et al.* (2004), where a seven-hole pressure probe was used to measure the velocity in the wake region for finite circular cylinders of small aspect ratio (AR =3, 5, 7 and 9) under conditions where the cylinder was partially immersed in a turbulent boundary layer (δ/D = 2.6). From

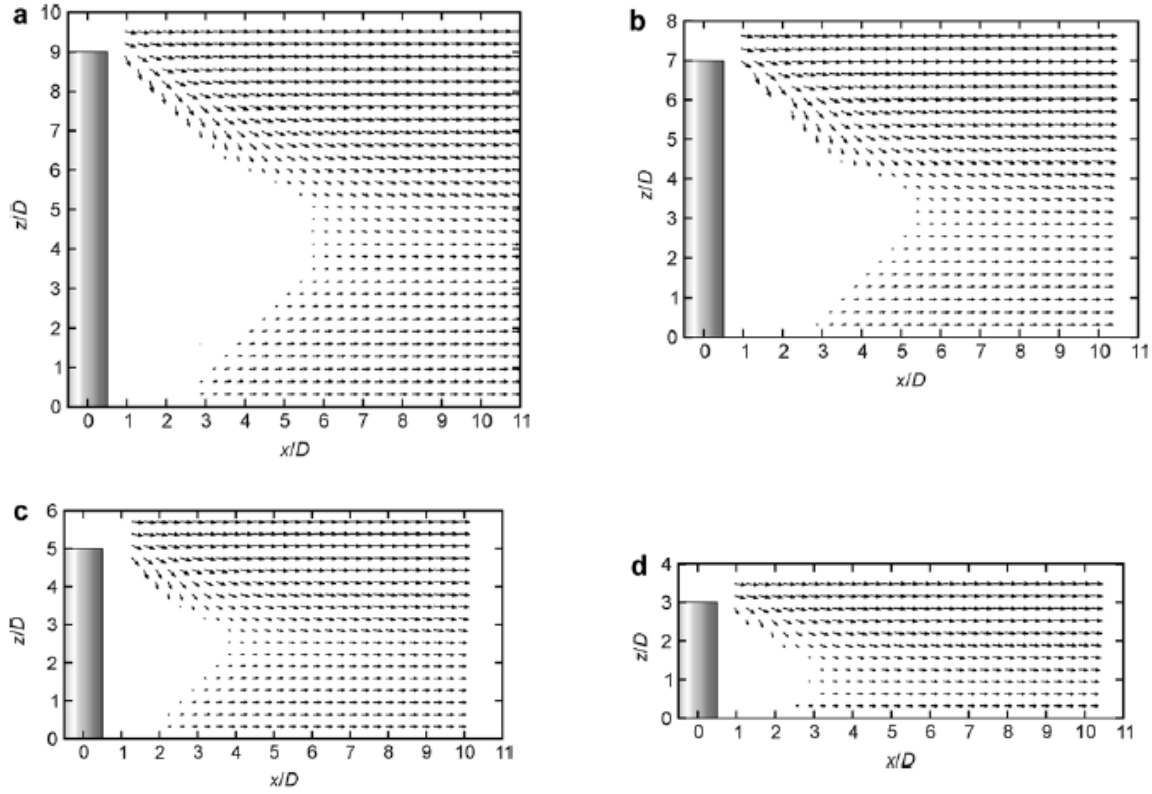

Figure 2.2: The time-averaged velocity filed along the wake centreline (y/D = 0) (a) AR = 9, (b) AR = 7, (c) AR = 5 and (d) AR = 3. (Reprinted from Sumner *et al*., 2004 with permission see, Appendix B, p. 228).

measurements of the time-averaged wake velocity field (Figure 2.2) and streamwise vorticity field (see Figure 2.3), they found that the wake structure of a very short circular cylinder of AR = 3 (Figures 2.2(d) and Figure 2.3(d)) was distinctly different from the more slender circular cylinders of AR = 5, 7, and 9 (Figures 2.2(a-c) and Figure 2.3(a-c)). For the case when AR = 5, 7 or 9, the wake was characterized by a strong downwash flow from the free end, an upwash flow from the base of the cylinder, a counter-rotating pair of tip vortex structures near the free end, and a second pair of counter-rotating vortices, known as base vortex structures, within the wall boundary layer. A strong Kármán vortex shedding signal was observed along most of the cylinder height. The streamwise vortex structures weakened with increasing streamwise distance from the cylinder. For AR = 3, which had a distinct wake structure, the tip vortices and downwash remained but the base vortices and upwash were absent. Furthermore, the

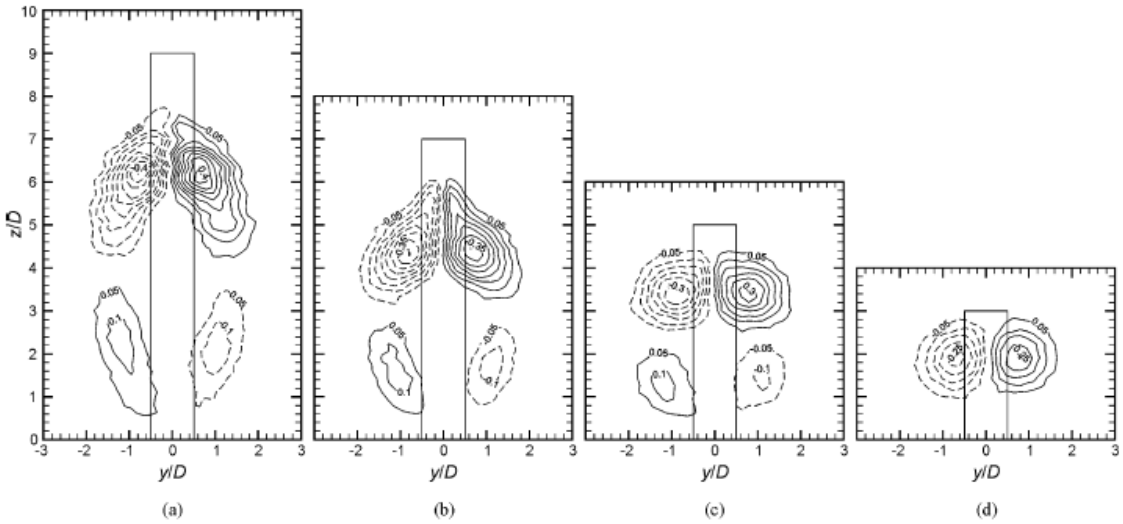

Figure 2.3: The time-averaged streamwise vorticity at x/D = 6 for (a) AR = 9, (b) AR = 7, (c) AR = 5 and (d) AR = 3. Vorticity contour increment is 0.05 and minimum vorticity contour is ±0.05, solid lines represent positive (CCW) vorticity and dashed lines represent negative (CW) vorticity. (Reprinted from Sumner *et al.*, 2004 with permission, see Appendix B, p. 228).

downwash extended almost to the wall and a strong vortex shedding signal was mostly absent along the cylinder height, except in the region close to the wall, where a weak signal was detected. Their study, however, was limited to the time-averaged properties of the flow.

The recent work of Wang *et al.* (2006) investigated the effect of the ground plane boundary layer thickness on the wake structure of a finite square cylinder of $AR = 5$ using particle image velocimetry (PIV). Three different boundary layer thicknesses at the location of the cylinder, $\delta/H = 0.10$, 0.20 and 0.38, were considered and the freestream Reynolds number was $Re_D = 1.2 \times 10^4$. They reported that with increasing boundary layer thickness, the upwash flow from the ground plane and, thus, the base vortex structures, were enhanced, while the tip vortex structures were weakened, thereby limiting the downwash flow within the vicinity of the cylinder's free end. In addition, as the boundary layer thickness increases, likelihood of antisymmetrical vortices increases near the free end, but reduces near the ground plane. For $\delta/H = 0.10$, they noted that "symmetrically arranged vortices overwhelm antisymmetrically arranged vortices" near the free end of the cylinder, which they argued was due to the strong downwash flow that dominates the free end.

2.4 Jet in Cross-flow

A jet in cross-flow can be injected through either an orifice on the ground plane, which is referred to as ground-level source jet, or from an elevated source, as in the case of a stack. Extensive work on the ground-level source jet is documented in the literature (e.g., Moussa et al., 1977; Andreopoulos and Rodi, 1984; Fric and Roshko, 1994; Smith and Mungal, 1998; Lim *et al*., 2001; Wegner *et al*., 2004; New *et al*., 2006) For a

ground-level source jet, four distinct vortical structures (see Figure 2. 4) have been identified (e.g. Fric and Roshko, 1994; Smith and Mungal, 1998), namely the horseshoe vortices, the jet shear layer or leading-edge vortices (Lim *et al*., 2001), the wake structures and the counter-rotating vortex pair. Wegner *et al.* (2004) reported that for a ratio of jet flow velocity to crossflow velocity, $R = 0.5$, the jet mixing and the strength of the counter-rotating vortex pair increases with angle of the inclination of the jet to the cross-flow. The jet geometries have also been observed to influence the jet flow behaviour and the vortical structures (e.g. Plesniak and Cusano, 2005; New *et al.,* 2006). For example, New *et al.* (2006) noted that there is an increase in the jet penetration and a reduction in the near-field entrainment of the cross-flow when the exit velocity profile is parabolic rather than when the velocity profile is "top-hat". With increasing R, Plesniak and Cusano (2005) reported that there is an increase in the size and strength of the counter-rotating vortex pair as well as in the jet penetration and entrainment and thus enhanced mixing of the jet flow with the cross-flow.

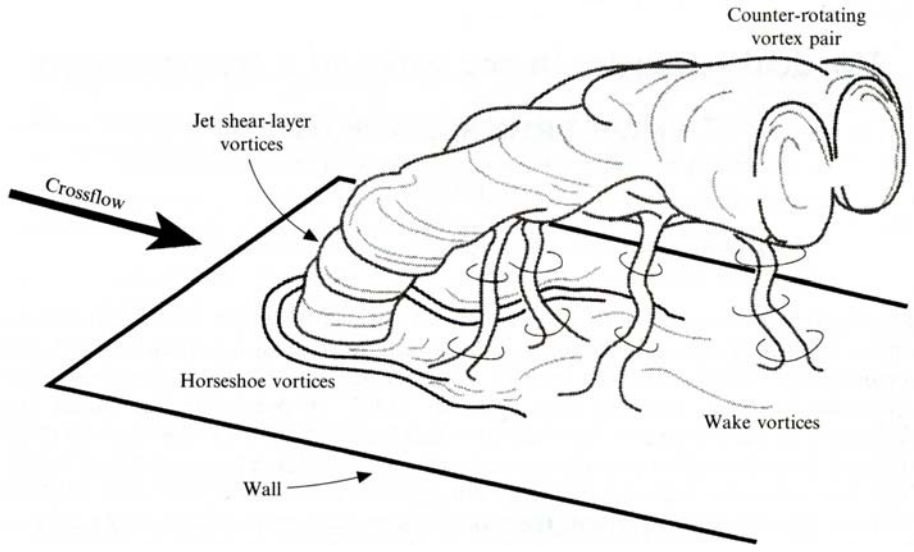

Figure 2.4: The vortical structures of the ground-source jet in the crossflow ((Reprinted from Fric and Roshko, 1994 with permission of Cambridge University Press, see Appendix B, p. 229).

For the elevated jet in cross-flow, considerable attention in the literature has focused on the jet rise (e.g., Overcamp and Ku, 1988) and recently, Canepa (2004) presented an overview of downwash effects on pollutant dispersion. But few relatively fewer studies centred on the local flow field of the combined stack and jet. These studies have shown the flow field to be characterized by the complex interactions between the jet and stack wake regions, shear produced by the upward momentum of the jet, and downwash (Moussa *et al*., 1977; Eiff *et al*., 1995; Eiff and Keffer, 1997, 1999; Huang and Hsieh, 2002, 2003; Huang and Lan, 2005, Mahjoub Säid *et al*., 2005).

From studies of the flow topology in the vertical plane along the wake centreline (the *x*-*z* plane) using LDV and flow visualization, Huang and Hsieh (2002, 2003) classified the stack and jet wake flow patterns into four regimes based on the

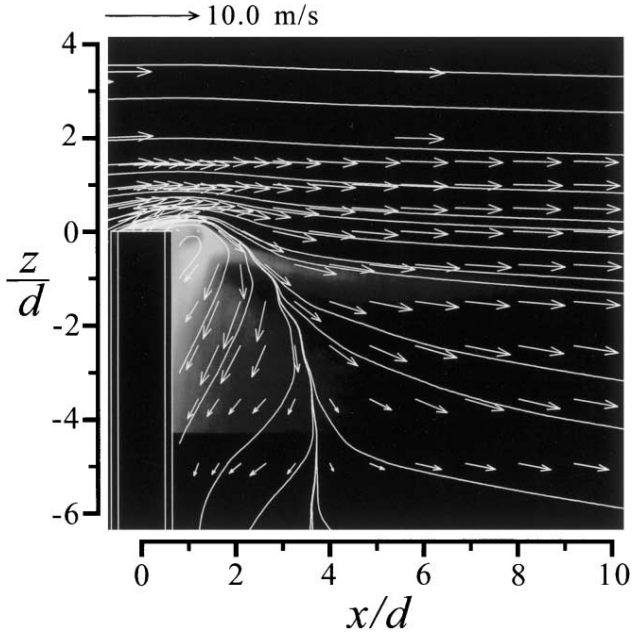

(a) Downwash flow, $R_m = 0.10$

Figure 2.5: The flow structures of downwash, crosswind-dominated, transitional and jet dominated flow for elevated jet in a cross-flow ((Reprinted from Huang and Hsieh, 2002 with permission, see Appendix B, p. 230).

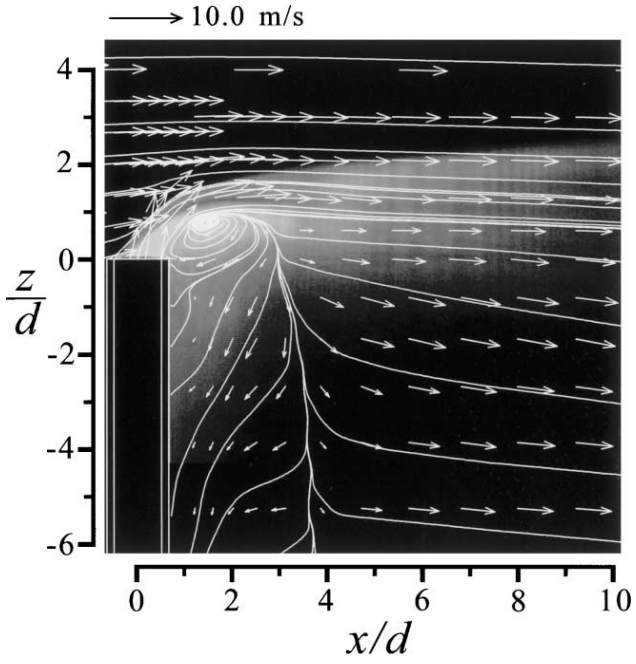

(b) Crosswind-dominated flow, $R_m = 0.95$

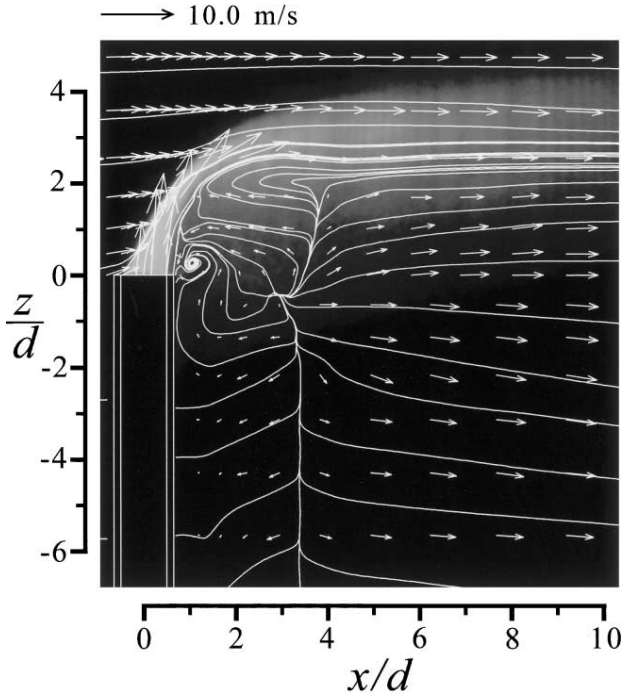

(c) Transitional flow, $R_m = 2.70$

Figure 2.5 continued.

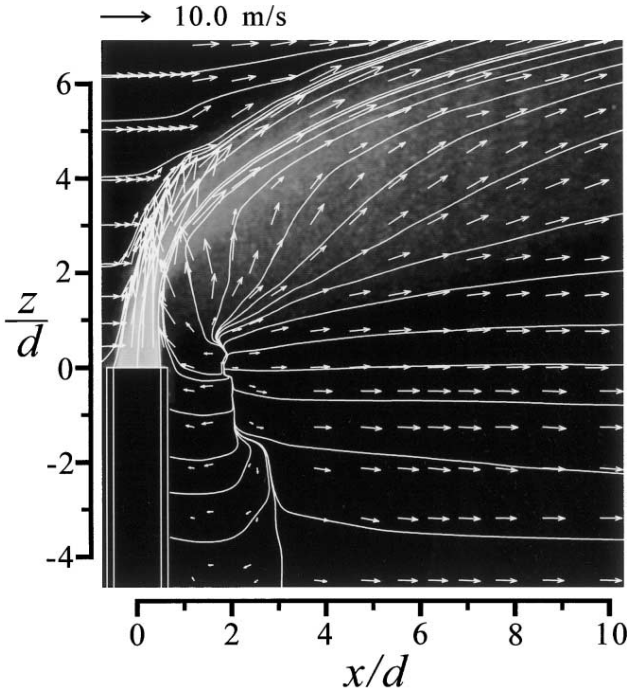

(d) Jet-dominated flow, R_m = 17.36

Figure 2.5 continued

approximate value of R (see Figure 2.5): (i) downwash flow ($R < 0.95$), (ii) crosswind-dominated flow ($0.95 < R < 1.4$), (iii) transitional flow ($1.4 < R < 2.4$), and (iv) jet dominated flow ($R > 2.4$). The classification was made for a stack of $AR = 25$ and $d/D = 0.78$ operating at $\mathrm{Re}_D = 2 \times 10^3$ and $\mathrm{Re}_d = 200$ to 8×10^3. The effect of Re_D, Re_d, AR, δ/H and other parameters on the number of flow regimes and the flow regime boundaries has not been extensively studied. In the downwash flow regime, the jet is deflected through a large angle from the vertical axis of the stack. In the cross-wind-dominated flow regime, the downwash effects are reduced in the jet wake. A clockwise vortex forms near the free end of the stack due to interaction between the jet shear and downwash (Huang and Hsieh, 2002, 2003). At higher jet-to-cross-flow velocity ratios, the upward momentum of the jet overcomes the downwash effect, and the jet rises and

bends into the freestream. For the jet-dominated flow regime, the high upward momentum of the jet, and the shear produced by the jet, result in a strong upwash velocity field, particularly in the jet wake region (Huang and Hsieh, 2002, 2003; Hsieh and Huang, 2003).

A similar study of the local flow field of a small-aspect-ratio stack, AR = 8.3 and d/D = 0.83, was carried out by Mahjoub Säid *et al*. (2005, 2007) and they identified three zones within the jet (see Figure 2.4): zone 1, immediately above the stack exit, where the jet dominates the flow; zone 2, where the jet begins to bend and the jet flow and cross-flow have the same velocity; and zone 3, further downstream, where the cross-

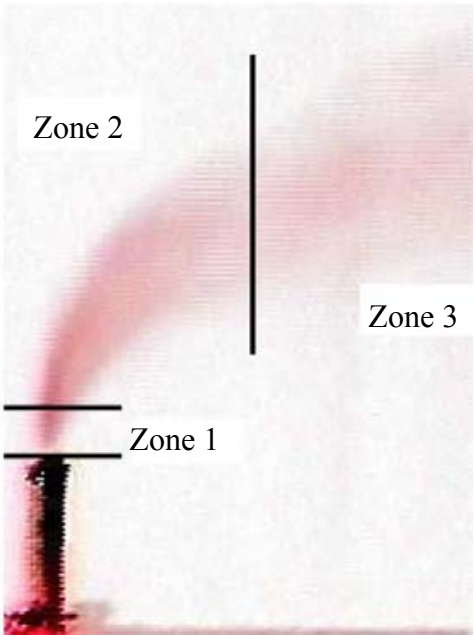

Figure 2.6: Different region of the plume evolution. ((Reprinted from Mahjoub Säid *et al*., 2005 with permission, see Appendix B, p. 231).

flow dominates the flow. Depending on the value of R and the corresponding flow regime, one or more of these zones may be absent. They also identified four different flow regimes which are the same as those of Huang and Hsieh (2002, 2003). These

authors also observed the presence of Kelvin-Helmoltz instabilities on the crosswind side of the elevated jet flow and the orientation of this structure was found to depend on the value of R. For this study, the ground plane boundary layer thickness relative to the stack height was 0.10, and the crosswind Reynolds number based on the stack external diameter ranged between $Re_D = 2.7 \times 10^4$ and 2×10^5.

The elevated jet in cross-flow, and the local flow field near the jet exit, were also studied by Eiff *et al*. (1995) and Eiff and Keffer (1997, 1999). Using spectral analysis, pattern recognition techniques and multipoint hot-wire measurements, they investigated the interaction between the jet and stack wakes at $x/D = 11$ for $AR = 6$, 8 and 11, $d/D = 0.42$, 0.63, and 0.83, $Re_D = 7.5 \times 10^3$ to 6.0×10^4, $Re_d = 3.8 \times 10^4$, and $R = 1.5$, 3, and 6. Their studies showed that Kármán-like vortex structures in the stack wake region are "locked-in" to, or synchronized with, similar vortex structures in the jet wake region over a range of velocity ratios ($R = 1.5$, 3 and 6) and diameter ratios ($0.63 \leq d/D \leq 0.83$). Lock-in does not occur at smaller d/D, rather, the vortex dynamics in the jet wake become similar to the ground-level source jet (Eiff and Keffer, 1999). The study conducted by Moussa *et al*. (1977) for a stack of $AR = 24$ and $d/D = 0.93$ also showed that the same vortex shedding frequency occurs in both the stack and jet wakes and they noted that the shedding from the jet flow is controlled by the shedding from the stack. They also observed that the dimensionless parameters that govern the similarity in the non-buoyant flow field of a jet in crossflow include Re_d, Re_D, R, and St.

A study of the shear-layer vortices in the stack jet and wake regions, and the dominant frequencies associated with these structures has been conducted by Huang and Lan (2005). Their study was conducted using a stack of $AR = 25$, $d/D = 0.78$, $Re_D = 2051$ and R varied between 0 and 1.4. Based on smoke flow visualization techniques,

they observed five characteristic flow structures, which are: mixing-layer type vortices ($R < 0.15$), backward-rolling vortices ($0.15 < R < 0.34$), forward-rolling vortices ($0.34 < R < 0.49$), swing-induced mushroom vortices ($0.49 < R < 0.1.01$), and jet-type vortices ($R > 1.01$). They noted that the "behaviours and mechanisms of the vortical flow structure" in the shear layer are significantly distinct for different flow structures. In addition, they observed that the value of St decays exponentially as R increases.

2.5 Summary

As mentioned above and in the previous Chapter, relatively few studies focus on the turbulent wake of a finite circular cylinder and comprehensive information about the turbulence characteristics of the wake are not available in the open literature. The effects of the aspect ratio on the Reynolds stress tensor and higher-order moments, for example, have not been fully addressed. The literature cited indicates that the wake structure of a stack, which has environmental implications, is yet to be fully understood. The effect of a jet flow from a stack on the vortex shedding frequency, vortex structures and turbulence characteristics of the stack, for example, are not well known. The focus of this study is, therefore, to address some of these important characteristics of the wake of a finite circular cylinder and a stack.

CHAPTER 3

EXPERIMENTAL SET-UP AND INSTRUMENTATION

3.1 Introduction

In this chapter, the experimental set-up and the instrumentation used for this study are described. The wind tunnel facility and the associated instrumentation and pressure probes are described in Sections 3.2 to 3.4. Detailed information on the thermal anemometry system and the seven-hole pressure, which were the velocity measurement techniques used, and their calibration, are presented in Sections 3.5 and 3.6. The air flow meter and the experimental models (finite circular cylinder and stack) are presented in Sections 3.7 and 3.8. The properties of the ground plane boundary layer, the description of the experiments, and the post processing and uncertainty analysis are presented in Sections 3.9, 3.10, and 3.11 respectively.

3.2 Wind Tunnel

The wind tunnel used for this work is a closed-return type located in the Department of Mechanical Engineering, University of Saskatchewan (Figure 3.1(a)). It has two separate test sections: the low-speed and high-speed test sections. The dimensions of the low-speed test section are 2.97 m (height) × 2.4 m (width) × 7.01 m (length), while those of the high-speed test section are 0.91 m (height) × 1.13 m (width) × 1.96 m (length). For

this study, experiments were performed within the high-speed test section of the wind tunnel. In this test section, the longitudinal freestream turbulence intensity was less than 0.6% and the velocity non-uniformity outside the test section wall boundary layers was less than 0.5% over the speed range of the present experiments (Sumner *et al.*, 2004).

(a)

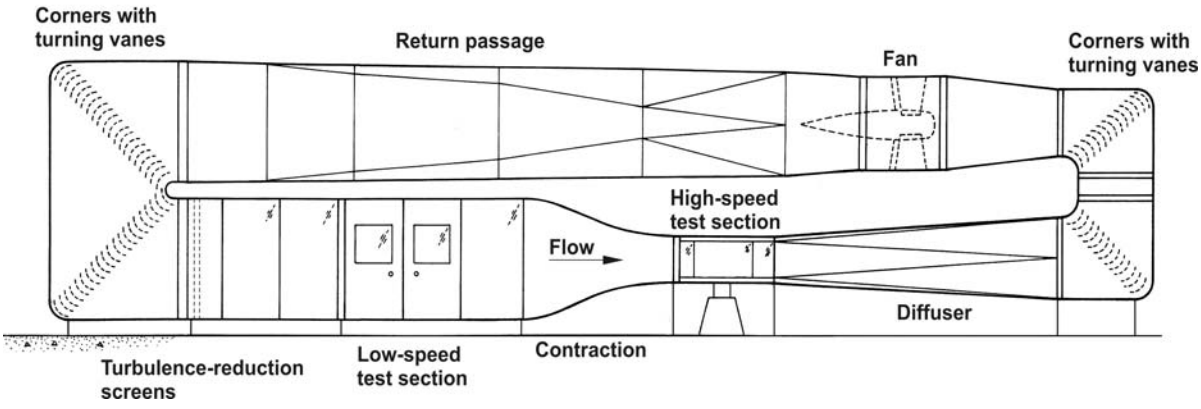

(b)

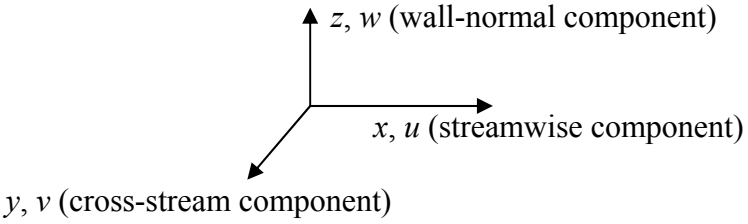

Figure 3.1: (a) Schematic diagram of the wind tunnel, and (b) Co-ordinate system.

The air flow is driven by a 75-kW, constant-speed, variable-pitch fan that can provide freestream velocities up to U_∞ = 60 m/s within the high-speed test section. As shown in Figure 3.1(a), the air flow generated by the fan passes through a diffuser (labelled as the return passage on Figure 3.1(a)) where it is expands and then passes through two sets of turning vanes located at the top and bottom corners where it redirected through 180^o. Turbulence reduction screens are located at the exit of the turning vanes. The screens reduce the turbulence intensity in the air flow produced by

the fan. The flow enters the low-speed test section which acts as a large settling chamber for the air flow, and then enters the high-speed test section through a 7:1 contraction. The flow then enters a diffuser to the fan region and recirculates as shown in Figure 3.1(a).

An aluminum ground plane with dimensions 1.03 m (width) x 1.82 m (length) was installed on the floor of the high-speed test section. This plane was clamped to a Plexiglas ground plane that is permanently fixed to the test section floor. A roughness strip located about 200 mm from the leading edge of the ground plane was used to enhance the development of a ZPG turbulent boundary layer on the ground plane. A circular hole was drilled on the ground plane at about 900 mm from the leading edge. The models used for these experiments were mounted vertically on a six-component force balance located below the test section and extended into the test section through this hole. The test section side-walls are made of Plexiglas in order to allow visual inspection of the probe position and model configurations as well as the flow behaviour during the experiments, especially for flow visualization. The wind tunnel data were acquired using a computer with a 1.8-GHz Intel Pentium 4 processor, a National Instruments PCI-6031E 16-bit data acquisition board, and LabVIEW software.

The test section is equipped with a traversing wing which enables automated flow measurements at any position, and is positioned by three stepper motors. The traversing wing can be used to mount hot-wire probes (Section 3.5) and the seven-hole probe (Section 3.6). The stepper motors are controlled using the LabVIEW software on the computer, which has a National Instruments PCI-7344 motion control board. The signal from the computer is sent through the Universal Motion Interface (UMI 7764) to the Intelligent Motion System (IMS 1007) micro-stepping (MS) drivers and each MS

driver can be adjusted from 400 to 51,200 steps per revolution. The signal from IMS controls the stepper motor, which has a movement of 1.8^{o} per step. Using the LabVIEW software, the location of the measurement probe was achieved by first setting a reference position within the test section region. For a set of measurements, the distances in the three directions (x, y, z) and the number of grid points are specified, and the program automatically moves the probe and stores the numerical values of the probe location as well as the measured parameters at each location in a named file. In order to prevent damage of a measuring probe by contact with the ground plane or a model mounted in the test section, the traversing wing is equipped with limit switches in each direction.

3.3 Pressure Probes

The freestream conditions were obtained with a Pitot-static probe (United Sensor, 3.2-mm diameter) and Datametrics Barocell absolute (600A-1000T-513-H21X-4) and differential (590D-10W-2QB-VIX-4D) pressure transducers. The probe was inserted into the side-wall of the test section and located at about 400 mm from the contraction exit, 340 mm above the ground plane, and extending 270 mm into the test section. This eliminated the effect of wall-proximity on the probe.

A modified United Sensor boundary layer Pitot probe (BA-.025-12-C-11-.650), with an outer diameter of d_p = 0.60 mm, was used to measure the boundary layer on the ground plane. The probe was mounted to the stepper-motor-controlled x-y-z traversing wing inside the test section (Section 3.2) and was connected to a Validyne Model P55D differential pressure transducer. In order to examine the development of the boundary layer profile on the ground plane, measurements were taken at three different locations:

x/D = -4, 0, and 4, for finite cylinder experiments and, *x/D* = -10, 0, and 10, for the stack experiments, where *x/D* = 0 is the location of the cylinder and stack which is 900 mm from the leading edge of the ground plane. The boundary layer thickness was defined as the point where the local mean velocity was 99% of the freestream velocity.

3.4 Temperature, Density and Viscosity Measurements

The freestream temperature was measured with an analog integrated circuit temperature sensor. It was located at the downstream end of the test section and connected to the control box of the wind tunnel with the analog output fed to the data acquisition system. The density of the air (ρ_∞) was determined using the ideal gas equation,

$$\rho_\infty = \frac{P_\infty}{R_g T_\infty} \ , \tag{3.1}$$

where R_g is the gas constant for air (287 J/kgK), T_∞ (K) is the freestream temperature, and P_∞ (Pa) is the absolute freestream static pressure. The kinematic viscosity of the air, v_∞, is determined using the Sutherland correlation as given below (White, 2003):

$$v_\infty = 1.453x10^{-6} \frac{T_\infty^{\ 1.5}}{\rho_\infty (T_\infty + 110.4)} \tag{3.2}$$

3.5 Thermal Anemometry

The thermal anemometry probes were used to measure the vortex shedding frequency, the ground plane boundary layer velocity profile and the wake velocity fields. In this study, a constant temperature anemometer (CTA) type of thermal anemometry was employed (Bruun, 1995). For the CTA type, the change in the current supplied to a

heated sensor (wire, film), due to the changes in flow conditions (e.g. velocity), show as changes in the voltage from the anemometer output. These probes have the ability to measure both the mean and fluctuating components of the velocity in a flow.

Measurements of the vortex shedding frequency, f_s, were made with a TSI IFA-100 constant temperature anemometer and a single-component hot-wire probe (TSI model 1210-T1.5, see Figure 3.2(a)). The sensor is made of platinum-plated tungsten wire and has a diameter of 3.8 μm, a sensing length of 1.27 mm, and the distance between supports is 1.52 mm. The hot-wire probe was not calibrated because it was only used to measure the velocity fluctuation power spectra to obtain the vortex shedding frequency. Five thousand samples were taken at a sampling frequency of 5,000 Hz. This sampling frequency is sufficiently high to measure a vortex shedding frequency of the order of 100 Hz. A total of 250 spectra were averaged in the frequency domain to produce each power spectrum. From the vortex shedding frequency

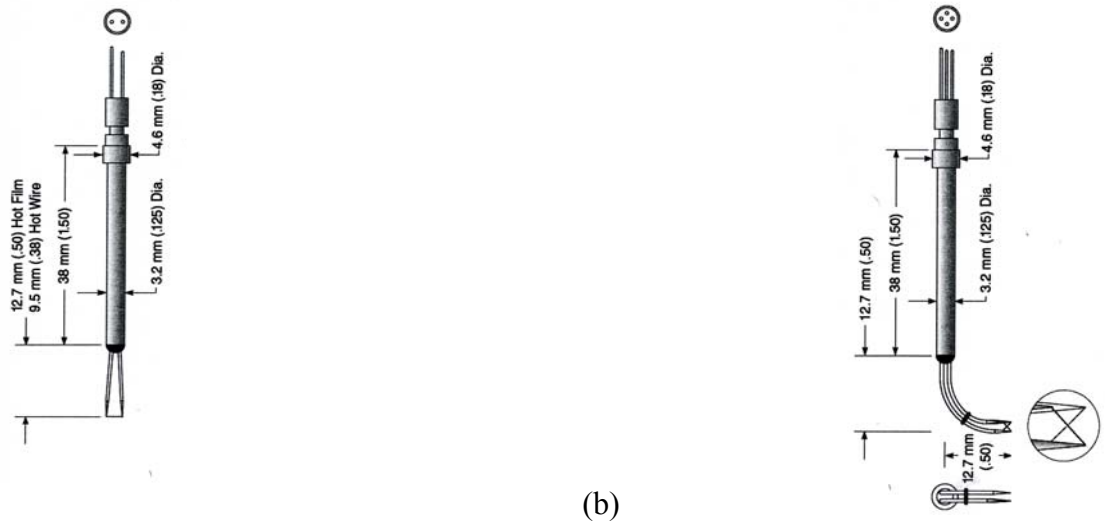

(a) (b)

Figure 3.2: Thermal anemometry probes (a) single sensor hot-wire, and (b) X-probe (Reprinted from TSI Catalogue with permission: *Courtesy: TSI Incorporated,* see Appendix B, p. 232).

information, the Strouhal number, *St*, was obtained.

Wake velocity measurements were made with a TSI model 1243-20 constant-temperature boundary layer cross-film (X) probe (see Figure 3.2(b)) and the TSI IFA-100 anemometer. The sensors of this probe are made of platinum wire and have a diameter of 50.8 μm, a sensing length of 1.02 mm, and the distance between the supports is 1.65 mm. The probe was oriented to measure the streamwise, u, and wall-normal, w, velocity components in the model wake. The probe was manoeuvred to the measurement points using the wind tunnel's three-axis computer-controlled traversing system (Section 3.2). At each measurement point, 100,000 instantaneous velocity measurements per channel were acquired at a sampling rate of 10 kHz per channel after low-pass filtering at 5 kHz. The same probe was also used to measure the boundary layer velocity profile on the ground plane (Section 3.9) and the jet exit velocity profile (Section 3.8.2).

The calibration of the X-probe was carried out by positioning it at known angles to the flow direction using an automated variable-angle calibrator mounted in the centre of the test section of the wind tunnel. This calibrator has an angular resolution of 0.9^o (and is described further in Section 3.6.1). For each velocity-yaw angle pair (U_∞, α), where U_∞ is the freestream velocity (see Figure 3.3), a unique voltage pair (E_1, E_2) is obtained. The probe is positioned so that the binormal velocity component, the velocity component perpendicular to both films, is equal to zero. For this probe, the angles α_1 and α_2 are both equal to 45^o, which give the flow-angle range for the probe to be $-45^o \leq \theta \leq 45^o$. The orientation of the probe to the flow (yaw angle, α) and velocity, U_∞, were varied between $\pm$ 32.4^o and 5 – 50 m/s, respectively. The freestream conditions were obtained with the Pitot-static probe and Datametrics Barocell absolute and differential

pressure transducers described earlier (Section 3.3). At a given freestream velocity, the angular position (α) of the probe was varied at an interval of 8.1°, and the corresponding voltage pair (E_1, E_2) is obtained, where E_1 and E_2 are the voltage from film 1 and film 2, respectively. Figure 3.4 shows a typical unique calibration map that presents the

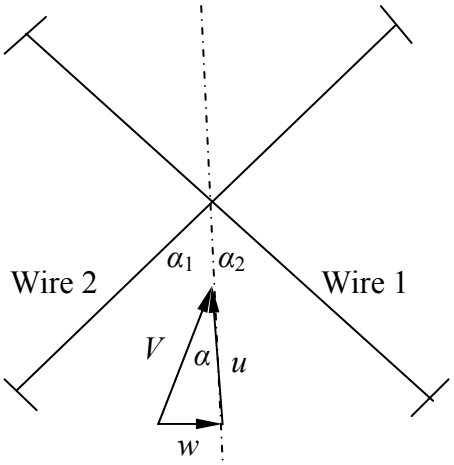

Figure 3.3: The definition of the yaw angle in the plane of the prong.

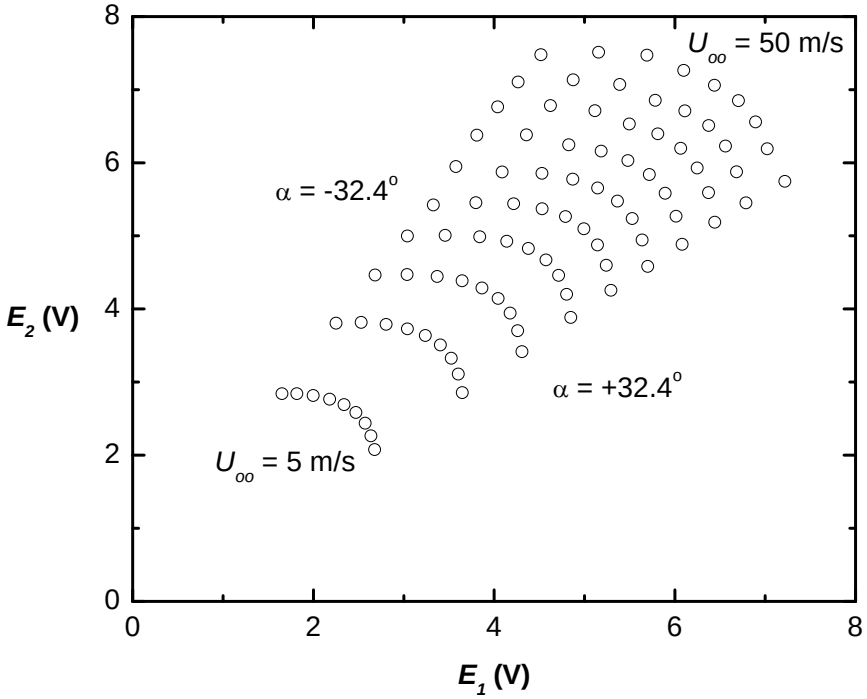

Figure 3.4: Calibration map for the X-probe anemometer with freestream ranging between U_∞ = 5 m/s and 50 m/s at an interval of 5 m/s and $\Delta\alpha = 8.1^o$.

relationship between (E_1, E_2) and (U_∞, α). Two variables X and Y, denoting the streamwise and wall-normal components of the probe, are determined from the film voltages, E_1 and E_2, as follows.

$$X = E_1 + E_2$$
$$Y = E_1 - E_2 \tag{3.3}$$

These two variables were then used to obtain two-dimensional third-order polynomials expressions, similar to the method used by Österlund (1999) and Akinlade (2005), for V and α,

$$V = a_1 + a_2 X + a_3 Y + a_4 X^2 + a_5 XY + a_6 Y^2 + a_7 X^3 + a_8 X^2 Y + a_9 XY^2 + a_{10} Y^3, \tag{3.4}$$

$$\tan\alpha = b_1 + b_2 X + b_3 Y + b_4 X^2 + b_5 XY + b_6 Y^2 + b_7 X^3 + b_8 X^2 Y + b_9 XY^2 + b_{10} Y^3, \tag{3.5}$$

where are a and b are constants.

The above equations were solved using a least-squares method, to determine the coefficients a_1 to a_{10} and b_1 to b_{10}. These coefficients are then stored and used in the experiments to determine the values V and α for given values of E_1 and E_2 when the probe is used in an unknown flow. The instantaneous streamwise and wall-normal velocities can then be obtained from the following equations.

$$u = V\cos\alpha$$
$$w = V\sin\alpha \tag{3.6}$$

To account for the variation in temperature during the calibration and actual experiment, the probe voltages were corrected before being used in equations (3.4) and (3.5). In this study, an expression suggested by Bruun (1995) was used to correct the probe voltage,

$$E_{corr} = E_{meas}\left(\frac{250 - T_{meas}}{250 - T_{cal}}\right)^{0.5} \tag{3.7}$$

where E_{corr} is the corrected voltage signal, E_{meas} is the measured voltage during the experiment, T_{meas} is the experimental air temperature, and T_{cal} is the calibration air temperature, both in degrees Celsius. Equation (3.6) is valid when the change in air temperature is ± 5°C (Akinlade, 2005).

3.6 Seven-Hole Pressure Probe

The seven-hole pressure probe (Figure 3.5) is a non-nulling, directional velocity probe used to measure the local time-averaged velocity vector of a flow. It is conical in shape with a cone angle between 30° and 45° and has one inner hole (or port), which is surrounded, by six outer holes (or ports). The probe can be used to measure (typically) three velocity components of the flow. The probe is capable of measuring both local

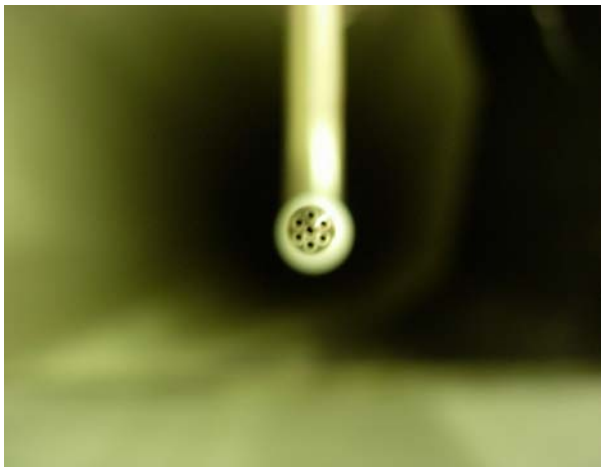

Figure 3.5: Picture of a seven-hole probe.

total and static pressures at flow angles up to 80° from the probe axis. The seven-hole probe is generally small in size so that its interference with the flow can be minimized.

Based on the pressure information from the seven holes, four flow properties, which are the local pitch angle coefficient, C_{Pr}, yaw angle coefficient, C_{Pt}, total pressure coefficient, C_{Ptotal}, and dynamic pressure coefficient, C_q, are computed at a specific location (Zilliac, 1993; Sumner, 2002).

The combination of the pressure information to be used to compute the four coefficients depends upon which the hole has the highest pressure. For flows with low angles, hole 7 (see Figure 3.6) experiences the highest pressure and the flow is attached to the probe. In this case all the measured pressures are used to calculate the four flow coefficients. In the case of high-angle flow (see Figure 3.7), the flow does not remain attached over the entire surface of the probe and therefore one of the six outer ports measures the highest pressure. The holes in the region of separated flow would not be

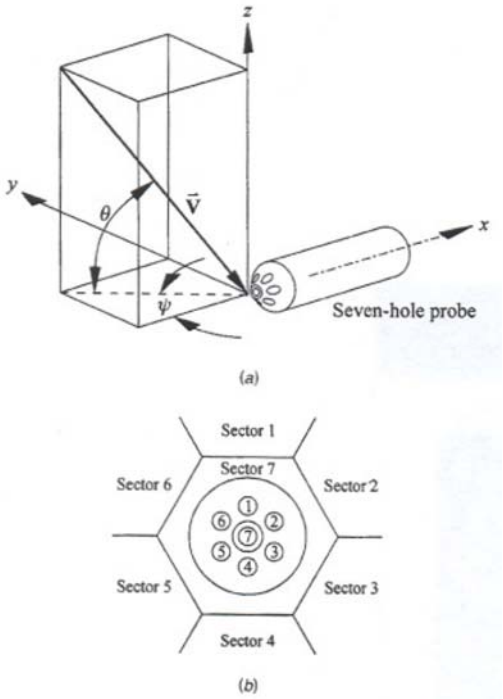

Figure 3.6: (a) Flow angle nomenclature; (b) sectoring scheme based on hole numbers 1 through 7 (Reprinted from Sumner, 2002 with permission, see Appendix B, p. 233).

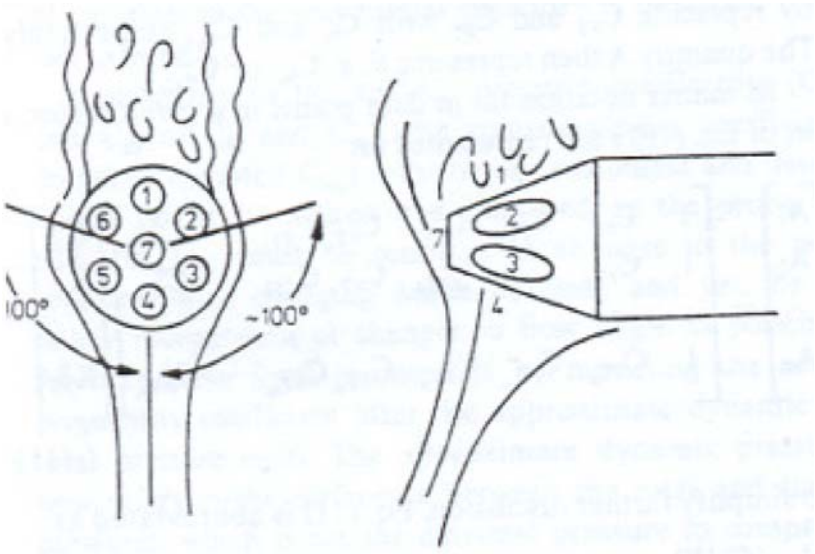

Figure 3.7: Flow over probe at high angle of attack (Reprinted from Gerner *et al*., 1984 with permission, see Appendix B, p. 234).

sensitive to the flow and therefore they cannot be used to determine the flow coefficients. As a result of this difference between the low-angle and high-angle flow, a sectoring approach is normally employed, based on the port that measures the highest pressure (see Figure 3.6b).

The four coefficients are defined (Sumner, 2002) for low-angle flow as follows:

$$C_{\mathrm{Pr},7} = \frac{2(P_4 - P_1) + (P_3 - P_6) + (P_2 - P_5)}{2(P_7 - \overline{P_7})}, \tag{3.8}$$

$$C_{Pt,7} = \frac{(P_3 - P_6) + (P_2 - P_5)}{\sqrt{3}(P_7 - \overline{P_7})}, \tag{3.9}$$

$$C_{Ptotal,7} = \frac{P_7 - P_{total}}{P_7 - \overline{P_7}}, \tag{3.10}$$

$$C_{q,7} = \frac{P_7 - \overline{P}_7}{q}, \tag{3.11}$$

where

$$\overline{P}_7 = \frac{1}{6}\sum_{n=1}^{6} P_n \tag{3.12}$$

and P_1 through P_7 are the respective pressures registered at holes 1-7, P_{total} is the local total pressure and q is the local dynamic pressure.

For high-angle flows, the above coefficients are modified to reflect the port n that measures the highest pressure, as follows:

$$C_{\mathrm{Pr},n} = \frac{P_n - P_7}{P_n - \overline{P}_n}, \tag{3.13}$$

$$C_{Pt,n} = \frac{P_{n-1} - P_{n+1}}{P_n - \overline{P}_n}, \tag{3.14}$$

$$C_{Ptotal,n} = \frac{P_n - P_{total}}{P_n - \overline{P}_n}, \tag{3.15}$$

$$C_{q,n} = \frac{P_n - \overline{P}_n}{q}, \tag{3.16}$$

where

$$\overline{P}_n = \frac{P_{n+1} + P_{n-1}}{2}. \tag{3.17}$$

In the equation (3.17), P_{n+1} and P_{n-1} are pressures at the ports adjacent to port P_n. From the determined flow properties, the local dynamic pressure, q, is computed using equation (3.18) below, and appropriate expressions from the above equations, depending on the nature of the flow,

$$q = \frac{P_n - \overline{P}_n}{C_q} \tag{3.18}$$

The local velocity vector V at a given location is calculated from

$$V = \sqrt{\frac{2q}{\rho_\infty}}. \tag{3.19}$$

The three velocity components which are function of V, pitch angle, θ, and yaw angle, ψ, as shown in Figure 3.6(a), are determined for each location using the following expressions.

$$u = V\cos\theta\cos\psi \tag{3.20}$$

$$u = V\cos\theta\sin\psi \tag{3.21}$$

$$u = V\sin\theta \tag{3.22}$$

There are three major sources of error in seven-hole probe measurements: the calibration process and the flow interference effects (Rediniotis *et al.,* 1993). First, because the probe is generally calibrated (see Section 3.6.1 below) under uniform, low-turbulence, steady-state conditions, using the probe in a high-turbulence flow or under unsteady conditions can introduce errors to the measurements. Second, being an intrusive probe, the seven-hole probe may interfere with the flow and therefore affect the properties and pattern of the flow. In addition, the performance of a seven-hole probe is sensitive to the probe Reynolds number (Sumner, 2002).

3.6.1 Calibration of Seven-Hole Probe

The seven-hole pressure probe used in the present study was manufactured by Engineering Shops, College of Engineering, University of Saskatchewan. It is made up of a 3.45-mm-diameter outer stainless steel sleeve with a cone angle of 30^{o} and seven close-packed 1-mm-diameter stainless steel tubes fitted inside the outer sleeve. The calibration of the probe was carried out inside the high-speed test section of the wind tunnel.

The probe was calibrated by positioning it at known angles to the flow direction using a two-axis, automated variable-angle calibrator in the centre of the test section of the wind tunnel as shown in Figure 3.8 (the same calibrator used for the X-probe, Section 3.5). The probe Reynolds number based on the probe diameter and freestream velocity of U_{∞} = 20 m/s is about 3300. The probe was aligned with the freestream flow

Figure 3.8: The automated variable-angle calibrator and the seven-hole probe.

by varying its orientation until the outer six ports all measured approximately the same pressure. The probe orientation was varied between +72.9^{o} and -72.9^{o} at an interval of 8.1^{o} for both pitch and yaw angles. At each location, the seven pressures were measured with a Scanivalve ZOC-17 pressure scanner. The Scanivalve ZOC (Zero, Operate, Calibrate) electronic pressure scanners make use of individual pressure sensors for each pressure input. The scanner contains a pneumatic calibration valve, a high-speed multiplexer and an instrumentation amplifier. The calibration valve allows the ZOC pressure sensors to be automatically calibrated on-line and utilizes 'Normally Px' valve logic (Scanivalve Corp. Catalogue). The on-line calibration process follows four modes of operation, which are: operate mode, calibrate mode, purge mode, and leak test mode. The detailed information about these modes and other information about ZOC 17 pressure scanner can be found in the Scanivalve Corp. Catalogue. For this study, a ZOC with eight pressure input channels (ZOC-17IP/8Px, SN: 541) is employed (see Figure 3.9). The pressure signals were sampled at 500 Hz for 20 s (i.e. 10,000 samples), with a

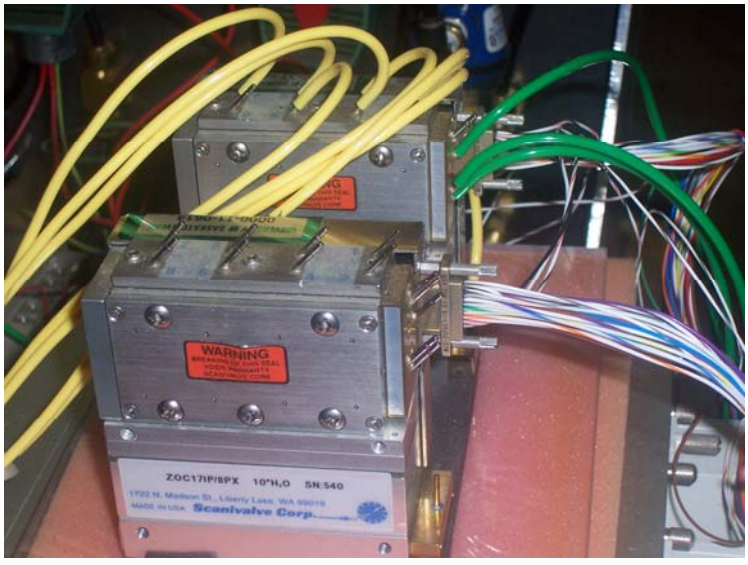

Figure 3.9: Diagram of two 8 channels ZOCs (only one was used).

20s delay time in order for conditions to reach steady-state and for the probe to be repositioned. Based on the pressure information, C_{Pr}, C_{Pt}, C_{Ptotal}, and C_q were determined using equations (3.8) to (3.12) for sector 7 and equations (3.13) to (3.17) for sectors 1-6.

The freestream conditions were obtained with a Pitot-static probe (United Sensor, 3.2-mm diameter) and Datametrics Barocell absolute and differential pressure transducers mentioned earlier in Section 3.3. The in-situ calibration of the probe under the same freestream conditions in which the experiments are to be performed reduces the errors caused by differences between the test flow and calibration conditions.

Figure 3.10 shows the $\theta - \psi$ map of the sectors as selected by the calibration scheme. Each sector of the map with their respective symbols indicates the port that

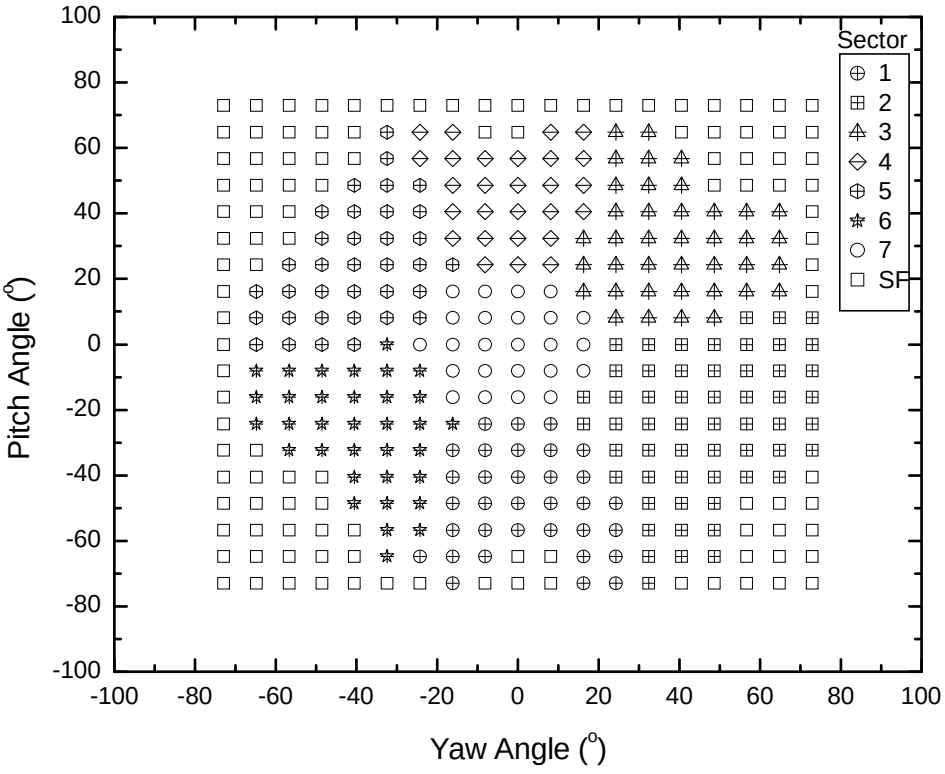

Figure 3.10: Seven-hole probe sectors. *SF* represents separated flow.

registered the highest pressure. Theoretically, the seven-hole probe can operate within ± 80^o to the orientation of the flow, but in practice it is not always possible as shown in Figure 3.10. The open square symbols represent the separated flow region where the probe is insensitive to the flow. This figure shows that the seven-hole probe senses the flow effectively when its orientation to the flow is within ± 65^o in yaw and pitch directions. For low flow angles, where the centre port (7) registered the highest pressure, this angular range is reduced to about ± 20^o in both directions. In addition, the probe orientation is almost symmetrical about both the yaw and the pitch directions.

3.6.2 Calibration Data-Reduction Methods

There are two calibration data-reduction methods that are generally in use. They are the polynomial curve-fit (PCF) method and the direct-interpolation (DI) method. Both of these methods are used in the present study for the calibrated probe. The curve-fit method developed by Gallington (1980) and Gerner *et al.* (1984), uses a least-squares technique to fit a third-order polynomial to the calibration data. The curve fit is applied to each sector separately and one expression, as a function of local pitch angle coefficient C_{Pr}, and yaw angle coefficient C_{Pt}, for each of the four flow properties (θ, ψ, C_q, C_{Pt}) is generated. Using all the calibration data from each sector, the 10 coefficients of the polynomial are determined for each flow property and a total of 280 calibration constants were determined for all seven sectors. For example, for a given flow property, ψ, and sector 1, the third order polynomial can be expressed as,

$$\psi_1 = a_{1,\psi_1} + a_{2,\psi_1} C_{\mathrm{Pr},1} + a_{3,\psi_1} C_{Pt,1} + a_{4,\psi_1} C_{\mathrm{Pr},1}^2 + a_{5,\psi_1} C_{Pt,1}^2 + a_{6,\psi_1} C_{\mathrm{Pr},1} C_{Pt,1} + a_{7,\psi_1} C_{\mathrm{Pr},1}^3 + a_{8,\psi_1} C_{Pt,1}^3 + a_{9,\psi_1} C_{\mathrm{Pr},1}^2 C_{Pt,1} + a_{10,\psi_1} C_{\mathrm{Pr},1} C_{Pt,1}^2 \quad (3.22)$$

where a_{i,ψ_i} is a calibration constant. When the probe is used in an unknown flow condition, depending on which sector reads the highest pressure, the appropriate curve fit coefficients for this particular sector are used to calculate the four flow parameters.

In the case of the direct interpolation method developed by Zilliac (1993), the calibration data are sorted by sector and tabulated. When the probe is used in an unknown flow condition, the directional pressure coefficients are calculated from the seven probe pressures, and the flow angle coefficient data (pitch angle coefficient, C_{Pr}, and yaw angle coefficient, C_{Pt}) are interpolated to obtain θ and ψ. The flow angle data are then interpolated to obtain C_{Ptotal}, and C_q.

In order to estimate the uncertainty in using this probe, as well as to compare the performance of the two calibration data-reduction methods used, independent data were collected using the probe which was rotated through a range of pitch and yaw angles that are different from those used for the calibration. Both pitch and yaw angles were varied between + 63^o and -65.7^o at an interval of 11.7^o. The estimated uncertainty of each flow property was determined using a standard error method and they are presented in Section 3.11.2. The results presented in this thesis were calculated using the DI method since it proved to be slightly more accurate than the PCF, especially at low flow angles (see Sumner, 2002 and Heseltine, 2003).

3.7 Mass Flow Controller

The exhaust (non-buoyant jet) from the stack was produced with the aid of a pair of MKS 20564 and MKS 20572 mass flow meters (TYPE 558A) and mass flow controllers (TYPE 1559A). The maximum flow rate for each of the mass flow meters is 230 L/min.

The flow rate required to achieve the maximum value of R (= 3) used in this study is 456 L/min. Since, this flow cannot be achieved by one mass flow controller, two mass flow controllers were arranged in parallel to produce the flow rates corresponding to R = 0 to 3. The air jet flow, taken from a compressed air tank, was introduced into the base of the stack using flexible tubing.

3.8 Experimental Models

3.8.1 Finite Circular Cylinder Models

For the finite cylinder experiments, four different, smooth, aluminium circular models with diameter D = 31.5 mm and aspect ratios of 3, 5, 7, and 9 (see Figure 3.11) were used. Each cylinder has a flat free end with a sharp edge. The same models were previously used by Heseltine (2003). Each cylinder model was mounted on a six-

Figure 3.11: Finite circular cylinder models.

component force balance below the test section, and located on the ground plane at a distance of 900 mm from the leading edge of ground plane (and 700 mm from the roughness strip on the ground plane). The cylinder extended vertically into the test section through a hole in the ground plane, with a circumferential gap of about 1 mm around the cylinder. The cylinder was partially immersed in the turbulent boundary layer on the ground plane. The solid blockage ratio was at most 0.9% and no wall interference corrections were made to the measured data. Using these models, experiments were conducted at a freestream velocity of U_∞ = 30 m/s, giving a Reynolds number, based on cylinder diameter, of $Re_D = 6\times10^4$.

3.8.2 Stack Model

For the stack experiments, a smooth cylindrical stack of height H = 171.5 mm, external diameter D = 19.1 mm, diameter ratio d/D = 0.67 (where d is the internal diameter), and aspect ratio $AR = H/D$ = 9, was used (see Figure 3.12). The stack was located at the same position as the finite circular cylinder. The stack measurements were conducted at a freestream velocity of U_∞ = 20 m/s, giving a Reynolds number, based on the stack external diameter, of $Re_D = 2.3\times10^4$. The solid blockage ratio was 0.3% and no wall interference corrections were made to the measurements.

In the stack experiments, two Reynolds number are essential: the internal stack flow/jet Reynolds number, Re_d, and the stack Reynolds number, Re_D. The flow inside the stack influences the exit velocity profile and turbulence level of the jet (Snyder and Lawson, 1991), which in turn affects the jet rise (Tsang, 1972). The stack Reynolds number influences the flow separation on the surface of the stack and thus, the width of

Figure 3.12: Stack model

the wake behind the stack and level of pressure deficit. The stack Reynolds number could therefore, influence the downwash flow into the wake of the stack.

For turbulent flow inside the stack, the flow is considered to be fully developed if $H > 18d$ (White, 2003) and $Re_d \geq 2300$ (Snyder and Lawson, 1991) or 2000 (Arya and Lape, 1990). For this study, the jet exit Reynolds number (which is the same for the flow inside the stack) varies between $Re_d = 7.6 \times 10^3$ ($R = 0.5$) and 4.6×10^4 ($R = 3.0$). The stack length is $13.5d$ and the length of the rubber tube is about $75d$. Therefore, the effective length of the flow is far more than $18d$ and the flow could be considered as a fully-developed turbulent pipe flow exiting the stack.

The profile of the exhaust jet from the stack was measured using the X-probe anemometer (Section 3.5) at a distance of d from the stack exit with the stack positioned horizontally. The mean velocity and the turbulence intensity profiles are shown in

Figures 3.13 and 3.14, respectively. The mean axial velocity (U_z/U_a, where U_z is the mean axial velocity and U_a is the centreline velocity) profiles (Figure 3.13(a)) show top-

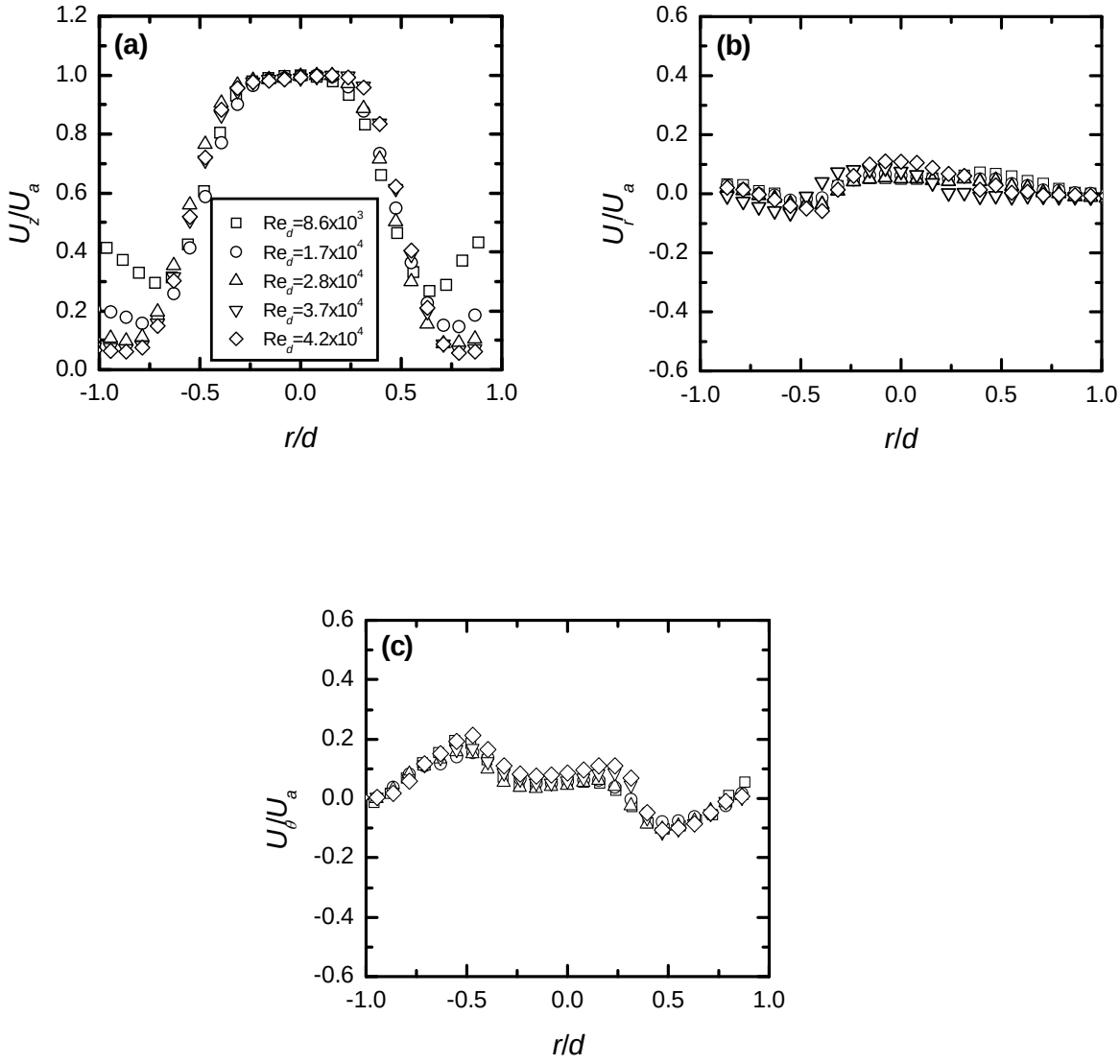

Figure 3.13: Mean velocity profiles of the exhaust jet flow at a distance of d from the stack exit (a) axial, (b) radial, and (c) tangential components.

hat profiles which are similar to the typical velocity profile of turbulent pipe flow (Arya and Lape, 1990). At low flow rates, the increase in the mean axial velocity at the outer edges of the jet (outside the stack internal diameter, $-0.5 < r/d < 0.5$, where r is the radial coordinate) may be attributed to aerodynamic interference between the measuring

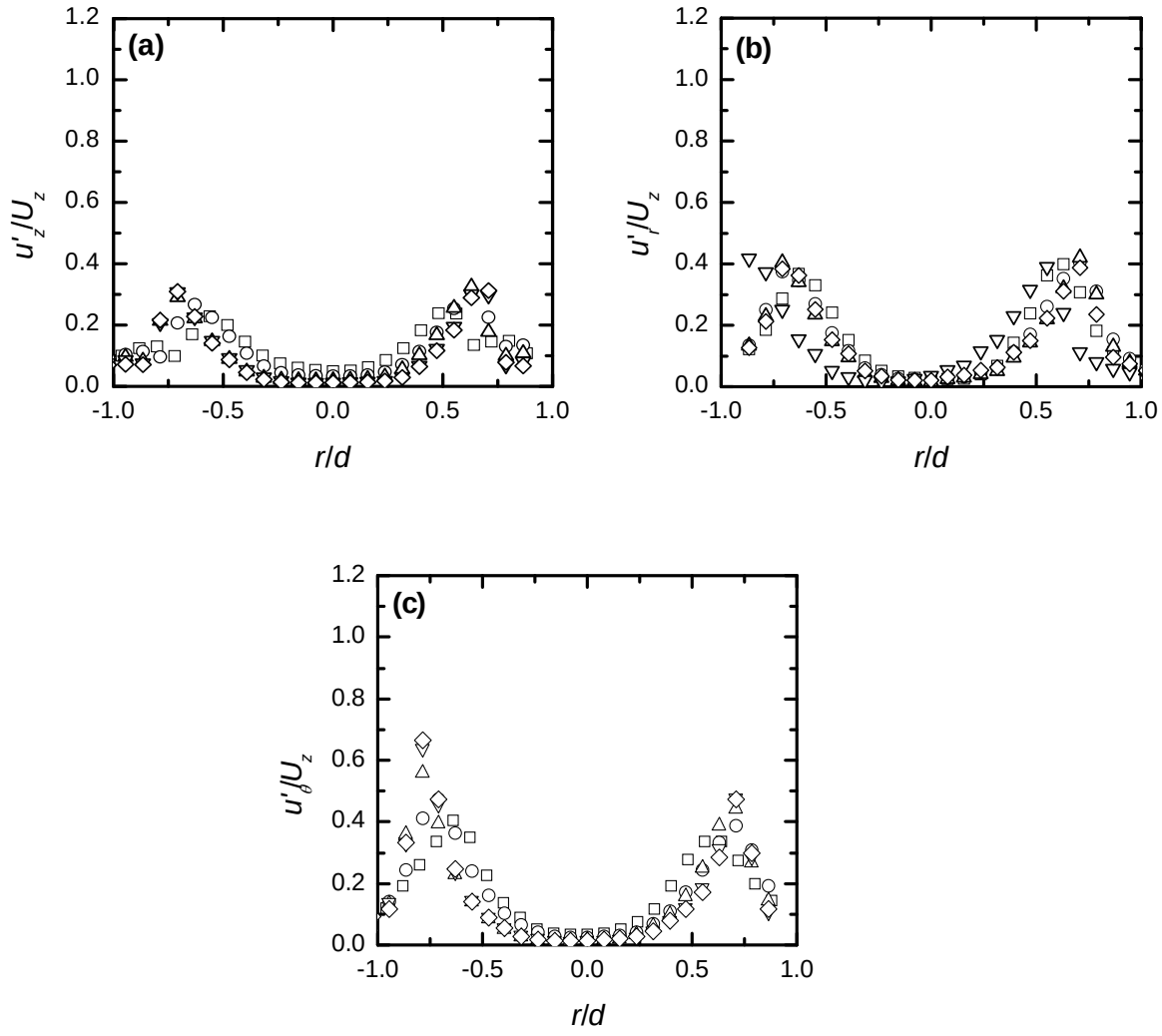

Figure 3.14: Turbulence intensity profiles of the exhaust jet flow at a distance of d from the stack exit (a) axial, (b) radial, and (c) tangential components. ($u_z^{'}$= axial turbulence intensity, $u_r^{'}$= radial turbulence intensity, and $u_\theta^{'}$= tangential turbulence intensity)

probe and the stack. Within the core of the jet flow, there is no significant Reynolds number effect on these profiles. This may be because all the Reynolds numbers considered are in the turbulent flow range and far above the critical Reynolds number for the pipe flow. The mean radial velocity, U_r, and mean tangential velocity, U_θ, (Figure 3.13(b,c)) are almost zero within the core region of the jet flow and this shows that the axial velocity component dominates the flow. Figure 3.13(c) shows the presence

of opposite swirl which may be due to the stack wall effect on the flow. The turbulence intensity profiles for all three components (Figure 3.14) show a similar trend that is not a function of Reynolds number. The profiles show relatively high turbulence intensity near the wall which approaches a zero value at the centre of the jet flow.

3.9 Ground Plane Boundary Layer

In addition to the finite circular cylinder and stack wake experiments, a set of experiments was performed to investigate the boundary layer profiles and properties on the ground plane with freestream velocities of 20 m/s and 30 m/s. These experiments were carried out with the cylinder and stack removed and measurements were taken with the modified Pitot tube (Section 3.3) and TSI model 1243-20 X-probe (Section 3.5).

Tables 3.1 and 3.2 present a summary of the boundary layer measurements on the ground plane for the finite cylinder and stack experiments, respectively. In this table, $x/D = 0$ (900 mm from the ground plane leading edge) is the location of the models. The Reynolds number, Re_x, is based on the distance measured from the ground plane leading edge. For the finite circular cylinder experiments, the boundary layer thickness-to-diameter ratio is $\delta/D = 3.0$ and the thickness-to-height ratio ranges from partially immersed, $\delta/H = 0.3$ (for $AR = 9$), to fully immersed, $\delta/H = 1.0$ (for $AR = 3$). In the case of the stack experiments, the boundary layer thickness-to-diameter ratio is $\delta/D = 4.6$ and the thickness-to-height ratio is $\delta/H = 0.5$, which indicates that the stack is partially immersed inside the ground plane boundary layer. The time-averaged streamwise velocity, turbulence intensity and Reynolds shear stress profiles of the ground plane

boundary layer at three locations for U_∞ = 30 m/s are shown in Figure 3.15. This figure indicates that in this region the flat-plate boundary layer is not yet fully developed.

Table 3.1: Summary of boundary layer measurements on the ground plane for the finite cylinder experiments, U_∞ = 30 m/s.

Location x/D	δ (mm)	δ^* (mm)	θ (mm)	H_δ	Re_x $x\ 10^6$	Re_θ $x\ 10^4$
-4	87	12.0	9.3	1.3	1.38	1.666
0	94	11.9	9.3	1.3	1.62	1.655
+4	100	11.9	9.4	1.3	1.83	1.673

Table 3.2: Summary of boundary layer measurements on the ground plane for the stack experiments, U_∞ = 20 m/s.

Location x/D	δ (mm)	δ^* (mm)	θ (mm)	H_δ	Re_x $x\ 10^6$	Re_θ $x\ 10^4$
-10	78	9.1	6.9	1.3	0.85	0.83
0	87	9.5	7.2	1.3	1.08	0.86
+10	95	9.8	7.5	1.3	1.31	0.90

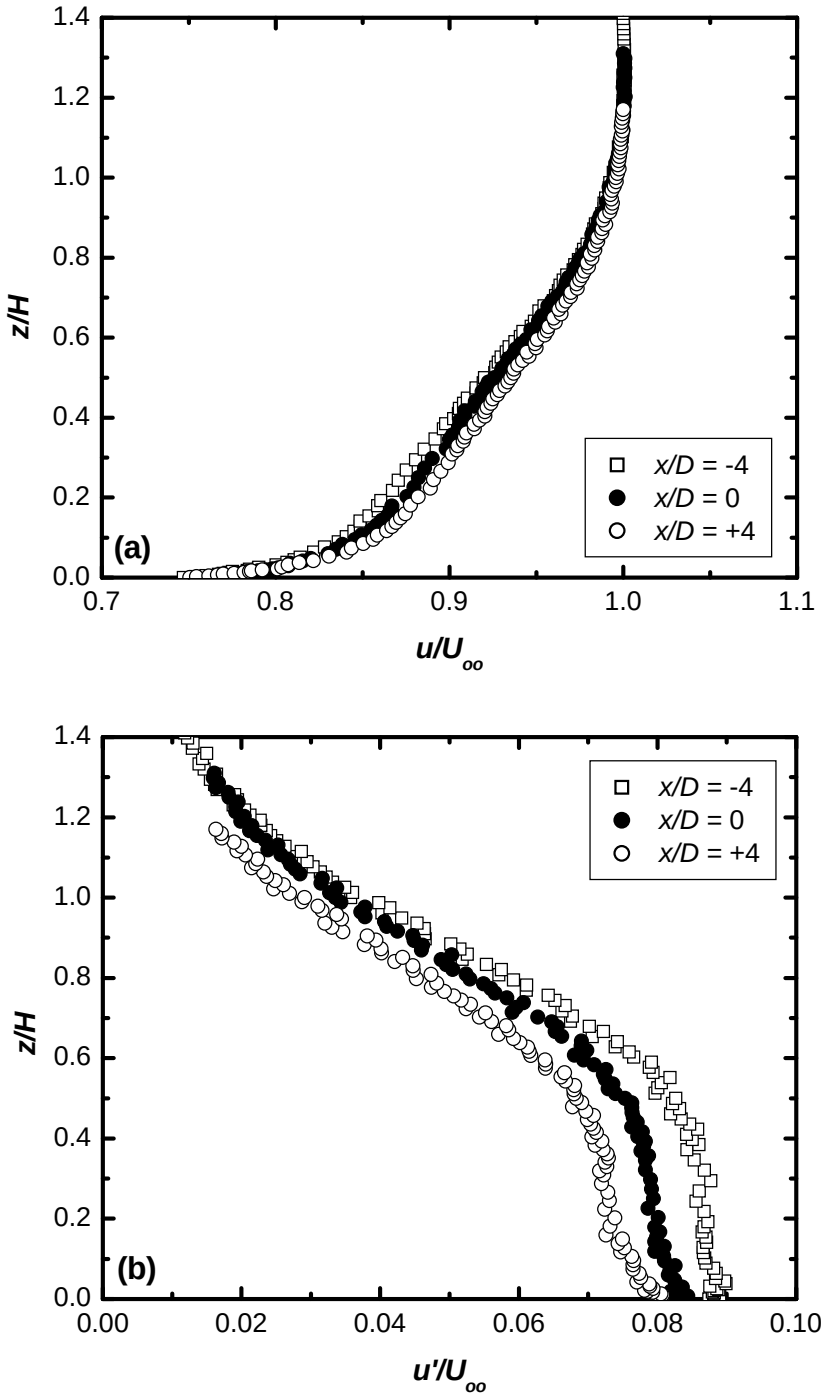

Figure 3.15: The ground plane boundary layer profiles at three different locations at a freestream velocity of U_∞ = 30 m/s: (a) time-averaged streamwise velocity, (b) streamwise turbulence intensity, (c) wall-normal turbulence intensity, and (d) Reynolds shear stress. ($\overline{U}$ = time-averaged streamwise velocity, u' = radial turbulence intensity, w' = radial turbulence intensity and <uw> = Reynolds shear stress).

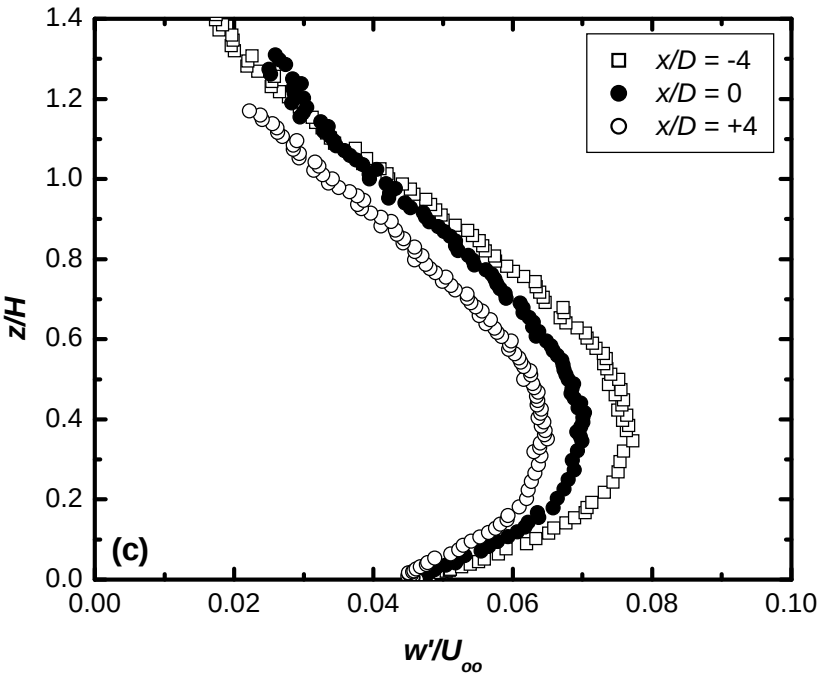

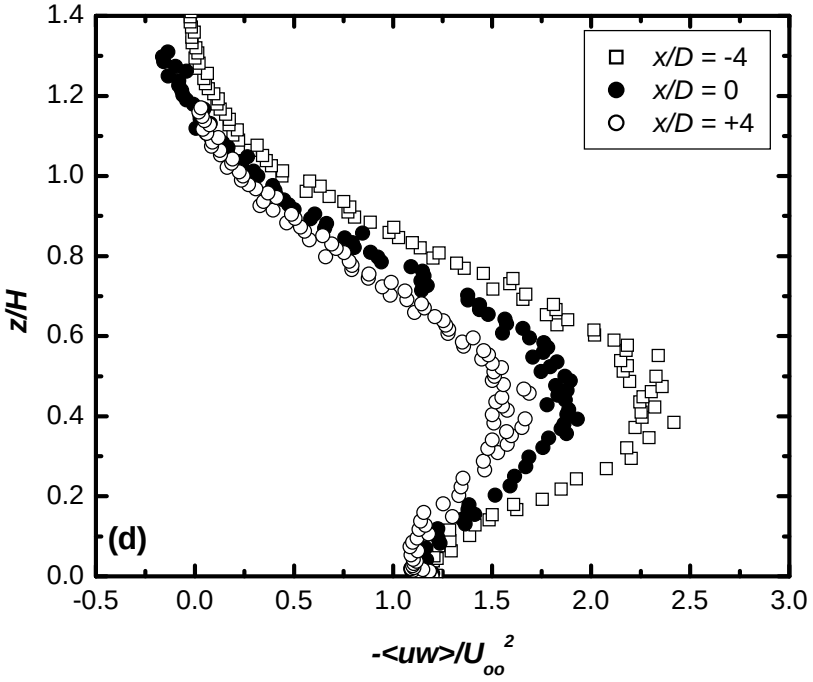

Figure 3.15 continued.

3.10 Description of Experiments

Two groups of experiments were conducted: the first group dealt with a finite circular cylinder of different aspect ratios (AR = 3, 5, 7, and 9) and the second group dealt with a stack of aspect ratio AR = 9, with an exhaust jet (at different velocity ratios, R = 0 to 3) exiting the stack.

Figure 3.16 shows the experimental set-up within the test section of the wind tunnel. For each cylinder, using the X-probe, the wake velocity field in the cross-stream (y-z) plane was measured over a 5-mm uniform grid at streamwise locations of x/D = 6 and 10 downstream of the cylinder, corresponding to two of the streamwise locations considered by Sumner *et al*. (2004). The measurement plane extended in the cross-stream direction to $y = \pm$ 80 mm, and in the wall-normal direction from z = 5 to 300 mm (for the cylinder of AR = 9). No measurements were made for x/D < 6 because of the high flow angles encountered in the downwash flow field close to the cylinder free end

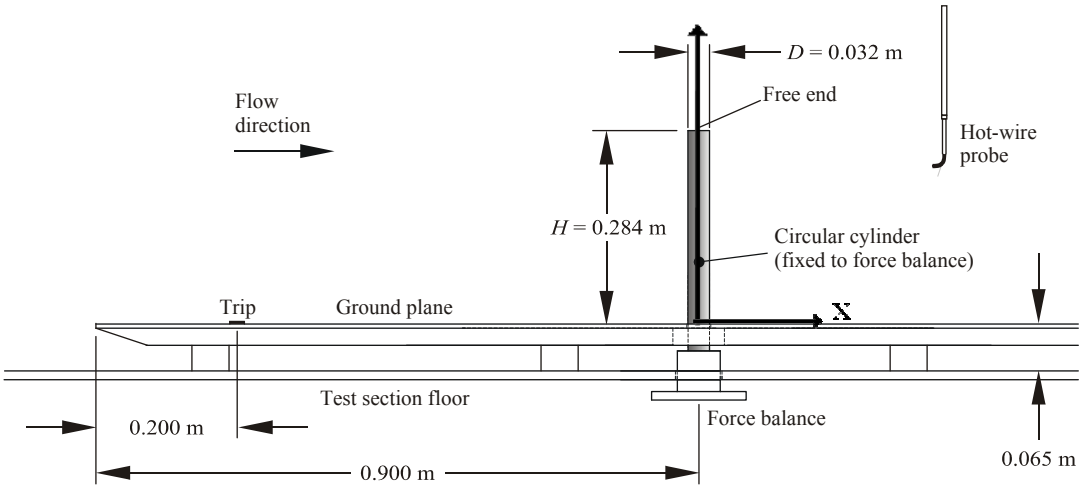

Figure 3.16: Experiment set-up in the wind tunnel (cylinder with AR = 9 shown).

(Sumner *et al*., 2004). The experiments were conducted at a freestream velocity of U_∞ = 30 m/s, giving a Reynolds number, based on cylinder diameter, of $Re_D = 6 \times 10^4$.

For the stack wake measurements, the X-probe and the seven-hole probes were used to measure the turbulent and the time-averaged velocity fields within the stack wake, respectively. The experiments were conducted at a single stack Reynolds number of $Re_D = 2.3 \times 10^4$. The jet Reynolds number for the minimum exit velocity, when R = 0.5, was $Re_d = 7.6 \times 10^3$. The jet Reynolds number for the maximum exit velocity, when R = 3, was $Re_d = 4.7 \times 10^4$. The experimental set-up is similar to that of Figure 3.15, expect that the finite cylinder is replaced by the stack.

For the X-probe measurements, for a given value of the velocity ratio, R, the wake velocity field (u, w) in the cross-stream (y-z) plane was measured over a 5-mm uniform grid at x/D = 10. The measurement plane extended in the cross-stream plane to $y/D = \pm 4$ and to z/D = 14 in the wall-normal direction. In addition, for a given value of R, velocity profile measurements were made in a vertical (x-z) plane on the wake centreline at x/D = 10, and 15. The centreline measurement plane extended to z/D = 14 in the wall-normal direction.

In the case of the seven-hole probe measurements, the time-averaged velocity field ($\overline{U}, \overline{V}, \overline{W}$) within the stack wake in the cross-stream (y-z) plane was measured over a 5-mm uniform grid at streamwise locations from x/D = 6 to 10 downstream of the stack for each value of R. The measurement plane extended in the cross-stream direction to $y/D = \pm 3$ and in the wall-normal direction to z/D = 14. In addition, the wake velocity field was measured in a vertical (x-z) plane parallel to the test-section centreline (at y/D = 0).

Measurements of the vortex shedding frequency were made with the single-component hot-wire probe (TSI model 1210-T1.5). The probe was located at a fixed streamwise and cross-stream position, x/D = 3 and y/D = 1.5, with the wall-normal position, z/H, allowed to vary (where z/H = 0 corresponds to the wall, $z/H = \delta/H$ = 0.5 corresponds to the wall boundary layer thickness at the location of the stack, and z/H = 1 corresponds to the height of the stack). This (x, y) location was chosen after a series of trial procedures produced a strong signal at this location.

The vortex formation length, L_f, was determined by measuring the streamwise turbulence intensity profile along the wake centreline (y/D = 0) at the mid-height of the stack (z/H = 0.5). The vortex formation length was defined as the location of the local maximum value of the streamwise turbulence intensity on the wake centreline (see e.g. Noca *et al.* 1998 and Szepessy, 1991).

3.11 Post Processing and Uncertainty Analysis

3.11.1 Post Processing: Time-Averaged Vorticity Structures

The seven-hole probe measured the time-averaged velocity field at three downstream locations (x/D = 6, 8 and 10) and along the wake centerline (y/D = 0). To examine the vortical structures within the stack wake, the time-averaged streamwise vorticity field, $\omega_x(y, z)$, was determined using a first-order central-difference approach as defined below:

$$\left(\omega_{i,j}\right) = \frac{w_{i+1,j} - w_{i-1,j}}{2 * \Delta y} - \frac{v_{i,j+1} - v_{i,j-1}}{2 * \Delta z} \tag{3.23}$$

In order to determine the circulation of the vortex structures and the vortex area, a vorticity cut-off of $\omega_x^* = 0.04$ ($\omega_x^* = \omega_x D/U_\infty$, where ω_x is the streamwise vorticity component) was used as a minimum vorticity level. This is similar to the approach used by Sumner *et al*. (2004). The total circulation (or strength), Γ, for each vortex structure was found from the time-averaged streamwise vorticity field by summing up the local circulation if the local vorticity is greater than the cut-off value. Likewise, the vortex area was determined by finding the area enclosed by the cut-off value of the vorticity. These approaches were used for each vortex structure taking in account the orientation of the structure. The peak value of vorticity, circulation and the area of the streamwise vortex structures presented in this study represent an average of the vortices on either side of the wake centre plane.

3.11.2 Uncertainty Analysis

Experimental work involves measurement systems which consist of a set of instrumentation (probes and sensors), data acquisition, data analysis and reduction processes as well as the test environment. All these systems influence the accuracy of the experimental results. In general, errors are always present in all measurements and they cannot be totally eliminated, but their effects on particular results can be minimized. In this study, efforts were taken to minimize or reduce any anticipated sources of errors.

Since measurements are made of individual variables in order to obtain a particular result, the errors in these variables will have a cumulative effect on the result. Based on the way errors enter into measurements, they can be classified into bias and

precision errors. The bias errors are fixed and depend on a particular instrument. The bias error can be reduced by proper calibration of the instrument and probe. Precision errors usually follow statistical distributions and result in values both above and below the true value of the result.

The uncertainty estimates of the measured variables can be determined by using the method of Coleman and Steele (1999). Consider a variable R that depends on n independent measured variables x as follows:

$$R = R(x_1, x_2, x_3 \ldots\ldots\ldots\ldots, x_n). \tag{3.24}$$

The uncertainty in R due to the uncertainties in the measured variables can be estimated by considering the partial derivatives of the above equation. A change of δx_i in variable x_i would produce the corresponding change in R as:

$$\delta R_i = \frac{\partial R}{\partial x_i}\delta x_i . \tag{3.25}$$

The above equation can be normalized by dividing both sides of the equation by R to give

$$\frac{\delta R_i}{R} = \frac{x_i}{R}\frac{\partial R}{\partial x_i}\frac{\delta x_i}{x_i} \tag{3.26}$$

Therefore, the uncertainty in the experimental result due to any variation in x_i can be estimated as

$$\frac{U_{R_i}}{R} = \frac{x_i}{R}\frac{\partial R}{\partial x_i}\frac{U_{x_i}}{x_i} , \tag{3.27}$$

where U_{Ri} and U_{xi} are the uncertainties in R and x_i. Thus, the overall uncertainty in R can be determined from

$$\frac{U_R}{R} = \left[\left(\frac{x_1}{R} \frac{\partial R}{\partial x_1} \frac{U_{x_1}}{x_1} \right)^2 + \left(\frac{x_2}{R} \frac{\partial R}{\partial x_2} \frac{U_{x_2}}{x_2} \right)^2 + \ldots\ldots\ldots\ldots\ldots \left(\frac{x_n}{R} \frac{\partial R}{\partial x_n} \frac{U_{x_n}}{x_n} \right)^2 \right]^{0.5} \tag{3.28}$$

For a measured variable θ, the uncertainty estimate is given by

$$U_\theta = \left[B^2 + P^2 \right]^{1/2} \tag{3.29}$$

where B and P are the bias and precision uncertainties in θ, respectively.

Based on the above approach, the summary of the uncertainty estimates in the freestream parameters, model dimensions, streamwise vorticity and the Strouhal number are presented in Table 3.3. The range and average uncertainty estimates in the exit jet flow parameters are shown in Table 3.4.

Table 3.3: Summary of uncertainty estimates in the freestream condition, model geometry, streamwise vorticity and Strouhal number.

Parameter	**Uncertainty (%)**
Freestream density, ρ_∞	±2.06
Freestream velocity, U_∞	±1.46
Cross-flow Reynolds number, Re_D	±2.54
Strouhal number, St	1.46
Model external diameter, D	±0.02 – 0.03
Model height, H	±0.01
Stack internal diameter, d	±0.04
Streamwise vorticity, ω_x	±1.86

Table 3.4: Summary of uncertainty estimates in the exit jet parameters.

Parameter	Range of uncertainty (%)	Average uncertainty (%)
Flow rate, Q	0.35 – 3.37	1.85
Exit jet flow velocity, U_e	0.62 – 5.96	3.29
Velocity ratio, R	0.21 – 5.02	1.46

The uncertainty estimates in the X-probe and seven-hole probe are estimated based on the precision errors only, because it is not feasible to make accurate estimates of the bias errors. These estimates were only based on the data reduction techniques. Therefore, the estimated errors presented in Tables 3.5 and 3.6, for X-probe and seven-hole probe, respectively, are likely to be under-estimated. In Table 3.6, the reference to low angle and high angle indicate that the flow angle is low (± 20^o) and high (± 65^o), respectively.

Table 3.5: Summary of uncertainty estimates in X-probe measurements.

Parameter	Uncertainty (%)
Flow angle, α	± 3.23
Resultant velocity, V	±1.96
Streamwise velocity component, u	±1.88
Wall-normal velocity component, w	± 5.58
Streamwise turbulence intensity, u'	± 4.00
Wall-normal turbulence intensity, w'	± 7.00
Reynolds shear stress, $\langle uw \rangle$	± 9.00

Table 3.6: Summary of uncertainty estimates in the seven-hole probe measurements.

Parameter	**Uncertainty (%)** (Polynomial curve fit)	**Uncertainty (%)** (Direct Interpolation)
Pitch angle, θ (Low angle)	0.14	0.18
Pitch angle, θ (High angle)	3.00	5.54
Yaw angle, ψ (Low angle)	0.30	0.24
Yaw angle, ψ (High angle)	2.14	1.40
Velocity, V (Low angle)	1.62	1.86
Velocity, V (High angle)	1.82	5.66

CHAPTER 4

TURBULENT WAKES OF FINITE CIRCULAR CYLINDERS

4.1 Introduction

The local flow field of a stack involves three fundamental flows: the plane wall boundary layer flow on the ground plane, the separated flow field and wake of a finite circular cylinder (representing the simplest possible stack geometry), and the development of an elevated round jet in cross-flow (representing the exhaust jet exiting the stack). In order to understand the wake of a stack and the influence of the jet flow, the wake structure of a finite circular cylinder was initially investigated using two-component thermal anemometry. As discussed in Chapter 2, there is limited information in the literature about the characteristics of the turbulence quantities in the wake of finite circular cylinder. In addition to providing background information for the study of a stack in a cross-flow, the studies reported in this chapter also provide further information that will improve the current understanding of this flow.

4.2 Time-Averaged Velocity Distribution

4.2.1 Streamwise Velocity

The time-averaged streamwise velocity fields ($\overline{U}/U_\infty$) of a finite circular cylinder in the cross-stream (y-z) plane, for the four aspect ratios AR = 3, 5, 7 and 9, at x/D = 6 and 10,

are shown in Figures 4.1 to 4.4. The lateral spread (in the *y*-direction) in the wake increases as the streamwise distance from the cylinder increased. This spread reducing as *AR* increases as the flow around the cylinder becomes more two-dimensional (Afgan *et al.*, 2007).

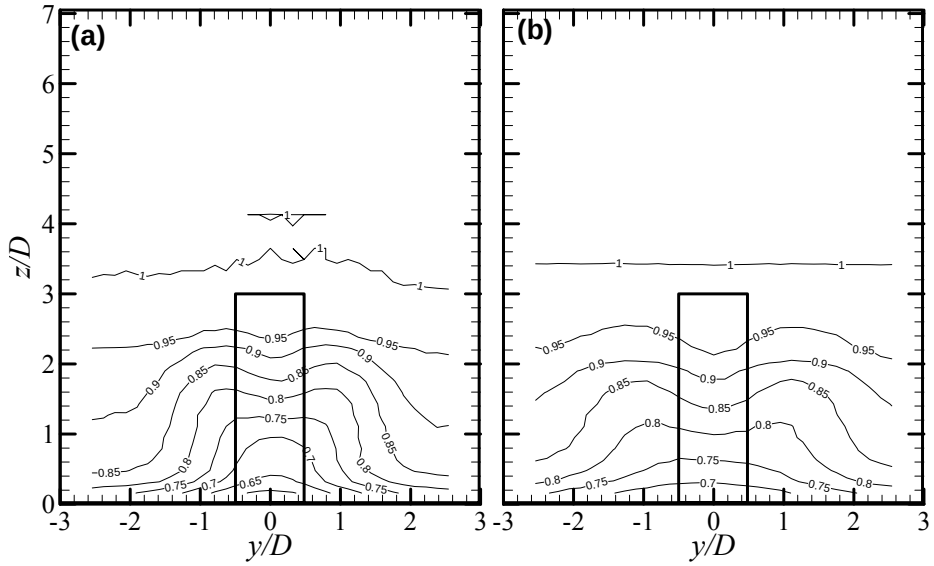

Figure 4.1: Time-averaged streamwise velocity field for *AR* = 3: (a) *x/D* = 6; and (b) *x/D* = 10. Contours of ($\overline{U}/U_\infty$), contour increment of 0.05.

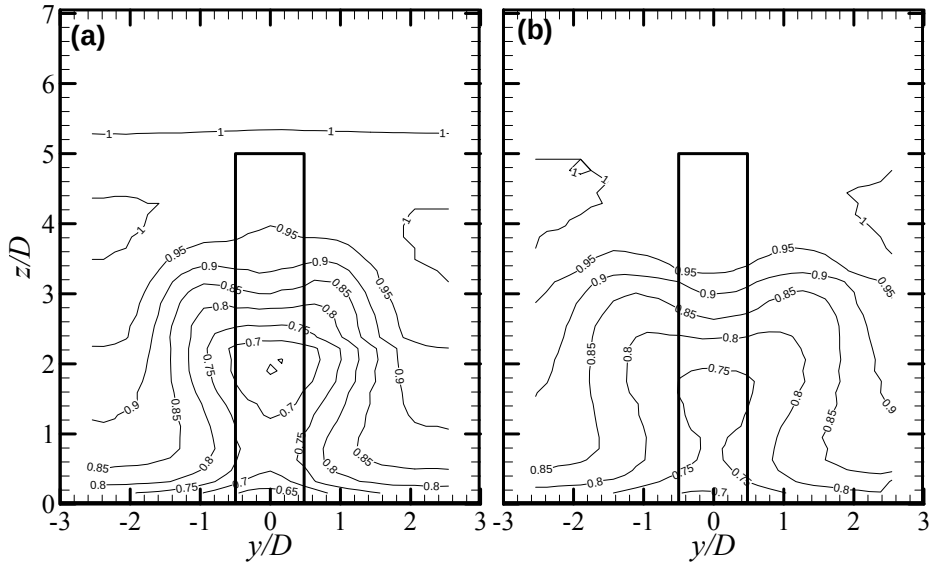

Figure 4.2: Time-averaged streamwise velocity field for *AR* = 5: (a) *x/D* = 6; and (b) *x/D* = 10. Contours of ($\overline{U}/U_\infty$), contour increment of 0.05.

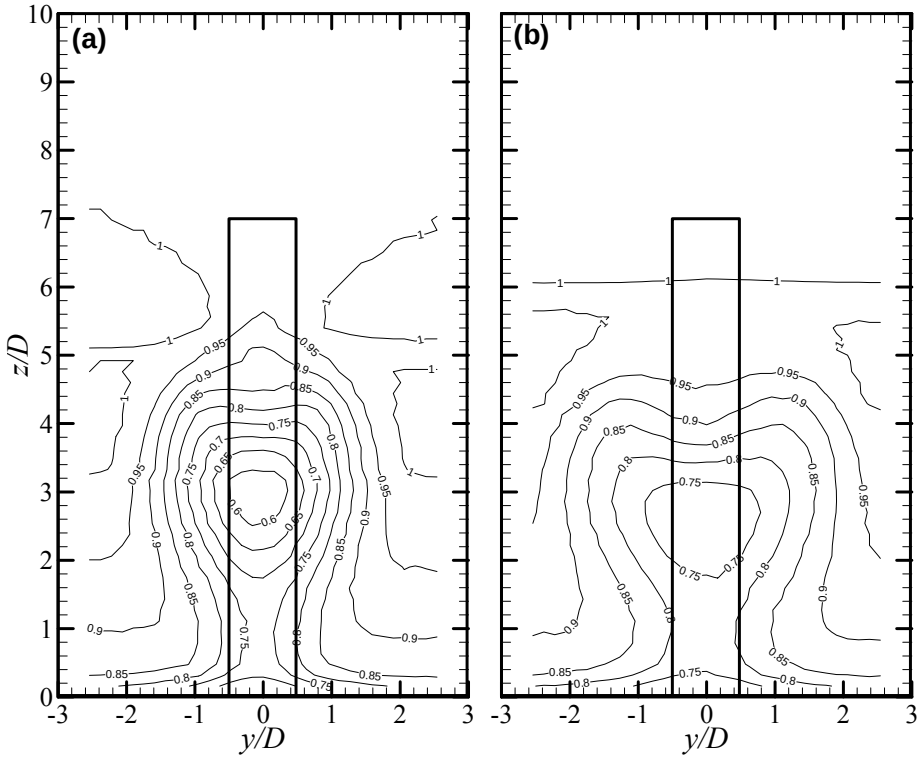

Figure 4.3: Time-averaged streamwise velocity field for AR = 7: (a) x/D = 6; and (b) x/D = 10. Contours of ($\overline{U}/U_\infty$), contour increment of 0.05.

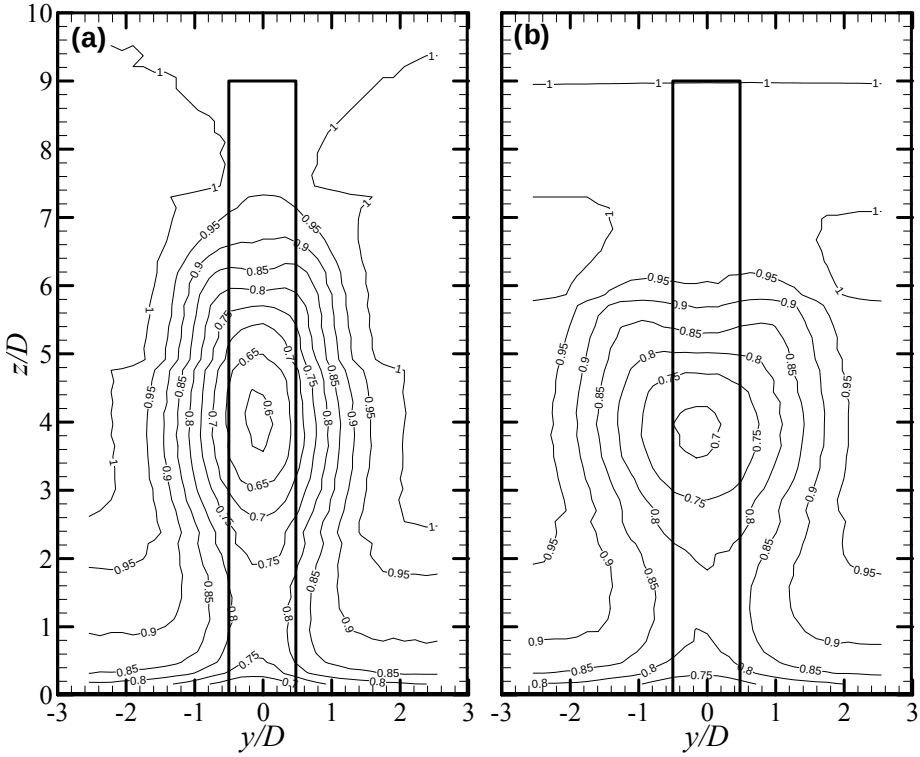

Figure 4.4: Time-averaged streamwise velocity field for AR = 9: (a) x/D = 6; and (b) x/D = 10. Contours of ($\overline{U}/U_\infty$), contour increment of 0.05.

For AR = 3, the lowest streamwise velocities occur very close to the ground plane immediately behind the cylinder, and the concentrated region of low velocity near mid-height observed for higher AR cylinders (Figures 4.2-4.4) is absent (Figure 4.1). This coincides with the absence of the base vortex structures within the ground plane boundary layer immediately behind the cylinder (Sumner *et al.,* 2004). For AR = 5, 7 and 9 (Figures. 4.2-4.4), the streamwise velocity fields are similar, with the local minimum time-averaged streamwise velocities found in a concentrated region behind the cylinder well above the ground plane (and close to the mid-height position, z/H = 0.5). Comparing to the study of Sumner *et al.,* (2004) for AR = 5, 7 and 9, it is seen that this region of low streamwise velocity is bounded on the four corners by the tip and base vortex structures. These results show the distinct wake structure for the cylinder of AR = 3 and indicates that the critical aspect ratio in these experiments lies between AR = 3 and 5. With increasing streamwise distance, x/D = 10, the centre of this low streamwise velocity region descends towards the ground plane AR = 5 (Figure 4.2(b)), AR = 7 (Figure 4.3(b)) and AR = 9 (Figure 4.4(b)).

The distinct features observed in this section (and later sections of this chapter) for the cylinder of AR = 3 are supported by previous studies. The downwash flow from the free end of the cylinder may suppress the Kármán vortex shedding from either side of the cylinder, if the aspect ratio is below a certain critical value. This critical aspect ratio value varies between the different studies in the literature, from AR = 1 to 7. The different critical values for AR are caused, in part, by the influence of the plane wall boundary layer (Luo, 1993), which differs in relative thickness (δ/D and δ/H) between various studies. For instance, for δ/D = 0.20, Okamoto and Sunabashiri (1992) observed

that the critical value may lie between AR = 2 and 4. They observed that there is a change from symmetrical vortex shedding for $AR \leq 2$ to antisymmetrical vortex shedding when $AR \geq 4$. Other critical values of AR identified in literature were previously discussed in Section 2.3.

4.2.2 Wall-Normal Velocity

The time-averaged wall-normal velocity fields ($\overline{W}/U_\infty$) in the cross-stream (y-z) plane, for the four aspect ratios, at x/D = 6 and 10, are shown in Figures 4.5 to 4.8. The presence of a strong downwash velocity (shown by the dashed contour lines) originating near the free end is observed for all four aspect ratios. The downwash is located between, and induced by, the prominent tip vortex structures (Park and Lee, 2000; Sumner *et al.,* 2004). The strength of the downwash flow depends on AR but decreases with x/D. For AR = 5, 7, and 9 (Figures. 4.6-4.8), there is an upwash velocity (shown by the solid contour lines) originating near the ground plane, the strength of which also increases with AR. In addition, the strength of the upwash flow decreases with x/D. The upwash flow is almost absent when AR = 5 (Figure 4.6(b)), due to the downwash flow that approaches the ground plane and as a result suppresses the upwash flow from the ground plane. The upwash flow is centred between, and induced by, the base vortex structures within the plane wall boundary layer (Sumner *et al.,* 2004). In the case of AR = 3 (Figure 4.5), the downwash flow extends to the ground plane and upwash flow is absent. The absence of the upwash flow for AR = 3 coincides with the absence of the base vortex structures (Sumner *et al.,* 2004), and is another characteristic of the distinct wake structure for the shortest cylinder.

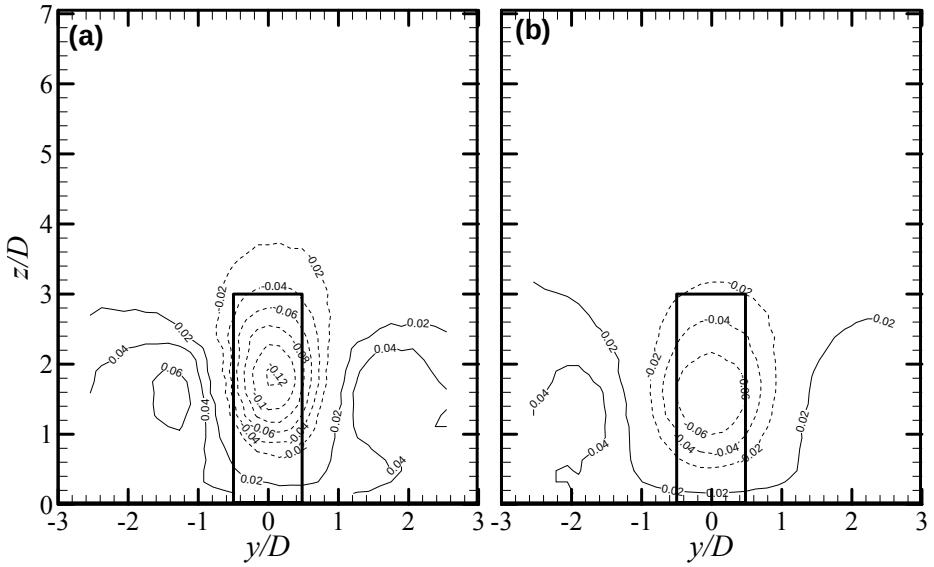

Figure 4.5: Time-averaged wall-normal velocity field for AR = 3: (a) x/D = 6; and (b) x/D = 10. Contours of ($\overline{W}/U_\infty$), contour increment of 0.02. Solid lines represent positive (upwards) velocity and the dashed lines represent negative (downwash) velocity.

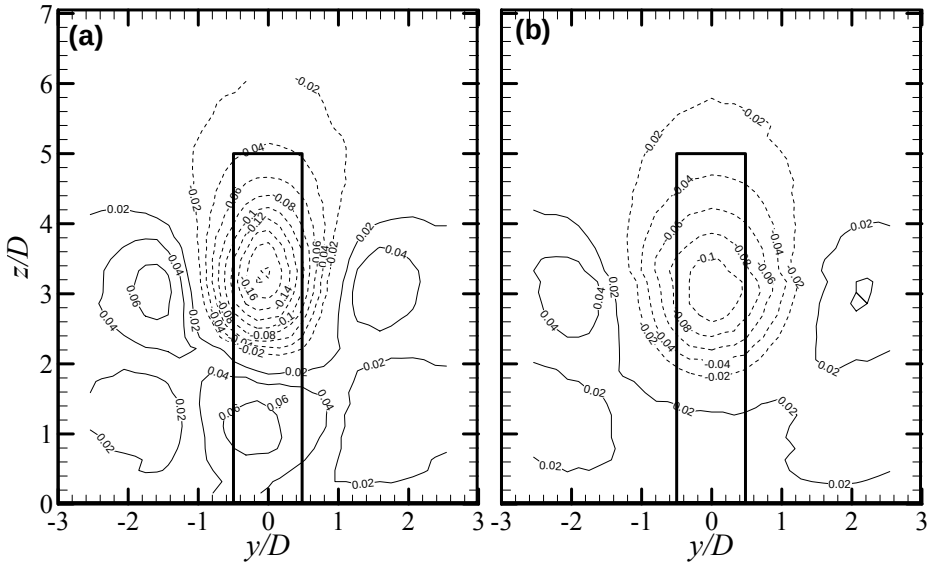

Figure 4.6: Time-averaged wall-normal velocity field for AR = 5: (a) x/D = 6; and (b) x/D = 10. Contours of ($\overline{W}/U_\infty$), contour increment of 0.02.

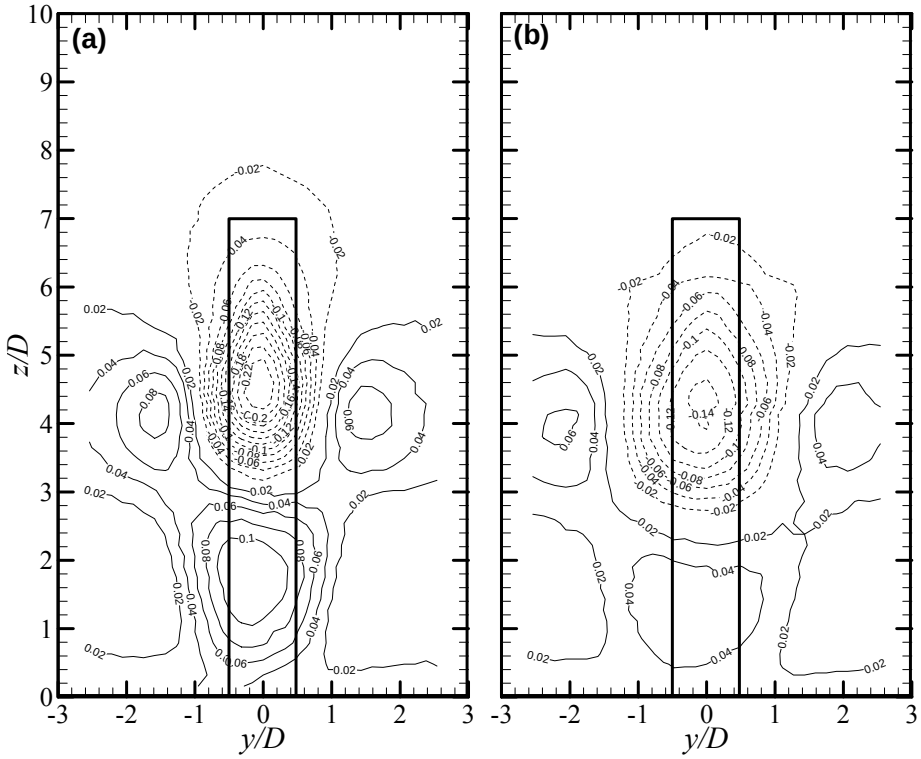

Figure 4.7: Time-averaged wall-normal velocity field for AR = 7: (a) x/D = 6; and (b) x/D = 10. Contours of ($\overline{W}/U_\infty$), contour increment of 0.02.

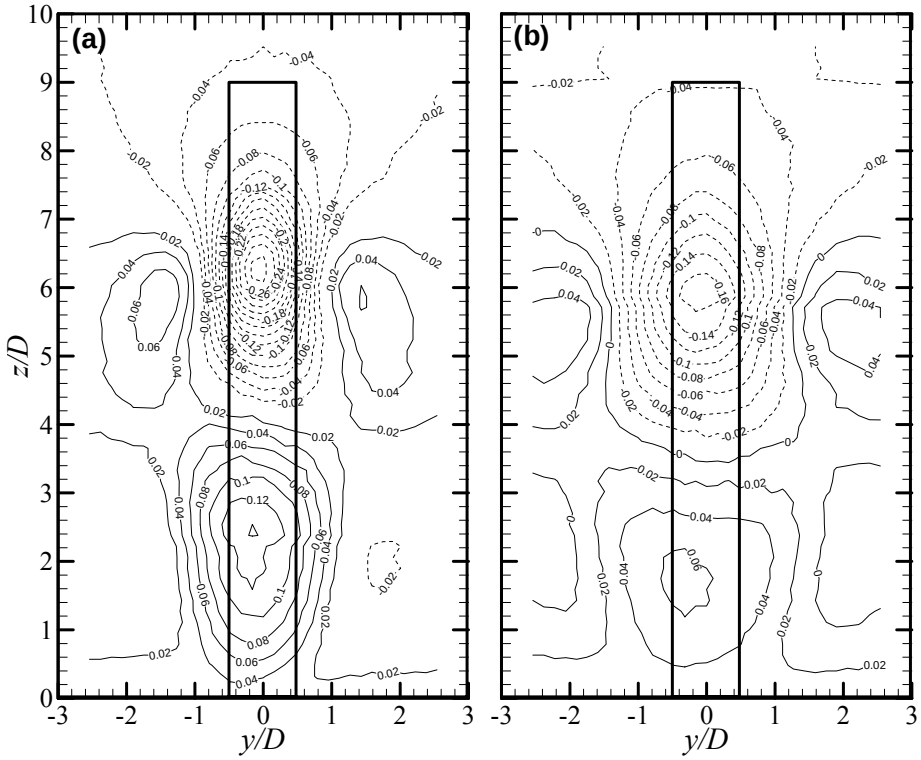

Figure 4.8: Time-averaged wall-normal velocity field for AR = 9: (a) x/D = 6; and (b) x/D = 10. Contours of ($\overline{W}/U_\infty$), contour increment of 0.02.

4.2.3 Spanwise Variation of the Velocity Profiles

4.2.3.1 Streamwise Velocity

Figures 4.9 and 4.10 present the time-averaged streamwise velocity profile at four locations along the cylinders' height at x/D = 6 and 10, respectively. At each spanwise

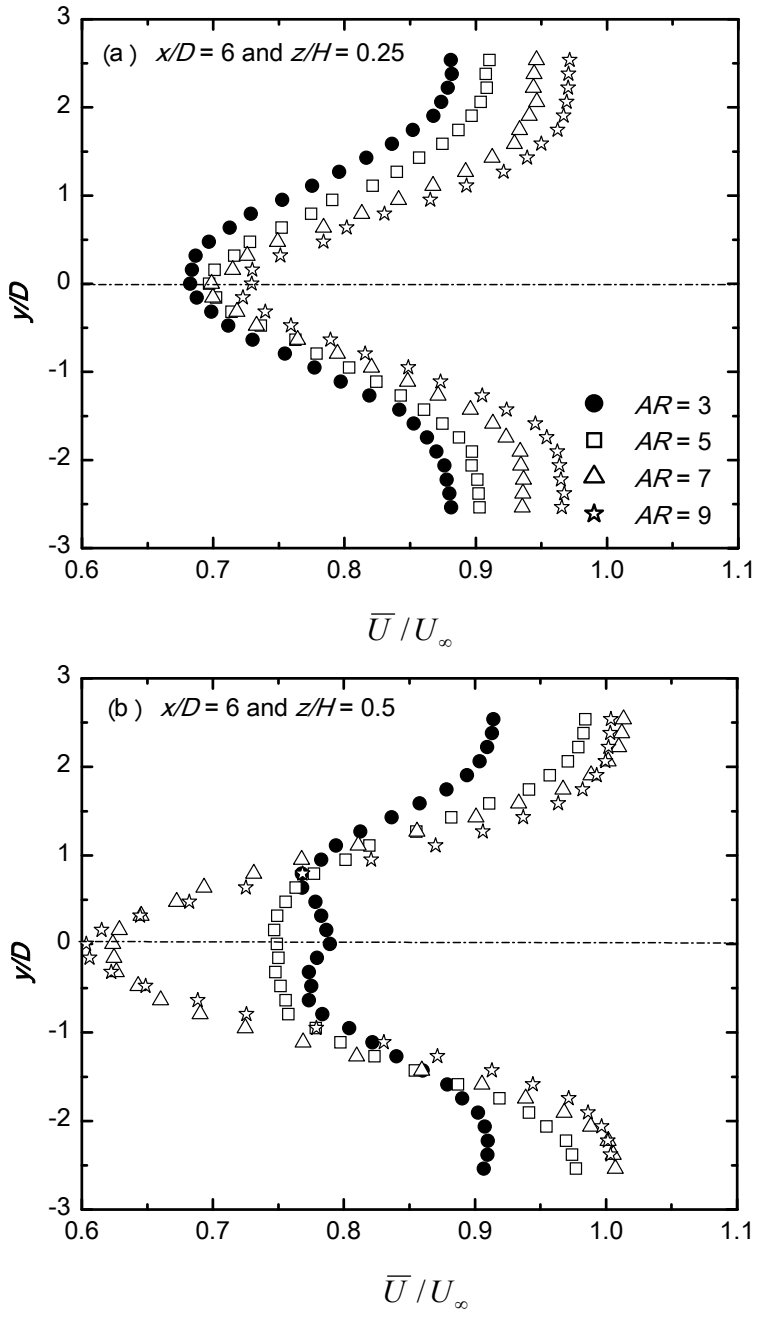

Figure 4.9: Time-averaged streamwise velocity ($\overline{U}/U_\infty$) profiles at x/D = 6 along the cylinder's height: (a) z/H = 0.25, (b) z/H = 0.5, (c) z/H = 0.75, and (d) z/H = 1.

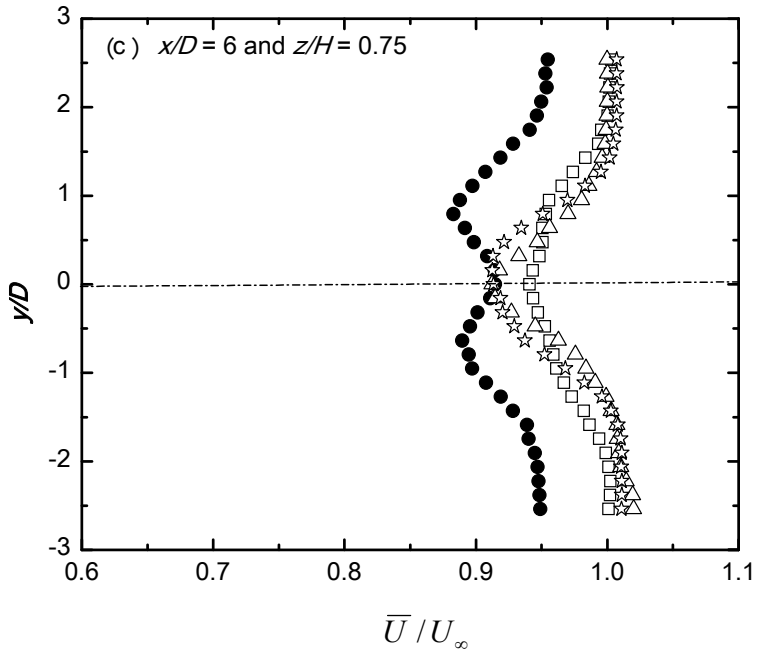

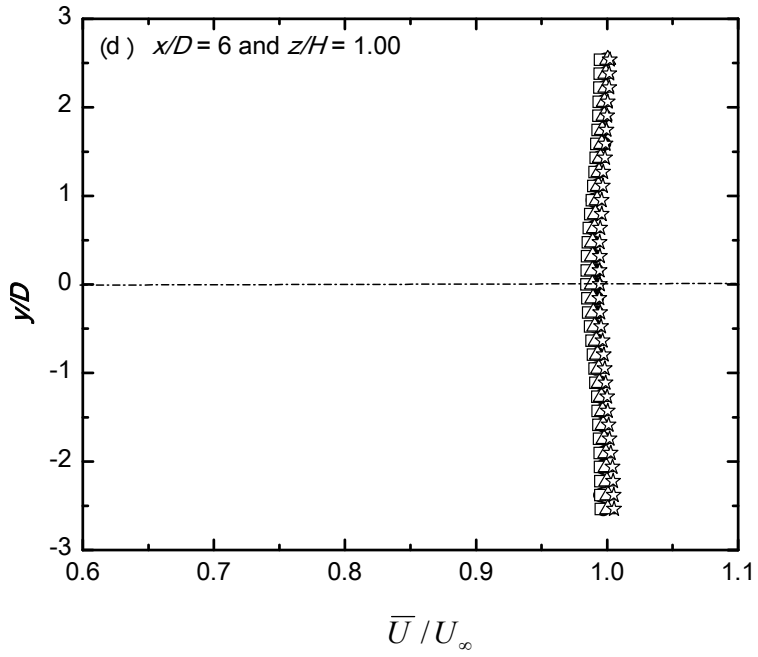

Figure 4.9 continued.

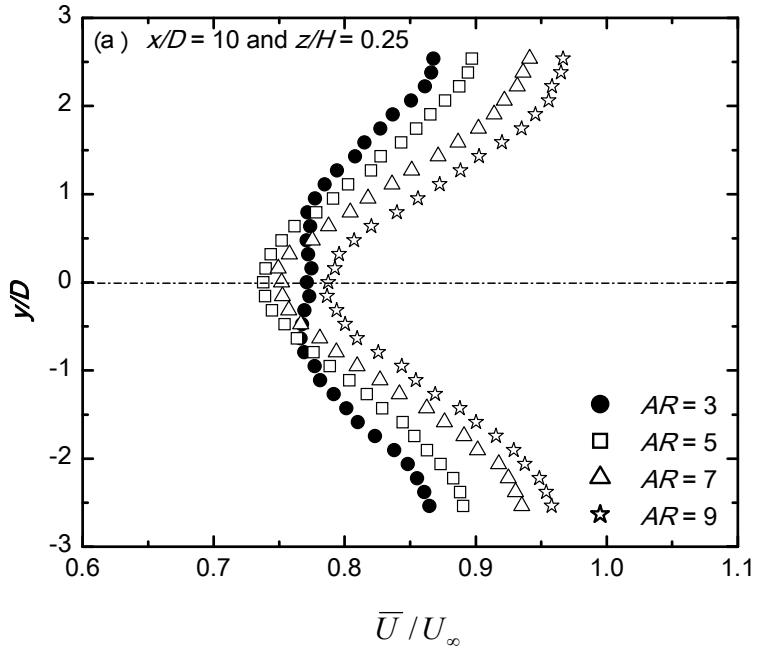

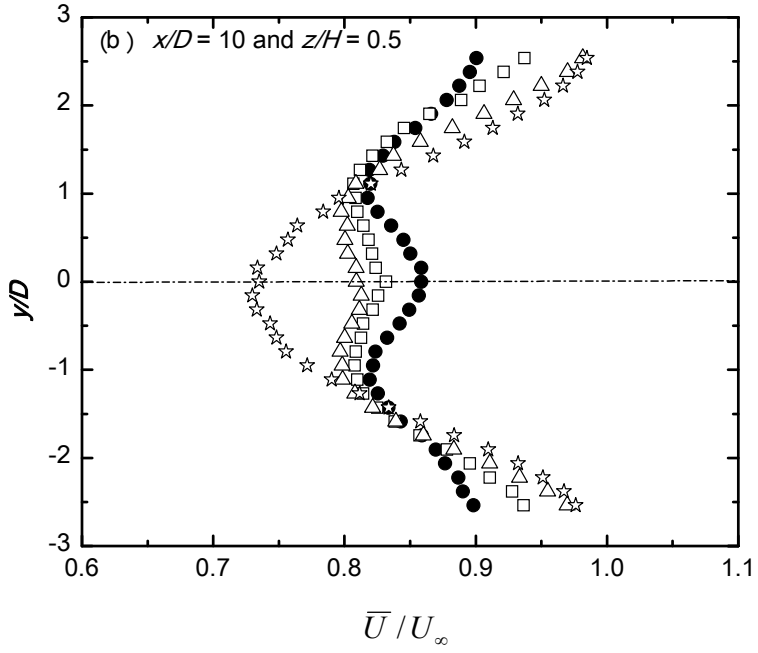

Figure 4.10: Time-averaged streamwise velocity ($\overline{U}/U_\infty$) profiles at x/D = 10 along the cylinder's height: (a) z/H = 0.25, (b) z/H = 0.5, (c) z/H = 0.75, and (d) z/H = 1.

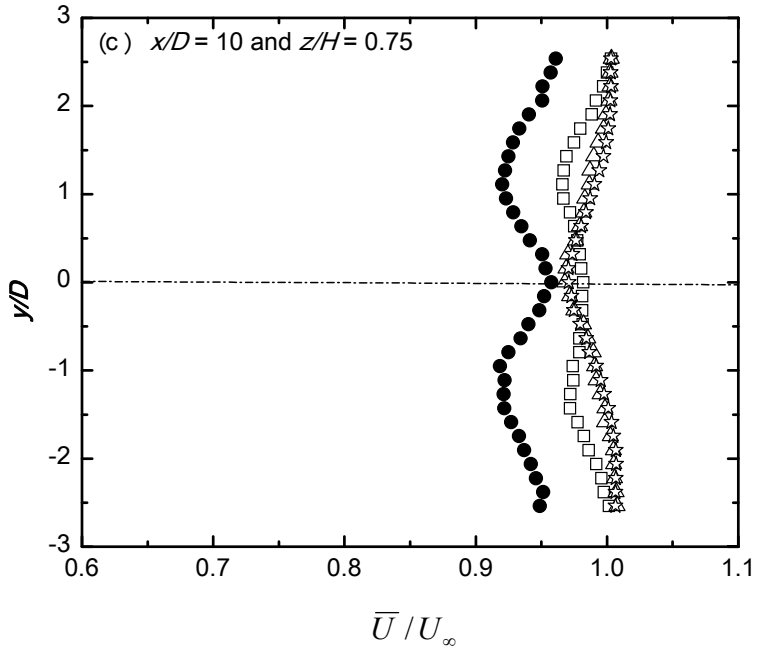

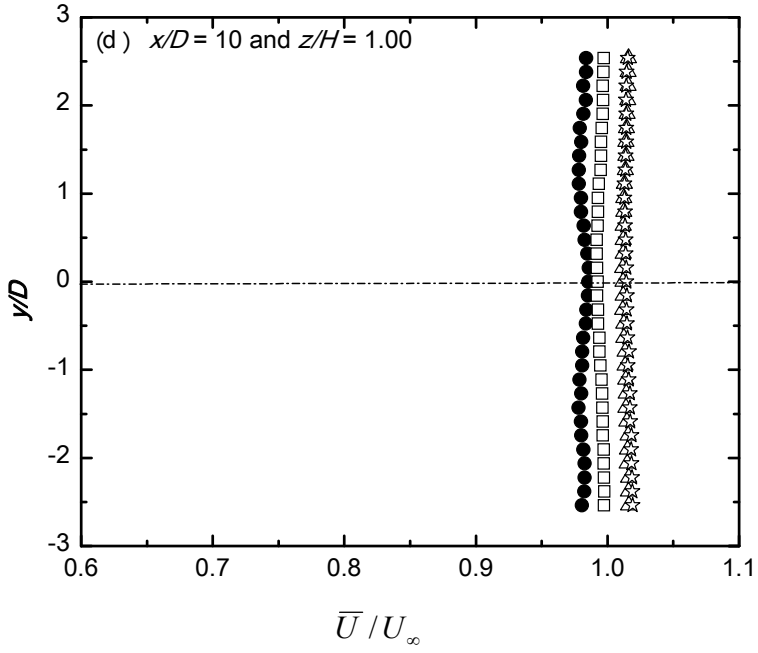

Figure 4.10 continued.

location, it is observed that the wake becomes narrower as the aspect ratio of the cylinder increases. This indicates that flow characteristics become closer to the infinite

(two-dimensional) cylinder as *AR* increases. In addition, as the streamwise distance increases (see Figure 4.10), the region with a defect velocity reduces, due to the downwash flow that approaches the ground plane farther away from the cylinder.

At $z/H = 0.25$ (Figure 4.9(a)), which is within the ground plane boundary layer for all the cylinders, all the profiles at $x/D = 6$ have a single peak streamwise velocity defect. The value of the velocity defect slightly decreases as the *AR* increases.

At $z/H = 0.5$ (Figure 4.9(b)), the cylinder with $AR = 3$ has two peaks while those for $AR = 5$, 7 and 9 have a single peak. The appearance of two peaks in some of the streamwise velocity profiles may be caused by the effect of downwash flow from the free end of the finite cylinder (Okamoto and Sunabashiri, 1992). For the distinct wake of $AR = 3$, the downwash flow extends to the ground plane and therefore two peaks are observed in the time-averaged streamwise velocity profiles at both $x/D = 6$ and 10 (Figure 4.10(b)). For the more slender cylinders of $AR = 5$, 7 and 9, downwash does not reach the centre section ($z/H = 0.5$) at $x/D = 6$, and the time-averaged streamwise velocity defect profiles have only a single peak (Figure 4.9(a)). This is similar to the results of Park and Lee (2002) for a cylinder of $AR = 6$ at $x/D = 5$, where only a single peak was observed in the time-averaged streamwise velocity defect profile at mid-height. At $x/D = 10$ (Figure 4.10(b)), downwash reaches the mid-height position for $AR = 5$ and 7, and there are now two peaks in the time-averaged streamwise velocity defect. Meanwhile, the number of peaks in the streamwise velocity profile cannot be used entirely to determine the location or extension of the downwash flow within the cylinder wake. The wall-normal velocity profiles (Section 4.2.3.2, see below) give a better picture of the spanwise extension of the downwash flow within the wake of the cylinder.

At z/H = 0.75 (Figure 4.9(c)), two peaks are still observed for AR = 3 while a single peak is observed for each of the other aspect ratios. At the cylinder free end, z/H = 1 (Figure 4.9(d)), the profiles for all values of AR are approximately one which indicates the flow is now outside the velocity defect (wake) region and has the properties of the freestream.

The reason for some differences in the defect profiles at z/H = 0.5 and 0.75 (Figure 4.9(b-c)) and (Figure 4.10(b-c)) may also be related to the boundary layer thickness (δ/H) relative to the mid-height of the cylinder (z/H = 0.5). For the tallest cylinder of AR = 9, the boundary layer thickness remains less than mid-height (z/H = 0.5) at x/D = 0 (δ/H = 0.3), x/D = 6 (δ/H = 0.38), and x/D =10 (δ/H = 0.40), leading to the single-peak velocity defect profile at both streamwise locations, x/D = 6 and 10. For the shortest cylinder of AR = 3, the cylinder is completely immersed in the boundary layer at x/D = 0 (δ/H = 1.0), and the two-peak velocity defect profile is seen at both x/D = 6 (δ/H = 1.1) and x/D = 10 (δ/H = 1.2). For the intermediate aspect ratios, AR = 5 and 7, where δ/H = 0.6 and 0.4 at the location of the cylinder (x/D = 0), respectively, the shape of the defect profile changes from the single-peak shape to the two-peak shape when moving from x/D = 6 to x/D = 10.

4.2.3.2 Wall-Normal Velocity

Figures 4.11 and 4.12 present the time-averaged wall-normal velocity at four locations along the cylinders' height at x/D = 6 and 10, respectively. At z/H = 0.25 (Figure 4.11(a)), the absence of upwash flow (positive $\overline{W}/U_\infty$) within the vicinity of the ground plane and behind the cylinder with AR = 3 is obvious. As discussed earlier, this is due to

the downwash flow which approaches the ground plane and suppresses the upwash flow from the ground plane. For the higher aspect ratio cylinders, the upwash flow is present and the profiles overlap for AR = 7 and 9, while for AR = 5, the profile lies below those for AR = 7 and 9. As the streamwise distance increases (Figure 4.12(a)), there is a reduction in the upwash flow from the ground plane for AR = 5, 7 and 9, and increases in the strength of the downwash flow for AR = 3.

For z/H = 0.5 (Figure 4.11(b)) and 0.75 (Figure 4.11(c)), downwash flow (negative $\overline{W}/U_\infty$) is present for all the aspect ratios within the vicinity of the wake centreline but its absolute value depends on the cylinder's aspect ratio. At z/H = 0.5, the cylinder of AR = 3 has the highest value while the cylinder AR = 9 has the lowest value.

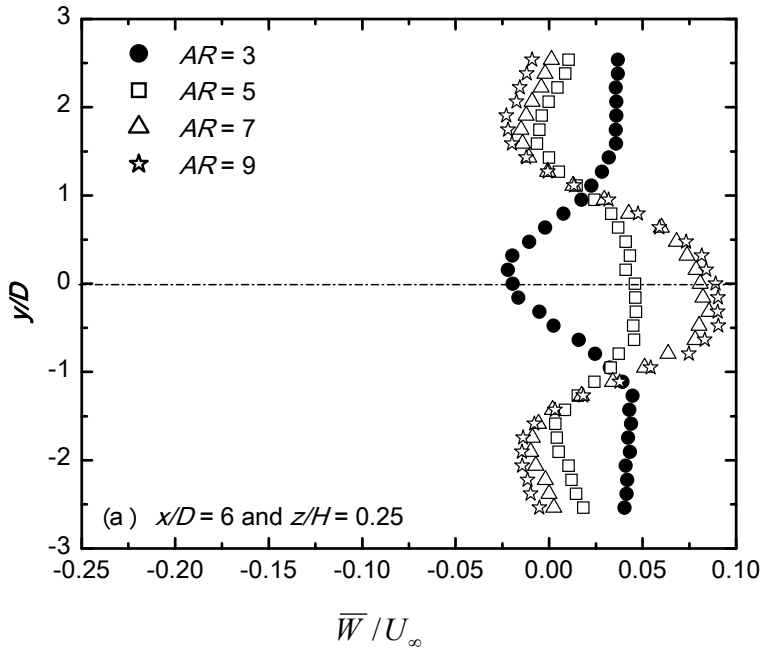

Figure 4.11: Time-averaged wall-normal velocity ($\overline{W}/U_\infty$) profiles at x/D = 6 along the cylinder's height: (a) z/H = 0.25, (b) z/H = 0.5, (c) z/H = 0.75, and (d) z/H = 1.

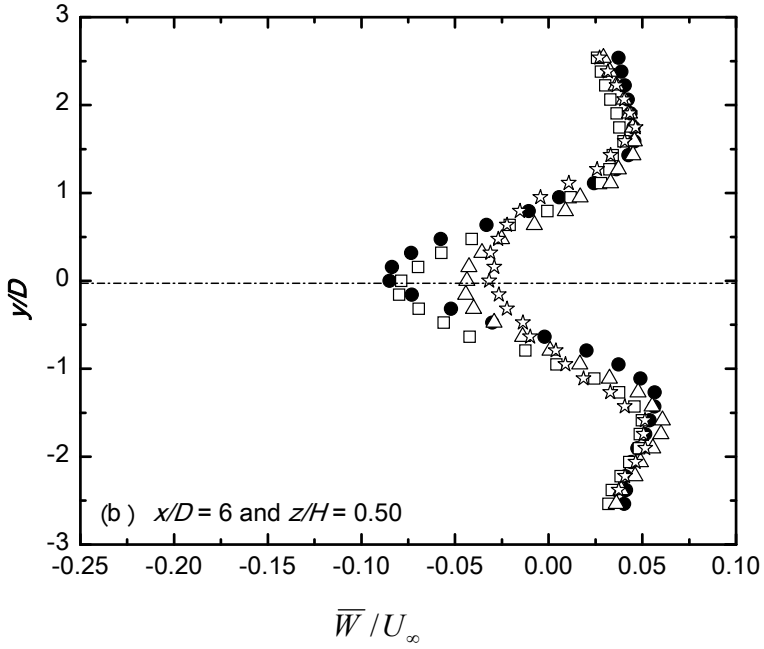

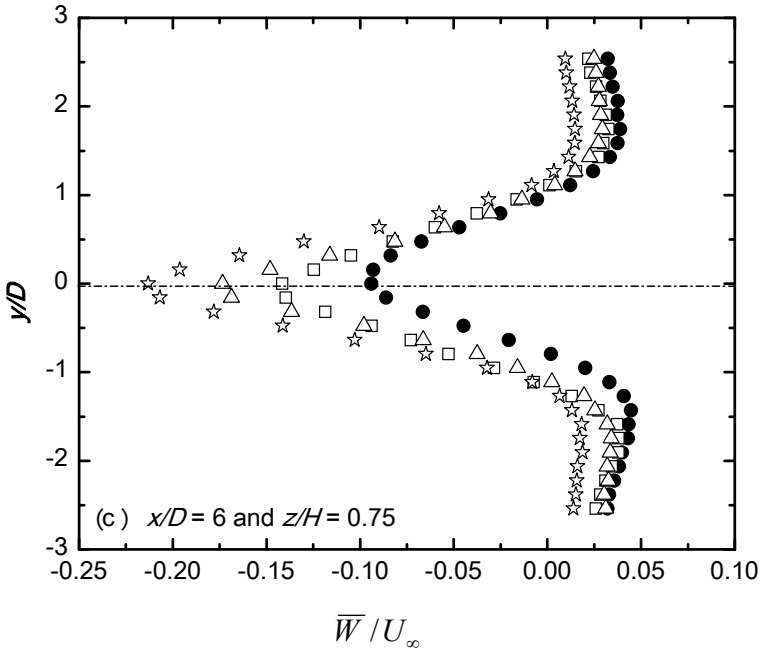

Figure 4.11 continued.

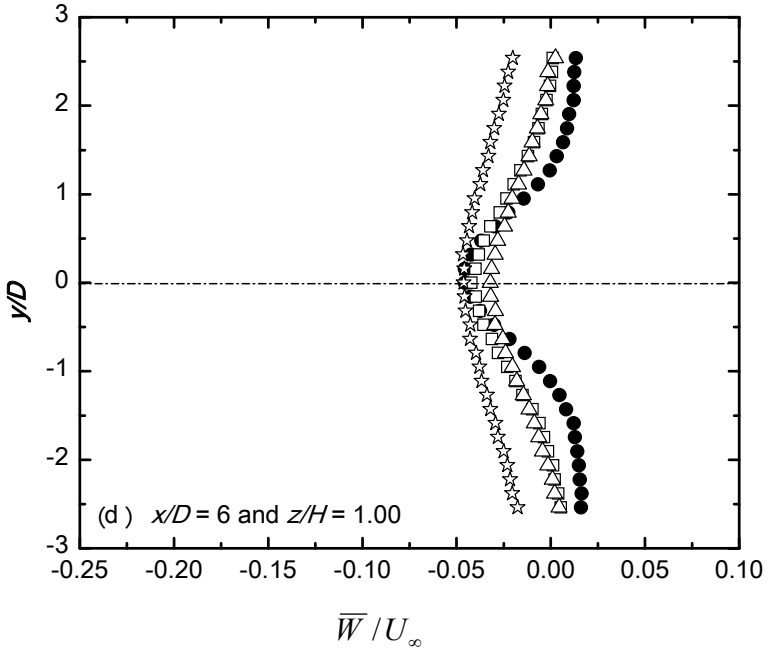

Figure 4.11 continued.

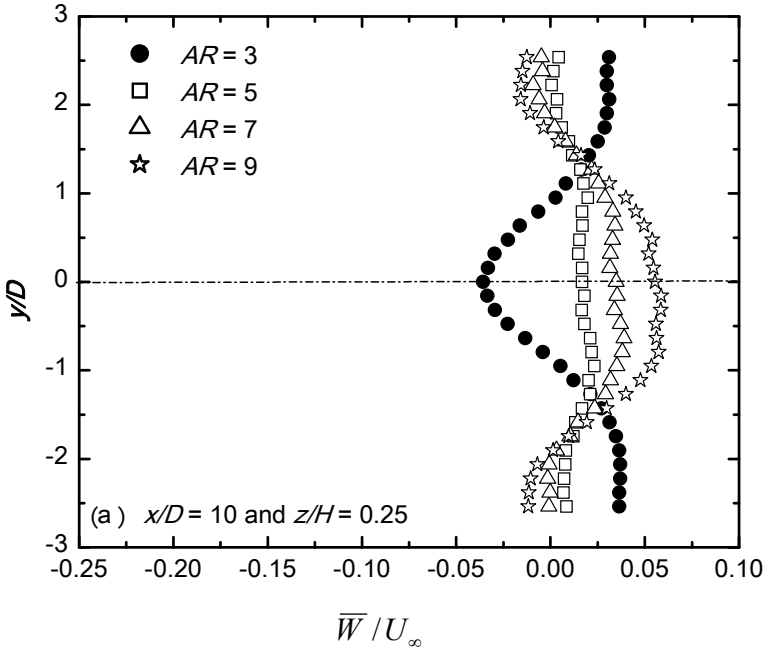

Figure 4.12: Time-averaged wall-normal velocity ($\overline{W}/U_\infty$) profiles at x/D = 10 along the cylinder's height: (a) z/H = 0.25, (b) z/H = 0.5, (c) z/H = 0.75, and (d) z/H = 1.

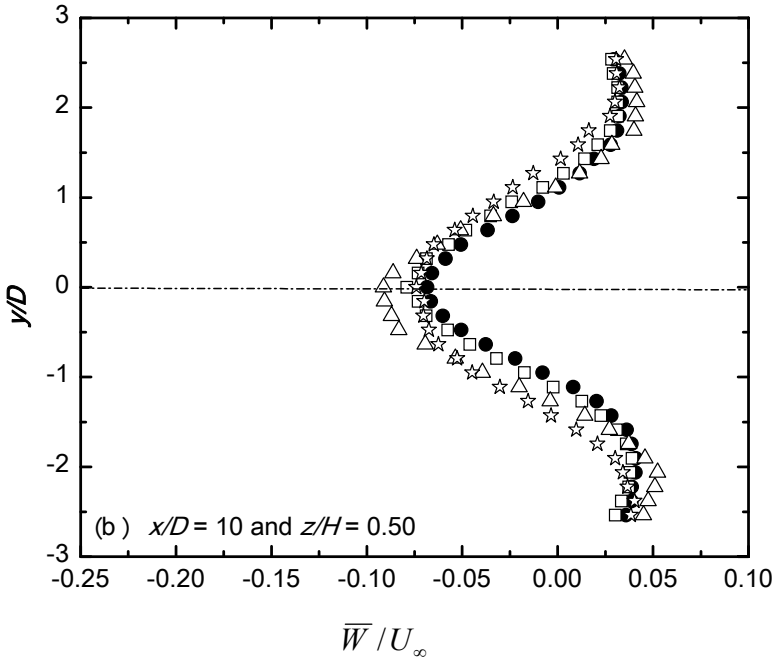

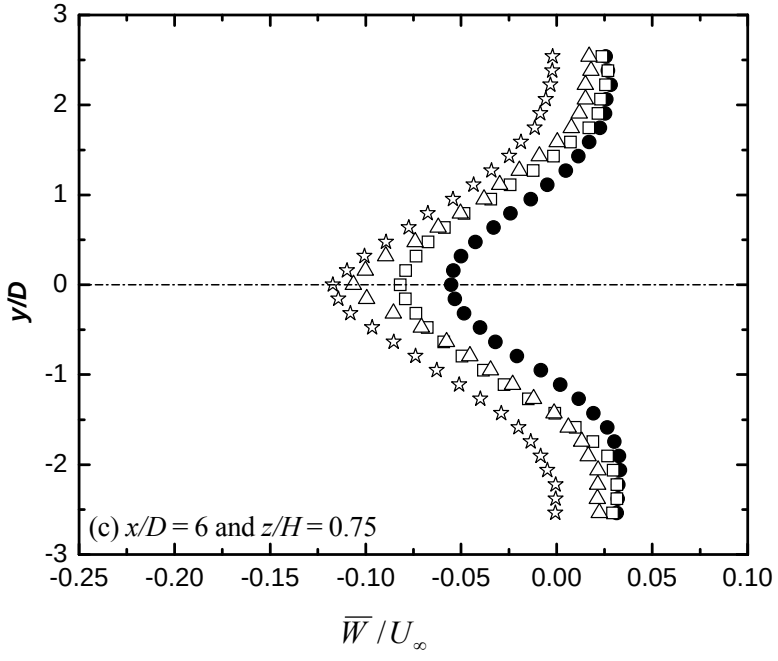

Figure 4.12 continued.

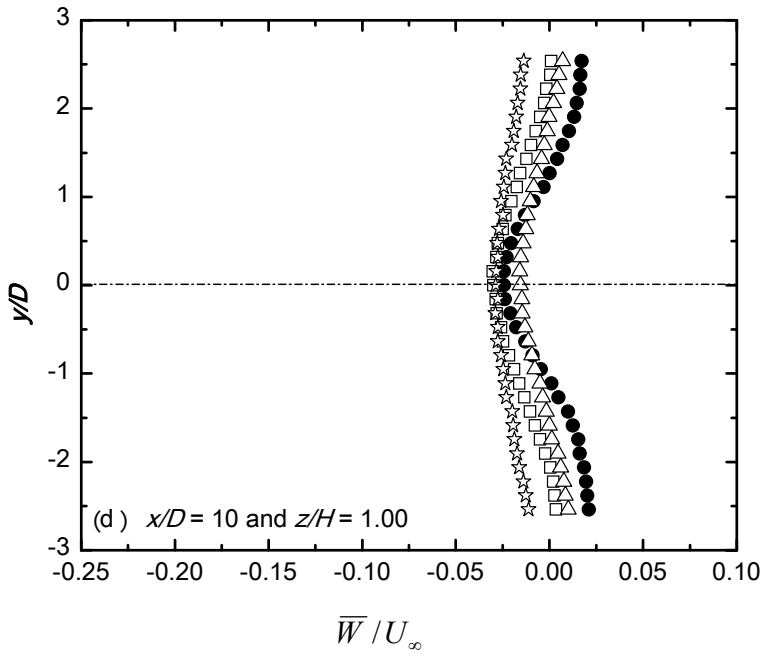

Figure 4.12 continued.

This implies or demonstrates that the downwash flow at the cylinder's mid-height is stronger for lower *AR* than higher *AR*. In the case of the profiles at *z/H* = 0.75, their characteristic is opposite to those at *z/H* = 0.5. The absolute value of the downwash flow increases with increasing *AR*, which indicates that the *AR* = 9 has the strongest downwash flow at this location. The presence of the downwash flow is still seen at *z/H* = 1 (Figure 4.11(d)) for all aspect ratios but with much lower magnitude when compared with profiles at *z/H* = 0.5 and 0.75. There is a general reduction in the strength of the downwash flow from the cylinder free end for all aspect ratios at *z/H* = 0.5, 0.75 and 1, as the streamwise distance increases (see Figure 4.12(b-d)).

4.2.4 Velocity Profiles along the Wake Centreline

The time-averaged streamwise velocity profiles on the wake centreline (y/D = 0) for each cylinder are presented in Figure 4.13. A strong velocity defect occurs within the cylinder wake for AR = 5, 7 and 9, and the minimum value of the velocity profile is below the mid-height of the cylinder. The strength of this velocity defect decreases with

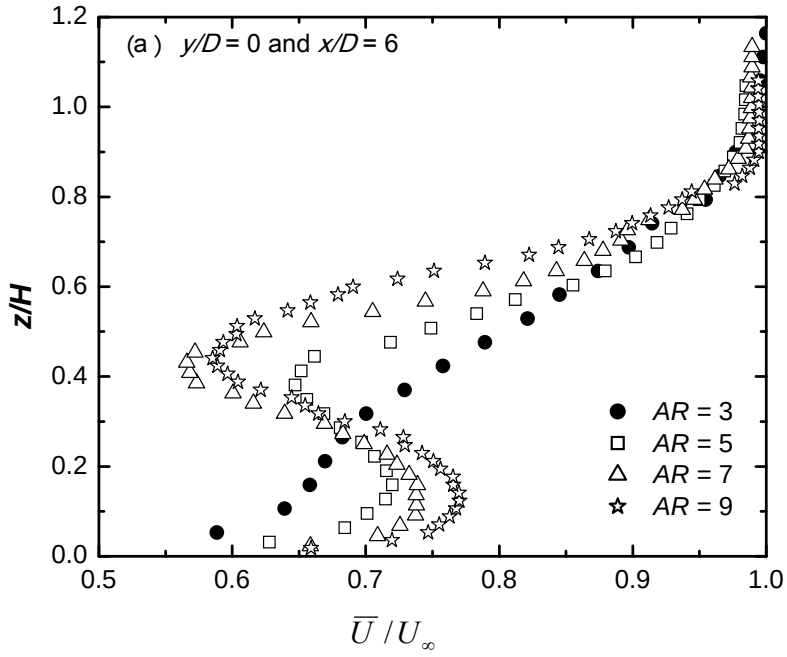

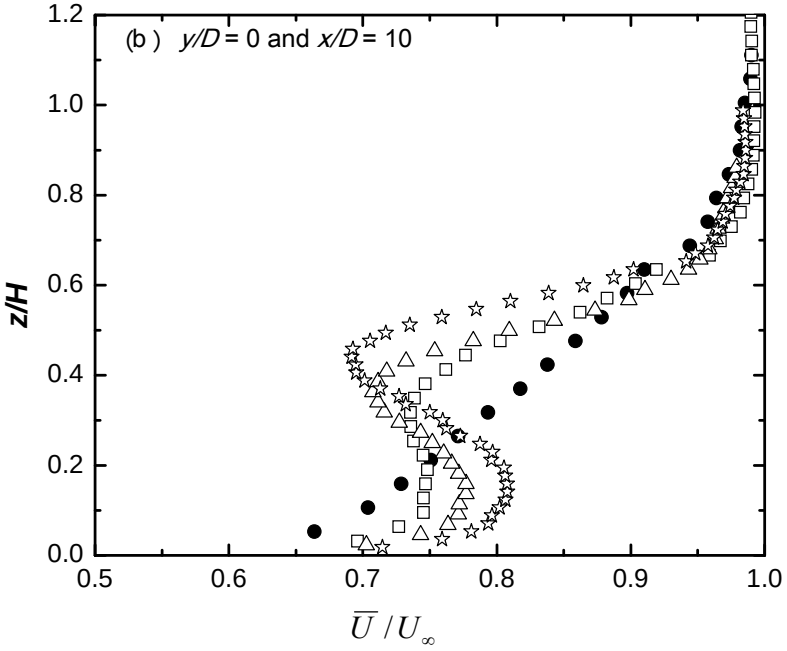

Figure 4.13: Time-averaged streamwise velocity profile at finite cylinder wake centreline ($y/D = 0$) at (a) $x/D = 6$ and (b) $x/D = 10$.

streamwise distance partly due to the influence of the downwash flow that approaches the ground plane further away from the cylinder. This region is not apparent for $AR = 3$, which also shows the distinct behaviour of the wake structure of this cylinder.

The time-averaged wall-normal velocity profiles on the wake centreline ($y/D = 0$) of the cylinder are presented in Figure 4.14. The profiles for $AR = 5$, 7 and 9 are all similar but differ in the relative location of the downwash flow region which moves upward toward the free end of the cylinder as AR increases. The profiles for $AR = 5$, 7 and 9 show two distinct flow regions within the cylinder wake: the upwash flow region which occurs closer to the ground plane, and the downwash flow region which occurs in the upper half of the cylinder. In the case of $AR = 3$, the downwash flow region is the main feature of this profile although there is a small upwash flow very close to the ground plane region (as seen in Figure 4.5). The absolute magnitude of the downwash

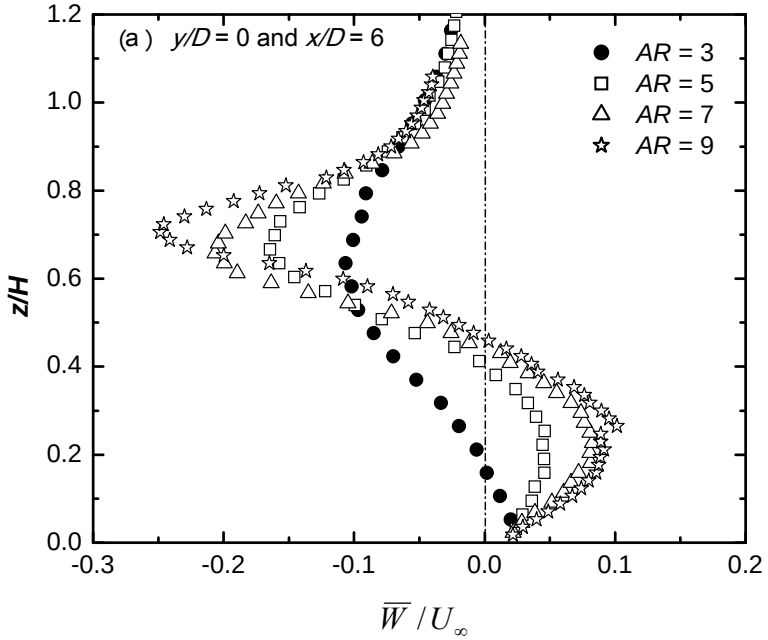

Figure 4.14: Time-averaged wall-normal velocity profile at finite cylinder wake centreline (y/D = 0) at (a) x/D = 6 and (b) x/D = 10.

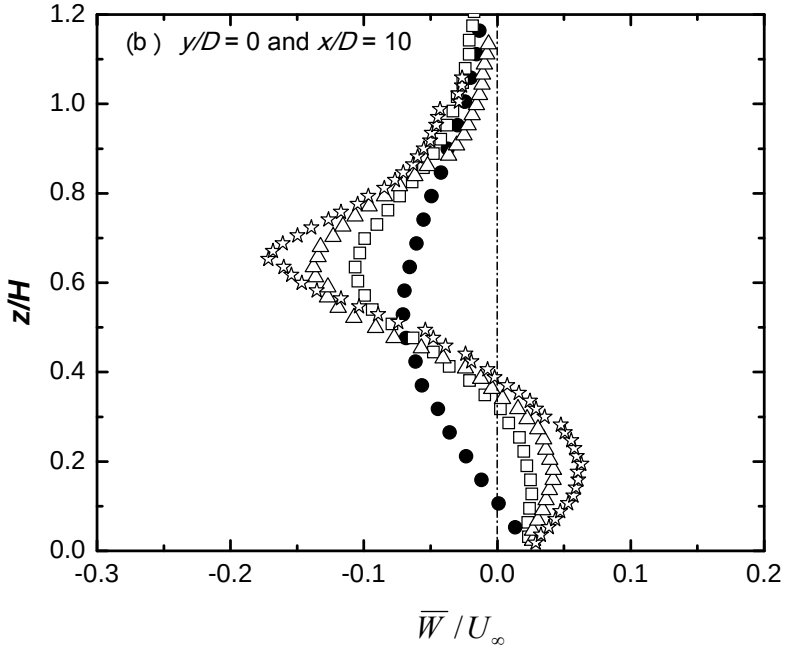

Figure 4.14 continued.

flow reduces with *AR*. There is a general reduction in the absolute magnitude of both downwash flow and the upwash flow as x/D increases (see Figure 14(b)).

4.3 Turbulent Statistics

4.3.1 Turbulence Intensity Distribution

The distributions of the streamwise turbulence intensity ($u'/\overline{U}$) and the wall-normal turbulence intensity ($w'/\overline{U}$) in the cross-stream plane at x/D = 6, shown in Figures 4.15 to 4.18, respectively, are similar to the time-averaged streamwise velocity fields (Figures. 4.1 to 4.4). For *AR* = 5, 7, and 9, the localized regions of high streamwise (Figure 4.16(a), 4.17(a)) and 4.18(a)) and wall-normal turbulence intensity (Figures.

4.16(b), 4.17(b) and 4.18(b)) behind the cylinder coincide with the regions of low streamwise mean velocity (Figure 4.1(a)-4.4(a)) and are bounded on the four corners by the tip and base vortices (Sumner *et al.,* 2004). This region of high turbulence intensity is caused by the interactions between the vortex structures, the vortex street, downwash

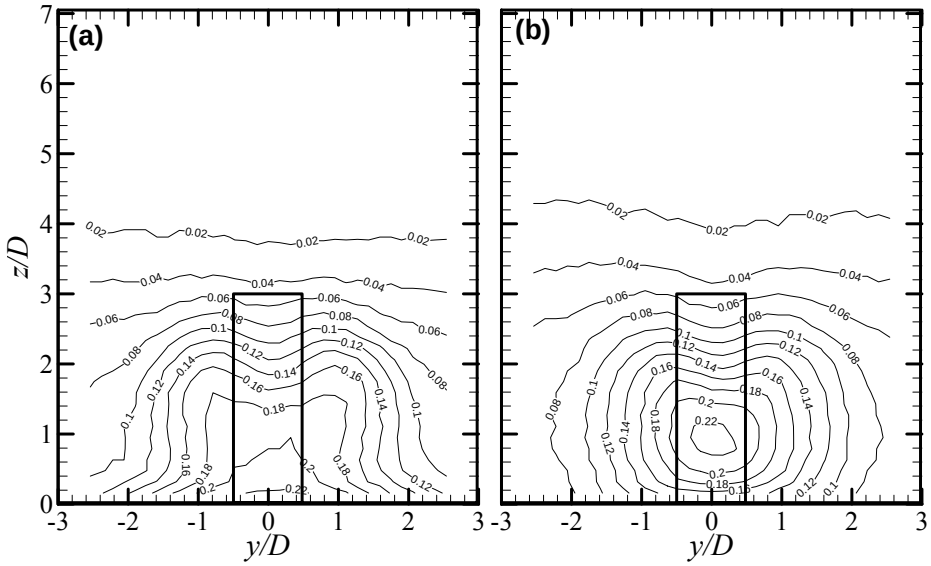

Figure 4.15: Turbulence intensity fields for AR = 3 at x/D = 6: (a) streamwise, $u'/\overline{U}$; and (b) wall-normal, $w'/\overline{U}$. Contour increment of 0.02.

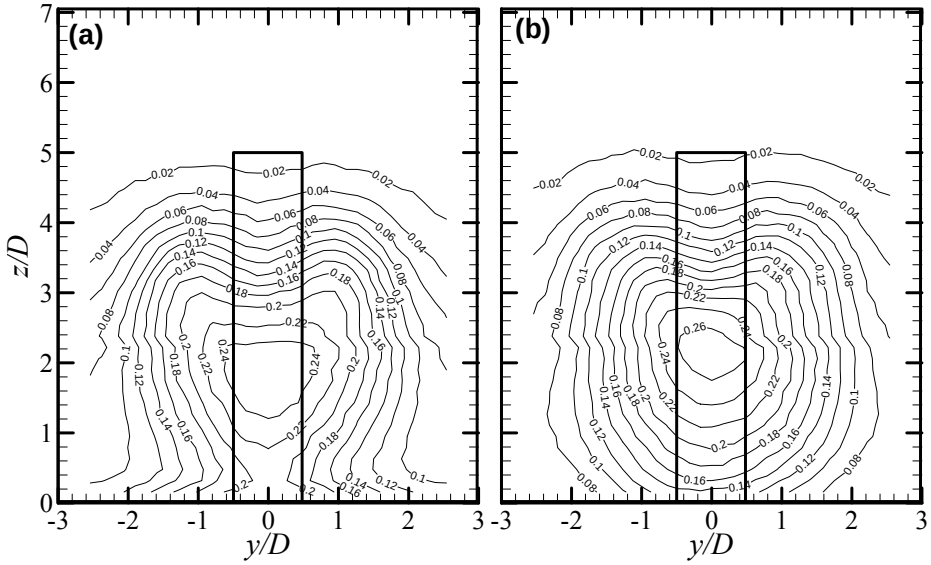

Figure 4.16: Turbulence intensity fields for AR = 5 at x/D = 6: (a) streamwise, $u'/\overline{U}$; and (b) wall-normal, $w'/\overline{U}$. Contour increment of 0.02

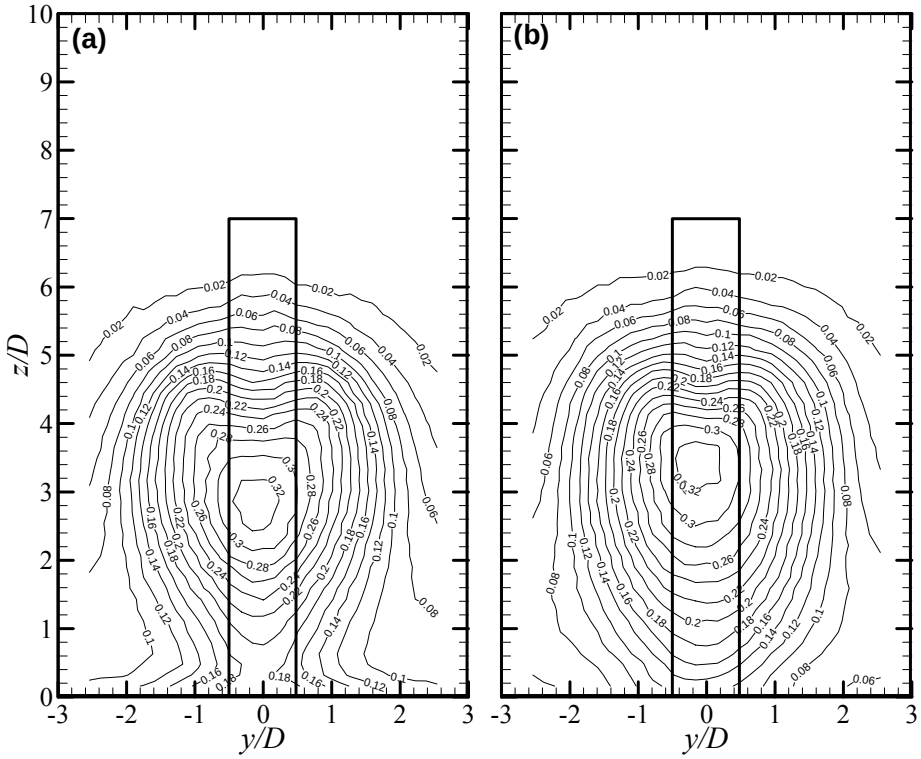

Figure 4.17: Turbulence intensity fields for AR = 7 at x/D = 6: (a) streamwise, $u'/\overline{U}$; and (b) wall-normal, $w'/\overline{U}$. Contour increment of 0.02.

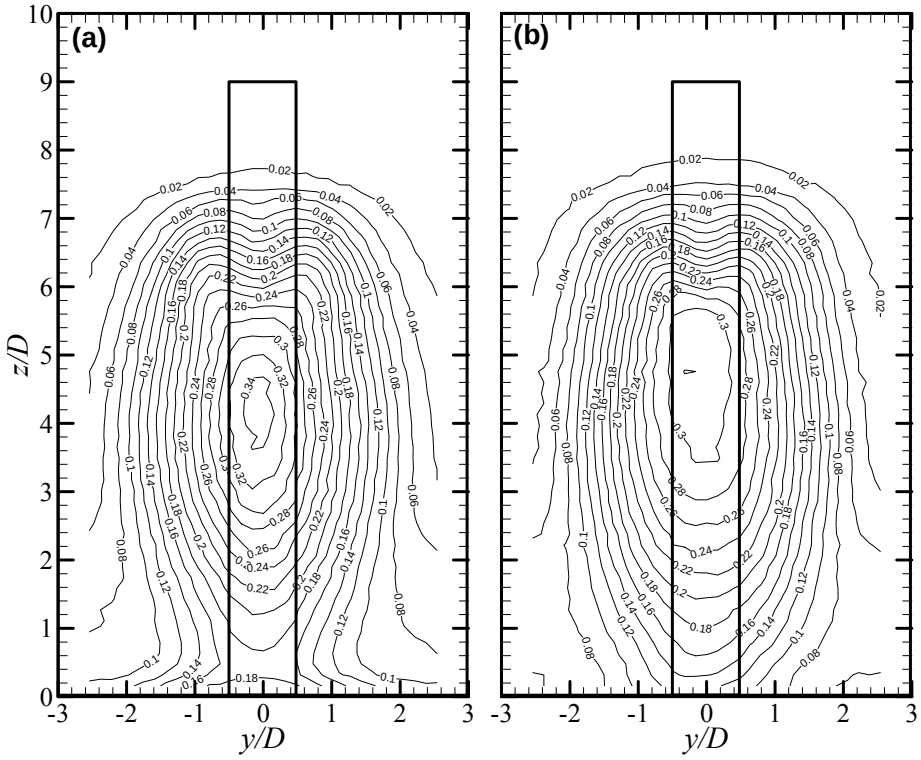

Figure 4.18: Turbulence intensity fields for AR = 9 at x/D = 6: (a) streamwise, $u'/\overline{U}$; and (b) wall-normal, $w'/\overline{U}$. Contour increment of 0.02

from the free end, and upwash from the ground plane. In the case of AR = 3, the localized region of high streamwise turbulence intensity disappears (Figure 4.15(a)) because the base vortex structures and upwash (Figure 4.5) are absent. However, a localized region of higher wall-normal turbulence intensity is still detected close to the ground plane ((Figure 4.15(b)). For all four cylinders, the maximum levels of turbulence intensity reduce with x/D (not shown), and the downwash flow causes them to move closer to the ground plane. In addition, the strength of the turbulence intensity increases with AR due to the strong influence of downwash flow and separated shear layers, which both increase with AR.

Profiles of the streamwise turbulence intensity (u'/U_∞) and wall-normal turbulence intensity (w'/U_∞) at four locations along the cylinders' height at x/D = 6 are presented in Figure 4.19 and 4.20, respectively. At z/H = 0.25 and 0.5, there is an overall

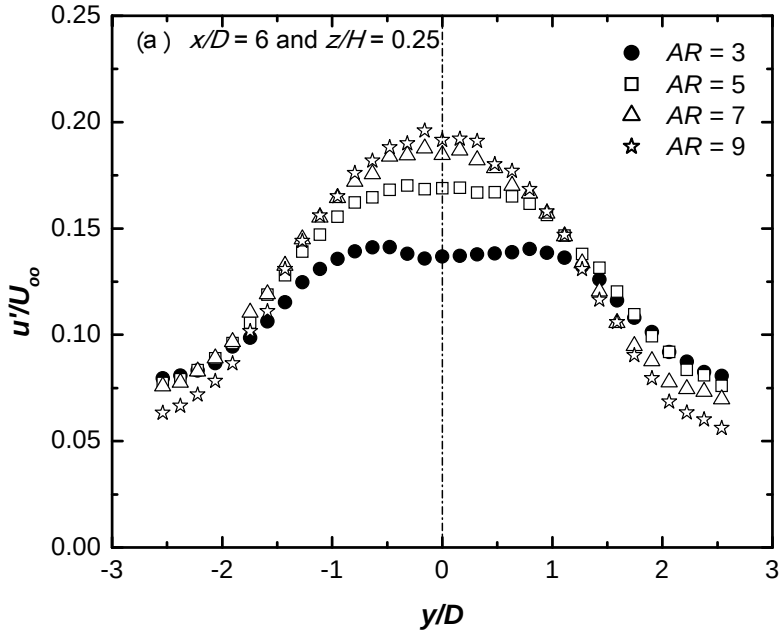

Figure 4.19: Streamwise turbulence intensity profiles at x/D = 6 along the cylinder's height: (a) z/H = 0.25, (b) z/H = 0.5, (c) z/H = 0.75, and (d) z/H = 1.

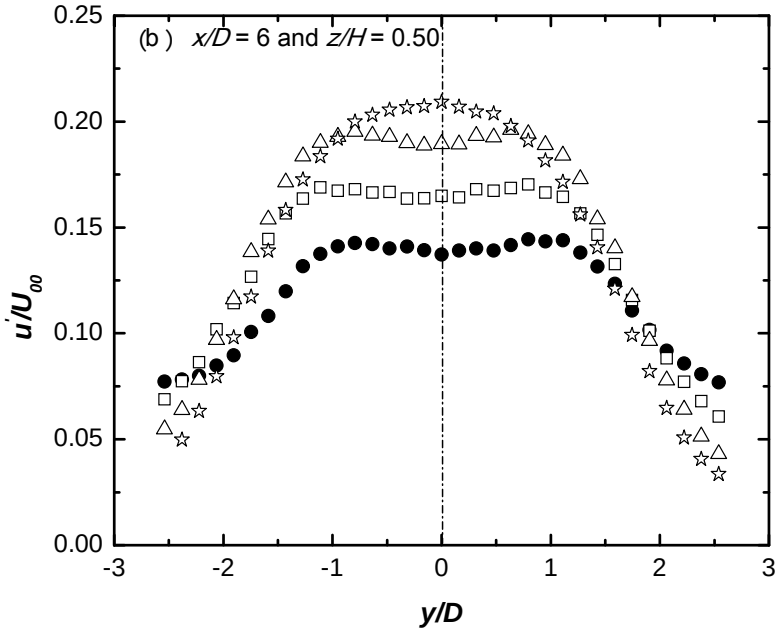

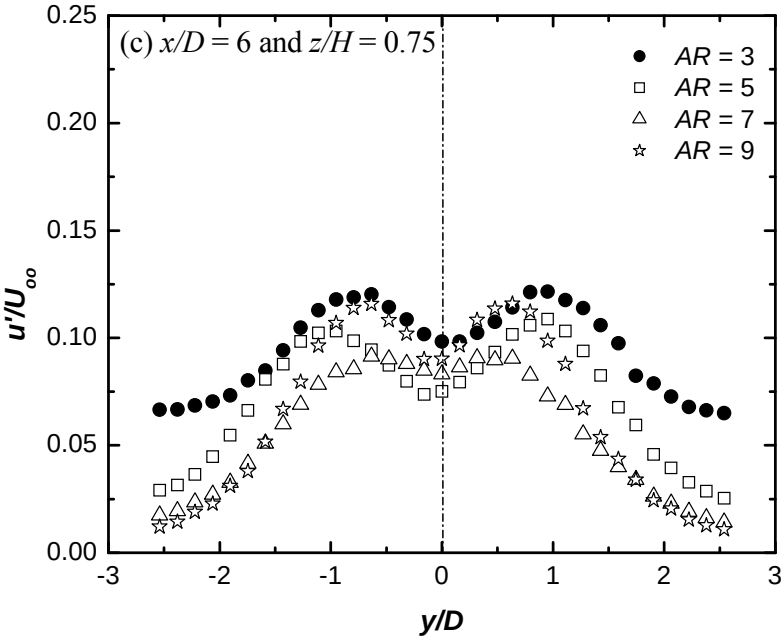

Figure 4.19 continued.

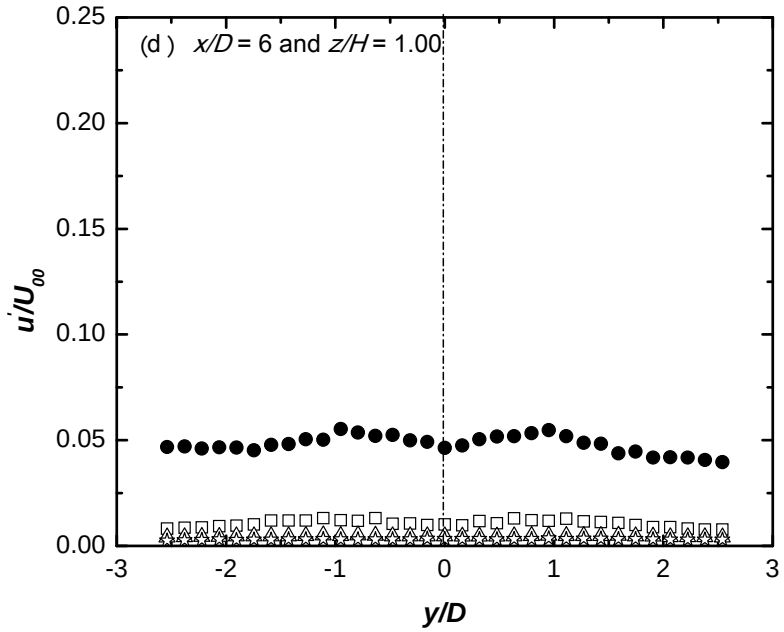

Figure 4.19 continued.

reduction in turbulence intensity as the value of *AR* decreases, and a gradual change from single-peak behaviour to double-peak behaviour, with increasing *x/D* (not shown). The reduction in the turbulence intensities may be due to the reduction in the vertical span of the separated layers on either side of the cylinder as *AR* decreases. The wall-normal turbulence intensities (Figure 4.20(a-b)) are slightly higher, especially for *AR* = 3, 5, and 7, than the streamwise turbulence intensities (Figure 4.19(a-b)). The data show the distinctly different wake structure for *AR* = 3, which has the lowest levels of turbulence intensity at these locations (*z/H* = 0.25 and 0.50) except at *z/H* = 0.75 (Figure 4.20(c) and the widest lateral wake spread of the four aspect ratios. Both the streamwise and the wall-normal turbulence intensities profiles (see Figure 4.19(a) and Figure 4.20(a)) nearly collapse for *AR* = 7 and 9 at *z/H* = 0.25, however, the profiles for *AR* = 5 are distinct, suggesting that the wake structure of *AR* = 5 may be slightly different from

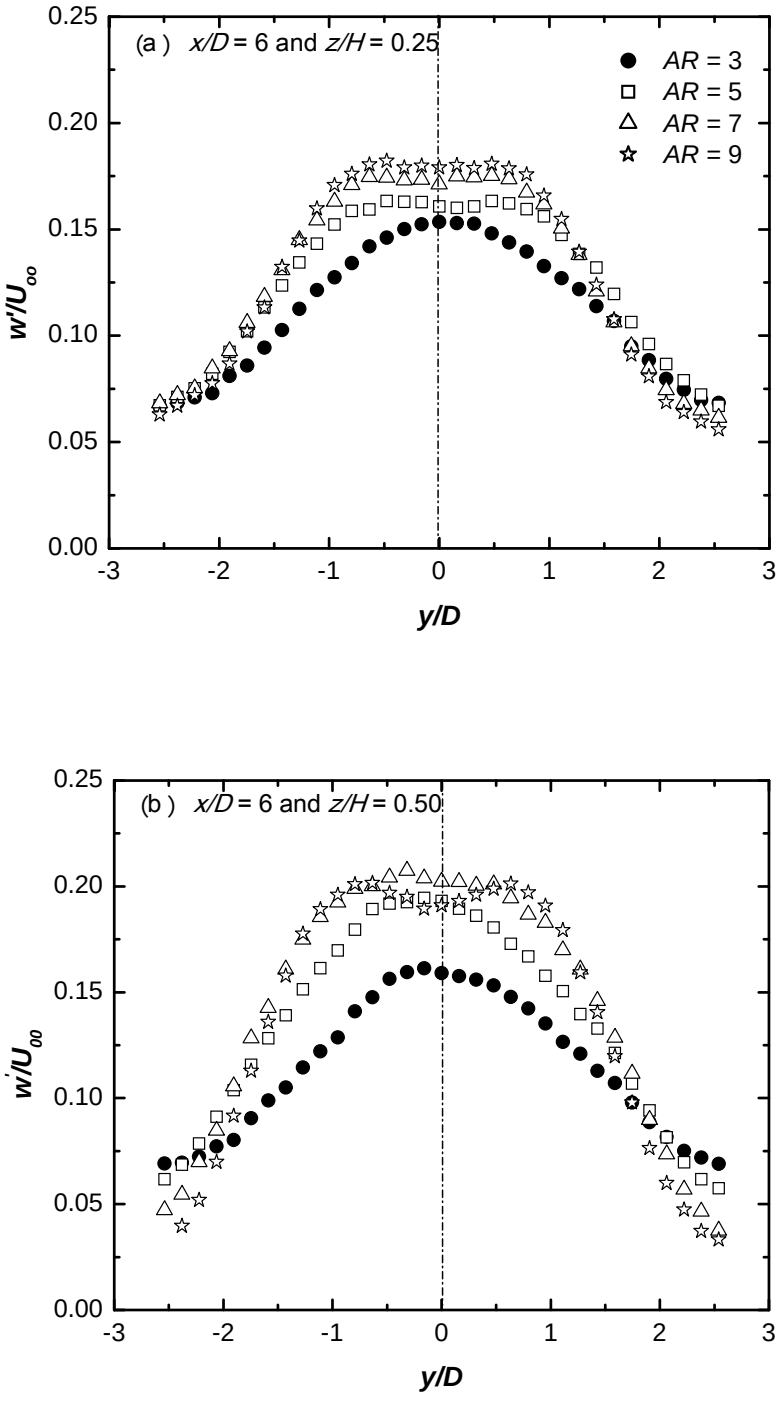

Figure 4.20: Wall-normal turbulence intensity profiles at $x/D = 6$ along the cylinder's height: (a) $z/H = 0.25$, (b) $z/H = 0.5$, (c) $z/H = 0.75$, and (d) $z/H = 1$.

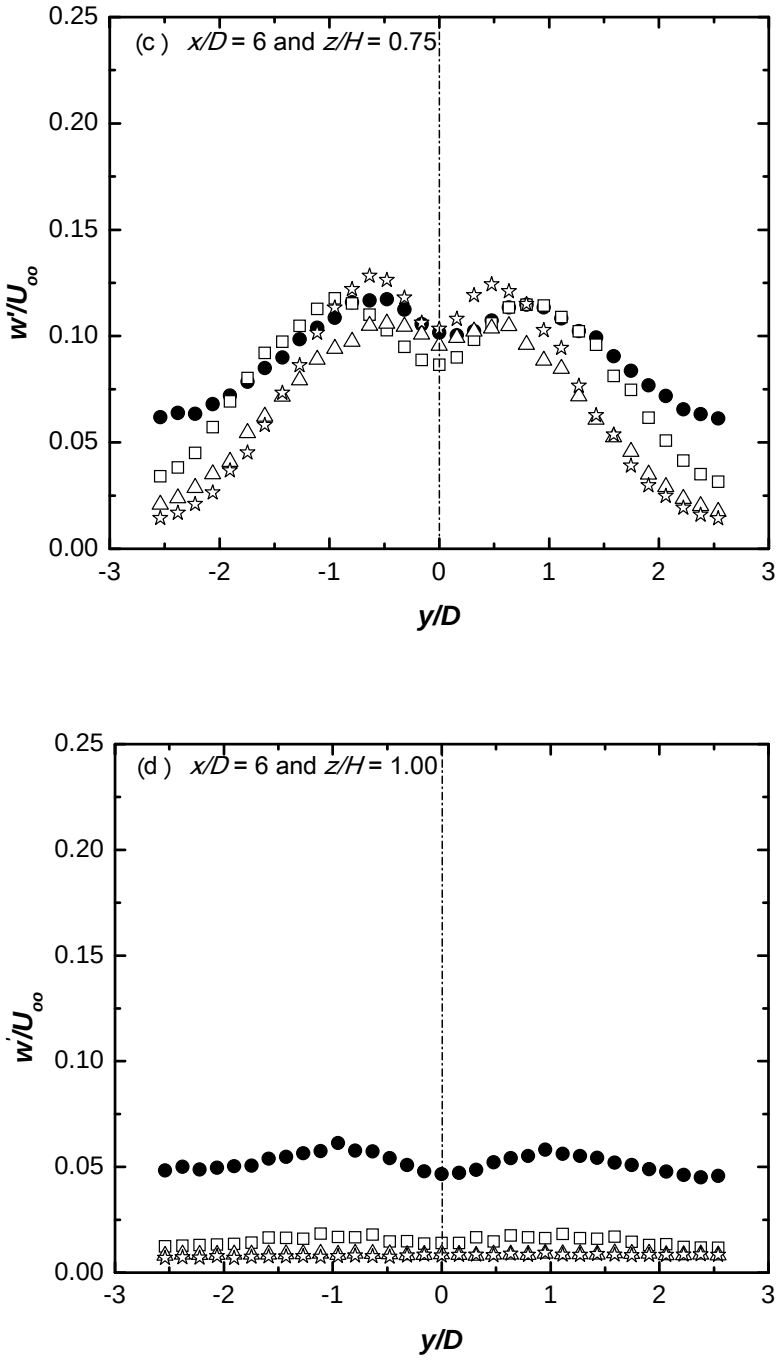

Figure 4.20 continued.

those of the AR = 7 and 9 cylinders. For the streamwise turbulence intensity at z/H = 0.5 (see Figure 4.19(b)), a peak is observed for AR = 9, a broad peak for AR = 7 and 5, and two peaks are observed for AR = 3. For AR = 6, Park and Lee (2002) and Afgan *et al.*

(2007) observed a single peak and double peaks, respectively, at the mid-height of the cylinder at $x/D = 5$. In addition, two peaks are observed in the wall-normal turbulence intensity at $z/H = 0.5$ for $AR = 9$ in the present study.

At $z/H = 0.75$, two peaks are observed in both the streamwise and the wall-normal turbulence intensity profiles (see Figure 4.19(c) and Figure 4.20(c)) for all aspect ratios. Wang *et al.* (2006) also observed two peaks in the streamwise turbulence intensity for a finite-height square cylinder of $AR = 5$ at $z/H = 0.8$ and $x/D = 6$. They argued that the two peaks are due to the "occurrence of two rows of vortices" or due to the shear layers from the two sides of the cylinder within the square cylinder wake. As reported by Okamoto and Sunabashiri (1992), the two peaks observed may also be due to the influence of the downwash flow from the cylinder free end.

At the cylinder free end, $z/H = 1$, the streamwise turbulence intensity (Figure 4.19(d)) and the wall-normal turbulence intensity profiles for $AR = 5$, 7 and 9 are almost zero, which indicates that the flow is now outside the velocity defect region and the flow has the freestream properties of about 0.6%. The non-zero profiles observed for $AR = 3$ may be due to the influence of the boundary layer since the cylinder is fully immersed within this layer (for $AR = 3$ at $z/H = 1$, $\delta/H = 1$). Since the cylinder is still within the boundary layer, the turbulence intensity is higher compared with the other cylinders which are only partially immersed inside the boundary layer.

Figure 4.21 shows the streamwise and wall-normal turbulence intensity distributions, respectively, along the wake centreline ($y/D = 0$) for all four cylinders at $x/D = 6$. Since the tip vortex and base vortex strengths increase with AR (Sumner *et al.*, 2004), there is a resultant overall increase in turbulence intensity with AR, due to the interactions between these streamwise vortices. The vortex structures, downwash flow

and upwash flow weaken with increasing distance from the cylinder (Figures. 4.5-4.8).This give rise to a decrease in turbulence intensity in the streamwise direction due reduction in turbulent production (not shown). There is also a reduction in turbulence intensity towards the free end similar to what was observed by Park and Lee (2000) for a

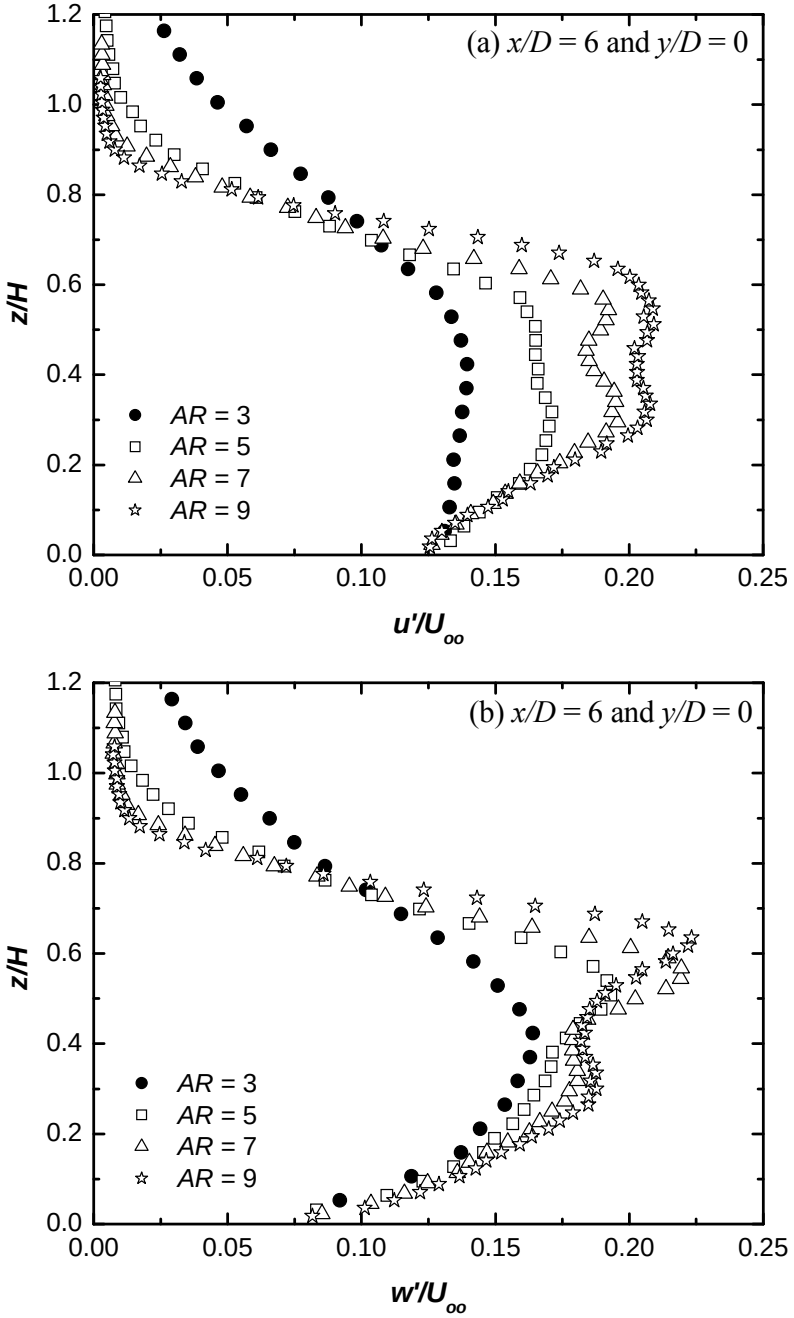

Figure 4.21: Wake profiles at wake centre plane ($y/D = 0$) at $x/D = 6$ for (a) streamwise turbulence intensity, (b) wall-normal turbulence intensity.

cylinder with AR = 10. A distinctly different turbulent wake structure is observed for AR = 3, which has the lowest overall levels of turbulence intensity within the cylinder wake (except at $z/H \sim 1$), the largest wake spread in the wall-normal direction at a given x/D, and an absence of a peak streamwise turbulence intensity near mid-height (Figure 4.21(a)). Similar to the cross-stream profiles at mid-height shown in Figures 4.12 to 4.15, the turbulence intensity data on the wake centreline for AR = 7 and 9 (Figure 4.21(a)) nearly collapse onto a single curve within the lower half of the wake but move apart within the upper half of the wake. The profile for AR = 5 lies between the shortest (AR = 3) and longest (AR = 7 and 9) cylinders.

4.3.2 Reynolds Shear Stress

The Reynolds shear stress, $-<uw>/U_\infty^2$, which physically relates to the transport of momentum due to the turbulent fluctuations in the flow, is presented in this section. Regions of elevated Reynolds shear stress may be associated with strong local production of turbulence, which depends on the local velocity gradients. The behaviour of the Reynolds shear stress can be deduced from the mean streamwise velocity profile. The streamwise development of the Reynolds shear stress distribution on the wake centreline (y/D = 0) is shown in Figure 4.22. Its behaviour is similar for AR = 5, 7, and 9, with two regions of elevated Reynolds shear stress, each of opposite sign. The Reynolds shear stress profiles for AR = 3 are different, where the absence of the base

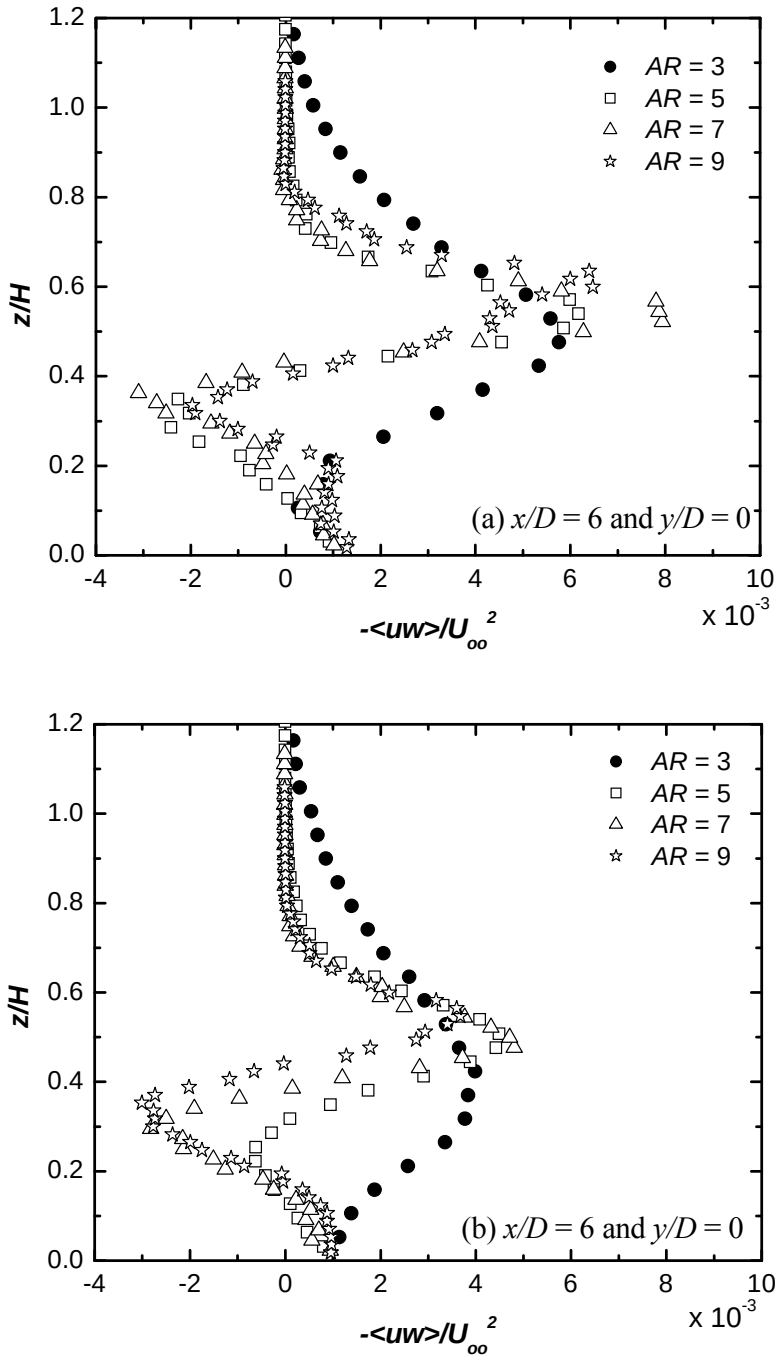

Figure 4.22: The Reynolds shear stress profile on the wake centreline (y/D = 0) at (a) x/D = 6 and (b) x/D = 10.

vortex structures and upwash coincides with the vanishing of the negative shear stress region. The Reynolds shear stress profiles for AR = 7 and AR = 9 at x/D = 10 (Figure

4.22(b)) are slightly different from that of $AR = 5$.

Profiles of the Reynolds shear stress at four locations along the cylinder height at $x/D = 6$ are presented in Figure 4.23. At $z/H = 0.25$ (Figure 4.23 (a)), the shear stress profile for $AR = 3$ is completely positive with a peak at the wake centreline. In the case of $AR = 5$, 7 and 9, the shear stress profiles are completely negative within the vicinity of the wake centreline with two negative peaks on either side of the wake centreline. The absence of the strong upwash flow from the ground plane for $AR = 3$ (see Fig 4.11(a)) is the major reason for the presence of the positive shear stress in this cylinder wake, while the cylinders with upwash flow within their wakes have different shear stress profiles.

At $z/H = 0.5$ (Figure 4.23 (b)), the shear stress profiles are almost entirely positive with one strong positive peak along the wake centreline for all the cylinders. The presence of the positive shear stress, irrespective of the aspect ratio, is due to the

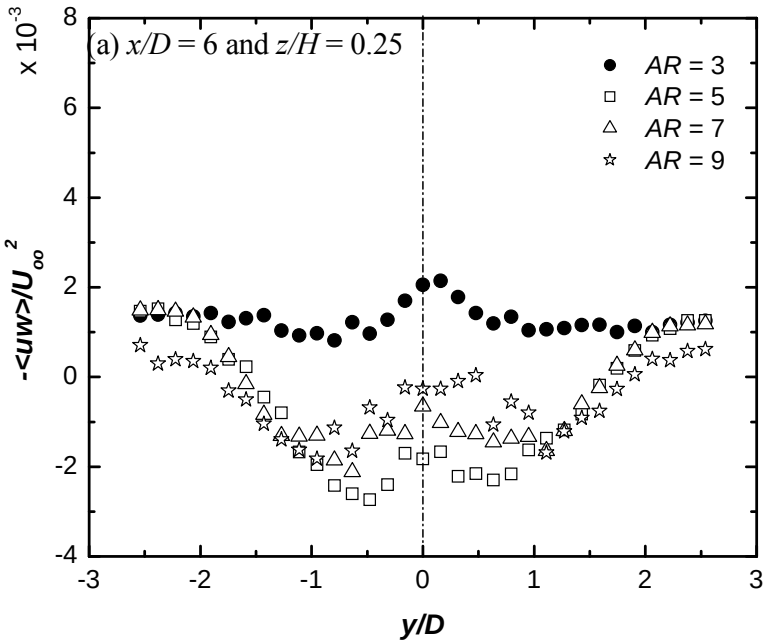

Figure 4.23: Reynolds shear stress profiles at $x/D = 6$ along the cylinder's height: (a) $z/H = 0.25$, (b) $z/H = 0.5$, (c) $z/H = 0.75$, and (d) $z/H = 1$.

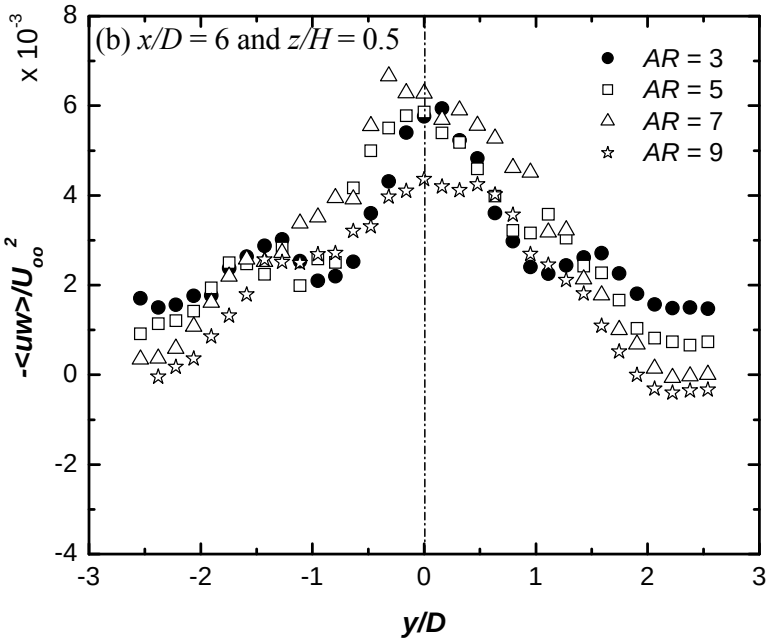

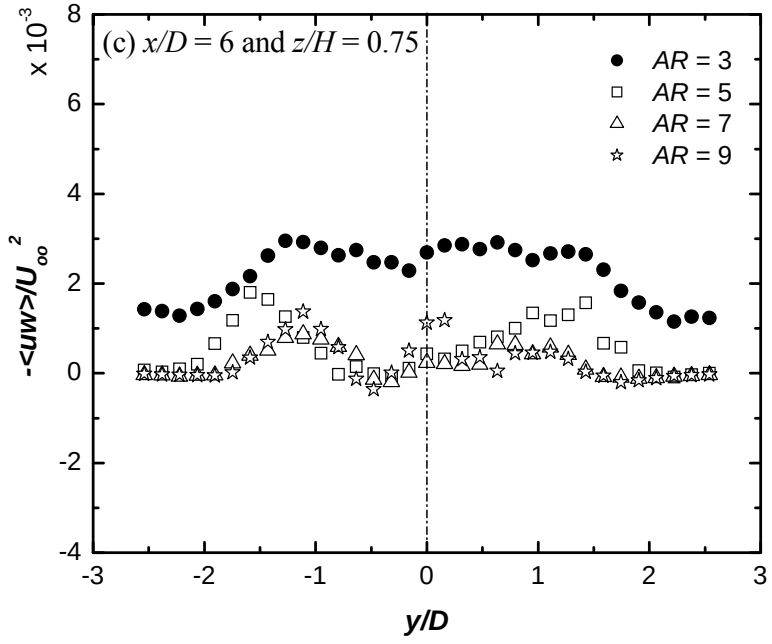

Figure 4.23 continued.

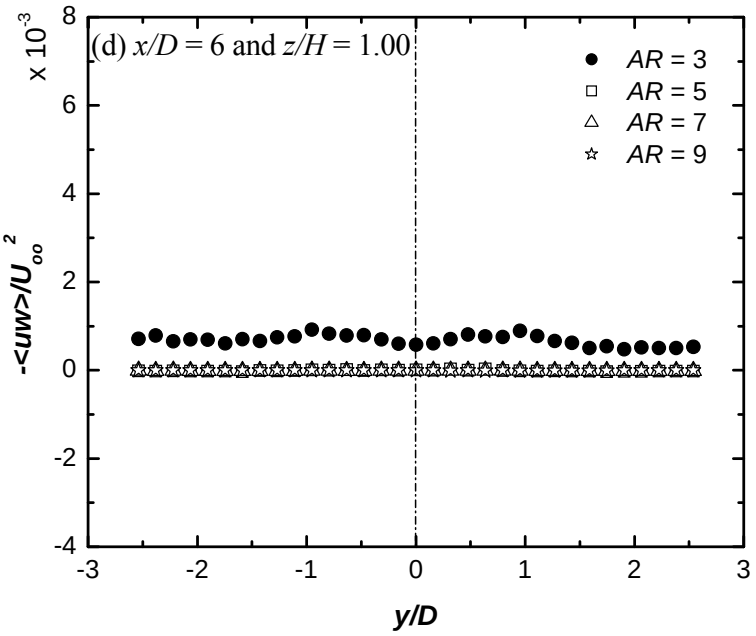

Figure 4.23 continued.

strong downwash flow (see Figure 4.11 (b)) from the cylinder free end that is common to all of them. In addition, two other peaks are observed on either side of the wake centreline for AR = 3. At z/H = 0.75, the shear stress profiles are entirely positive with two peaks, irrespective of the aspect ratio of the cylinder. The profile for AR = 3 has a higher magnitude than the other cylinders.

At the cylinder free end, z/H = 1 (Figure 4.23(d)), the shear stress profiles for AR = 5, 7 and 9 are almost zero, which indicate that the flow is now outside the velocity defect region and the flow has the freestream properties. The non-zero profile observed for AR = 3 may be due to the effect of the flat-plate boundary layer as mentioned earlier.

The streamwise development of the Reynolds shear stress ($-<uw>/\overline{U}^2$) distribution in the cross-stream (y-z) plane is shown in Figures 4.24 to 4.27. Its behaviour is similar for AR = 5, 7, and 9 (Figures 4.25-4.27), with two regions of

elevated Reynolds shear stress, each of opposite sign, located behind the cylinder. The region of positive Reynolds shear stress is located in the region of downwash flow from the free end and centred between the tip vortex structures (Sumner *et al.,* 2004). The region of negative Reynolds shear stress occurs within the plane wall boundary layer in the region of the upwash flow, and is centred between the base vortex structures (Sumner *et al.,* 2004). The boundary between these two regions approximately coincides with the regions of lowest time-averaged streamwise velocity (Figures 4.1-4.4) and highest turbulence intensity (Figures 4.15-4.18), and is centred in the midst of the four vortex structures where the downwash and upwash flows interact. The Reynolds shear stress distribution for AR = 3 (Figure 4.23) is different, where the absence of upwash from the ground plane and the base vortex structures means the absence of any negative Reynolds shear stress. For all cylinders, the maximum values of Reynolds shear stress (both positive and negative) decrease with streamwise distance from the cylinder.

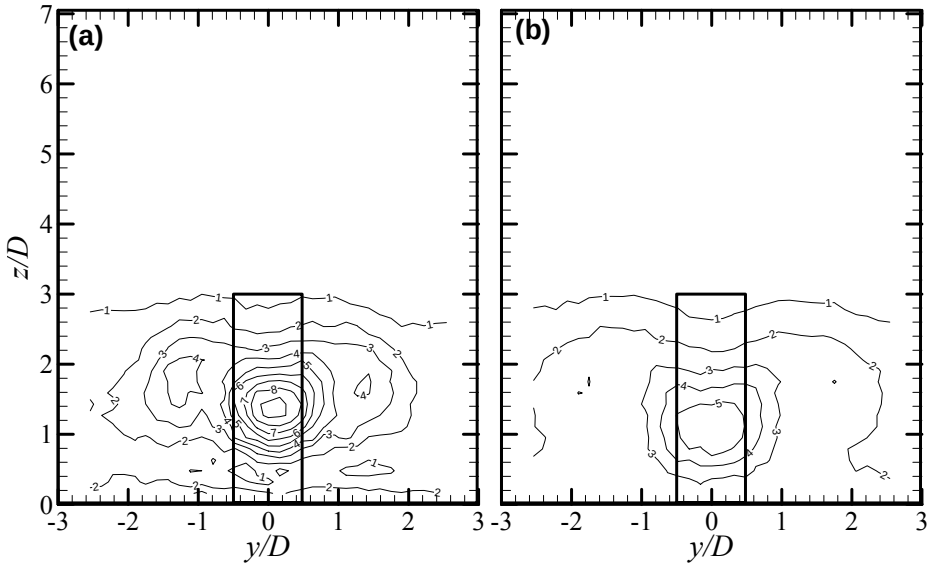

Figure 4.24: Reynolds shear stress ($-<uw>/\overline{U}^2$) field for AR = 3 at (a) x/D = 6 and (b) x/D = 10. Contour value is multiplied by 10^{-3}. Contour increment of 1 x 10^{-3}.

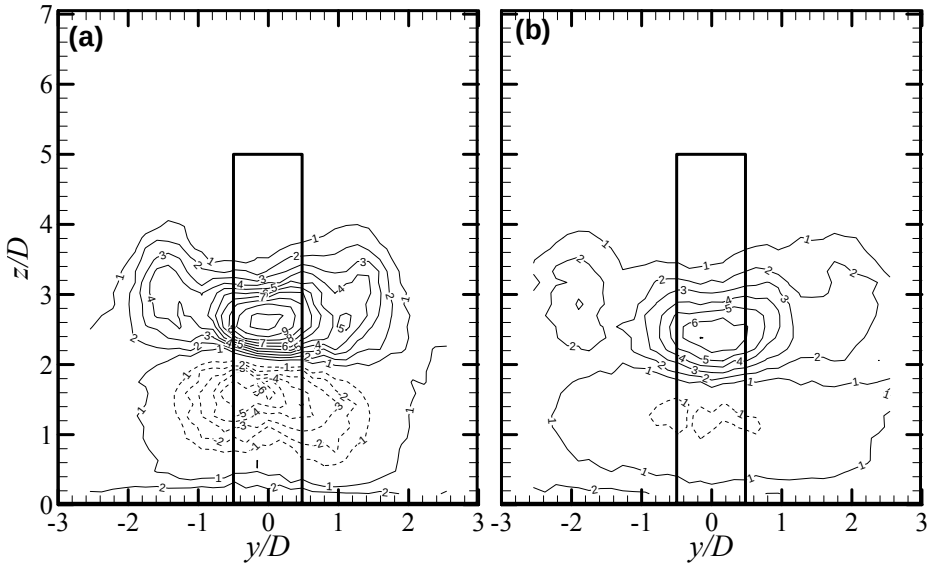

Figure 4.25: Reynolds shear stress ($-<uw>/\overline{U}^2$) field for AR = 5 at (a) x/D = 6 and (b) x/D = 10. Contour value is multiplied by 10^{-3}. Contour increment of 1 x 10^{-3}.

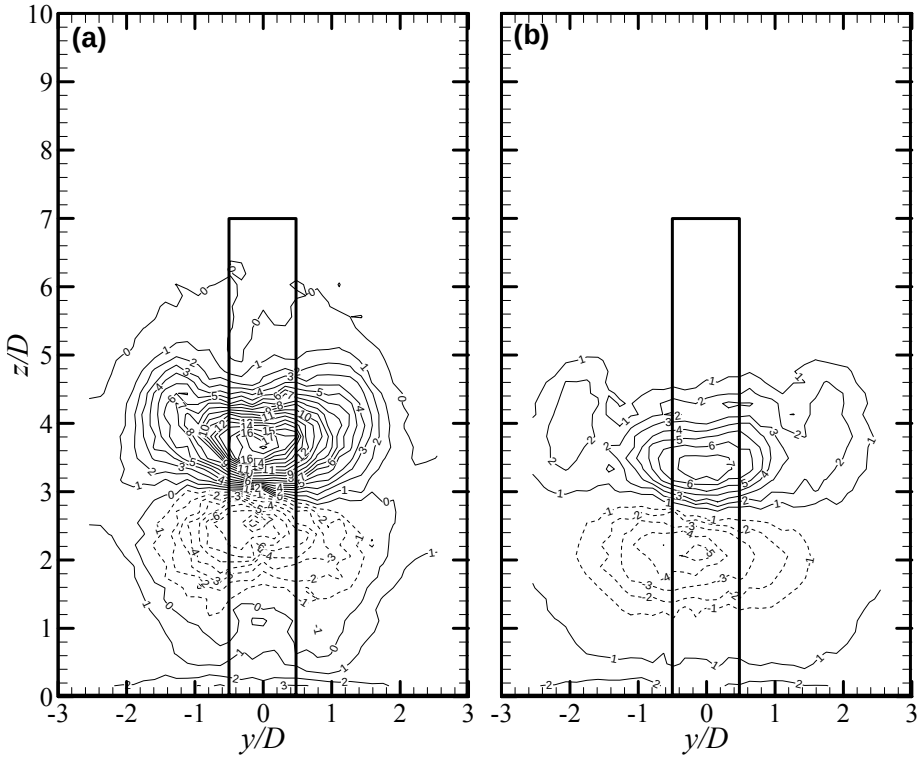

Figure 4.26: Reynolds shear stress ($-<uw>/\overline{U}^2$) field for AR = 7 at (a) x/D = 6 and (b) x/D = 10. Contour value is multiplied by 10^{-3}. Contour increment of 1 x 10^{-3}.

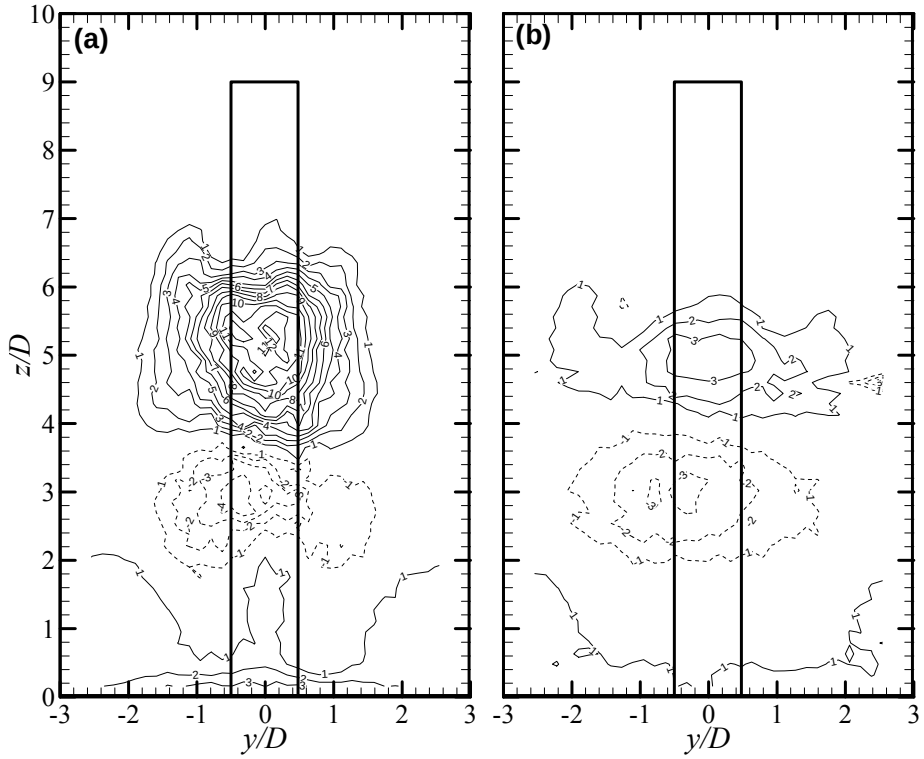

Figure 4.27: Reynolds shear stress ($-<uw>/\overline{U}^2$) field for AR = 9 at (a) x/D = 6 and (b) x/D = 10. Contour value is multiplied by 10^{-3}. Contour increment of 1 x 10^{-3}.

4.3.3 Triple Correlation

Triple correlations contain statistical information that relates to the turbulent flux of the Reynolds stress. Their spatial gradients represent part of the turbulent diffusion terms in the Reynolds stress transport equations (Gad-el-Hak and Bandyopadhyay, 1994).

The profiles of $-<u^2w>/U_\infty^3$, which are associated with the average transport of $<u^2>$ by the turbulent motion in the wall-normal direction, are shown in Figure 4.28. The pattern of this triple correlation profile, which is related to the gradient of the shear stress, can be deduced from the Reynolds shear stress profiles. While there is only one negative region for AR = 3, the other cylinders have one positive region within the boundary layer region and one negative region just above the mid-height of the cylinder at x/D = 6 (Figure 4.28(a)). The negative region is located in the downwash flow region

for all the values of *AR*, while the positive region for *AR* = 5, 7 and 9 is within the upwash flow region. The absence of the positive region in the case of *AR* = 3 might be

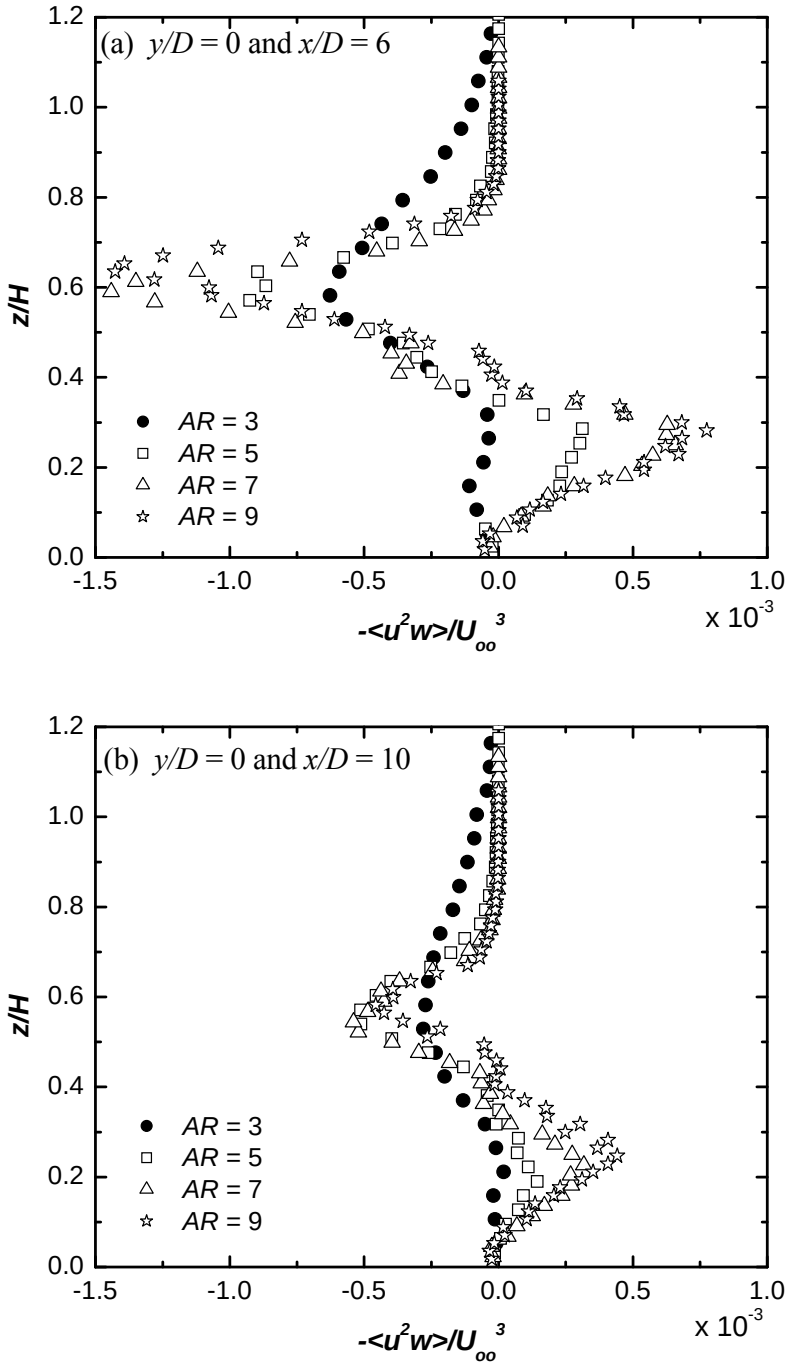

Figure 4.28: The triple correlation ($-\langle u^2w\rangle/U_\infty^3$) along the wake centreline at (a) $x/D = 6$, and (b) $x/D = 10$.

the result of the absence of upwash flow within the cylinder base region due to the suppressing effect of the downwash flow that extends to the ground plane (see e.g. Sumner *et al.,* 2004). As the streamwise distance increases (see Figure 4.28(b)), the absolute values of these peaks reduce for all the cylinders.

The profiles of $-\langle uw^2\rangle / U_\infty^3$, which represent transport of the wall-normal Reynolds stress, $\langle w^2\rangle$, in the streamwise direction, are presented in Figure 4.29. At $x/D = 6$ (Figure 4.29(a)), two positive regions, one within the boundary layer on the ground plane and upwash flow region, and the second region within the downwash flow region below the free end of the cylinder; and a third negative region, between these positive regions, are observed for $AR \geq 5$. Only one positive peak region, within the downwash flow region, is observed for $AR = 3$. The absence of both the negative region and the (base) positive region may be related to the influence of the downwash flow that reaches the vicinity of the ground plane as well as the absence of base vortex structures in the

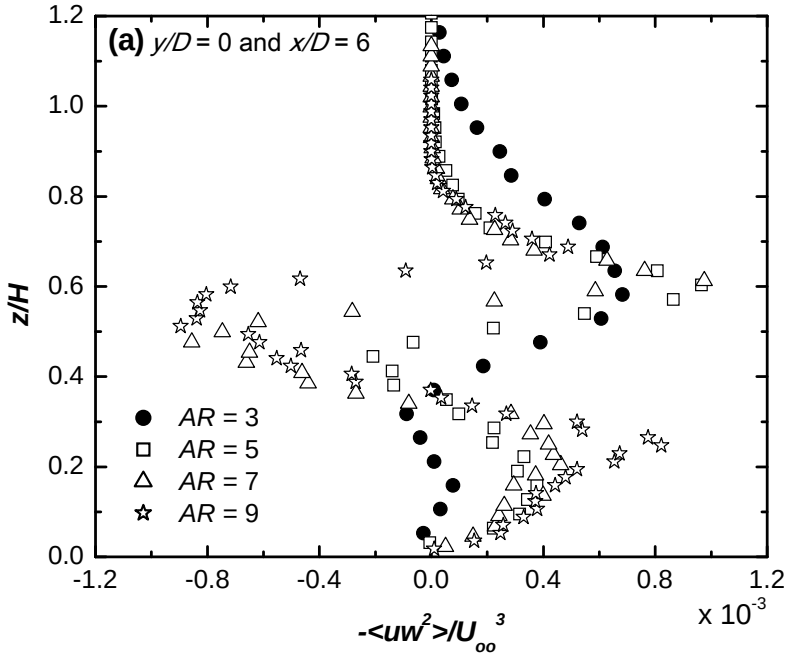

Figure 4.29: The triple correlation ($-\langle uw^2\rangle / U_\infty^3$) along the wake centre plane at (a) $x/D = 6$, and (b) $x/D = 10$.

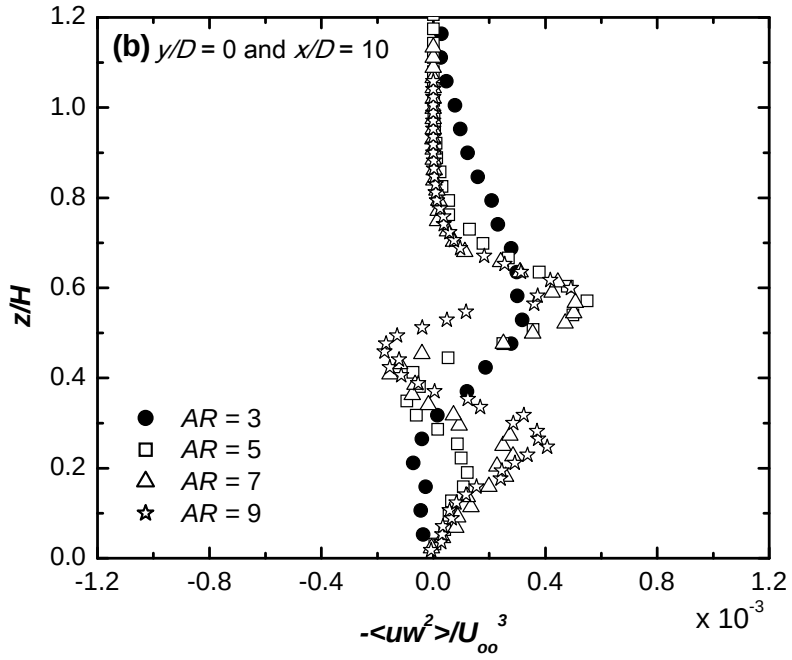

Figure 4.29 continued.

case of AR = 3. Again, as the streamwise distance increases (see Figure 4.29(b)), the absolute values of these peaks reduce for all cylinders.

4.3.4 Skewness and Flatness Factors

The skewness and flatness factors are, respectively, defined as follows:

$$S_u = \frac{< u^3 >}{(u')^3}, \quad \text{and} \quad S_w = \frac{< w^3 >}{(w')^3} \tag{4.1}$$

$$F_u = \frac{< u^4 >}{(u')^4}, \quad \text{and} \quad F_w = \frac{< w^4 >}{(w')^4} \tag{4.2}$$

The skewness and flatness factors can be used to provide information about the distribution of the velocity fluctuation around its mean value; e.g. to determine whether the velocity fluctuation is symmetric about its mean value. For a Gaussian fluctuation, the skewness and flatness factors are, respectively, 0 and 3. A non-zero value of the

skewness factor indicates the degree of temporal irregularity in the fluctuation and a flatness factor more than 3 is attributed to a "peaky signal" (Gad-el-Hak and Bandyopadhyay, 1994), due to irregular turbulent events.

Figure 4.30 shows the streamwise and wall-normal skewness profiles along the cylinder wake centreline at x/D = 6. For all cylinders, a highly negative region is observed toward the free end for the streamwise skewness (Figure 4.30(a)), while a positive region is observed for the wall-normal skewness (Figure 4.30(b)), which is more pronounced for AR = 5 and 7. In the case of the streamwise skewness, the strong negative value shows that negative values of u occur more frequently than large positive values close to the cylinder free end. For the wall-normal skewness factor, the slightly positive value may indicate that the positive values of w occur more frequently than

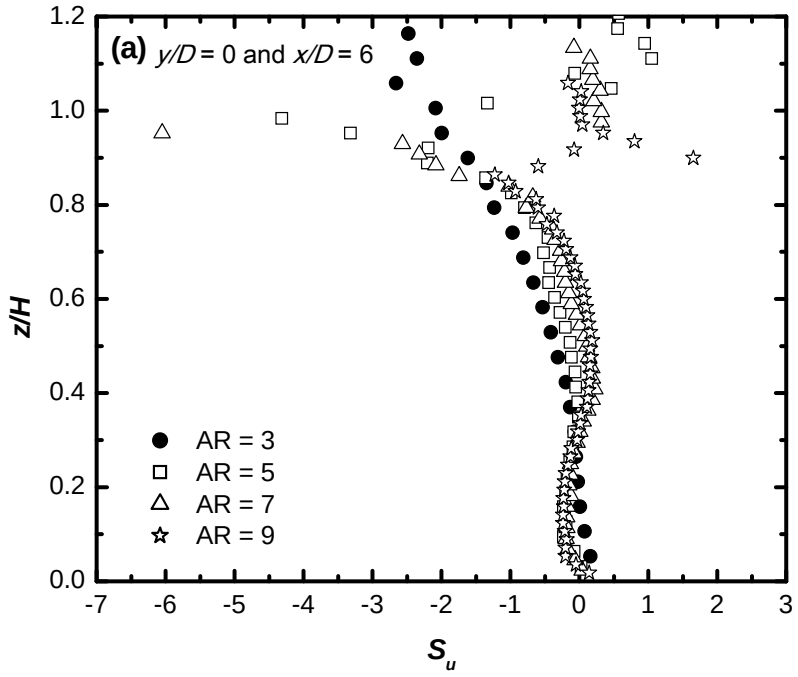

Figure 4.30: Skewness factor along the wake centreline at x/D = 6: (a) streamwise direction, and (b) wall-normal direction.

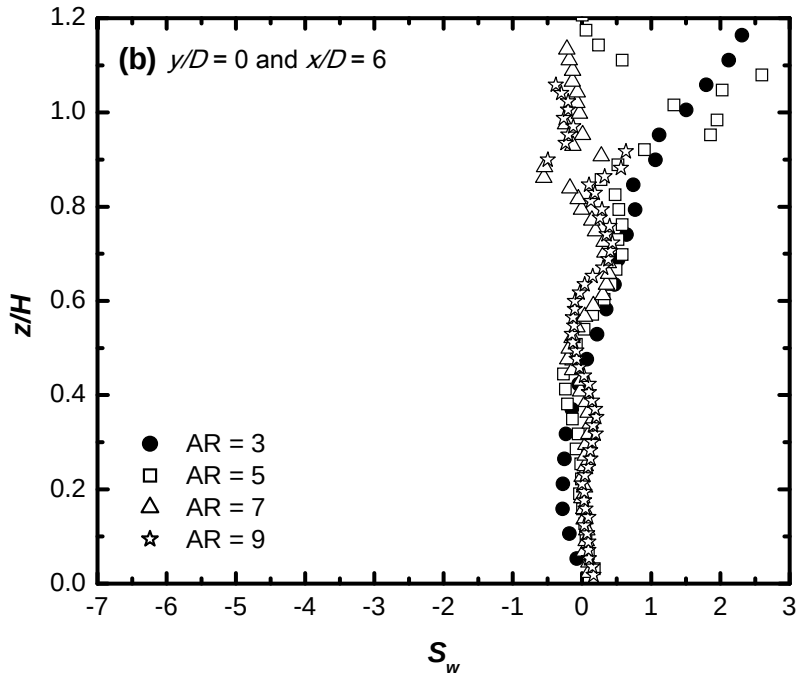

Figure 4.30 continued.

large negative values near the cylinder free end.

Figure 4.31 shows the streamwise and wall-normal flatness factors along the cylinder wake centreline at $x/D = 6$. Irrespective of the value of AR, there is a region with a flatness factor larger than 3 in both the streamwise and wall-normal directions, which indicates that there are strong intermittent turbulent events near the free end of the cylinder. Since, there is an absence of upwash flow and base vortex structures for $AR = 3$, the strong positive values of the flatness factors may be the result of the interaction between the tip vortex structures (see e.g., Sumner *et al.,* 2004) and the downwash flow from the finite cylinder free end. The higher value of flatness factor occurs near the region where the streamwise skewness factor has a high negative value. The profiles of $AR \geq 5$ are similar for both the skewness and flatness factors, but different from $AR = 3$.

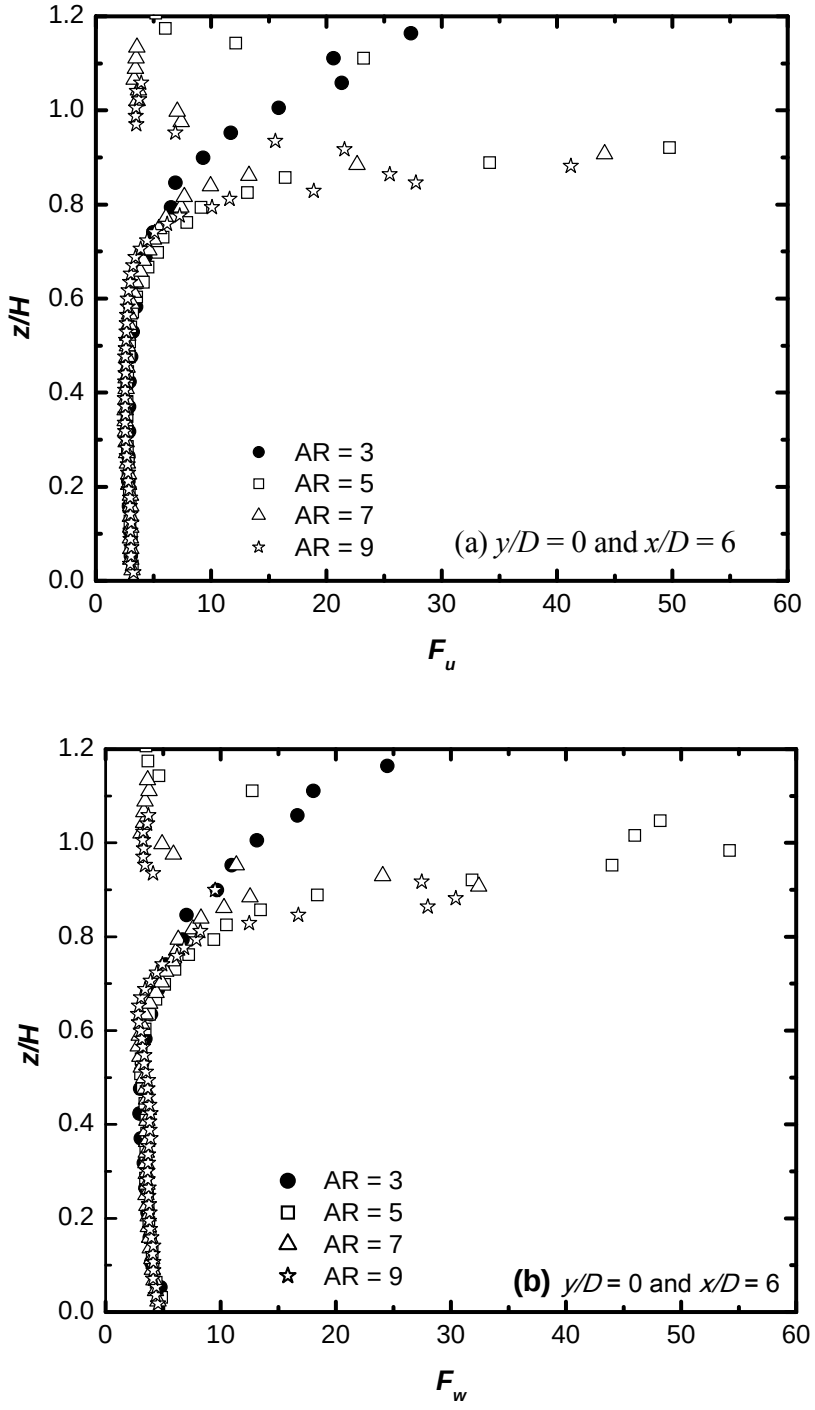

Figure 4.31: Flatness factor along the wake centreline at x/D = 6: (a) streamwise direction, and (b) wall-normal direction.

4.4 Summary

It was shown in this Chapter that the cylinders of AR = 9, 7, and 5 had a similar turbulent wake structure, with a localized region of low streamwise mean velocity and high turbulence intensity behind the cylinder, which was centred between the four main streamwise vortex structures. A strong downwash velocity field was found between the tip vortex structures close to the free end, and an upwash velocity field was found between the base vortex structures closer to the ground plane. The mean velocity, turbulence intensity, and Reynolds shear stress fields for the cylinder with AR = 3 indicate that this cylinder had a distinct turbulent wake structure because of the absence of the base vortex structures and their associated upwash velocity field from the ground plane. Some of the data suggest a transitional turbulent wake structure may exist for the cylinder with AR = 5. The Reynolds shear stress, the triple correlations as well as the skewness and flatness factors are affected by the aspect ratio of the cylinder.

In the next Chapters (5, 6 and 7), the effect of the velocity ratio on the turbulence field in the wake of a stack, and on the vortex shedding frequency from the stack will be discussed.

CHAPTER 5

THE MEAN PROPERTIES IN THE WAKE OF A STACK

5.1 Introduction

It was shown in Chapter 4 that the aspect ratio influences the characteristics of the wake of a finite circular cylinder (which effectively represents the case of a stack with no effluent jet). It was noted that the cylinder with $AR = 3$ has distinct wake features when compared with $AR \geq 5$. The presence of a jet issuing from a stack will make its wake more complex compared with that of a finite circular cylinder. For a non-buoyant jet, the extent of this complexity depends primarily on the jet-to-cross-flow velocity ratio, R ($=U_e / U_\infty$). The flow field is characterized by the interactions between the jet flow and the stack wake, shear produced by the upward momentum of the jet, and downwash flow. In this chapter, effects of the velocity ratio on the time-averaged properties (streamwise velocity and vorticity, and the wall-normal velocity) within the stack wake are presented and discussed. Following the definition of Eiff and Keffer (1999), the stack wake is defined as the region $0 < z/H \leq 1$, while the region of $z/H > 1$ comprises the jet wake.

5.2 Velocity Profiles along the Wake Centreline

The time-averaged streamwise velocity profiles ($\overline{U}/U_\infty$) on the wake centreline ($y/D = 0$) measured with the X-probe at $x/D = 10$ and $x/D = 15$, are shown in Figure 5.1 for

different values of R. Generally, the extension of the stack wake and jet wake in the wall-normal direction increases with increasing R.

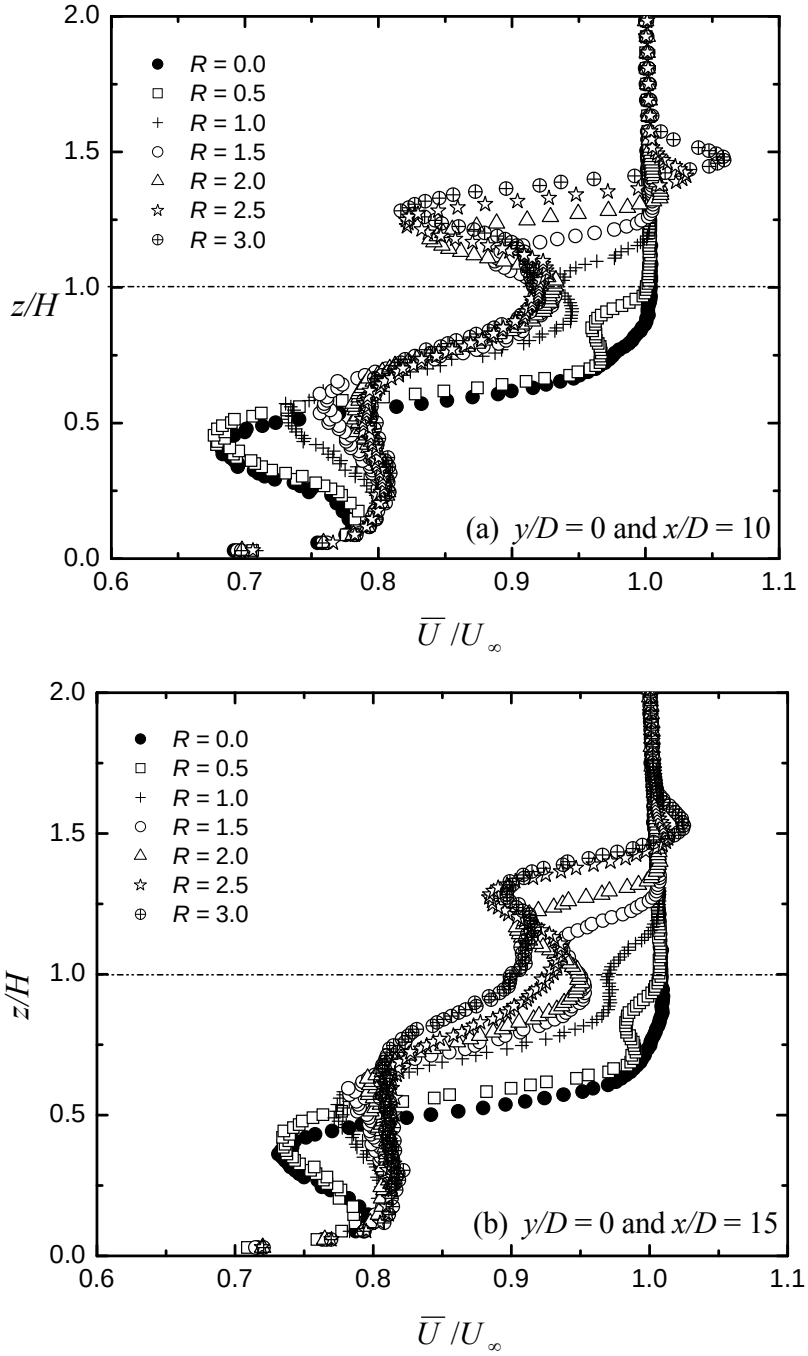

Figure 5.1: The time-averaged streamwise velocity profiles along the wake centerline ($y/D = 0$) at (a) $x/D = 10$ and (b) $x/D = 15$.

When R = 0 (Figure 5.1(a)), the large velocity defect shows that only the stack wake is observed. When R = 0.5, the velocity profile is almost similar to that of R = 0, but there is a second, smaller velocity defect within the stack wake below the stack free end. For R = 1, the time-averaged velocity profile is distinct from those for R = 0 and 0.5. The main velocity defect in the stack wake is reduced, while the second region of velocity defect is greater in size and magnitude and is shifted upwards towards the free end of stack.

At R = 1.5, the bent jet strongly behaves as another bluff body and produces a jet wake in addition to the stack wake. This is indicated by the presence of a velocity defect region above the stack's free end. This is in agreement with other studies which showed (e.g., Onbaşioğlu, 2001; Mahjoub Säid *et al*., 2005, 2007) that a jet discharged into a cross-flow behaves similarly to an obstacle placed in the flow. As the value of R increases, the vertical extent of the jet wake also increases, since the jet rise increases with R. When $R \geq 2$, in addition to the wake features, there is another region in the profile corresponding to the stack jet where the local streamwise velocity is greater than the freestream velocity ($\overline{U}/U_\infty > 1$) due to the presence of the jet flow. Eiff *et al*. (1995) reported a similar feature in the streamwise velocity profile for R = 3 at x/D = 7.

The location of the jet flow centreline can be determined using either the location of the maximum streamwise velocity (see e.g., Kamotani and Greber, 1972) or the maximum value of the in-plane velocity magnitude, $(\overline{U}^2 + \overline{W}^2)^{0.5}$. Based on both approaches, the jet centerline at x/D = 10 (Figure 5.1(a)) is located at z/H = 1.31, 1.34, 1.41 and 1.47 for R = 1.5, 2, 2.5, and 3, respectively, above the ground plane. This

clearly shows that the jet rise increases with R due to the increased penetration strength of the jet.

Figure 5.1(b) shows that the velocity defects within the stack wake and jet wake reduce with the downstream distance from the stack for all values of $R < 1.5$. In the case of the $R \geq 1.5$, the vertical location of the maximum streamwise velocity and the vertical extension of the velocity defect within the jet wake increase, which shows that the jet rises higher at $x/D = 15$ compared with $x/D = 10$. Also, due to the entrainment of the cross-flow, there is a weakening of the jet centreline velocity.

Based on the time-averaged streamwise characteristics (as shown in Figure 5.1), the flow around the stack can be roughly categorized into three flow regimes. The flow regime that falls within $R \leq 0.5$ is termed the "downwash flow regime", which is similar to the downwash flow regime identified by Huang and Hsieh (2002, 2003). Within this flow regime, the weak jet flow and downwash flow due the free end of the stack is completely entrained within the near wake of the stack due to the strong cross-flow. When the value of R lies within $0.5 < R < 1.5$, the regime is referred to as the "crosswind-dominated flow regime". In this flow regime, the jet flow has higher momentum and can penetrate the cross-flow deeper than in the downwash regime, and, thus, the jet downwash occurs further away from the stack. When $R \geq 1.5$, the flow regime is referred to as the "jet-dominated flow regime" which corresponds to the transitional and jet-dominated flow regimes proposed by Huang and Hsieh (2002, 2003). In this regime, the jet momentum is higher than the cross-flow momentum and therefore, is able to penetrate deeper into the cross-flow. The three distinct regions identified by Mahjoub Säid *et al.* (2005, 2007) for an elevated jet in cross-flow are now evident.

The time-averaged wall-normal velocity profiles at x/D = 10 along the centre plane measured with the X-probe are shown in Figure 5.2(a). These profiles show two

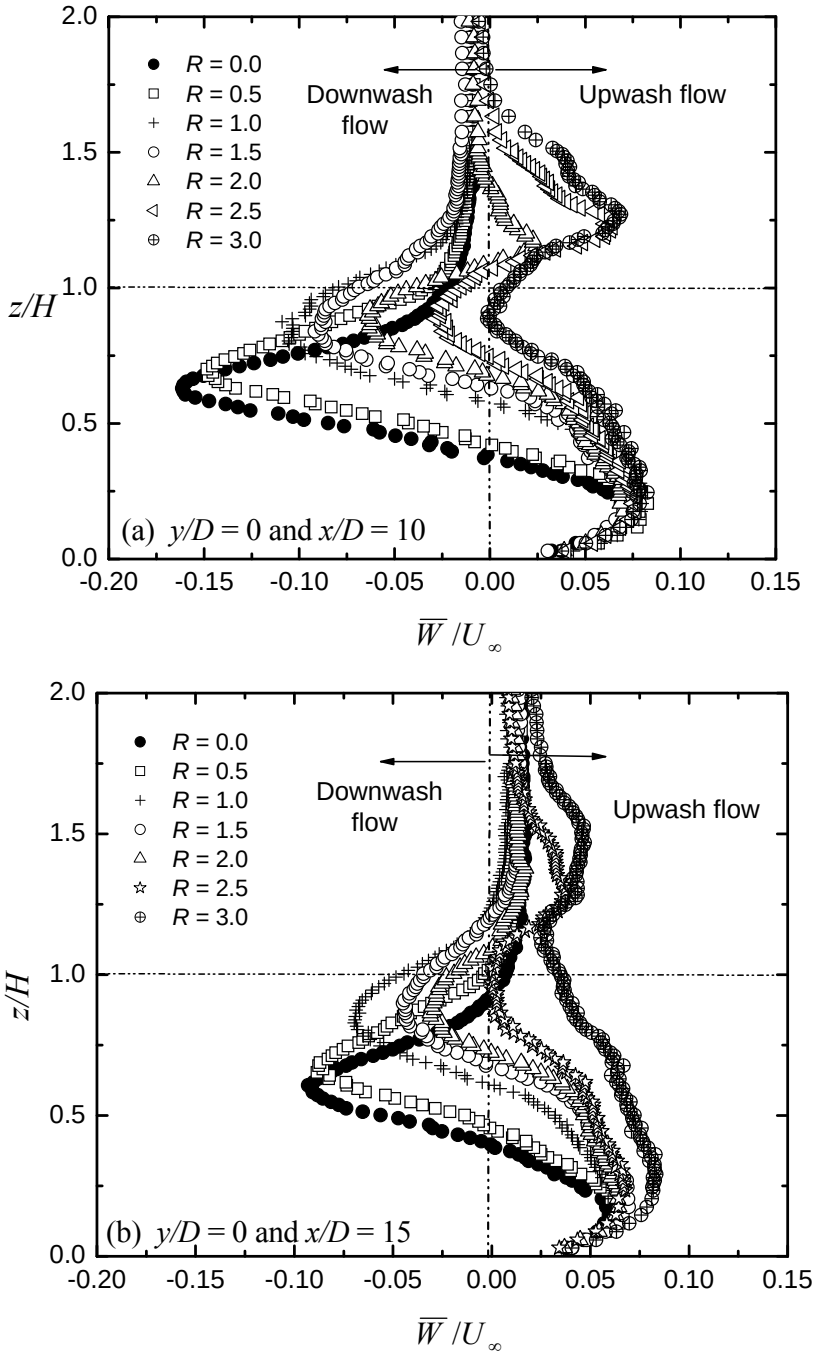

Figure 5.2: The time-averaged wall-normal velocity profiles along the wake centerline (y/D = 0) at (a) x/D = 10; and (b) x/D = 15.

distinct flow regions within the stack and jet wakes: the upwash flow region which occurs closer to the ground plane and the downwash flow region which occurs in the upper half of the stack wake. The profiles for R = 0, 0.5, 1, 1.5, 2 and 2.5 are all similar but differ in the relative location of the downwash flow region which moves upward toward the free end of the stack as R increases. In addition, the absolute magnitude of the downwash flow reduces with increasing R. For R = 3, the downwash flow region is completely absent. For R = 2, 2.5 and 3, another upwash flow region, which is a direct consequence of the jet flow, is also observed above the stack free end and within the jet wake. The strength of this second upwash flow increases with R. This shows the increased momentum of the jet and the associated jet rise, and is characteristic of the jet-dominated flow regime.

As the streamwise distance increases (see Figure 5.2(b)), the downwash flow region descends slightly toward the ground plane, but still remains above the ground plane boundary layer. In addition, the absolute value of the downwash flow is smaller when x/D = 15 than when x/D = 10 (Figure 5.2(a)). For R = 2.5 and 3, no downwash flow is observed at x/D = 15. This is due to an increase in the jet rise at this location. Also, the upwash flow observed within the jet wake for $R \geq 2$ at x/D = 10 (Figure 5.2(a)) is now weaker and this may be a result of the mixing of the jet flow with the cross-flow.

5.3 Velocity Fields along the Wake Centreline

The time-averaged velocity field along the vertical centre plane (i.e., y/D = 0) of the stack wake measured with the seven-hole probe is shown in Figures 5.3 to 5.5 for R = 0 to 3. When R = 0 (Figure 5.3(a)), strong downwash flow occurs within the near wake of the stack and this downwash persists in the streamwise direction and approaches the

mid-height of the stack. Also, an upwash flow is observed near the ground plane and within the ground plane boundary layer. These downwash and upwash flows are similar to the results of Tanaka and Murata (1999) for $AR = 10$, Sumner *et al.* (2004) for $AR \geq 5$ and as also presented in Chapter 4 for a finite cylinder. The blank space behind the stack indicates a region where the flow exceeded the angular range of the seven-hole probe (Sumner *et al.*, 2004), or a region of reverse flow, and therefore the probe could not measure the flow velocity. The length of the recirculation region varies along the stack height. The maximum streamwise extent of this region has been observed to decrease as

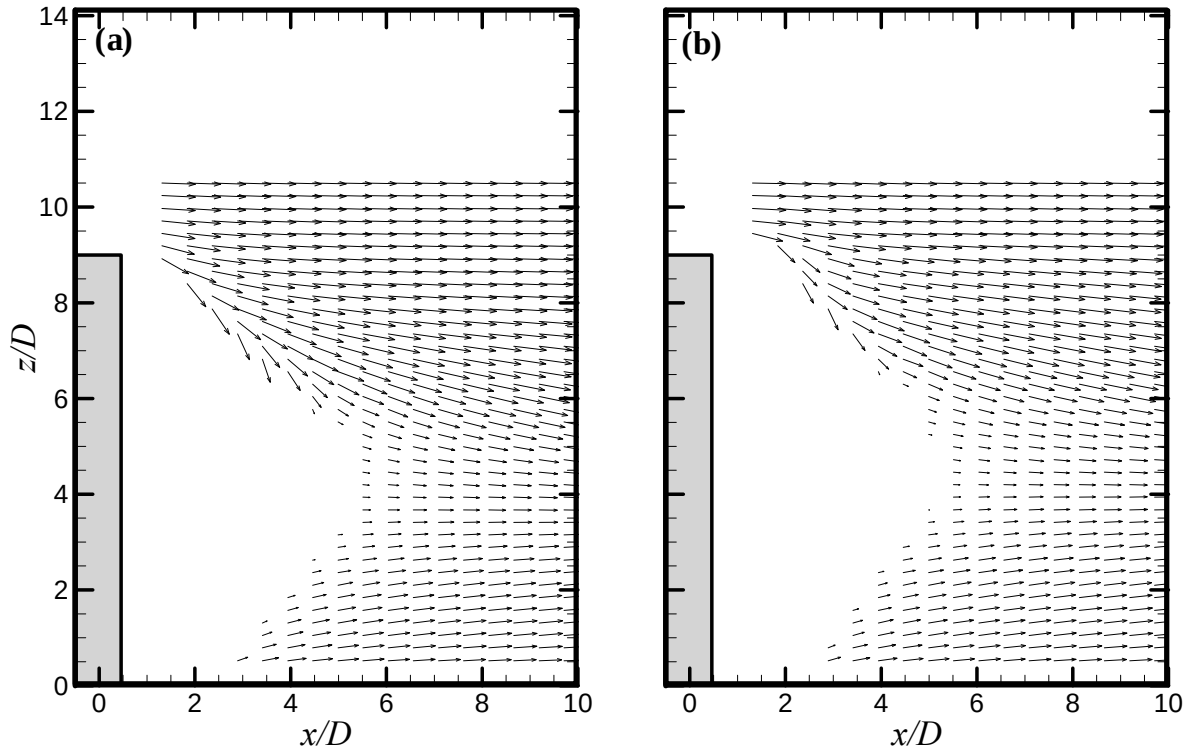

Figure 5.3: The time-averaged velocity field along the wake centreline ($y/D = 0$) for the downwash flow regime measured with the seven-hole probe for (a) $R = 0$ and (b) $R = 0.5$.

the aspect ratio of a finite circular cylinder increases (e.g., Okamoto, 1991; Tanaka and Murata, 1999; and Sumner *et al.*, 2004).

In the case of R = 0.5 (Figure 5.3(b)), which corresponds to the downwash flow regime, the downwash flow and upwash flow are similar to that observed for R = 0 (see Figure 5.3(a)). Compared with the results of Sumner *et al.* (2004) for a finite circular cylinder of $AR \geq 5$, and the case of R = 0 (Figure 5.3(a)), the magnitude of the downwash flow and the streamwise and vertical extent of the upwash flow for R = 0.5 are smaller. In addition, the streamwise extent of the recirculation region is smaller, and the region extends more toward the stack free end. This may be due to the presence of the weak jet flow that reduces the downwash flow into the stack wake but is not yet strong enough to prevent it entirely. As mentioned in Section 5.2, the flow regime that falls in this range of R is referred to as the downwash flow regime.

For the crosswind-dominated flow regime, R = 1 (Figure 5.4), the downwash flow is observed to be much weaker and almost absent in the near wake of the stack. The

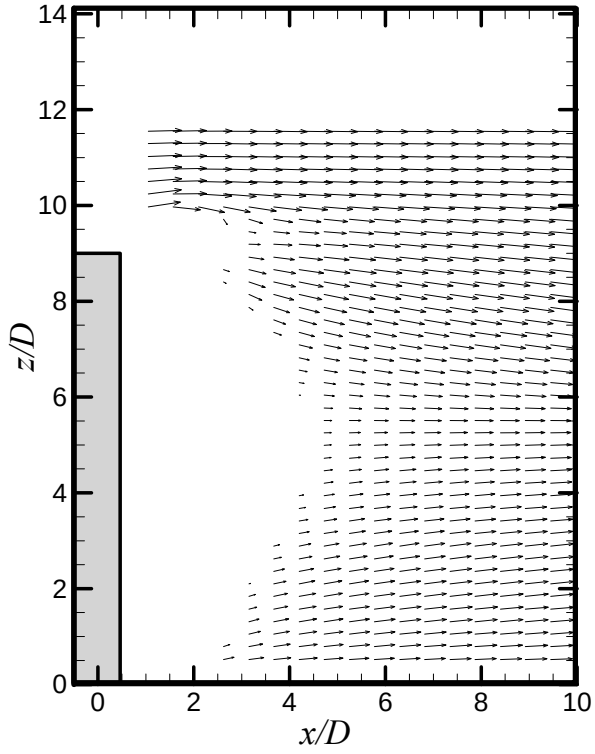

Figure 5.4: The time-averaged velocity field along the wake centreline (y/D = 0) for the crosswind-dominated flow regime measured with the seven-hole probe for R = 1.

streamwise extent of the upwash flow and the recirculation region within the stack wake is now smaller compared with $R = 0.5$ (Figure 5.3(b)). This is due to the presence of the jet flow that behaves like a bluff body and thereby increases the effective aspect ratio of the stack. A second recirculation region is also observed above the free end of the stack and within the jet wake. This region may contain the rotating vortex formed within the jet wake as observed by Huang and Hsieh (2002) for $0.95 < R < 2.4$, which they reported to be a result of the "interaction between the jet shear layer and downwash flow".

In the case of the jet-dominated flow regime, when $R \geq 1.5$ (Figure 5.5), the stronger momentum of the jet flow allows it to penetrate deeper into the cross-flow, as shown by the strong upward-directed velocity vectors above the free end of the stack. With the increased jet rise, the size of the recirculation region within the jet wake is now larger compared to the crosswind-dominated flow regime when $R = 1$ (Figure 5.4). Huang and Hsieh (2002) also observed a smaller (in comparison with the crosswind-dominated flow regime in their study) rotating vortex region underneath the jet flow. A strong recirculation region within the jet wake was also observed by Mahjoub Säid *et al*. (2005, 2007). There is also a corresponding reduction in the size of the recirculation region within the stack wake, and the streamwise extent of this region becomes more uniform along the stack height. The reduction in the stack wake is probably a result of the reduction in the downwash flow which normally increases the size of the recirculation region within the wake of a finite cylinder. This indicates that the stack wake tends to behave as the wake of an infinite circular cylinder as R increases, which implies that the presence of the jet flow increases the effective aspect ratio of the stack. Within this range of R, the jet rise and the recirculation region within the jet wake

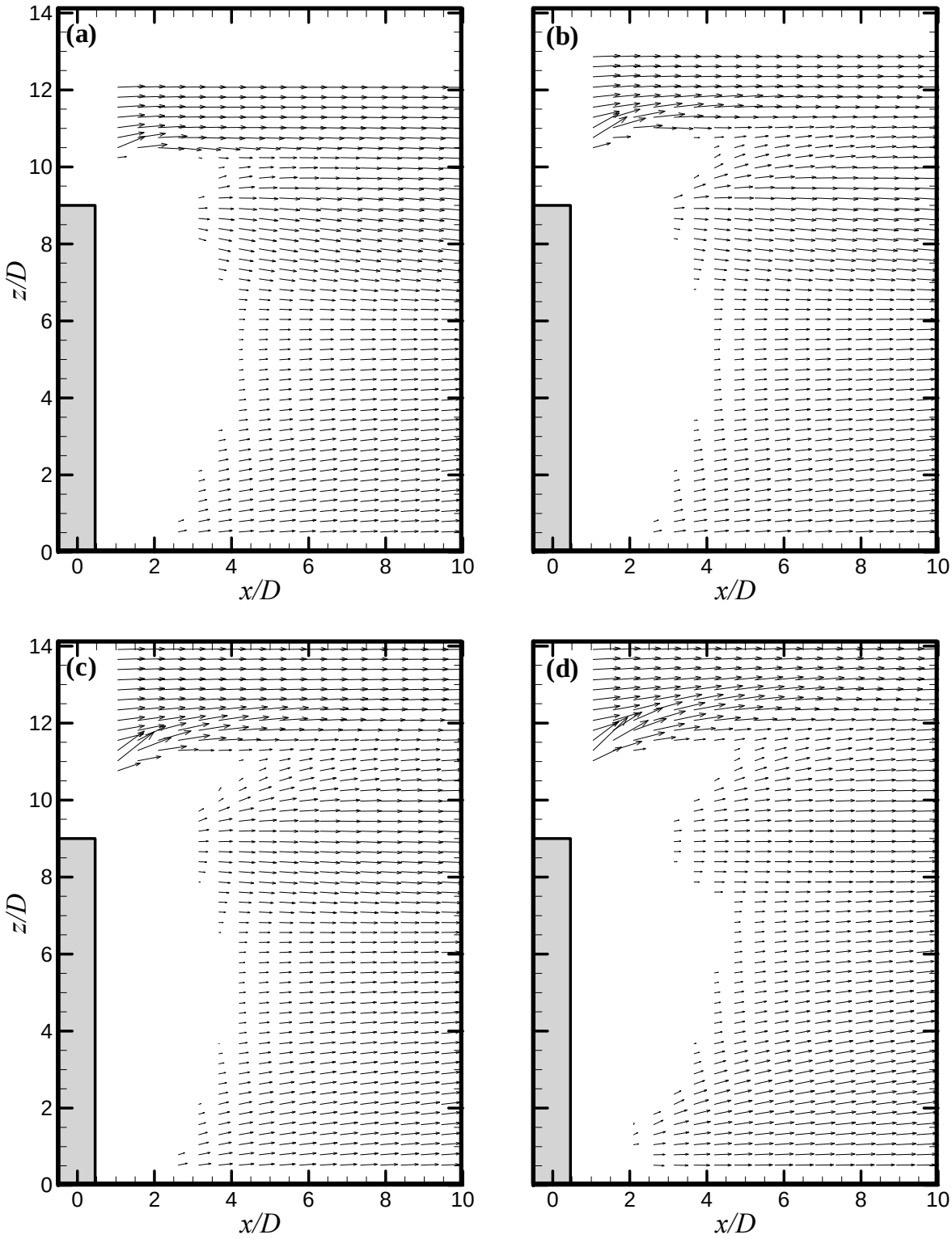

Figure 5.5: The time-averaged velocity field along the wake centreline ($y/D = 0$) for the jet-dominated flow regime measured with the seven-hole probe for (a) $R = 1.5$, (b) $R = 2$, (c) $R = 2.5$ and, (d) $R = 3$.

increase with increasing R. The increase in the recirculation region may be a result of the increased interaction between the jet flow and cross-flow. This increase may also be due to the increase in the wall-normal extension of the jet wake and the separated shear layer from the sides of the jet.

5.4 Cross-Stream Velocity Vector Fields

The time-averaged cross-stream velocity vector fields (v, w velocity components, measured in the y-z plane) measured with the seven-hole probe at x/D = 6 and 10 are presented in Figures 5.6 to 5.12 for values of R ranging from 0 to 3. For the downwash flow regime (Figures 5.6 and 5.7, R = 0 and 0.5, respectively) and the crosswind-dominated flow regime (Figure 5.8, R = 1), the vector fields show two pairs of counter-rotating flow structures within the stack wake, one closer to the free end and the other closer to the ground plane. For the jet-dominated flow regime (Figures 5.9-5.12, R = 1.5 to 3), an additional pair is observed in the jet wake region. For all values of R, an upwash flow is observed within the flat-plate boundary layer on the ground plane. The strength of this upwash flow is strongest within the boundary layer and reduces towards the mid-height of the stack.

For R = 0.5 (Figure 5.7), a strong downwash flow is present within the stack wake and below the stack free end, which is the main characteristic of the downwash flow regime. The strength of the downwash flow reduces along the height of the stack when moving away from the free end towards the ground plane, similar to the case of the finite circular cylinder as observed by Sumner *et al.* (2004), for R = 0 (Figure 5.6) and as shown in Section 4.2.2 and Figures 4.5-4.8 for a finite circular cylinder. For R = 1

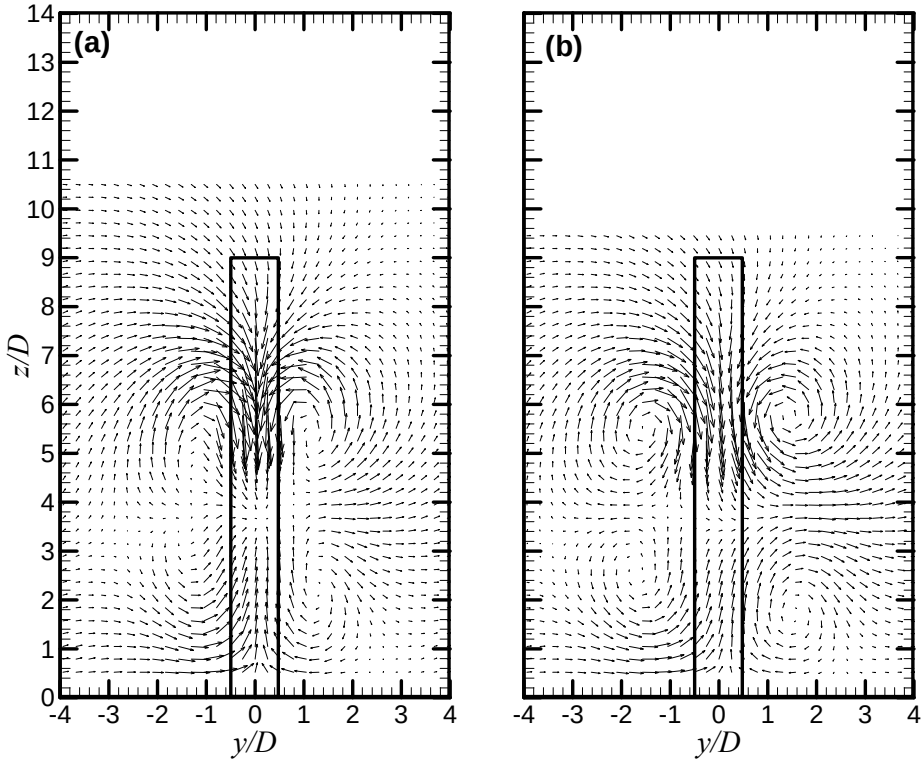

Figure 5.6: The time-averaged velocity vector field (v, w) downstream of the stack for R = 0 (downwash flow regime) at (a) x/D = 6 and (b) x/D = 10.

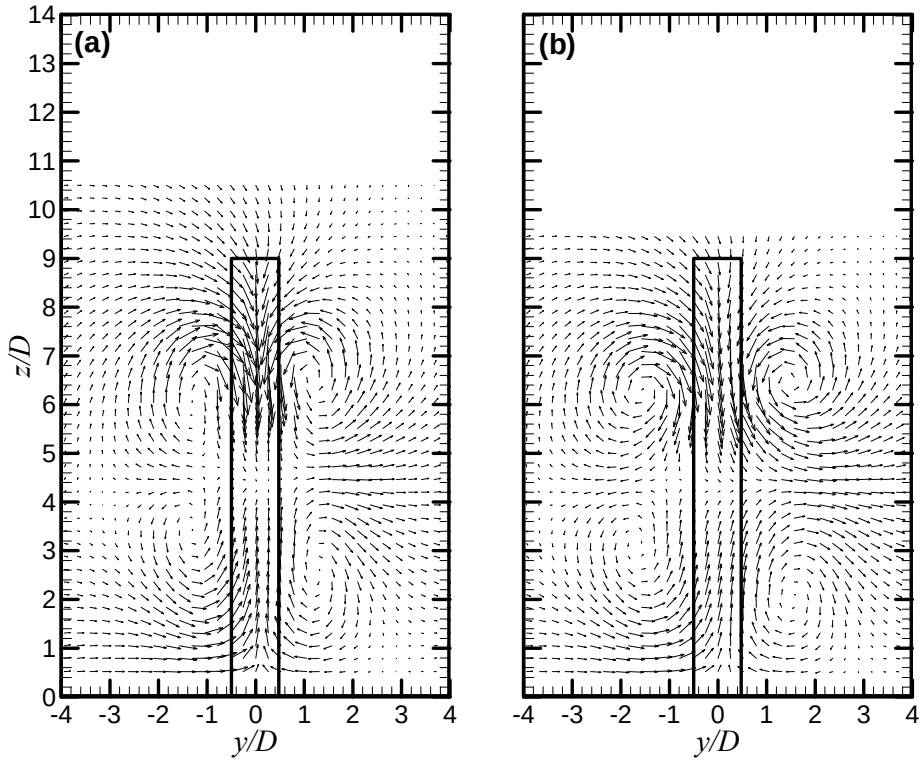

Figure 5.7: The time-averaged velocity vector field (v, w) downstream of the stack for R = 0.5 (downwash flow regime) at (a) x/D = 6 and (b) x/D = 10.

(Figure 5.8), representing the crosswind-dominated flow regime, the downwash velocity field is located further away from the ground plane and closer to the stack's free end. The downwash flow for R = 1 is weaker than for R = 0.5 (Figure 5.7). In addition, for the same streamwise position, the upper pair of the two counter-rotating flow structures now occurs closer to the free end of the stack.

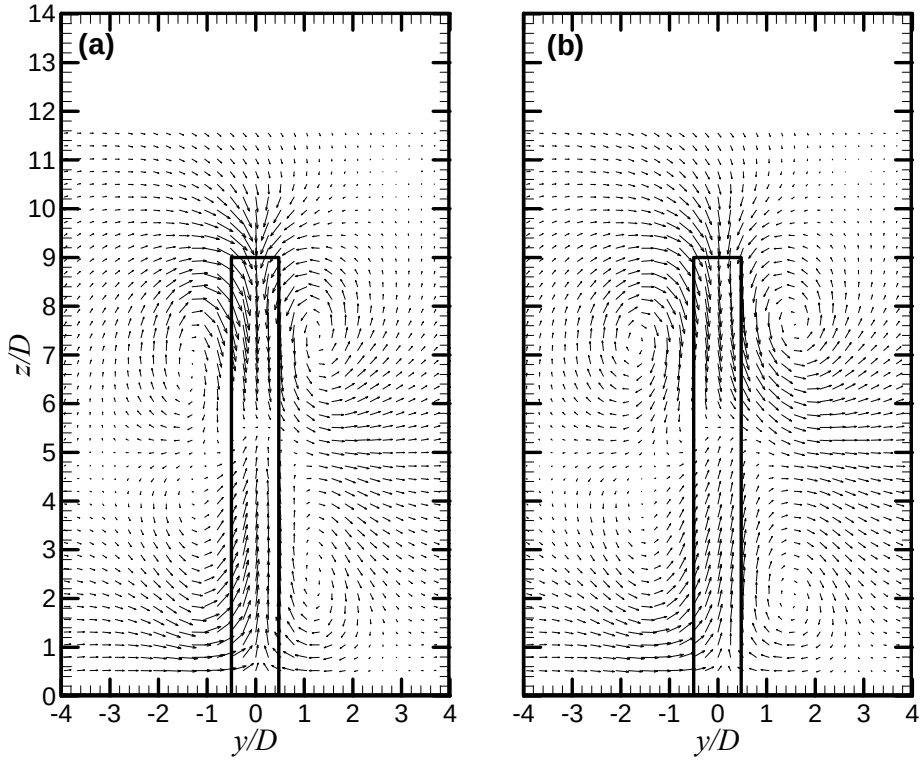

Figure 5.8: The time-averaged velocity vector field (v, w) downstream of the stack for R = 1 (crosswind-dominated flow regime) at (a) x/D = 6 and (b) x/D = 10.

In addition to the upwash flow within the stack base region, for R = 1.5 to 3 (Figures 5.9-5.12), another, and much stronger, upwash flow occurs above the free end of the stack within the jet wake region. This upwash flow, depending on R, extends as much as 2 to 4 stack diameters above the free end, and is associated with the third pair of the counter-rotating flow structures. These features characterize the jet-dominated flow

regime and result from the stronger jet flow exiting the stack. In addition, the counter-rotating flow structures near the stack free end reduce in strength with increasing *R*. This is due to the opposing effect of the upwash jet flow on the downwash from the stack free end. Within the jet-wake, there is a location along the wake centre plane (*y/D* = 0), where the velocity field (*v*, *w*) is zero. This location separates the pair of counter-rotating structures within the stack free end from those within the jet wake. This is due to the opposite orientation of the tip counter-rotating flow structures and the jet-wake counter-rotating flow structures that produce downwash flow and upwash flow, respectively, and eventually cancels out at the vertical wake centre plane. The position of this location within the jet wake and above the stack free end is observed to be slightly elevated with increasing *R*. In addition, as mentioned in Section 5.2 and shown in Figure 5.1, the

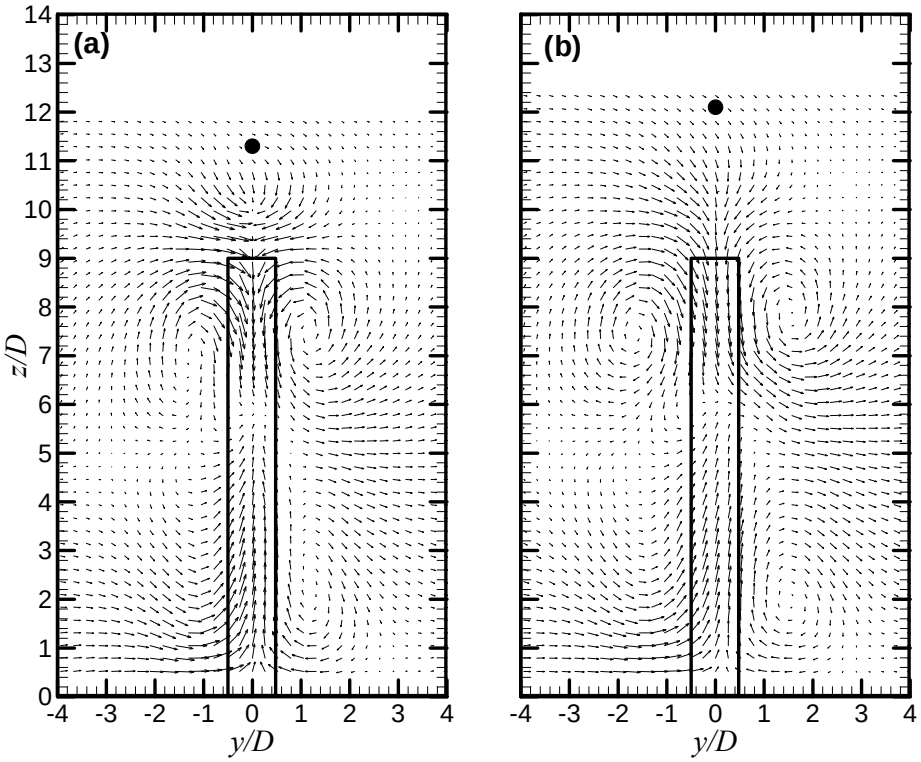

Figure 5.9: The time-averaged velocity vector field (*v*, *w*) downstream of the stack for *R* = 1.5 (jet-dominated flow regime) at (a) *x/D* = 6 and (b) *x/D* = 10. The black dot represents the jet flow trajectory point.

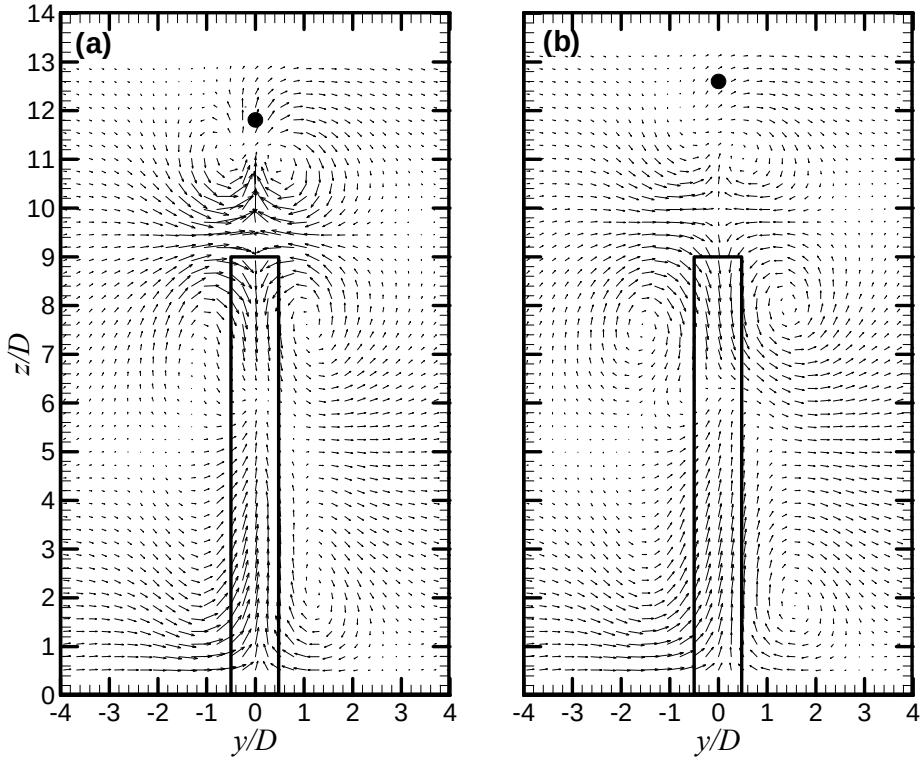

Figure 5.10: The time-averaged velocity vector field (v, w) downstream of the stack for $R = 2$ (jet-dominated flow regime) at (a) $x/D = 6$ and (b) $x/D = 10$.

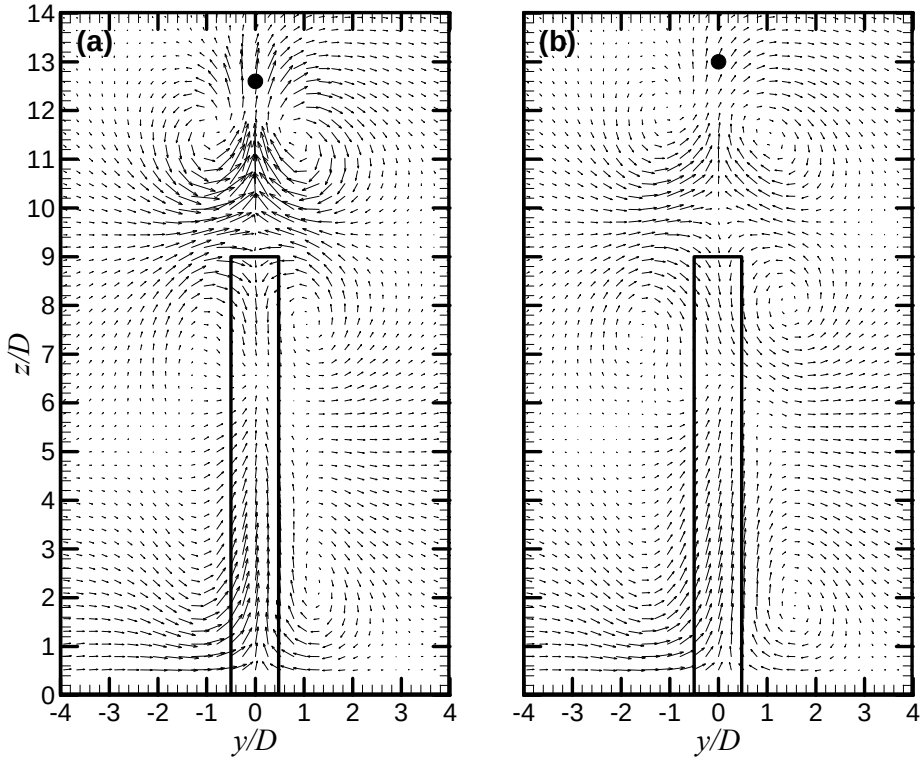

Figure 5.11: The time-averaged velocity vector field (v, w) downstream of the stack for $R = 2.5$ (jet-dominated flow regime) at (a) $x/D = 6$ and (b) $x/D = 10$.

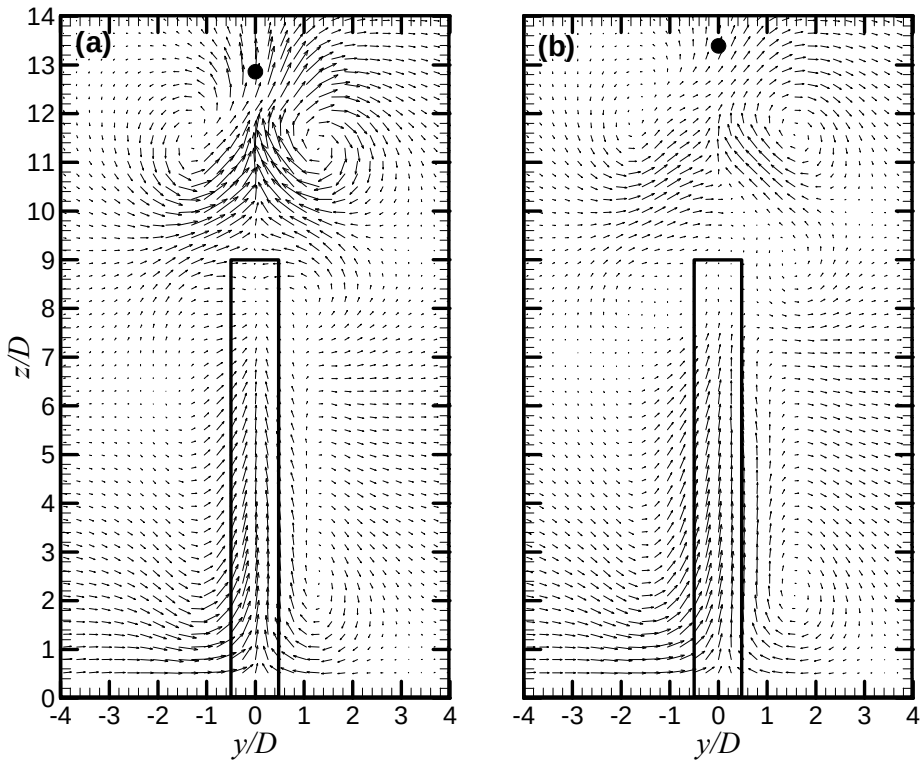

Figure 5.12: The time-averaged velocity vector field (v, w) downstream of the stack for R = 3 (jet-dominated flow regime) at (a) x/D = 6 and (b) x/D = 10.

elevation of the jet flow increases with streamwise distance from the stack. This is evident in the location of the solid black dots in these figures (and other iso-contour plots presented in this chapter), which represent the locations of the maximum jet centreline velocity, that occur at a relatively higher location at x/D = 10 compared with x/D = 6.

5.5 Streamwise Velocity Contour Fields

The time-averaged streamwise velocity fields ($\overline{U}/U_\infty$) in the cross-stream (y-z) plane at x/D = 6 and 10 measured with the seven-hole probe are shown as contour plots in Figures 5.13 to 5.19 for different jet-to-cross-flow velocity ratios. As R increases, the lateral spread of the stack wake decreases and the maximum velocity defect reduces.

Similar reductions are observed for a finite circular cylinder when the aspect ratio is increased, as shown in Chapter 4. In the downwash flow regime, a region of low mean streamwise velocity is observed behind and within the wake of the stack and well above the ground plane (for R = 0, Figure 5.13) and a second low velocity region begins to

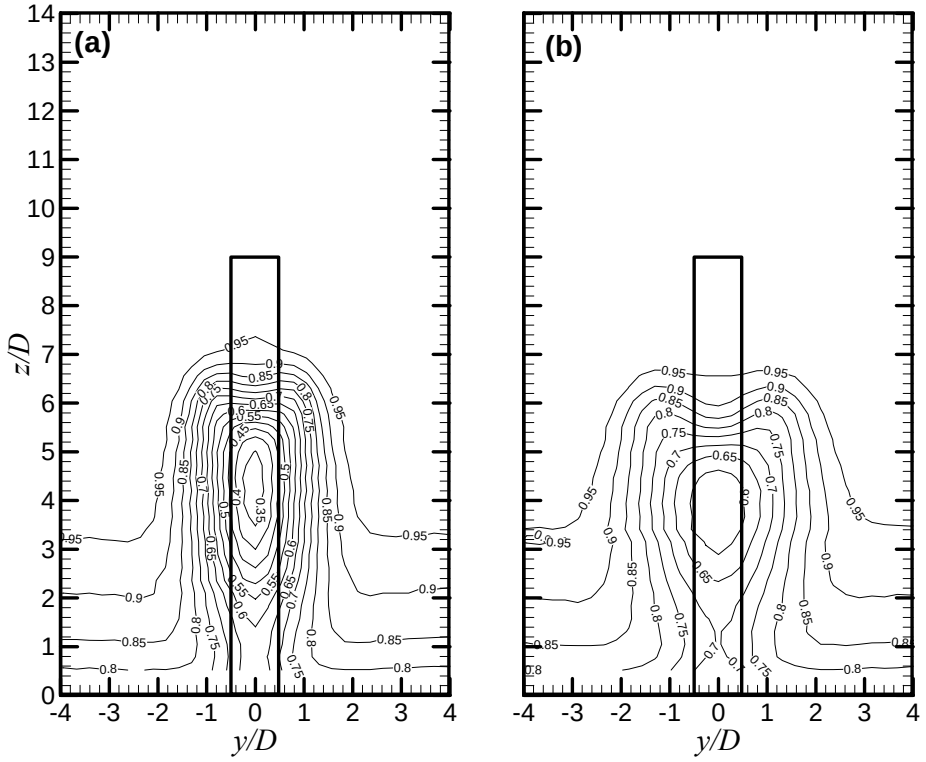

Figure 5.13: The time-averaged streamwise ($\overline{U}/U_\infty$) velocity field downstream of the stack for R = 0 (downwash flow regime) at (a) x/D = 6 and (b) x/D = 10. Contour increment of 0.05.

form near the top of the stack but within the stack wake (when R = 0.5, Figure 5.14). In the crosswind-dominated flow regime, this second region forms just above the stack free end (when R = 1, Figure 5.15). In the case of the jet-dominated flow regime (when R = 1.5, Figure 5.16; R = 2, Figure 5.17; R = 2.5, Figure 5.18; R = 3, Figure 5.19), the second region occurs above the free end of the stack, and is now better defined and more isolated from the stack wake, and clearly represents the jet wake. As R increases, this

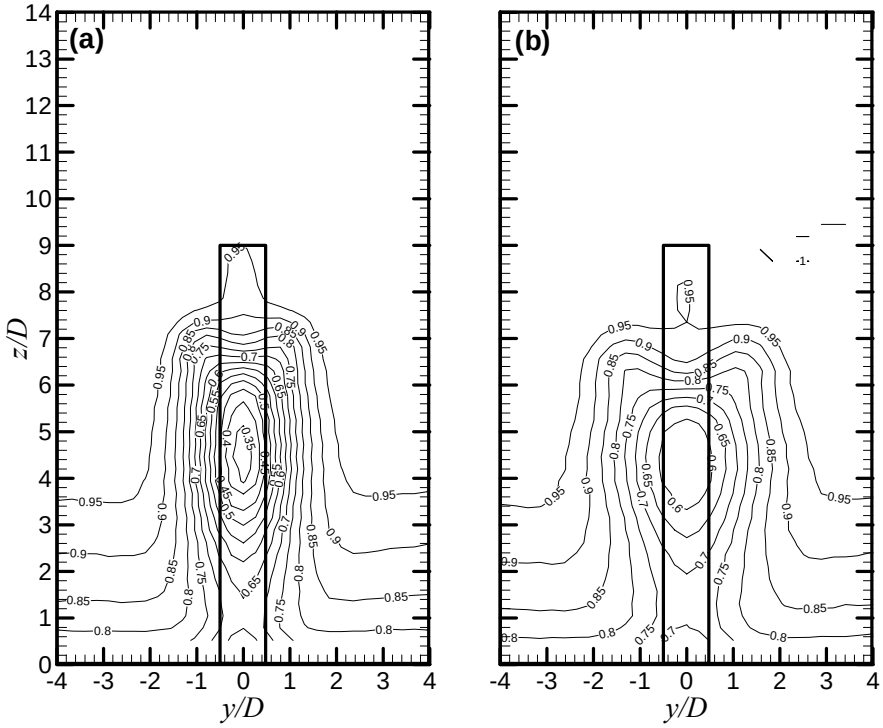

Figure 5.14: The time-averaged streamwise ($\overline{U}/U_\infty$) velocity field downstream of the stack for R = 0.5 (downwash flow regime) at (a) x/D = 6 and (b) x/D = 10. Contour increment of 0.05.

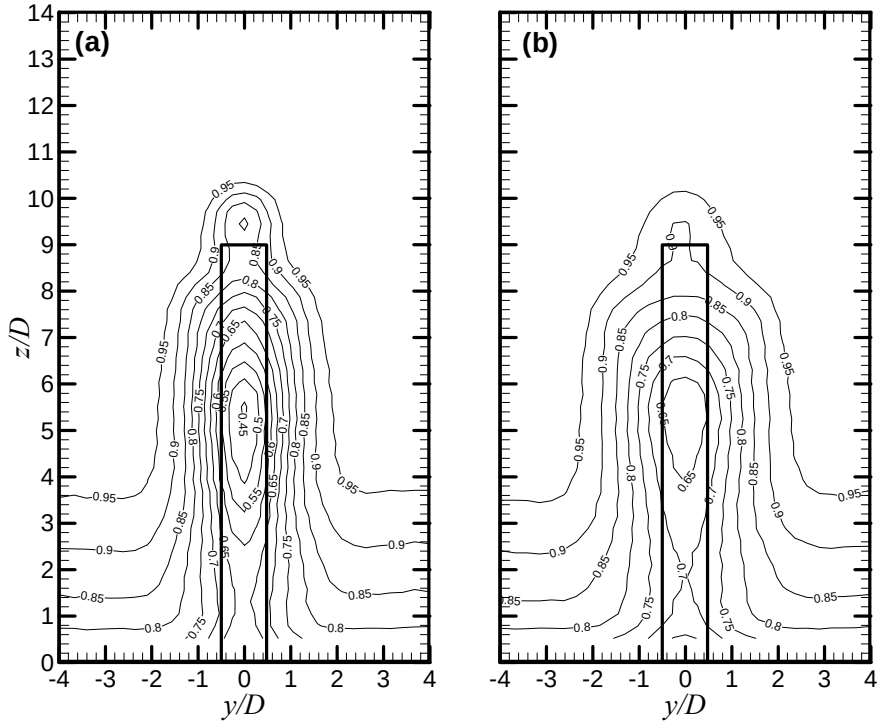

Figure 5.15: The time-averaged streamwise ($\overline{U}/U_\infty$) velocity field downstream of the stack for R = 1 (crosswind-dominated flow regime) at (a) x/D = 6 and (b) x/D = 10. Contour increment of 0.05.

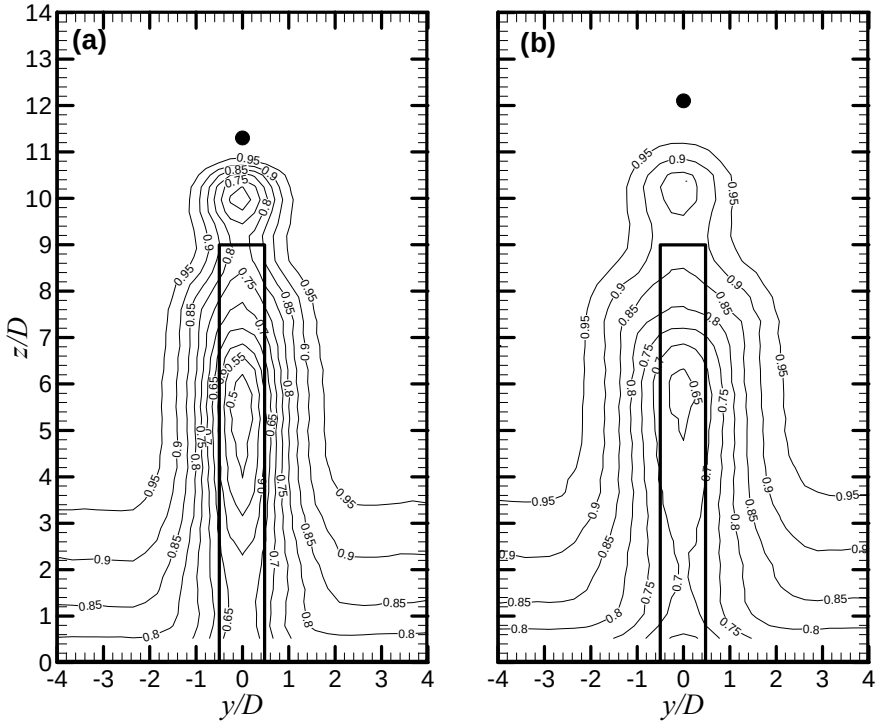

Figure 5.16: The time-averaged streamwise ($\overline{U}/U_\infty$) velocity field downstream of the stack for R = 1.5 (jet-dominated flow regime) at (a) x/D = 6 and (b) x/D = 10. Contour increment of 0.05. The black dot represents the jet flow trajectory point.

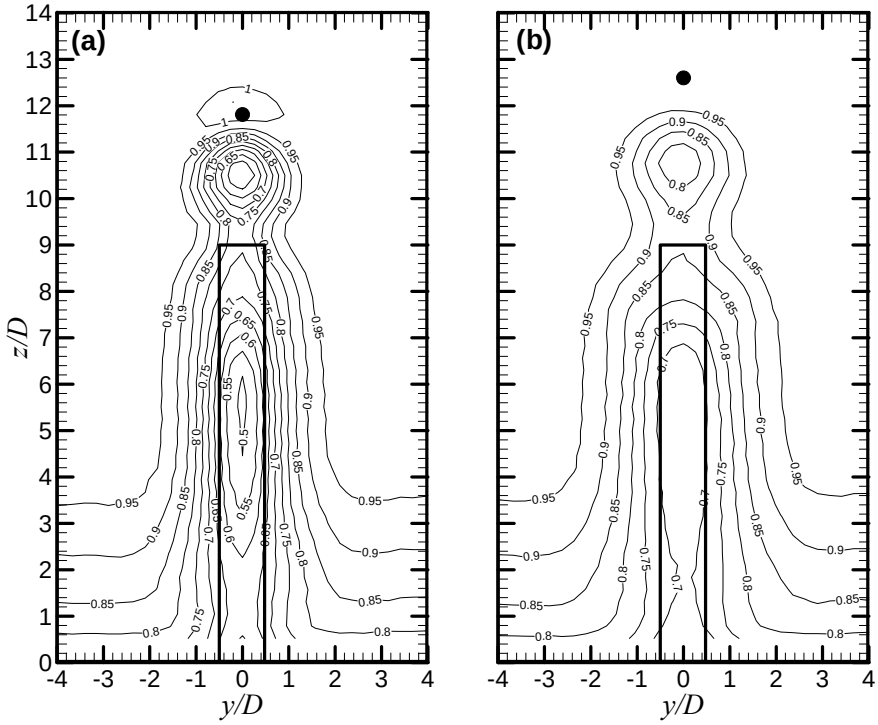

Figure 5.17: The time-averaged streamwise ($\overline{U}/U_\infty$) velocity field downstream of the stack for R = 2 (jet-dominated flow regime) at (a) x/D = 6 and (b) x/D = 10. Contour increment of 0.05.

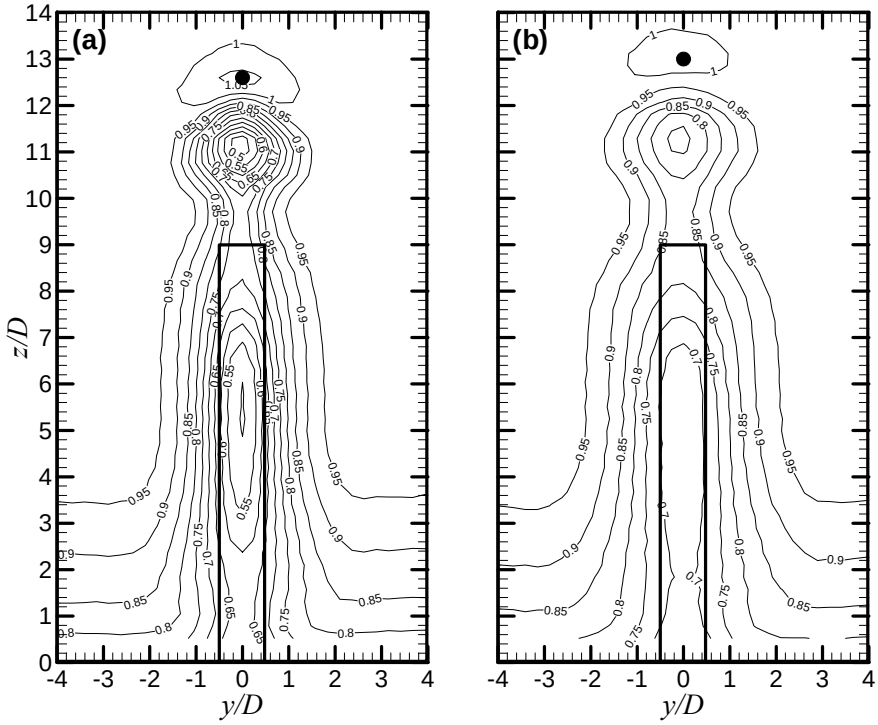

Figure 5.18: The time-averaged streamwise ($\overline{U}/U_\infty$) velocity field downstream of the stack for R = 2.5 (jet-dominated flow regime) at (a) x/D = 6 and (b) x/D = 10. Contour increment of 0.05.

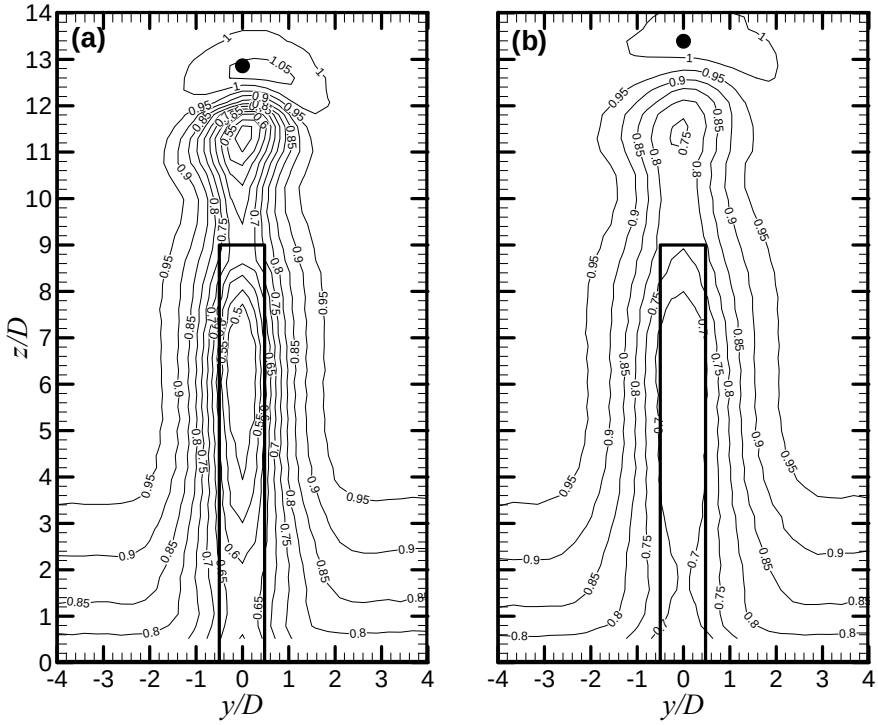

Figure 5.19: The time-averaged streamwise ($\overline{U}/U_\infty$) velocity field downstream of the stack for R = 3 (jet-dominated flow regime) at (a) x/D = 6 and (b) x/D = 10. Contour increment of 0.05.

region moves further above the free end of the stack and the extent of the region expands. This shows that the jet wake size as well as the jet rise increases. In addition, at *x/D* = 6, another region is observed above the jet wake, where the local streamwise velocity is greater than the cross-flow velocity ($\overline{U}/U_\infty > 1$) due to the presence of the jet flow. This region represents the jet flow region and it is similar to the observation made in Figure 5.1. This region is weakened at *x/D* = 10 and this is due to spreading of the jet flow and the mixing of the cross-flow with the jet flow.

Contours of the wall-normal mean velocity ($\overline{W}/U_\infty$) in the cross-stream plane at *x/D* = 6 and 10 measured with seven-hole probe are shown in Figures 5.20 to 5.26. The presence of a strong downwash flow (represented by the dashed contour lines) around the wake centreline is observed for nearly all values of *R* except for the highest velocity ratios tested in the jet-dominated flow regime (see also Figure 5.2, for profiles along the wake centreline). The position of the downwash flow region above the ground plane increases with increasing *R* due to the strengthening of the jet. Also, upwash flow (represented by the solid contour lines) around the wake centreline is observed for all values of *R* (see also Figure 5.2, for profiles along the wake centreline). In addition, the size and strength of the upwash and downwash are slightly influenced by the downstream location.

In the downwash flow regime (Figures 5.20 and 5.21), the downwash flow without the jet (or with a weak jet) is almost completely inside the stack wake. In the case of the crosswind-dominated flow regime (Figure 5.22), the strength of the downwash flow reduces due to the increase in the penetrating power of the jet. For the jet-dominated flow regime (Figures 5.23-5.26), the downwash flow weakens further and

by R = 3 (Figure 5.26) is entirely absent. The strength of the downwash flow, which was estimated from the plots, reduces with increasing R, with a maximum downwash magnitude of $\overline{W}/U_\infty$ = -0.16, -0.14, -0.10, -0.06, and -0.05 for R = 0, 0.5, 1, 1.5, and 2, respectively.

Closer to the ground plane, upwash flow from the ground plane and within the wake of the stack and the ground plane boundary layer region is observed for all values of R. The strength of this upwash flow seems to be relatively independent of the value of R but stretches upward toward the free end of the stack as the value of R increases.

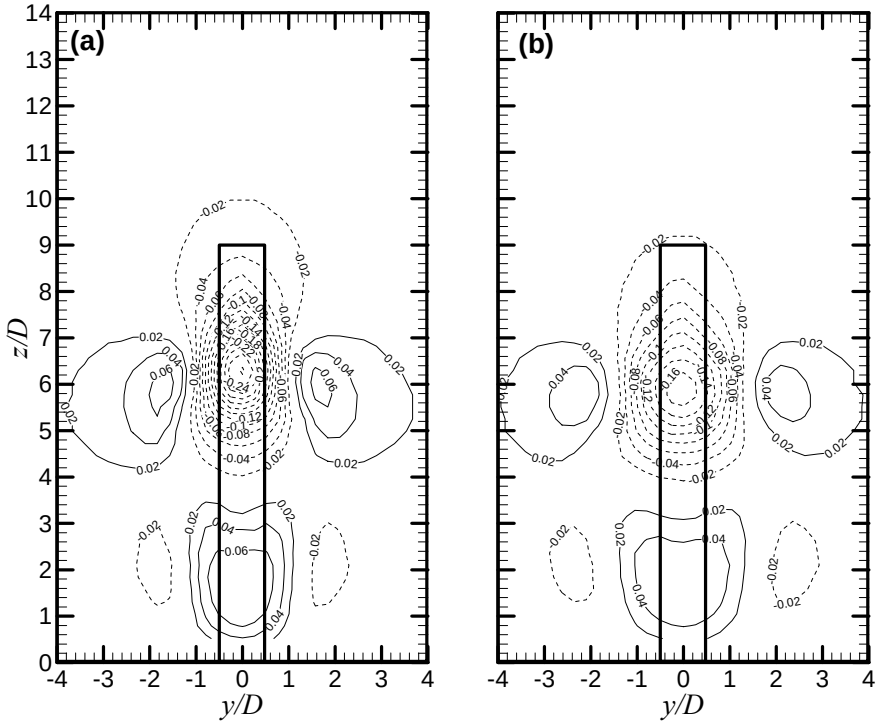

Figure 5.20: The time-averaged wall-normal ($\overline{W}/U_\infty$) velocity field downstream of the stack for R = 0 (downwash flow regime) at (a) x/D = 6 and (b) x/D = 10. Solid contour lines represent the upwash flow, while dashed lines represent the downwash flow. Contour increment of 0.02.

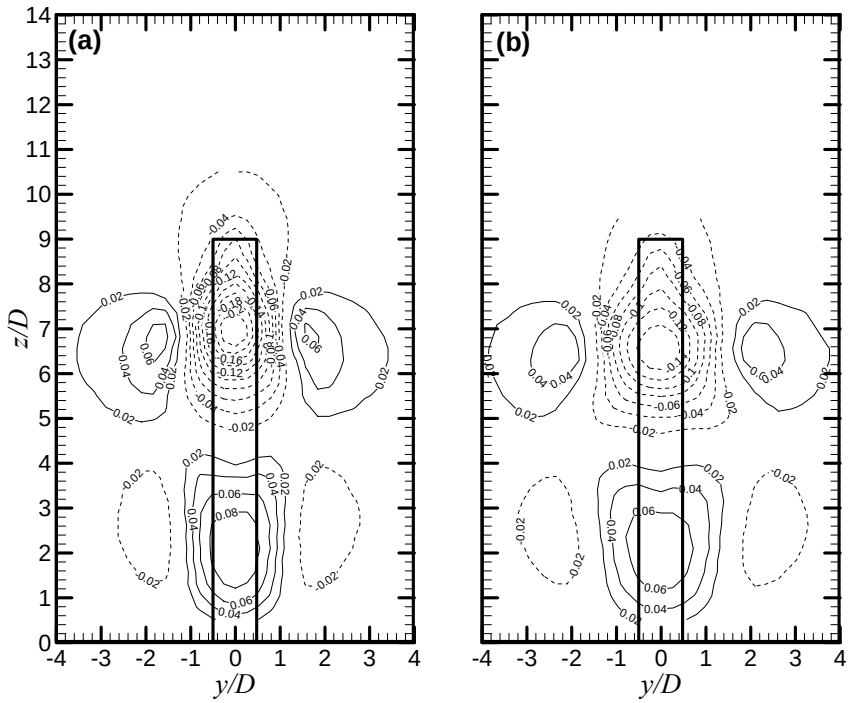

Figure 5.21: The time-averaged wall-normal ($\overline{W}/U_\infty$) velocity field downstream of the stack for R = 0.5 (downwash flow regime) at (a) x/D = 6 and (b) x/D = 10. Contour increment of 0.02.

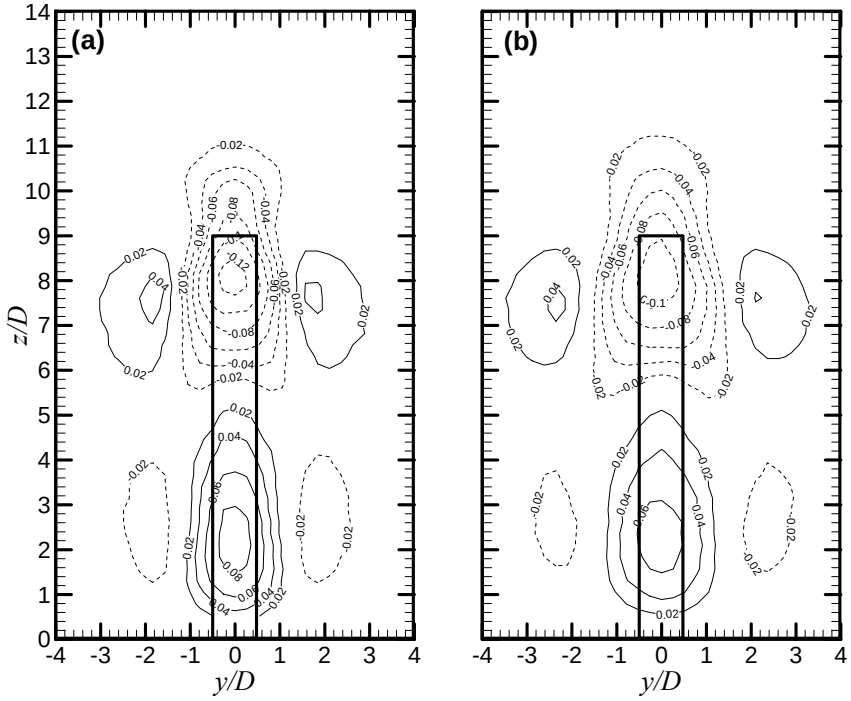

Figure 5.22: The time-averaged wall-normal ($\overline{W}/U_\infty$) velocity field downstream of the stack for R = 1 (crosswind-dominated flow regime) at (a) x/D = 6 and (b) x/D = 10. Contour increment of 0.02.

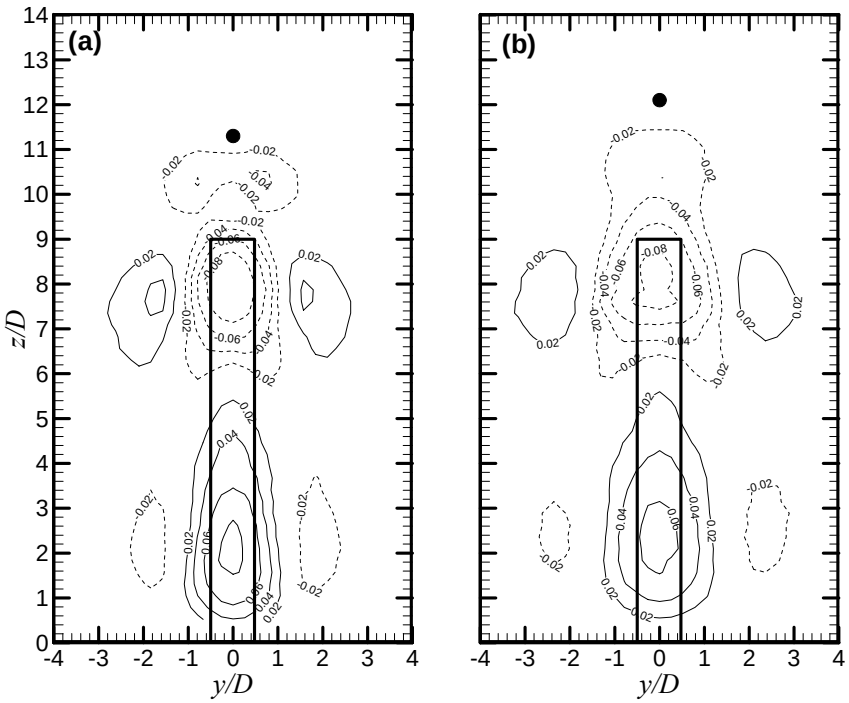

Figure 5.23: The time-averaged wall-normal ($\overline{W}/U_\infty$) velocity field downstream of the stack for R = 1.5 (jet-dominated flow regime) at (a) x/D = 6 and (b) x/D = 10. Contour increment of 0.02.

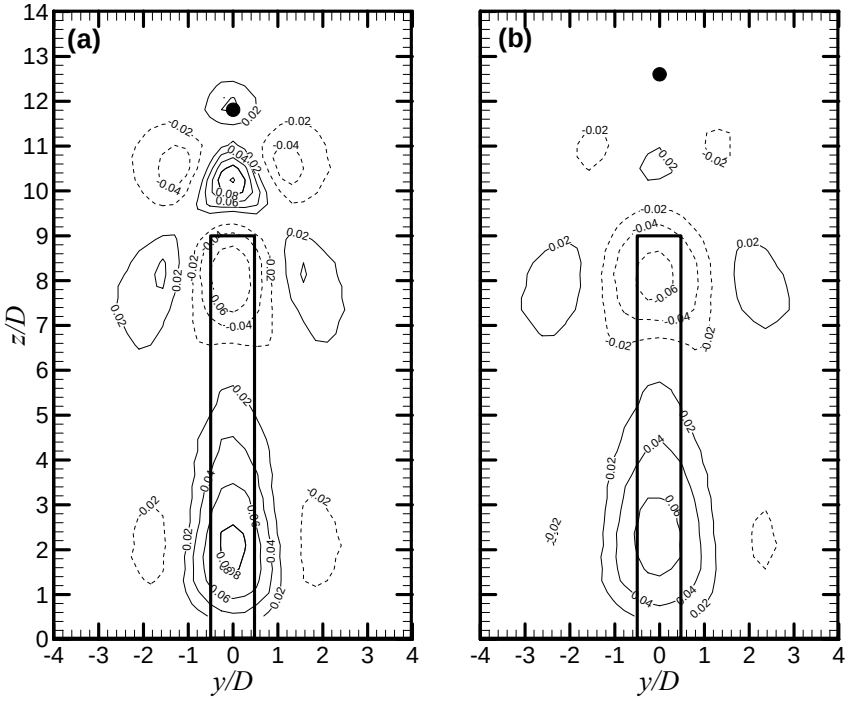

Figure 5.24: The time-averaged wall-normal ($\overline{W}/U_\infty$) velocity field downstream of the stack for R = 2 (jet-dominated flow regime) at (a) x/D = 6 and (b) x/D = 10. Contour increment of 0.02.

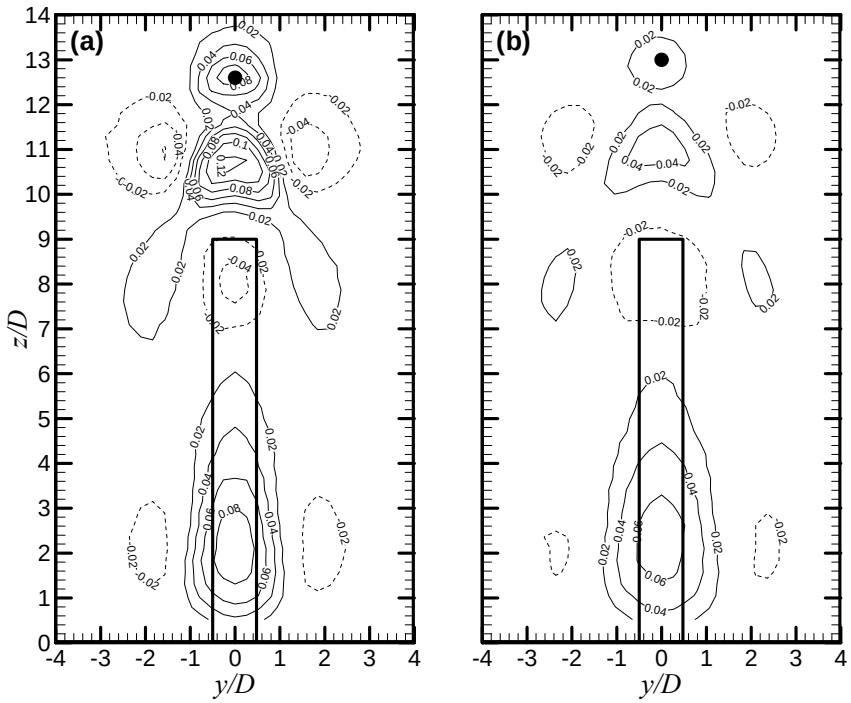

Figure 5.25: The time-averaged wall-normal ($\overline{W}/U_\infty$) velocity field downstream of the stack for R = 2.5 (jet-dominated flow regime) at (a) x/D = 6 and (b) x/D = 10. Contour increment of 0.02.

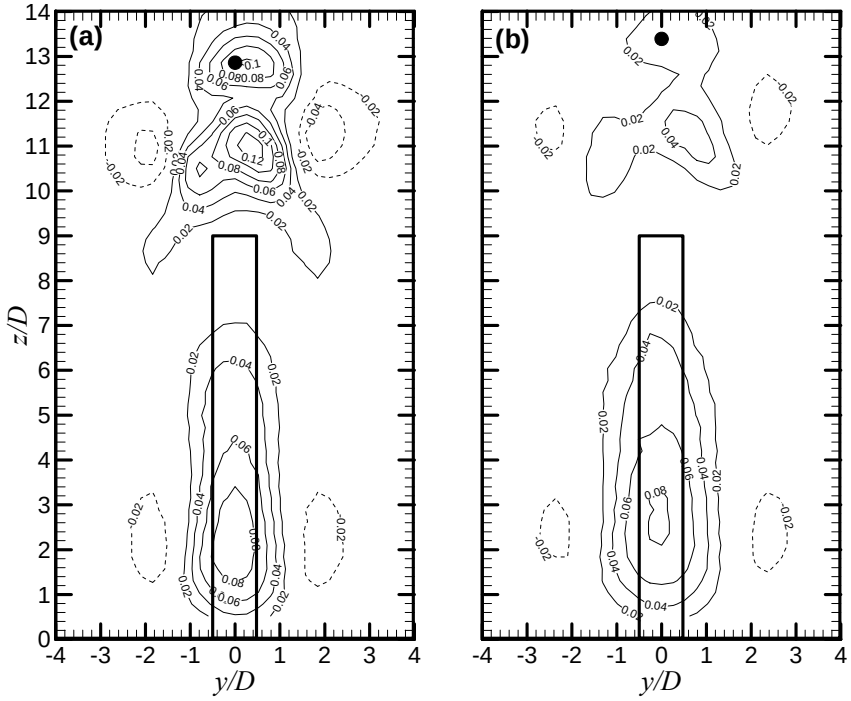

Figure 5.26: The time-averaged wall-normal ($\overline{W}/U_\infty$) velocity field downstream of the stack for R = 3 (jet-dominated flow regime) measured with the seven-hole at (a) x/D = 6 and (b) x/D = 10. Contour increment of 0.02.

When $R \geq 2$ (Figures 5.24-5.26), another upwash flow region develops within the jet wake and above the stack free end, which is characteristic of the jet-dominated flow regime. The size and strength, as well as the vertical position, of this upwash region in the jet wake increase with increasing R.

5.6 Streamwise Vorticity Fields

The time-averaged streamwise vorticity ($\omega_x^* = \omega_x D/U_\infty$, where ω_x is the streamwise vorticity component) fields in the y-z plane at $x/D = 6$ and 10 are shown in Figures 5.27 to 5.33. In these figures, the solid contour lines represent positive (counter-clockwise, CCW) vorticity, while the dashed contour lines represent negative (clockwise, CW) vorticity. For each value of R, the streamwise vorticity field shows two counter-rotating vortex pairs within the stack wake: one pair near the stack free end, referred to as the "tip vortex pair", and another with opposite sense of rotation closer to the base of the stack, referred to as the "base vortex pair." These two pairs of vortex structures were evident in the mean cross-stream velocity vector fields, shown in Figures 5.6 – 5.12, and are also observed in the wake of a finite circular cylinder (Tanaka and Murata, 1999; Sumner *et al*., 2004; Wang *et al*., 2006).

For $R = 0$ (Figure 5.27), the tip vortex pair at $x/D = 6$ is located below the free end. This is similar to the observation of Tanaka and Murata (1999) and Sumner *et al*. (2004) for a finite circular cylinder. For the downwash flow regime, ($R = 0.5$, Figure 5.28), the tip vortex pair moves closer to the free end of the stack but still lies within the stack wake. In the case of crosswind-dominated flow ($R = 1$, Figure 5.29), the tip vortex

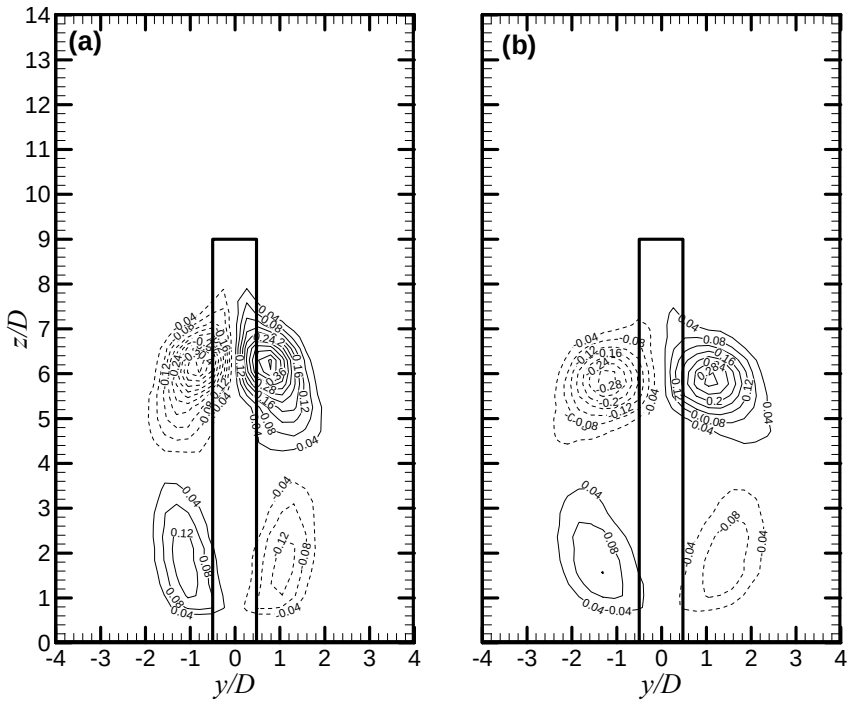

Figure 5.27: The time-averaged streamwise vorticity ($\omega_x D/U_\infty$) field downstream of the stack for R = 0 (downwash flow regime) at (a) x/D = 6 and (b) x/D = 10. Solid contour lines represent positive (CCW) vorticity; dashed contour lines represent negative (CW) vorticity. Minimum vorticity contour of ω_x^* = ± 0.04, contour increment of $\Delta\ \omega_x^*$ = 0.04.

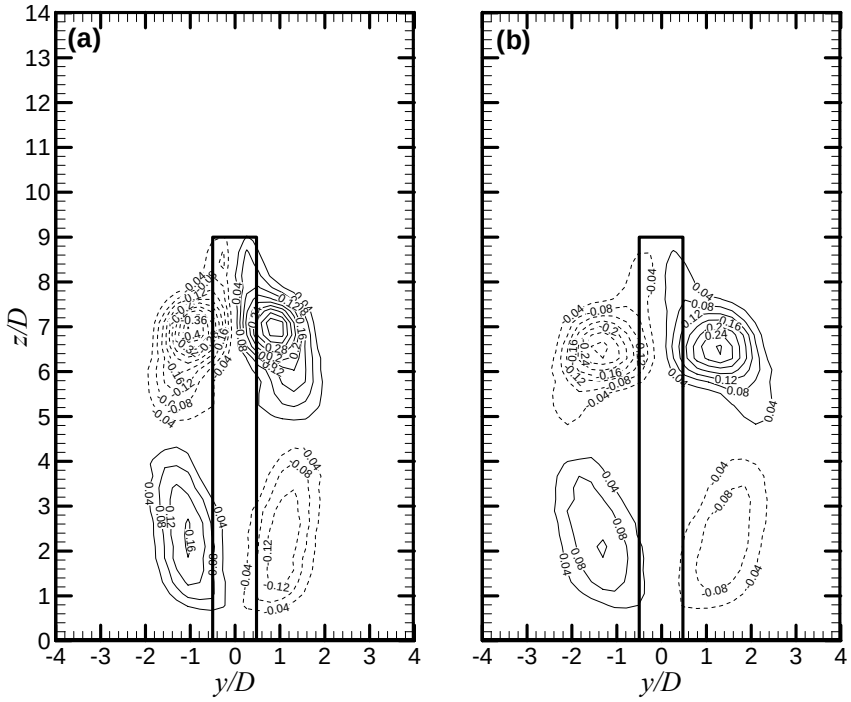

Figure 5.28: The time-averaged streamwise vorticity ($\omega_x D/U_\infty$) field downstream of the stack for R = 0.5 (downwash flow regime) at (a) x/D = 6 and (b) x/D = 10. Minimum vorticity contour of ω_x^* = ± 0.04, contour increment of $\Delta\ \omega_x^*$ = 0.04.

pair which is much weaker than with R = 0.5 (Figure 5.28) but similar to those of R = 1.5 , 2.0 and 2.5 (Figures 5.30-5.32), now extends above the free end. In addition, the base vortex structures are stretched upward along the sides of the stack towards the mid-height position.

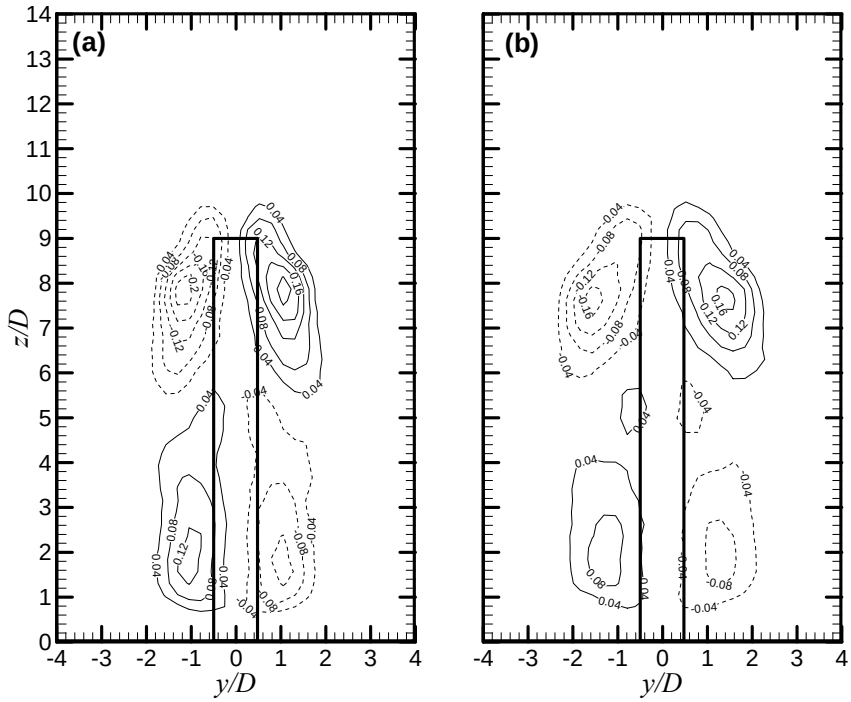

Figure 5.29: The time-averaged streamwise vorticity ($\omega_x D/U_\infty$) field downstream of the stack for R = 1 (crosswind-dominated flow regime) at (a) x/D = 6 and (b) x/D = 10. Minimum vorticity contour of ω_x^* = ± 0.04, contour increment of $\Delta\ \omega_x^*$ = 0.04.

In the jet-dominated flow regime, R = 1.5 to 3 (Figures 5.30-5.33), the tip vortex pair has weakened considerably compared to the downwash and crosswind-dominated flow regimes (Figures 5.27 and 5.28). In addition to the two pairs of streamwise vortex structures found within the stack wake region, a third counter-rotating vortex pair is now found in the jet wake region. Evidence of this vortex pair was seen in the velocity

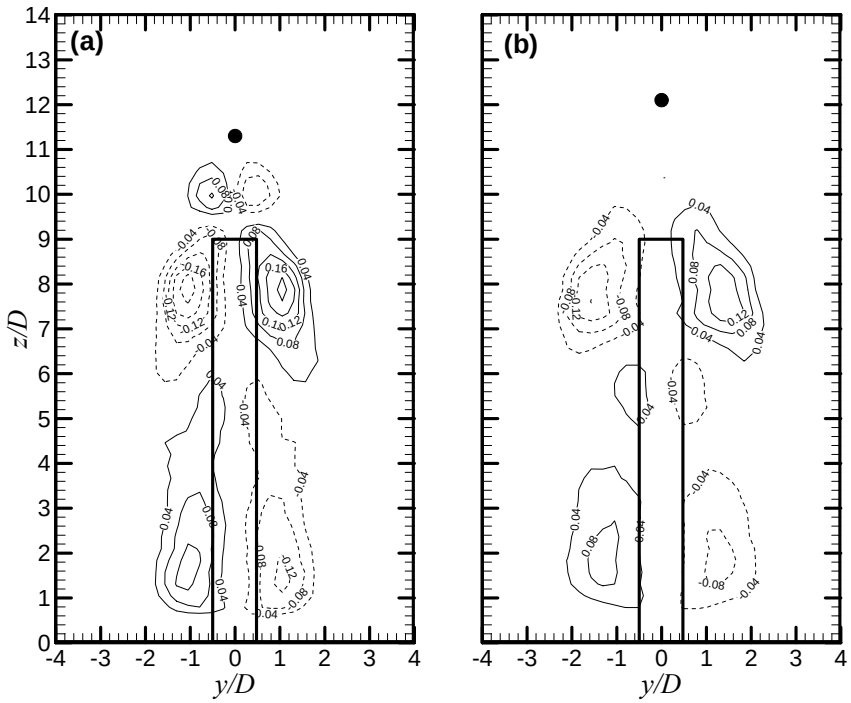

Figure 5.30: The time-averaged streamwise vorticity ($\omega_x D/U_\infty$) field downstream of the stack for R = 1.5 (jet-dominated flow regime) at (a) x/D = 6 and (b) x/D = 10. Contour increment of 0.04.

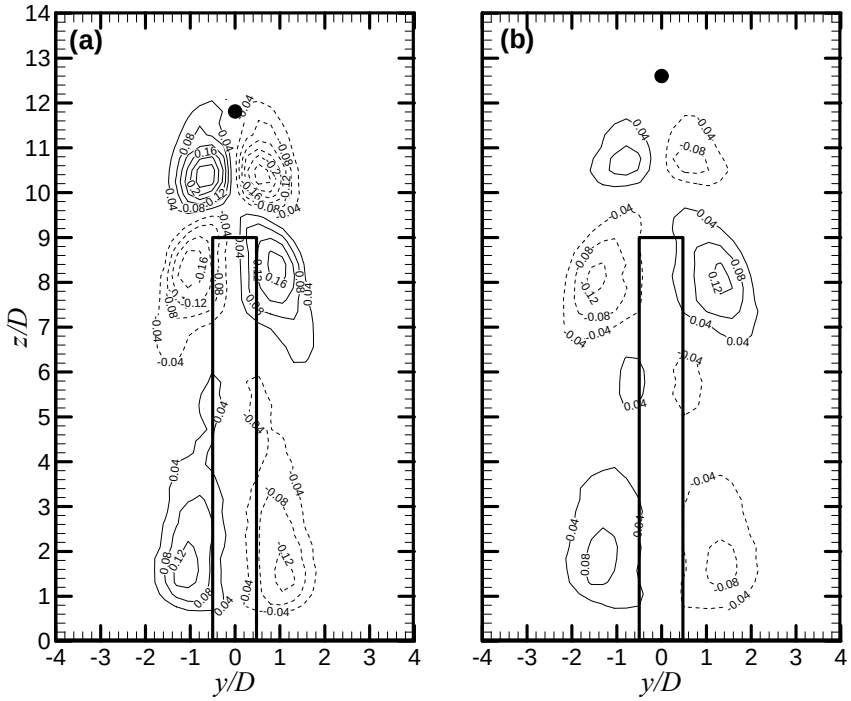

Figure 5.31: The time-averaged streamwise vorticity ($\omega_x D/U_\infty$) field downstream of the stack for R = 2 (jet-dominated flow regime) at (a) x/D = 6 and (b) x/D = 10. Contour increment of 0.04.

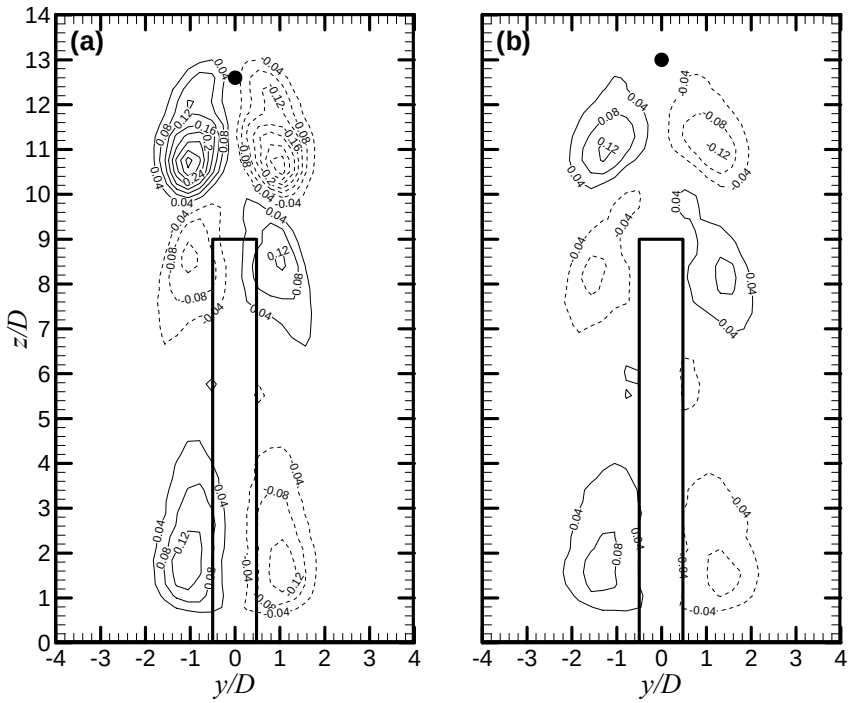

Figure 5.32: The time-averaged streamwise vorticity ($\omega_x D/U_\infty$) field downstream of the stack for R = 2.5 (jet-dominated flow regime) at (a) x/D = 6 and (b) x/D = 10. Contour increment of 0.04.

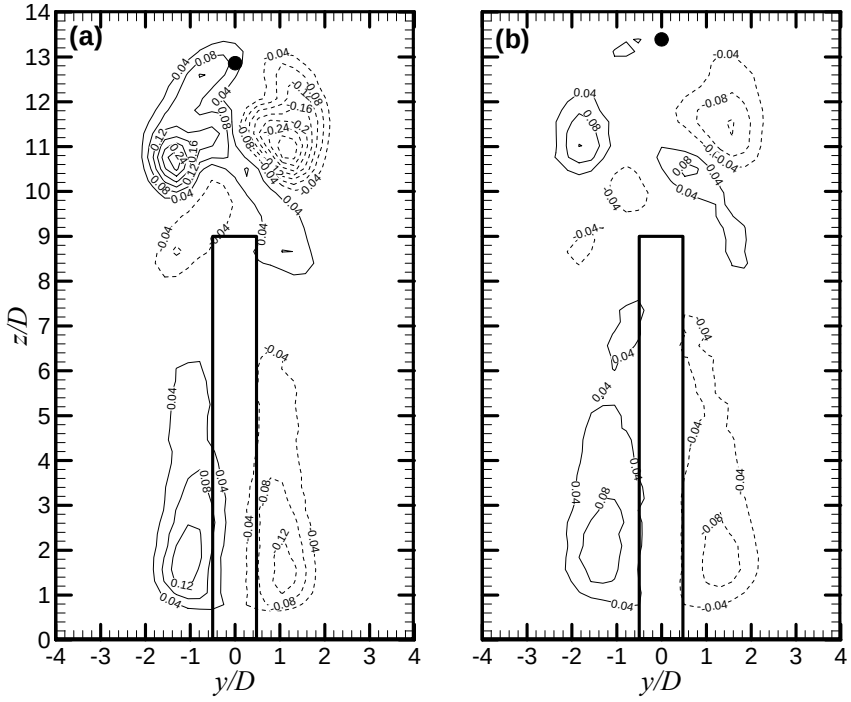

Figure 5.33: The time-averaged streamwise vorticity ($\omega_x D/U_\infty$) field downstream of the stack for R = 3 (jet-dominated flow regime) at (a) x/D = 6 and (b) x/D = 10. Contour increment of 0.04.

vector field (see Figures 5.9-5.12), which indicated the presence of the jet flow at x/D = 6 (Smith and Mungal, 1998). This third vortex pair, referred to as the "jet-wake vortex pair", is located above the free end of the stack. The sense of rotation of jet-wake vortex pair is the same as the base vortex pair but opposite to the tip vortex pair. The jet-wake vortex structures are associated with the jet rise and the strong upwash velocity field above the free end of the stack (see Figures 5.9-5.12), and are stronger than the tip vortex structures. The size and strength of the jet-wake vortex pair increases with R similar to the observation of Plesniak and Cusano (2005) for a ground-level source jet flow. In addition, the tip vortex structures are reduced in size for this flow regime and almost disappear when R = 3.

5.7 Time-Averaged Properties of the Streamwise Vortex Structures

The values of the time-averaged peak streamwise vorticity, strength (circulation) and area of the base vortex, tip vortex and the jet vortex structures are presented in Table 5.1 and in Figures 5.34 to 5.37. The values presented in the figures represent an average of the vortices on either side of the wake centreline vertical plane. Changes in the streamwise vortex structures properties with x/D and/or R (as shown in Table 5.1 and Figures 5.34 to 5.37), may be attributed to several factors, including the redistribution of streamwise vorticity to other coordinate directions (cross-stream or wall-normal vorticity components, neither of which were measured in the present experiments), the diffusion of vorticity due to turbulence, or the cancellation of vorticity due to vorticity of opposite sign.

5.7.1 Peak Streamwise Vorticity

At a given streamwise location, for instance at x/D = 6 (similar trends are observed at x/D = 8 and 10), the peak streamwise vorticity (Figure 5.34(a)) of the base vortex structures is relatively independent of R. But for the tip vortex structures, the peak vorticity value decreases as R increases. This coincides with a reduction in the downwash flow from the stack free end; it is noted that the tip vortex pair has been reported to induce the downwash flow from the free end of a finite circular cylinder (see for example, Sumner *et al*., 2004). The figure also shows the trend of the peak streamwise vorticity of the jet vortex structures. Unlike the tip vortex structures, the peak vorticity value of jet vortex structures increases with R. This may be a result of a strong jet flow from the stack free end

Table 5.1: The vortex structure properties

	R	Vorticity Peak ($\omega D/U_\infty$)			Circulation ($\Gamma/U_\infty D$)			$Area/D^2$		
		x/D=6	x/D=8	x/D=10	x/D=6	x/D=8	x/D=10	x/D=6	x/D = 8	x/D= 10
Base	0.0	0.14	0.13	0.12	0.13	0.13	0.12	1.38	1.52	1.65
	0.5	0.16	0.13	0.12	0.18	0.18	0.17	1.79	2.08	2.34
	1.0	0.14	0.09	0.10	0.32	0.13	0.13	3.72	1.79	1.93
	1.5	0.13	-	0.09	0.32	-	0.12	4.00	-	1.79
	2.0	0.14	-	0.10	0.31	-	0.07	3.86	-	1.10
	2.5	0.15	0.09	0.10	0.26	0.12	0.21	2.76	1.65	3.03
	3.0	0.14	-	-	0.41	-	-	5.10	-	-
Tip	0.0	0.46	0.35	0.29	0.70	0.62	0.55	4.13	4.55	4.41
	0.5	0.40	0.33	0.29	0.67	0.61	0.51	4.55	4.68	3.86
	1.0	0.22	0.22	0.17	0.49	0.51	0.47	4.68	5.24	5.24
	1.5	0.16	-	0.16	0.12	-	0.19	1.52	-	2.21
	2.0	0.10	-	0.11	0.07	-	0.05	0.96	-	0.69
	2.5	0.08	0.10	0.09	0.05	0.07	0.05	0.83	0.96	0.83
	3.0	0.04	-	-	0.00	-	-	0.00	-	-
Jet	1.5	0.12	-	0.00	0.03	-	0.00	0.28	-	0.00
	2.0	0.27	-	0.10	0.21	-	0.03	1.38	-	0.55
	2.5	0.32	0.201	0.13	0.36	0.26	0.18	2.20	2.76	2.20
	3.0	0.29	-	-	0.41	-	-	3.17	-	-

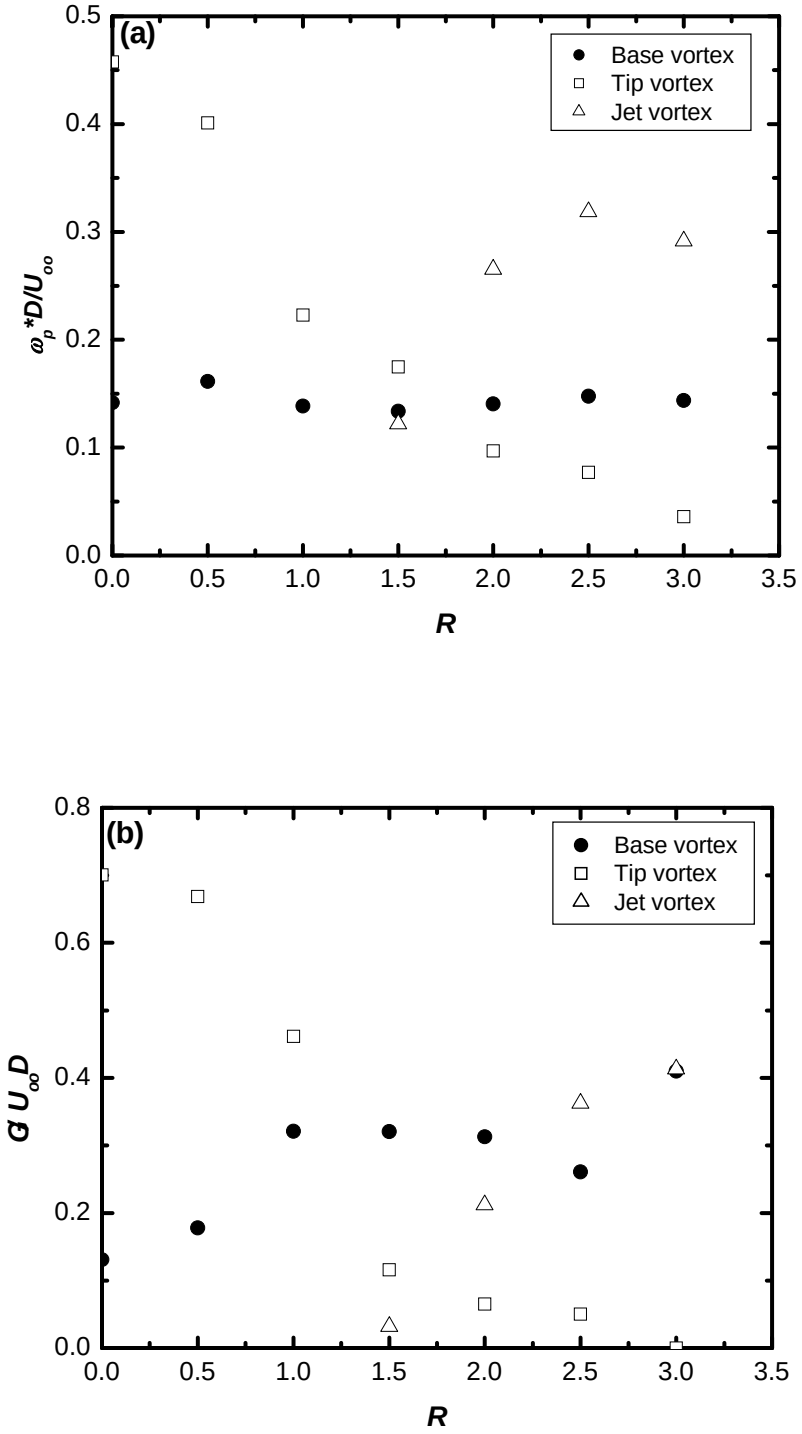

Figure 5.34: The time-averaged streamwise vortex structures properties at $x/D = 6$: (a) peak vorticity value, (b) circulation, and (c) area.

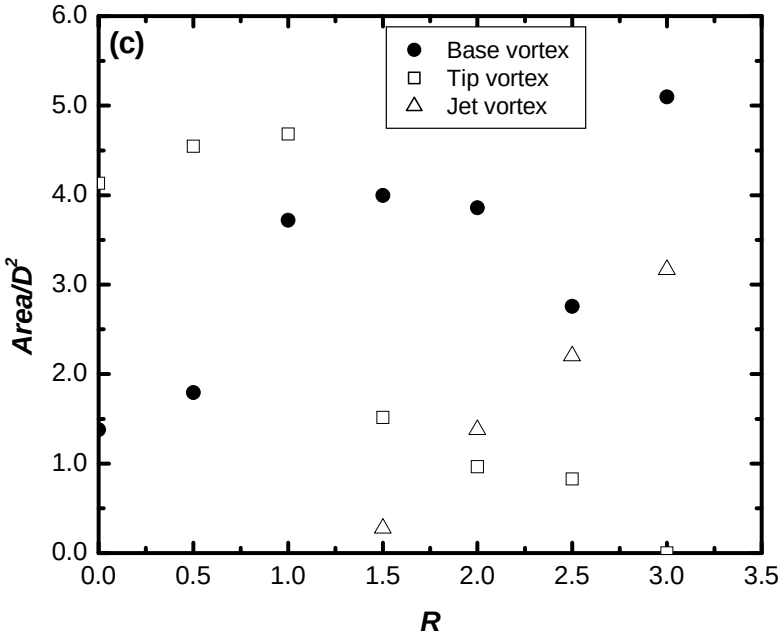

Figure 5.34 continued.

and thereby weakens the tip vortex structures and strengthens the jet vortex structures. Generally, there is a reduction in both the base vortex and the tip vortex peak vorticity values with streamwise distance from the stack (see Figure 5.35(a)).

5.7.2 Vortex Strength (Circulation)

The base vortex circulation (Figure 5.34(b)) increases gradually from $R = 0$ (downwash flow regime) to $R = 3$ (jet-dominated flow regime). The slight scatter in the data might be related to the measurement uncertainty, and this trend is also seen in the area of the vortices (see Figure 5.34(c)).

In the case of the tip vortex structures, their circulation decreases as R increases with a slight change between the values for $R = 0$ and 0.5 (which represents the downwash flow regime) and gradual reduction in strength for $R \geq 1.5$ (the jet-dominated

flow regime). The circulation of the tip vortex structures was 0.7 for $R = 0$ (equivalent to a finite circular cylinder) in this study, which is similar to the result of Sumner *et al*. (2004) for cylinder of $AR = 9$, $Re_D = 6.0 \times 10^4$ and $\delta/H = 0.3$ (see Figure 5.35). The base vortex strength is, however, slightly higher for this study when compared with their result. This observation might be related to the boundary layer on the ground plane, which is slightly thicker in the present study. The strength of the jet vortex structures is zero for $R < 1.5$ due to the absence of jet vortices within this range of R, but increases with R when $R \geq 1.5$. This is due to the increasing interaction between the jet flow and the cross-flow due to the increase in the jet flow momentum as the value of R increases.

5.7.3 Vortex Area

The trend of the base vortex area (Figure 5.34(c)) with R is similar to the vortex circulation behaviour. The tip vortex structure area increased within the downwash flow and crosswind-dominated flow regimes, but decreased with R within the jet-dominated flow regime. The base vortex and tip vortex areas for $R = 0$ are similar to those of Sumner *et al*. (2004) for a cylinder of $AR = 9$ and freestream Reynolds number of 6.0×10^4. Within the jet-dominated flow regime, the area of the jet vortex structures increases with increasing R.

5.7.4 Streamwise Development

The streamwise development of the peak streamwise vorticity, circulation and area for the base and tip vortices for $R = 0$, 0.5, 1 and 2.5, are shown in Figures 5.35, 5.36 and 5.37, respectively. Also included are the results of Sumner *et al.* (2004) for $AR = 9$. For the base vortex structures, the peak vorticity value slightly decreases with x/D for all

values of R (Figure 5.35(a)) and the circulation (Figure 5.36a) decreases with x/D for R = 0 and 0.5, and behaves almost the same for R = 1 and 2.5. Also, the base vortex area

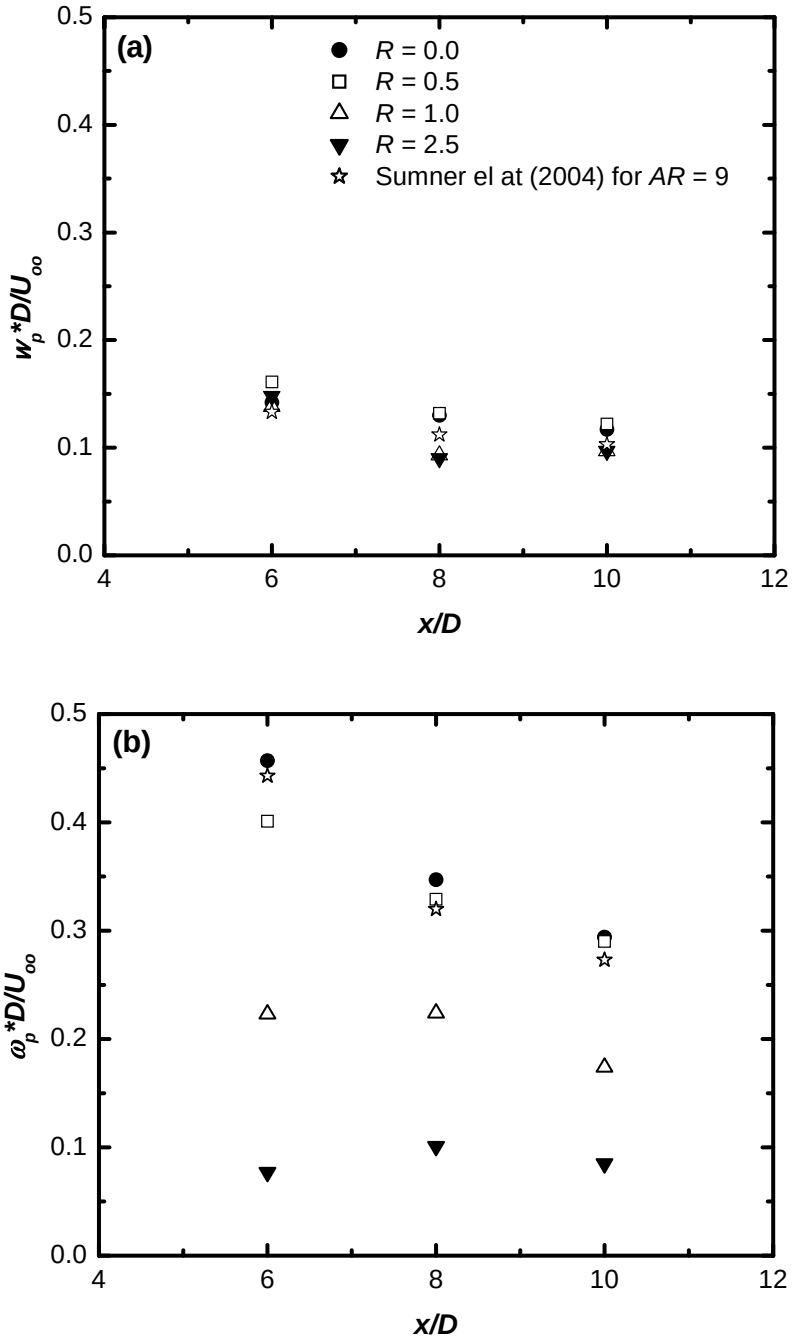

Figure 5.35: The streamwise development of the peak vorticity for the (a) base vortices and (b) tip vortices.

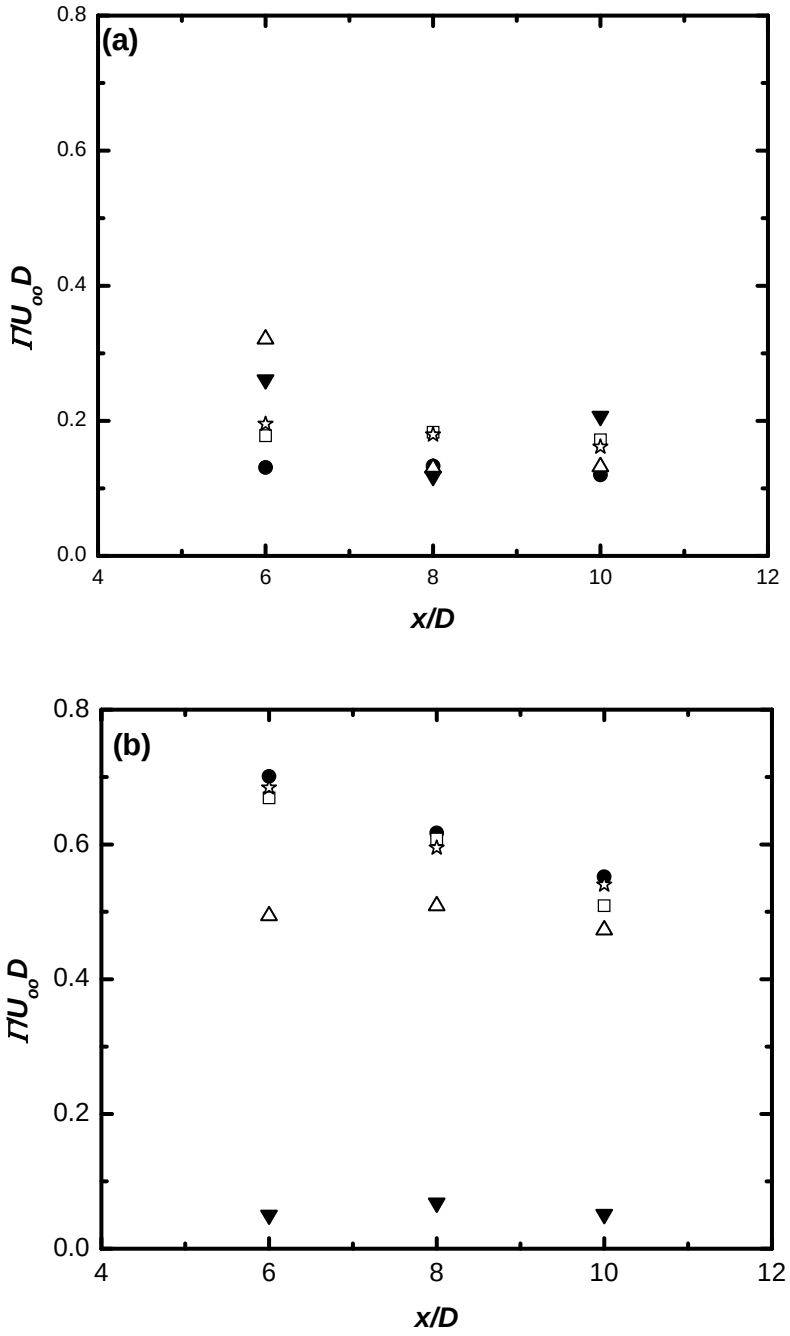

Figure 5.36: The streamwise development of the vortex strength for (a) base vortices and (b) tip vortices. (Symbols as defined in Figure 5.35).

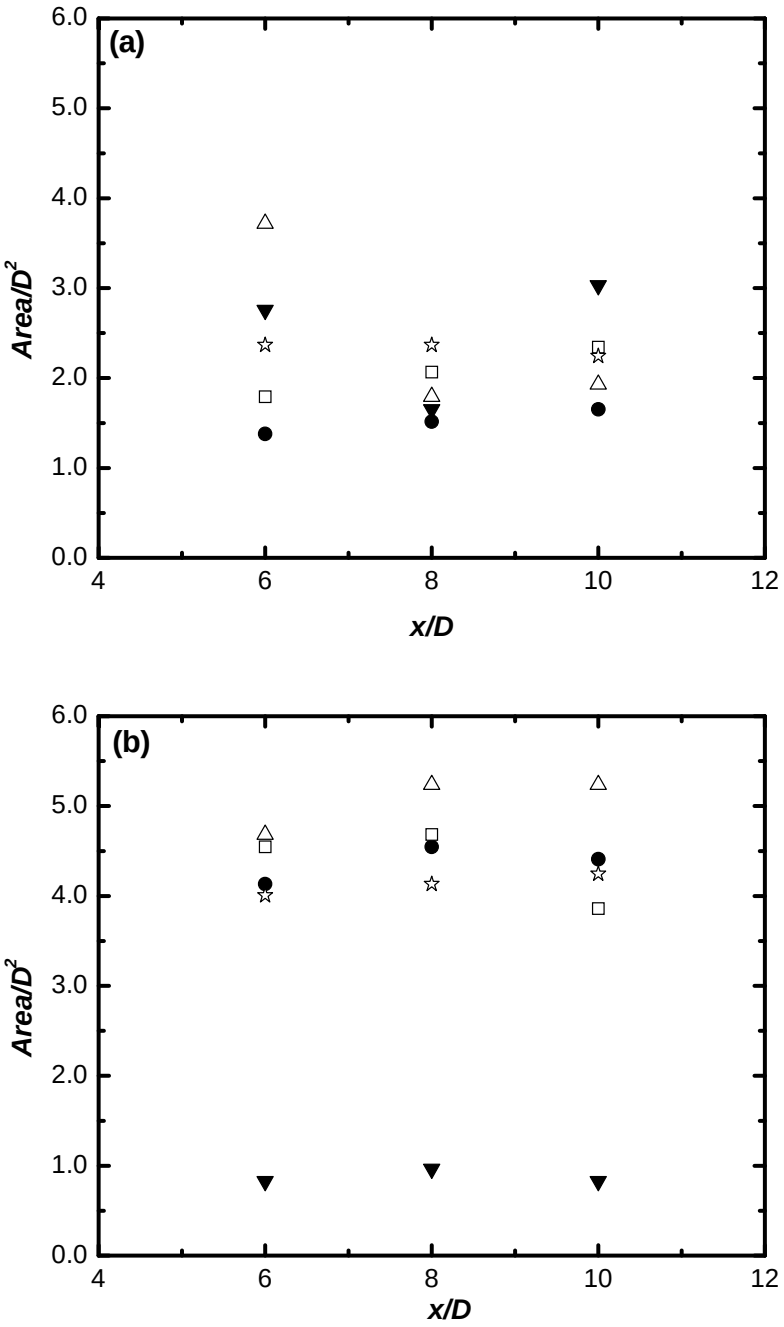

Figure 5.37: The streamwise development of the vortex area for (a) base vortices and (b) tip vortices. (Symbols as defined in Figure 5.35).

(Figure 5.37a) follows a similar trend as the circulation. There is a slight difference in the values of the base vortex peak vorticity value, circulation and area for $R = 0$, when compared the results of Sumner *et al.* (2004). This deviation might be due to the influence of the ground plane boundary layer.

The stack tip vortex peak vorticity value (Figure 5.35(b)) and the circulation (Figure 5.36(b)) generally decrease with x/D for $R = 0$ and 0.5, while those of $R = 1$ and 2.5 are either relatively constant or slightly decrease with x/D. This may be a result of the jet flow that weakens the tip vortex structure formation. As discussed earlier, these values generally decrease with R at a given downstream location. The tip vortex area (Figure 3.57(b)) slightly decreased with x/D for $R = 0.5$, and slightly increased for $R = 1$, but remained fairly constant for $R = 0$ and 2.5.

5.8 Summary

In this chapter, the effect of the velocity ratio, R, on the time-averaged velocity field properties in the wake of a stack was presented. Based on the data presented, three flow regimes were identified: downwash flow, crosswind-dominated flow, and jet-dominated flow. In the next chapter, the influence of this variable, R, on the turbulence field within the stack wake and the relationship with time-averaged velocity field properties will be presented.

CHAPTER 6

THE TURBULENCE FIELD IN THE WAKE OF A STACK

6.1 Introduction

In the previous Chapter, the influence of the jet-to-cross-flow velocity ratio, R, on the time-averaged velocity and vorticity fields within the wake of a stack was reported. It was observed that the flow structure within the stack wake is strongly influenced by R, and the flow around the stack could be classified into three distinct regimes: the downwash, crosswind-dominated and jet-dominated flow regimes. In this Chapter, the effect of R on the turbulence field within the stack wake and their relationship with the time-averaged parameters is presented and discussed. Due to the limitations of the instrument used (X-probe, section 3.5), only two turbulence intensities, u' and w', and one component of the Reynolds shear stress in the x-z plane, $-\langle uw \rangle$, and two higher-order moments, $\langle uw^2 \rangle$, and $\langle u^2 w \rangle$, were measured. In addition, the effect of R on the skewness and flatness factors in both the streamwise and wall-normal directions is presented.

In order to reduce the amount data presented, results for three values of R, which represent the three distinct flow regimes identified in Chapter 5, are presented and discussed. They are: $R = 0.5$ (downwash flow regime), $R = 1$ (crosswind-dominated flow regime) and $R = 2.5$ (jet-dominated flow regime). In addition, the data for $R = 0$,

which represents the finite circular cylinder case, are included for comparison purposes. Similar to the definition adopted in Chapter 5, the stack wake is defined as the region $0 < z/H \leq 1$, while the region of $z/H > 1$ is considered the jet wake.

6.2 Turbulence Intensities

Profiles of the streamwise turbulence intensity (u'/U_∞) along the wake centreline at x/D = 10 and 15 are shown in Figure 6.1 for different values of R. In these figures, the turbulence intensities are made dimensionless by the freestream velocity. This information is equivalent to the streamwise normal Reynolds stress. For each value of R, the turbulence intensity varies along the stack height and approaches the freestream value of about 0.6% above the stack free end for R = 0, and above the jet wake for R = 0.5, 1 and 2.5. The wall-normal turbulence intensity (w'/U_∞) profiles (see Figure 6.2) are similar to the streamwise turbulence intensity data for all values of R. In addition, there is an upward shift in the peak values of the turbulence intensities for R = 1 and 2.5 compared with R = 0 and 0.5.

For R = 0 and 0.5 (corresponding to the downwash flow regime) at x/D = 10 (Figure 6.1(a)), there is a localized region of high streamwise turbulence intensity within the stack wake. This high turbulence intensity behind the stack can be attributed to the diffusion of fluid (from the downwash from the free end, the upwash from the ground plane and the separated shear layers) into the wake of the stack. This is a result of interactions between the streamwise vortex structures. In this figure, the region of the maximum turbulence intensity, which occurs within the ground plane boundary layer, coincides with the region of maximum time-averaged streamwise velocity deficit (see Figure 5.1) within the stack wake.

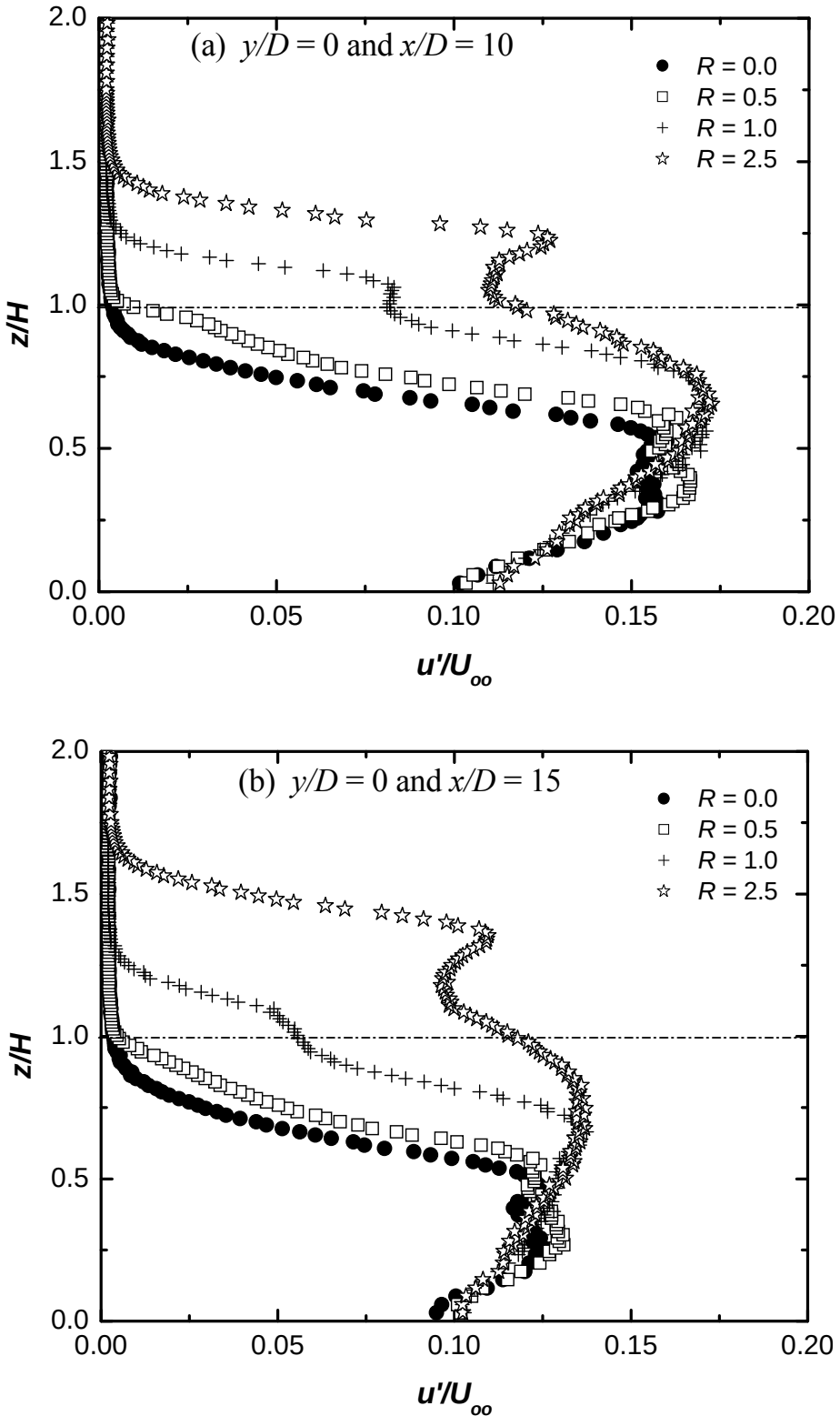

Figure 6.1: The streamwise turbulence intensity (u'/U_∞) profiles along the wake centreline ($y/D = 0$) at (a) $x/D = 10$ and (b) $x/D = 15$.

When R = 1, (crosswind-dominated flow regime) a second peak of high streamwise turbulence intensity appears just above the free end of the stack and within the jet wake. The second peak may be due to shear associated with the jet and the interaction of the jet flow with the cross-flow. This second region coincides with a region of velocity deficit (see Figure 5.1) in the jet wake.

For R = 2.5 (corresponding to the jet-dominated flow regime), the second region of high turbulence intensity within the jet wake is now well defined. The peak turbulence intensity values in the jet wake are smaller in magnitude compared to the highest turbulence values within the stack wake.

As the streamwise distance increases (Figure 6.1(b)), there is an overall reduction in the turbulence intensity within both the stack wake and jet wake. In addition, there is a slight upward shift (in the wall-normal direction) in the location of the peak (within the jet wake) in the turbulence intensity for R = 2.5, which corresponds to the jet-dominated flow regime. This is due to the increase in the jet wake span (in the wall-normal direction) which is the result of an increase in the height of the jet flow centerline trajectory at x/D = 15 compared with jet flow profile at x/D = 10, as discussed in Chapter 5.

The wall-normal turbulence intensity (w'/U_∞) profiles along the wake centerline at x/D = 10 and 15 are shown in Figure 6.2 for different values of R. This information is equivalent to the wall-normal normal Reynolds stress. Similar to the streamwise turbulence intensity profiles, a region of strong turbulence intensity is observed within the stack wake for R = 0, 0.5 and 1, while two regions are observed for R = 2.5, one within the stack wake and the other within the jet wake. There is an overall reduction in the turbulence intensity as the streamwise distance increases (see Figure 6.2(b)).

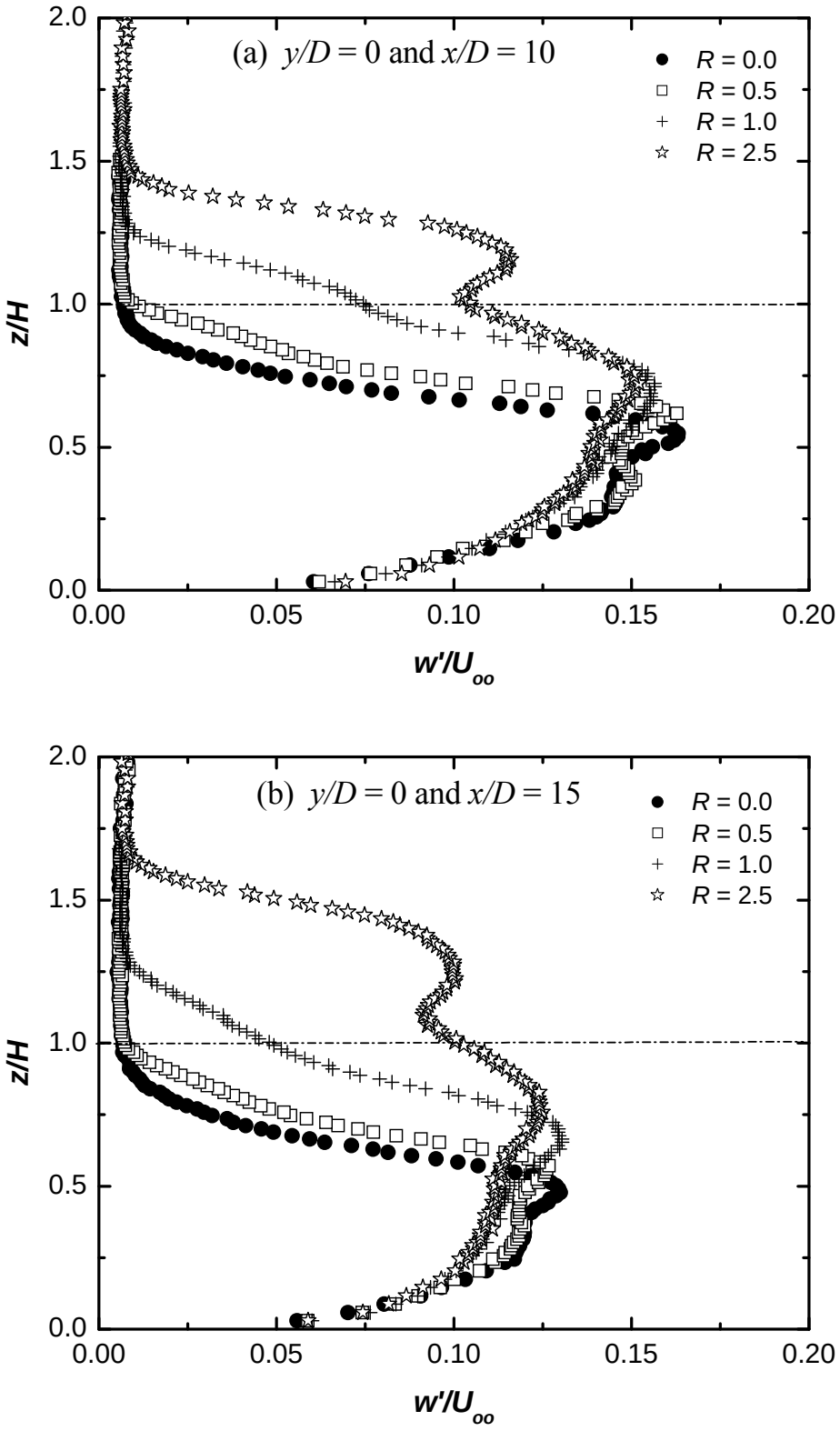

Figure 6.2: The wall-normal turbulence intensity (w'/U_∞) profiles along the wake centreline ($y/D = 0$) at (a) $x/D = 10$ and (b) $x/D = 15$.

The streamwise turbulence intensity profiles (u'/U_∞) at x/D = 10 and at different vertical locations along the stack height are shown in Figure 6.3, for different values of R. As would be expected, the turbulence intensity profiles are symmetrical about the wake centreline (y/D = 0) at all locations. For the streamwise turbulence intensity at z/H = 0.5 (Figure 6.3(a)), a double peak is observed for R = 0. This is similar to the results of Okamoto and Sunabashiri (1992) for AR = 7 at x/D = 10 and Afgan *et al.* (2007) for AR = 6 at x/D = 5. Similar characteristics for the finite circular cylinder were also reported in Chapter 4 for AR = 7 and 9. The profile for R = 0.5 is similar to that of R = 0. However, in the case of R = 1 and 2.5, only one peak is observed.

At z/H = 0.75 (Figure 6.3(b)), a twin-peak distribution is observed for R = 0 and 0.5, which is similar to the result presented for the finite circular cylinder in Chapter 4 for AR = 9. In contrast, a single peak is observed for R = 1 and 2.5. Wang *et al.* (2006) also observed two peaks in the streamwise turbulence intensity for a finite-length square cylinder of AR = 5 at z/H = 0.8 and x/D = 6. They argued that the two peaks are due to the "occurrence of two rows of vortices" within the square wake. As reported by Okamoto and Sunabashiri (1992), the two peaks observed for R = 0 and 0.5 are due to the influence of the downwash flow from the stack. Generally, the turbulence intensity at the wake centreline increases with increasing R. The absence of double peaks for R = 1 and 2.5 may indicate the absence of the downwash flow at the mid-height of the stack, z/H = 0.5.

At the stack free end, z/H = 1 (Figure 6.3(c)), the streamwise turbulence intensity for R = 0 approaches the freestream turbulence. For R = 0.5, a small peak is observed within the vicinity of the wake centreline (y/D = 0), which is due to the presence of the

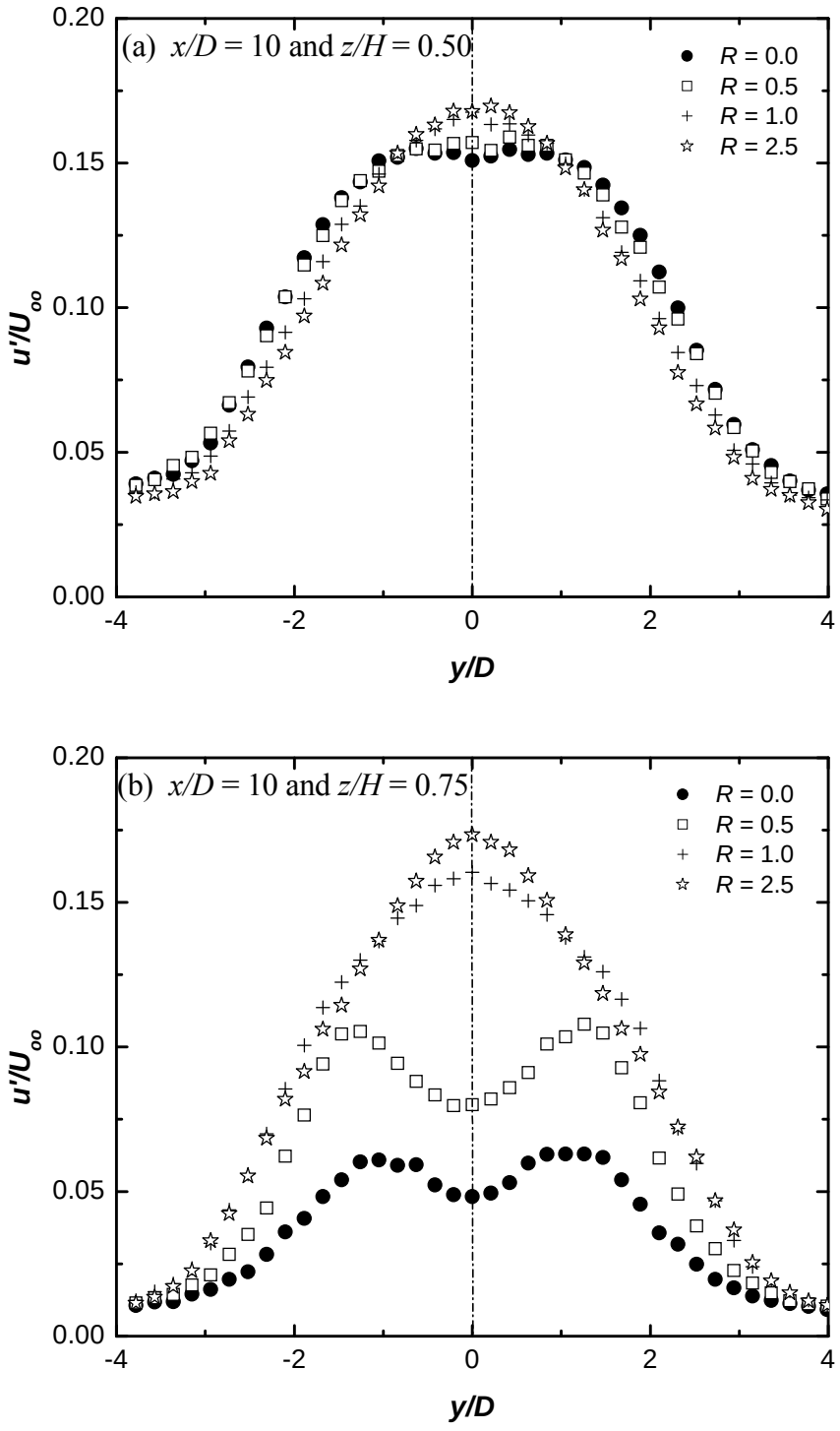

Figure 6.3: The streamwise turbulence intensity (u'/U_∞) profiles at $x/D = 10$ for (a) $z/H \approx 0.5$, (b) $z/H \approx 0.75$, and (c) $z/H \approx 1$.

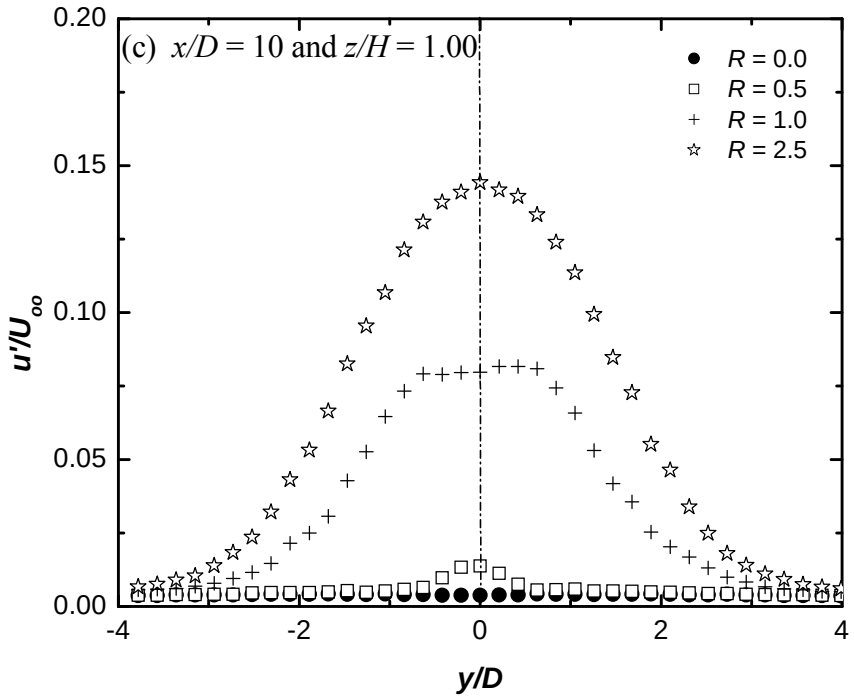

Figure 6.3 continued.

small velocity defect as a result of the weak jet flow (see Figure 5.1). A broad-band peak and a strong single peak are observed for the R = 1 and 2.5 profiles, respectively, which are due to the interactions between the cross-flow and the jet flow. The peak values are associated with the jet wake within the vicinity of the stack free end for R = 1 and above the stack free end for R = 2.5 (see Figure 5.1).

The wall-normal turbulence intensity (w'/U_∞) at x/D = 10 and at different vertical locations along the stack height are shown in Figure 6.4. At z/H = 0.5, two peaks are observed for R = 0, 0.5 and 1, while a broad-band profile is observed for R = 2.5. At this location, the flow turbulence intensity profiles are slightly asymmetrical about the wake centreline (y/D = 0) for R = 0, 0.5 and 1. This is different from the result of Okamoto and Sunabashiri (1992) for AR = 7 at z/H = 0.5 and x/D = 10, who reported two symmetric peaks, in the wall-normal turbulence intensity. This asymmetric profile

observed in this study is likely due to a small misalignment in the probe orientation in the cross-flow direction.

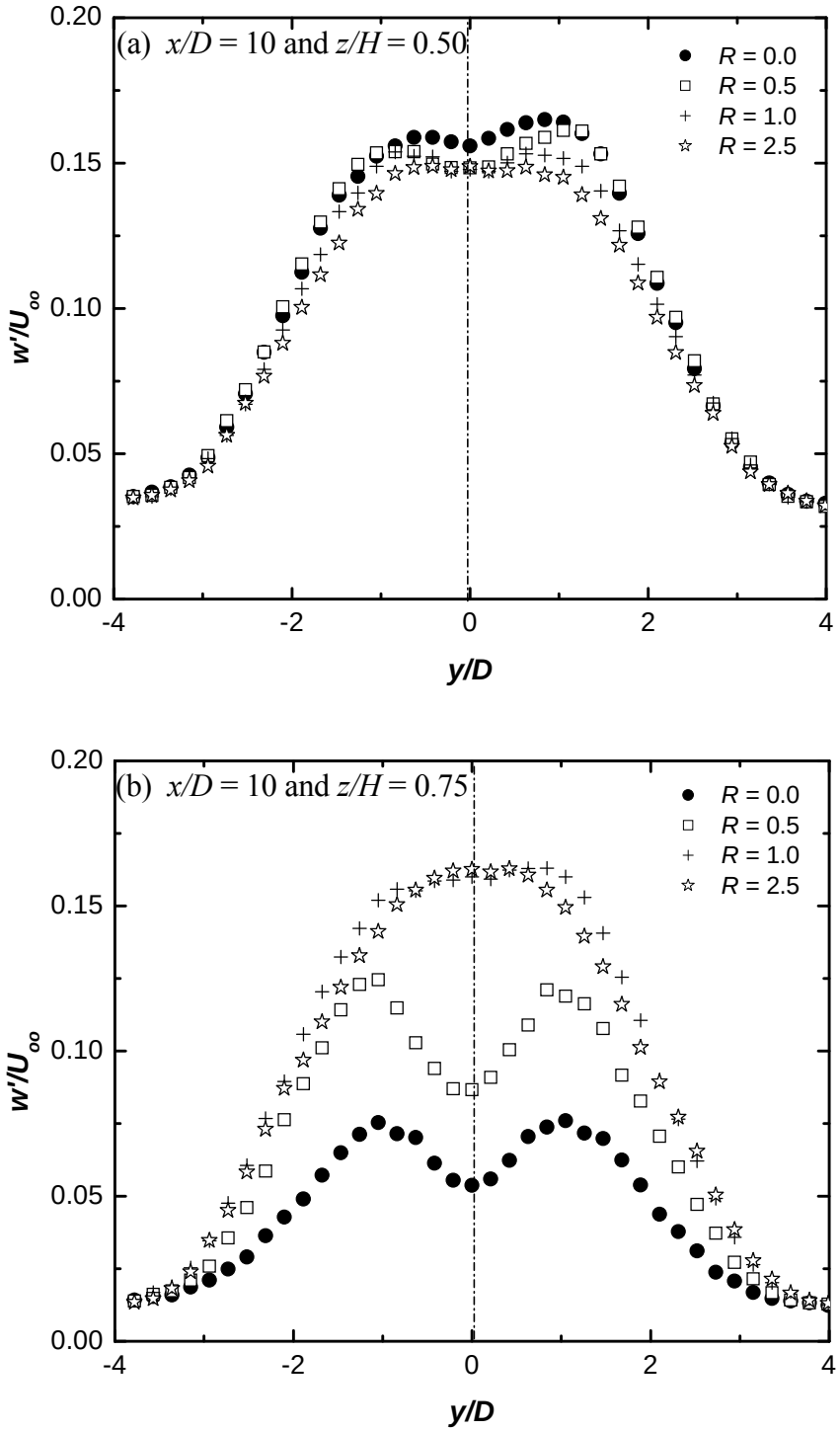

Figure 6.4: The wall-normal turbulence intensity (w'/U_∞) profiles at $x/D = 10$ for (a) $z/H \approx 0.5$; (b) $z/H \approx 0.75$; and (c) $z/H \approx 1.0$.

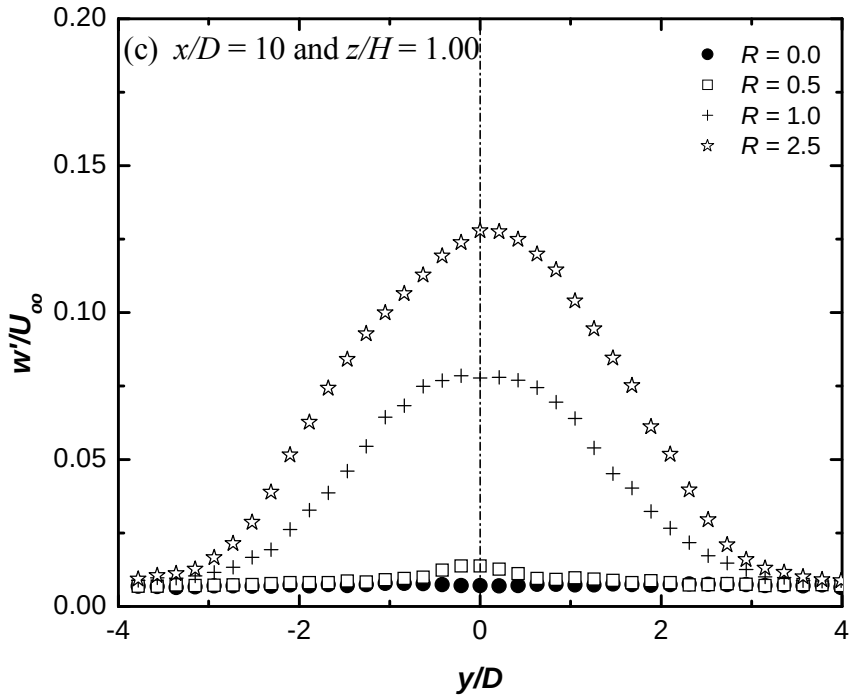

Figure 6.4 continued.

At z/H = 0.75 (Figure 6.4(b)), similar to the streamwise turbulence intensity (Figure 6.3(b)), a twin-peak distribution is observed for R = 0 and 0.5, which is similar to the result presented in Chapter 4 for a finite cylinder of AR = 9. A single peak is, however, observed for R = 1 and 2.5. In contrast to in this study, Wang *et al.* (2006) observed only one peak in the wall-normal turbulence intensity profile for a square cylinder of AR = 5 at z/H = 0.8 and x/D = 6. Generally, the turbulence intensity at the wake centreline increases with R.

At the stack free end, z/H = 1 (Figure 6.4(c)), similar to the streamwise turbulence intensity (Figure 6.3(c)), the wall-normal turbulence intensity for R = 0 approaches the freestream turbulence intensity and the flow reflects the properties of the freestream conditions. For R = 0.5, a small peak is observed within the vicinity of the

wake centreline ($y/D = 0$). This may be due to the interaction between cross-flow and the weak jet flow (see Figure 5.1). Also similar to the streamwise turbulence intensity, a single peak is observed for the $R = 1$ and 2.5 profiles. Again, the turbulence intensity at the wake centreline increases with R.

Figures 6.5 to 6.7 show contour plots for the streamwise turbulence intensity ($u'/\overline{U}$) fields in the cross-stream plane at $x/D = 10$. In these figures, the turbulence intensities are made dimensionless by the local time-averaged streamwise velocity. Localized regions of high streamwise turbulence intensity within the stack and jet wakes are observed in these figures to coincide with the regions of low (time-averaged) streamwise velocity within these wakes (see Chapter 5). For the finite circular cylinder ($R = 0$, Figure 6.5(a)), the high turbulence intensity behind the stack is attributed to the interactions between the streamwise vortex structures, the vortex street, downwash from the free end, and upwash from the ground plane, which produces strong shear (Sumner *et al*., 2004). In the downwash flow regime, when $R = 0.5$ (Figure 6.5(b)), a second region of high turbulence intensity begins to form near the top of the stack within the stack wake. This second region is due to the interaction between the cross-flow and the weak jet flow. In the cross-wind-dominated flow regime ($R = 1$, Figure 6.6), this second region extends above the free end of the stack and is observed to be stronger than for $R = 0.5$.

In the jet-dominated flow regime, ($R = 2.5$, Figure 6.7), this second region of elevated streamwise turbulence intensity becomes more distinct, increases in size, and

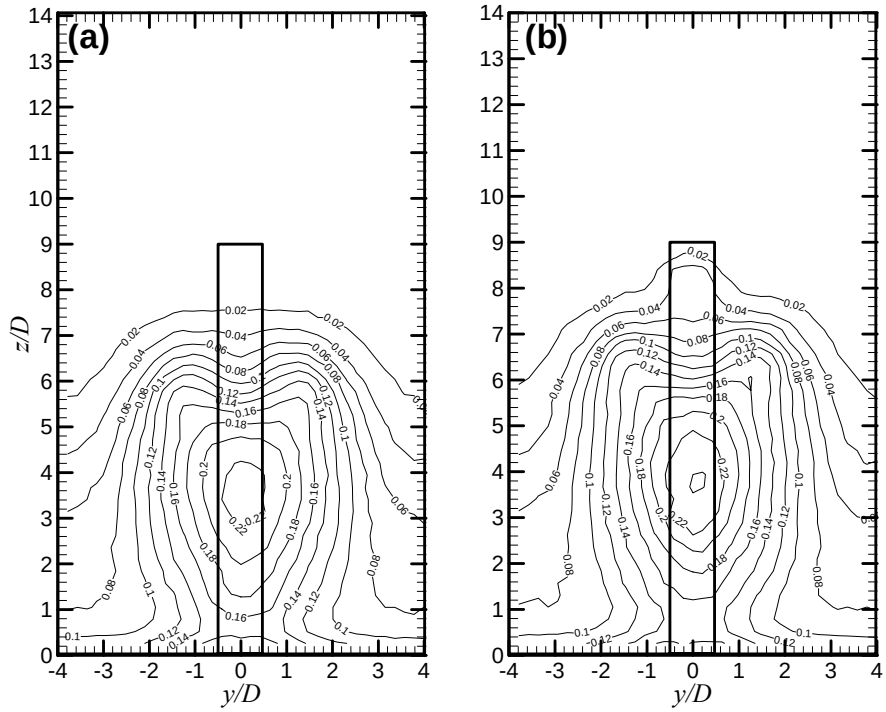

Figure 6.5: The streamwise turbulence intensity ($u'/\overline{U}$) field downstream of the stack at x/D = 10 for the downwash flow regime: (a) R = 0, and (b) R = 0.5. Contour increment of 0.02.

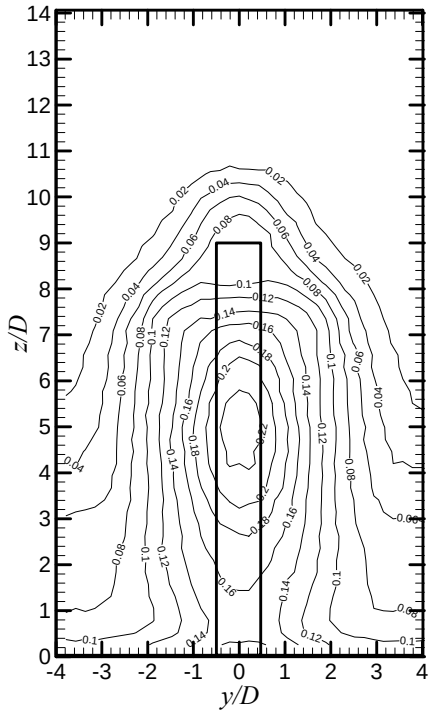

Figure 6.6: The streamwise turbulence intensity ($u'/\overline{U}$) field downstream of the stack at x/D = 10 for the crosswind-dominated flow regime, R = 1. Contour increment of 0.02.

moves further above the free end of the stack, characterizing the jet wake region. The behaviour of the second region of high turbulence intensity demonstrates the influence of the jet flow, which is relatively weak when $R < 1.5$, but becomes increasingly stronger when $R > 1.5$. The high turbulence intensities within the jet wake can be attributed to the strong mixing (which increases with R) between the jet flow and cross-flow, especially in the crosswind-dominated and jet-dominated flow regimes.

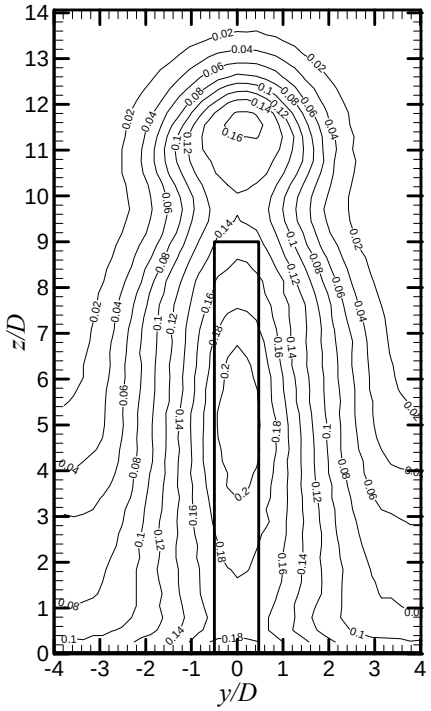

Figure 6.7: The streamwise turbulence intensity ($u'/\overline{U}$) field downstream of the stack at $x/D = 10$ for the jet-dominated flow regime, $R = 2.5$. Contour increment of 0.02.

The contour plots for the wall-normal turbulence intensity ($w'/\overline{U}$) fields in the cross-stream plane at $x/D = 10$, shown in Figures 6.8 to 6.10, behave similarly to the streamwise turbulence intensity data for all values of R. For the jet-dominated flow regime, in contrast to Huang and Hsieh (2002, 2003), it was observed that the streamwise turbulence intensity is generally greater in the stack wake than in the jet

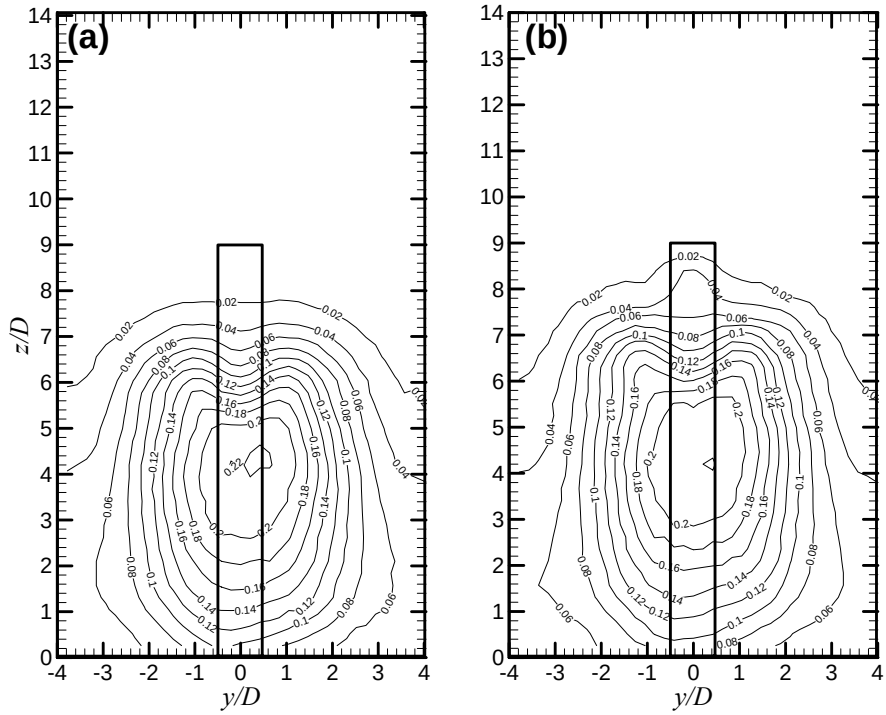

Figure 6.8: The wall-normal turbulence intensity ($w'/\overline{U}$) field downstream of the stack at x/D = 10 for the downwash flow regime: (a) R = 0 and (b) R = 0.5. Contour increment of 0.02.

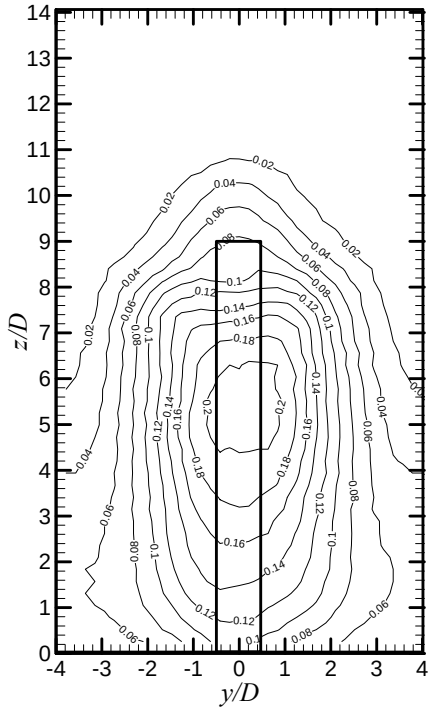

Figure 6.9: The wall-normal turbulence intensity ($w'/\overline{U}$) field downstream of the stack at x/D = 10 for the crosswind-dominated flow regime, R = 1. Contour increment of 0.02.

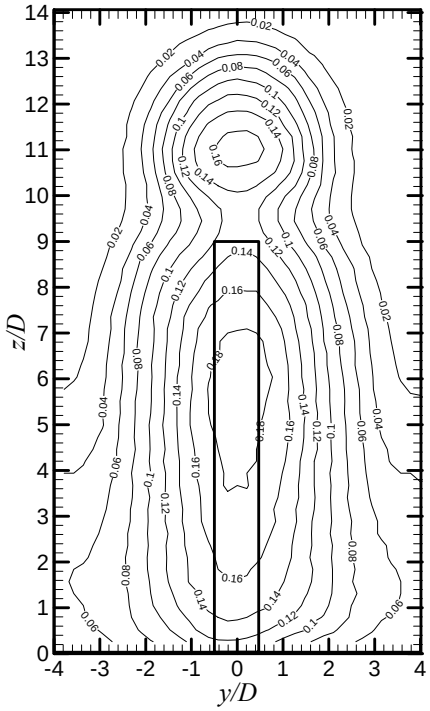

Figure 6.10: The wall-normal turbulence intensity ($w'/\overline{U}$) field downstream of the stack at x/D = 10 for the jet-dominated flow regime, R = 2.5. Contour increment of 0.02.

wake. As well, the wall-normal turbulence intensity within the stack wake is slightly greater than or equal to that within the jet wake. This may be due to the interaction between the separated shear layers and the upwash flow from the ground plane.

6.3 Reynolds Shear Stress

Figure 6.11 presents the measurements of the Reynolds shear stress, $-\langle uw \rangle / U_\infty^2$, along the wake centreline (y/D = 0) at x/D = 10 and 15. The Reynolds shear stress physically relates to the transport of momentum due to the turbulent fluctuations in the flow in the x-z plane. Regions of elevated Reynolds shear stress may be associated with strong local production of turbulence, which depends on the local velocity gradients. The characteristics of the Reynolds shear stress are thus related to the gradient of the time-

averaged streamwise velocity component (see Chapter 5), especially for lower values of R within the stack wake and for higher values of R within the jet wake. For R = 0 and 0.5

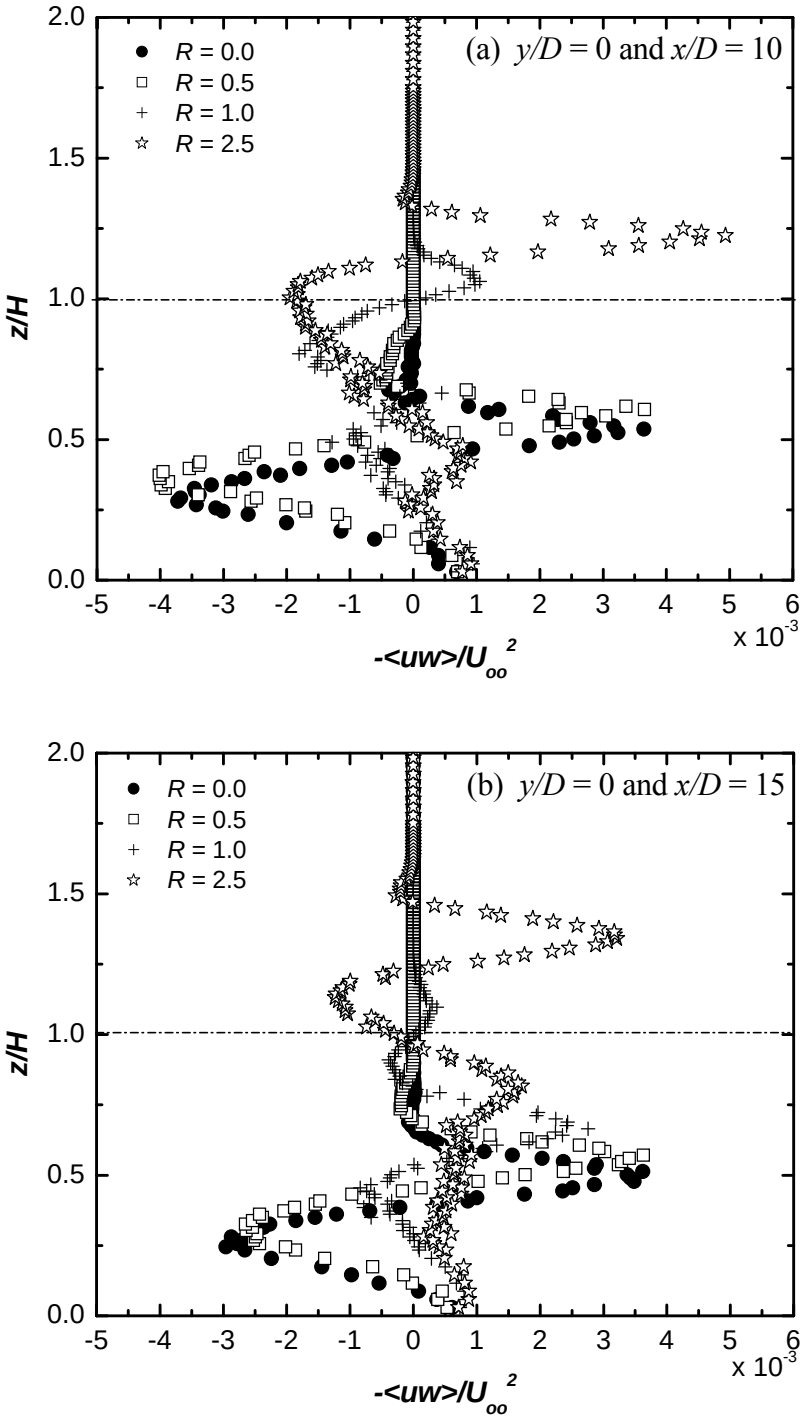

Figure 6.11: The Reynolds shear stress ($-\langle uw\rangle/U_\infty^2$) profiles along the wake centreline (y/D = 0) at (a) x/D = 10 and (b) x/D = 15.

at x/D = 10, there are two regions (opposite in sign) of elevated Reynolds shear stress, located behind the stack. This is similar to what was shown in Chapter 4 for a finite circular cylinder of $AR \geq 5$. The region of positive Reynolds shear stress is located in the region of downwash flow from the free end of the stack, while the negative Reynolds shear stress region occurs within the ground plane boundary layer in the region of upwash flow.

For the crosswind-dominated flow regime, R = 1, there is a reduction in the magnitude of the Reynolds shear stress within the upwash flow region compared with R = 0 and 0.5. In addition, a second negative Reynolds shear stress region is observed close to the stack free end and a region of positive elevated Reynolds shear stress within the jet wake. This is due to the mixing or interaction of the jet flow with the cross-flow that increases the turbulence of the flow within this region.

In the case of the jet-dominated flow regime, R = 2.5, the Reynolds shear stress is entirely negative in the upper half of the stack wake, and two regions of elevated Reynolds shear stress, having opposite signs, are observed in the jet wake. The negative Reynolds shear stress is located just above the stack free end and has a smaller absolute value than the strong positive Reynolds shear stress that occurs inside the jet wake. The strong positive shear stress observed within the jet wake is due to the strong interaction between the jet flow, cross-flow and the separated shear layers from either sides of the jet flow. In addition to these features, another smaller, positive shear stress region is observed below the mid-height of the stack.

As the streamwise distance increases (Figure 6.11(b)), there is an overall small reduction in the peak value of the shear stress within both the stack wake and jet wake.

In addition, there is a slight upward shift (in the wall-normal direction) in the location of the peak in the shear stress for R = 2.5, which corresponds to the jet-dominated flow regime. This is due to the increase in the jet wake span (in the wall-normal direction) and increase in the turbulence intensity in the flow, as previously discussed in Section 6.2 and shown in Figure 6.2.

The contour plots for the Reynolds shear stress fields in the cross-stream plane behind the stack at x/D = 10 are presented in Figures 6.12 to 6.14. In these figures, the solid contour lines represent positive Reynolds shear stress, while dashed contour lines represent negative Reynolds shear stress. In the downwash flow regime (R = 0 and 0.5, Figure 6.12), there is a concentrated region of negative Reynolds shear stress within the

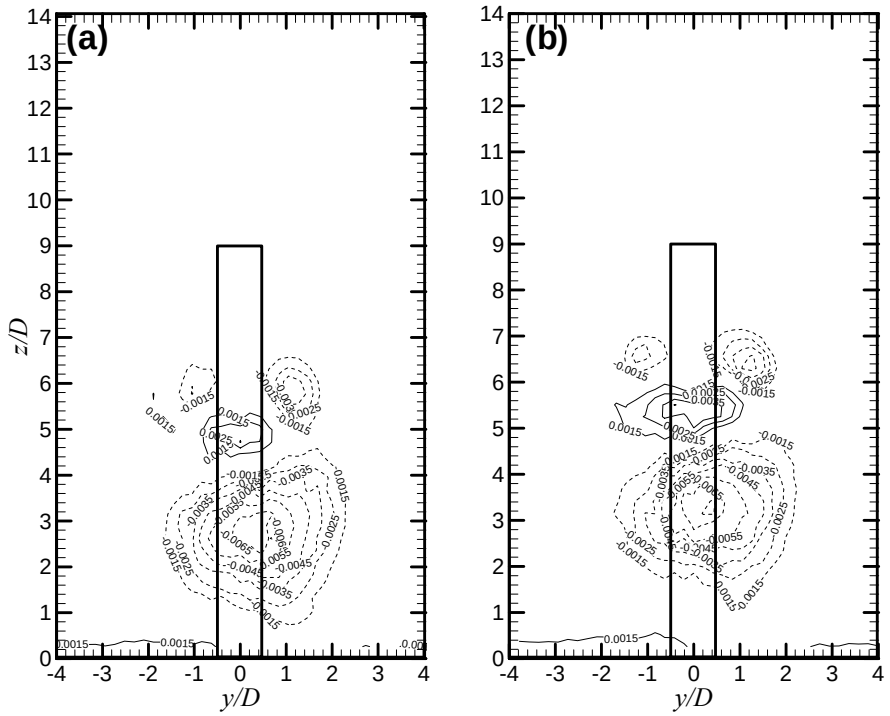

Figure 6.12: The downwash flow regime Reynolds shear stress ($-<uw>/\overline{U}^2$) field downstream of the stack at x/D = 10 for (a) R = 0 and (b) R = 0.5. Minimum contour magnitude 0.0015 and contour increment of 0.001. Solid lines represent positive shear stress and dashed lines represent negative shear stress.

boundary layer on the ground plane that coincides with the upwash flow (see Chapter 5) from the ground plane. It is in this region where the base vortex structures are located (Sumner *et al*., 2004), and the Kármán vortex axes have been observed to bend upstream towards the base of the stack (Okamoto and Yagita, 1973; Johnston and Wilson, 1997; Tanaka and Murata, 1991). There are also two regions of negative Reynolds shear stress on either side of the stack closer to the free end. This pair may be due to several aspects of the flow field, including the upwash flow on the outer edges of the stack wake (see Chapter 5), the tip vortex structures (Sumner *et al*., 2004) and the bending of the Karman vortex axes toward the free end (Okamoto and Yagita, 1973; Johnston and Wilson, 1997; Tanaka and Murata, 1999). The strength of this pair is lower than that of the concentrated region inside the flat-plate boundary layer because the upwash flow from the ground plane is stronger than the upwash flow in the upper half of the stack wake. The pair moves closer to the free end when a jet flow occurs (compare $R = 0$ with $R = 0.5$). In between these regions of negative Reynolds shear stress, at the edge of the ground plane boundary layer is a small region of concentrated positive Reynolds shear stress. The absolute strength of this positive region is lower than that of the negative region, and is higher for $R = 0.5$ than for $R = 0$.

In the crosswind-dominated flow regime ($R = 1$, Figure 6.13), the Reynolds shear stress in the stack wake is weakened considerably and the positive region disappears. This is also seen throughout the stack wake in the jet-dominated flow ($R = 2.5$, see Figure 6.14). In the jet-dominated flow regime (Figure 6.14), these two separate regions have merged and maintain their strength. In addition, another small region of positive Reynolds shear stress is observed above the stack free end and within the jet wake; it

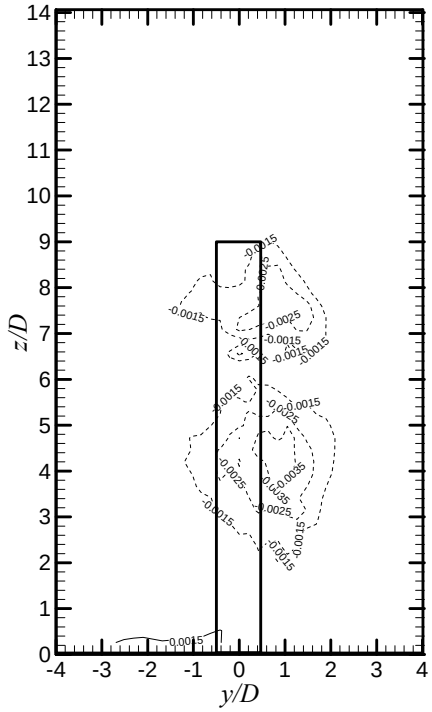

Figure 6.13: The crosswind-dominated flow regime Reynolds shear stress ($-<uw>/\overline{U}^2$) field downstream of the stack at x/D = 10 for R = 1.

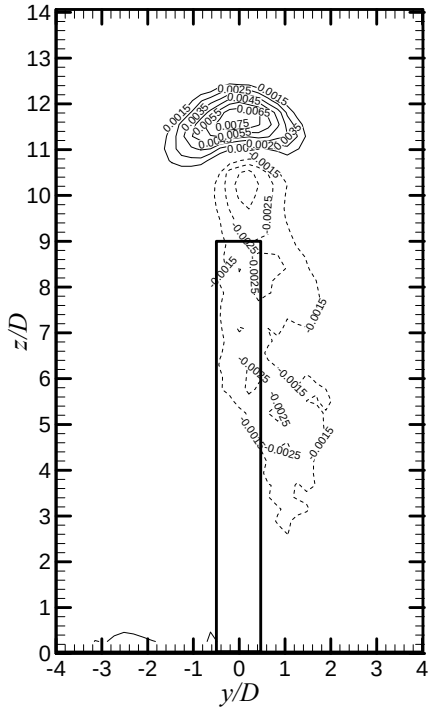

Figure 6.14: The jet-dominated flow regime Reynolds shear stress ($-<uw>/\overline{U}^2$) field downstream of the stack at x/D = 10 for R = 2.5.

coincides with region of low time-averaged streamwise velocity that occurs within the jet wake (see Chapter 5). As R increases and the jet rises further, the size, strength, and vertical position of this region of positive Reynolds shear stress increases, while the region of negative Reynolds shear stress extends upward above the stack's free end (Figure 6.14).

6.4 Triple Correlation

The profiles of $-\langle u^2 w \rangle / U_\infty^3$, which can be interpreted as the transport of $\langle u^2 \rangle$ by the turbulent motion in the wall-normal direction, are shown in Figure 6.15 for different values of R. For R = 0 and 0.5 (corresponding to the downwash flow regime) at x/D = 10 (Figure 6.15(a)), one negative and one positive peak are observed, which occur above and below the mid-span of the stack, respectively. Comparing with the profiles at x/D = 10, the profiles at x/D = 15 (Figure 6.15(b)) are similar but have smaller negative and positive peaks.

For R = 1 (crosswind flow regime) at x/D = 10 (Figure 6.15(a)), a strong positive peak within the ground plane boundary layer region is observed along with two negative peaks, one below the stack free end and the other within the jet wake region. At x/D = 15 (Figure 6.15(b)), a blunt positive region and strong negative peak below the stack free end are observed. The negative peak in the jet wake at x/D = 15 (Figure 6.15(b)) is smaller compared with that at x/D = 10.

For the jet-dominated flow regime, R = 2.5, the profile of $-\langle u^2 w \rangle / U_\infty^3$ at x/D = 10 (Figure 6.15(a)) has alternately two negative and positive peaks. The positive peaks are located within the ground plane boundary layer and near the free end of the stack, while the negative positive peaks are located closer to the free end and within the jet

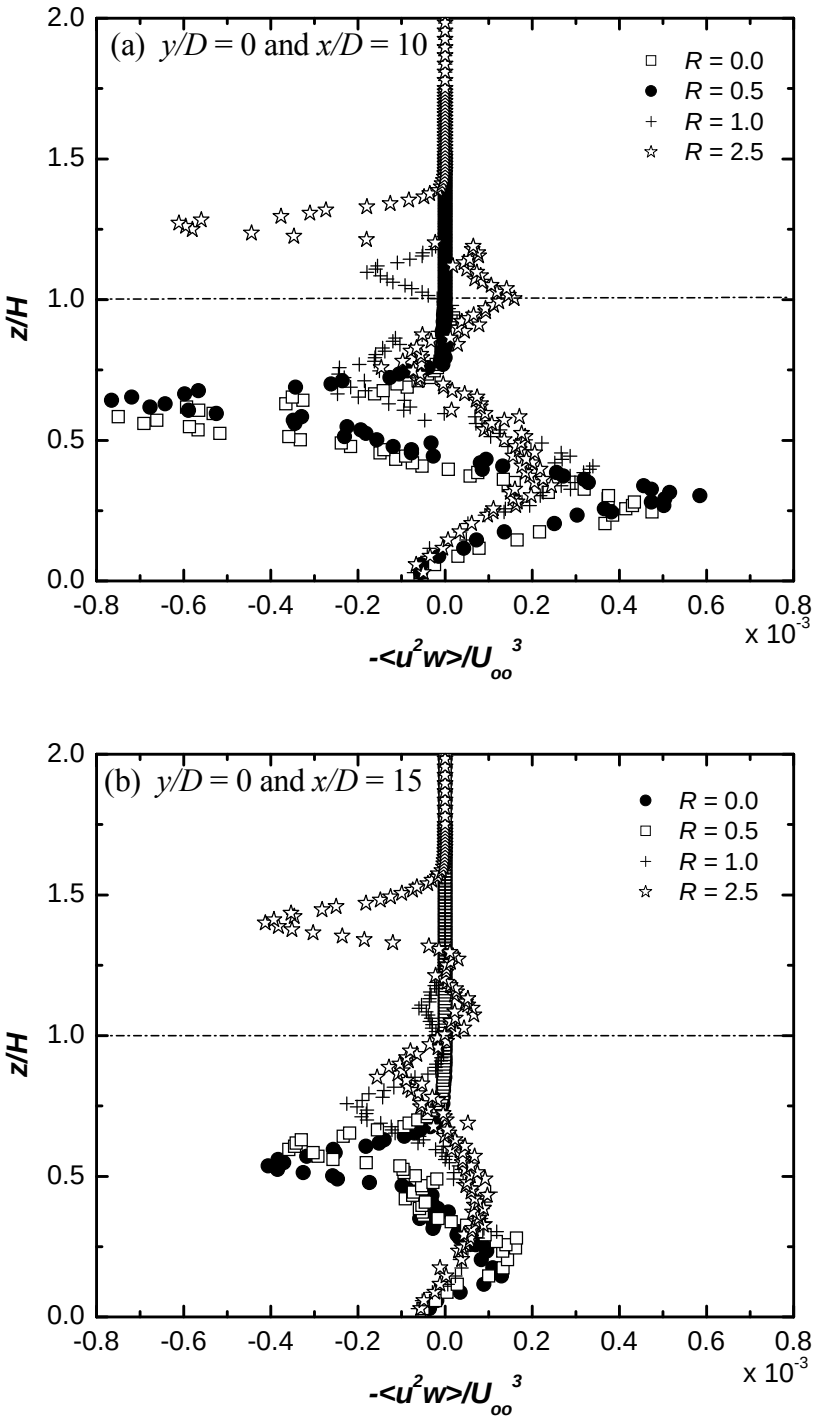

Figure 6.15: The triple correlation ($-\langle u^2 w \rangle / U_\infty^3$) profiles along the wake centreline ($y/D = 0$) at (a) $x/D = 10$ and (b) $x/D = 15$.

wake. The positive and negative values indicate, respectively, an inward and outward transport of u^2 into the stack wake. The location of the negative peak within the jet wake

at x/D = 15 (Figure 6.15(b)) is higher than for x/D = 10. This is due to the increase in the jet wake span (in the wall-normal direction) which is the result of an increase in the jet flow elevation at x/D = 15 compared with the jet profile at x/D = 10.

Figure 6.16 shows the profiles of $-\langle uw^2 \rangle / U_\infty^3$, which represent the transport of the wall-normal Reynolds stress in the streamwise direction for different values of R. For R = 0, two positive peaks and one negative peak are observed for at x/D = 10 (Figure 6.16(a)). The profile at x/D = 15 (Figure 6.16(b)) for R = 0, is almost the same but has smaller absolute peak values compared with that at x/D = 10. When R = 0.5, the profiles are similar to those observed for R = 0. For R = 1, the profiles at x/D = 10 and 15 are entirely positive within the stack and jet wakes with two distinct peaks, one within the stack wake and the other, which is weaker, within the jet wake. In addition, these peaks have a lower values at x/D = 15 than at x/D = 10. Similar to the profiles of R = 1, the profiles for R = 2.5 are entirely positive within the stack wake and have two distinct peaks, one within the stack wake and other within the jet wake, for both values of x/D. These peaks have a lower value at x/D = 15 than at x/D = 10. In addition, a small negative region is observed above the free end of the stack. Like other turbulence profiles, the location of the peak within the jet wake at x/D = 15 (Figure 6.16(b)) is relatively higher (located further above the ground plane) compared to the case of x/D = 10.

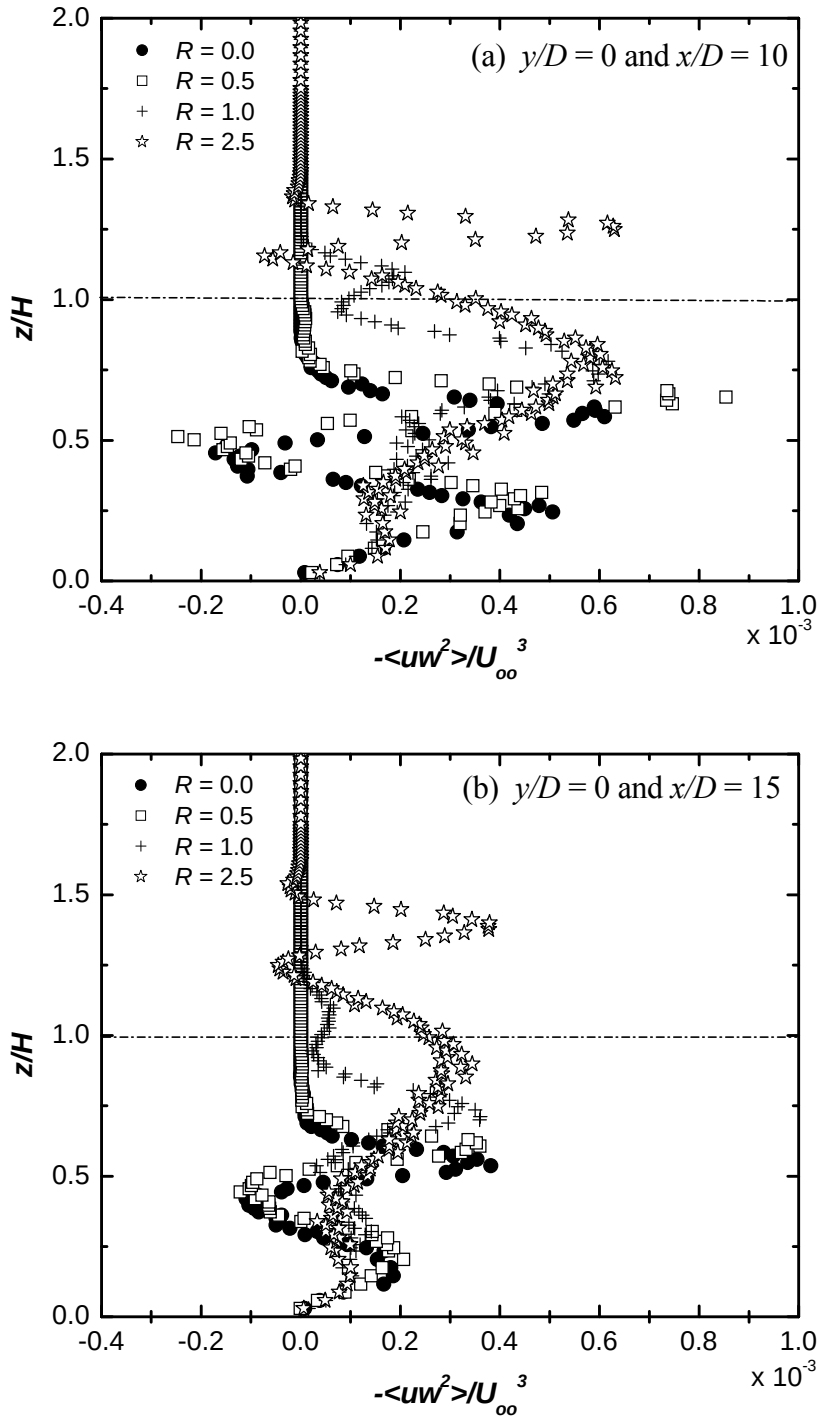

Figure 6.16: The triple correlation ($-\langle uw^2 \rangle / U_\infty^3$) profiles along the wake centreline ($y/D = 0$) at (a) $x/D = 10$ and (b) $x/D = 15$.

6.5 Skewness and Flatness factors

6.5.1 Skewness Factor

The skewness profiles for the streamwise velocity component, S_u, at x/D = 10 and 15, are presented in Figure 6.17 for different values of R. The existence of asymmetry in the fluctuation is indicated by the non-zero value of the skewness factor for all values of R. In general, two regions of elevated peak values, each of opposite sign, are observed within the combined stack and jet wakes. The positive region is observed to occur immediately above the negative region. However, the specific locations and absolute values of these peaks depend on R. The negative region indicates the occurrence of the arrival of low-speed fluid from the ground plane and the stack wake as a result of the upwash flow motion. The positive region indicates the occurrence of the arrival of high-speed fluid due to the downwash flow from the outer region above the combined stack and jet wake.

At x/D = 10 (see Figure 6.17(a)), these two regions are located just below the stack free end for R = 0. The skewness factor is almost independent of the downstream distance (see Figure 6.17(b)), especially within the base region and above the free end of the stack. For R = 0.5, the negative peak region occurs at the stack free end while the positive peak region has almost disappeared. In addition, the numerical value of the negative peak region of S_u is higher for R = 0.5 than R = 0. This may be due to the presence of a weak jet flow, which increases the amount of low-speed fluid in this region and the mixing of the jet fluid with the cross-flow fluid. The almost non-existence of the positive peak region may be due to the strong effect of the cross-flow on the jet flow.

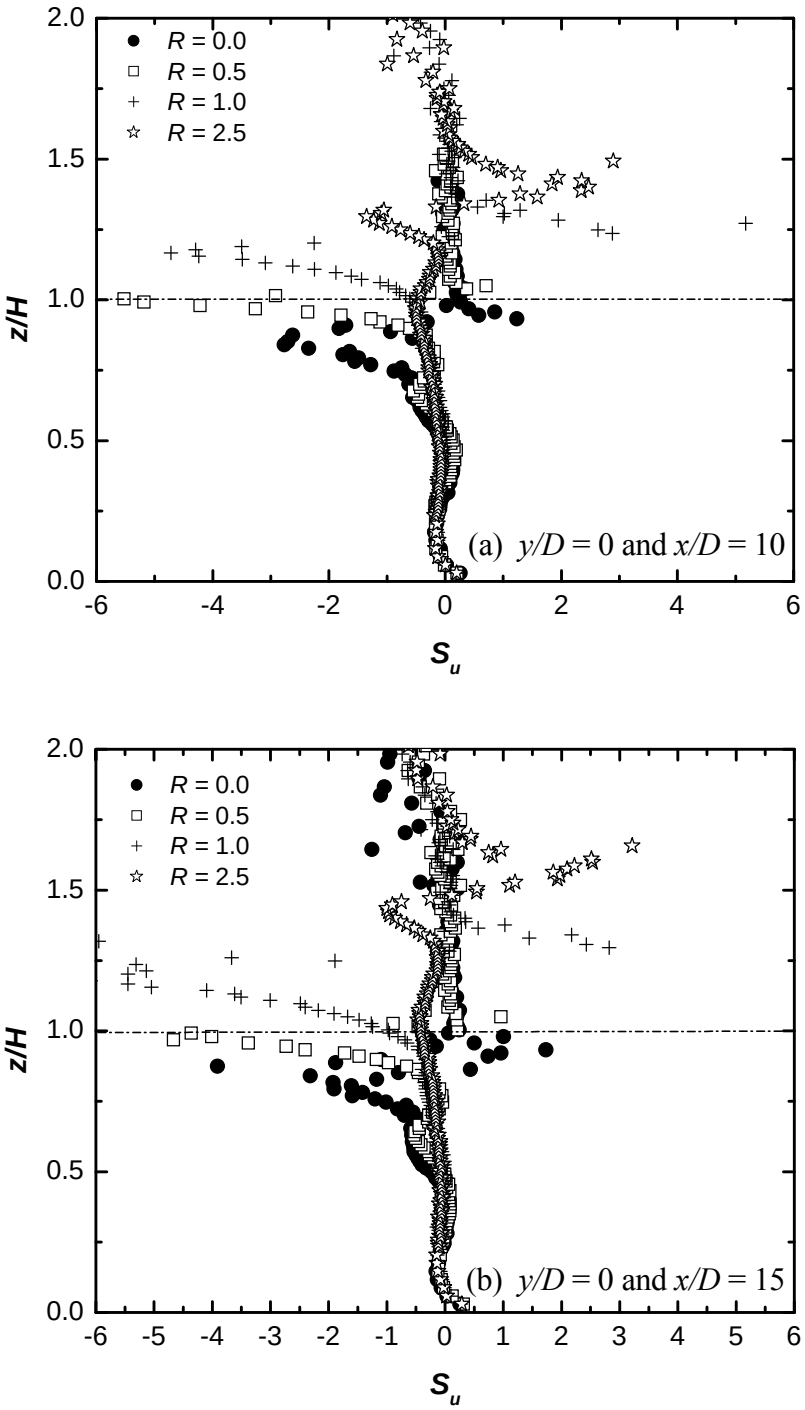

Figure 6.17: The streamwise skewness factor (S_u) profiles along the wake centreline ($y/D = 0$) at (a) $x/D = 10$ and (b) $x/D = 15$.

In the case of $R = 1$, the two peak regions are completely above the stack free end. Compared with $R = 0$ and 0.5, the absolute value of the positive peak is much

higher. This is due to the interaction between the cross-flow and the jet flow. For R = 2.5, within the stack wake, the skewness factor is only slightly less than the corresponding Gaussian probability distribution of zero. Relatively weak negative and strong positive regions are observed within the jet wake and occur at a relatively higher position above the ground plane, when compared with lower values of R. The skewness factor behaviour within the jet wake shows the strong interaction between the cross-flow and the jet flow.

The skewness profiles for the wall-normal velocity component at x/D = 10 and 15 are presented in Figure 6.18. Unlike the streamwise direction component, the wall-normal skewness factor, S_w, has only one positive peak region and the location of this peak strongly depends on the value of R. The increase in S_w as R increases shows the increasing influence of the jet momentum on the wake flow dynamics. Located within

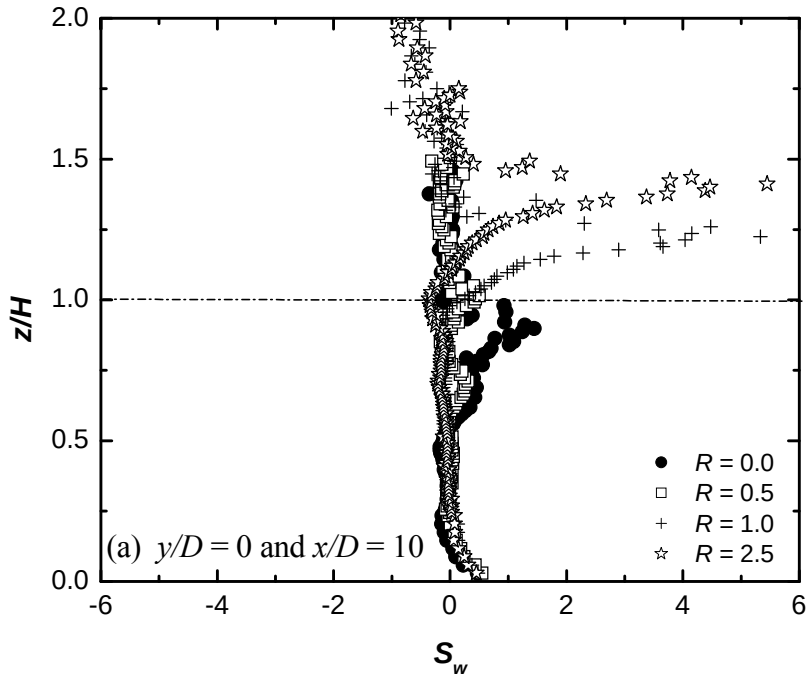

Figure 6.18: The wall-normal skewness factor (S_w) profiles along the wake centreline (y/D = 0) at (a) x/D = 10 and (b) x/D = 15.

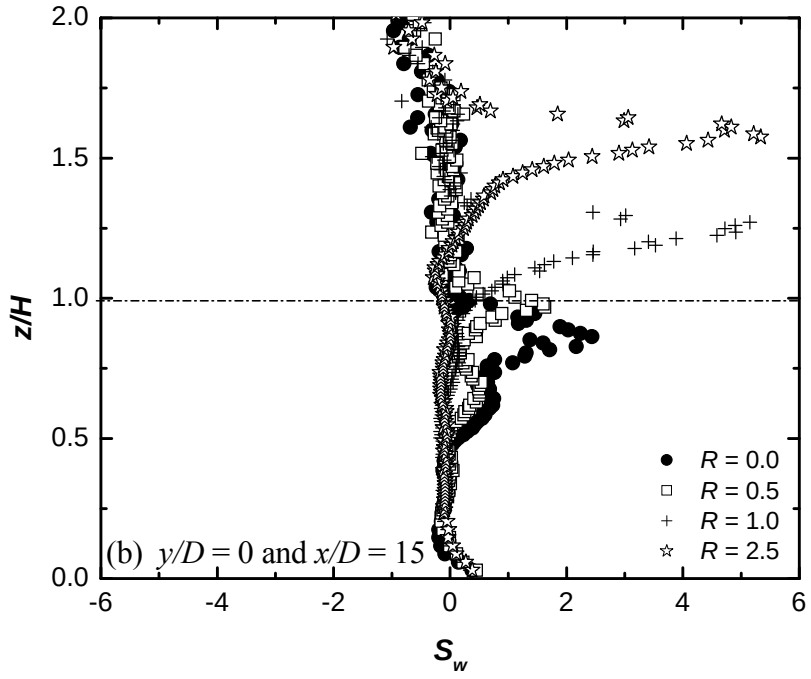

Figure 6.18 continued.

the stack wake for R = 0 (Figure 6.18(a)), the positive peak region gradually moves upward beyond the end of the stack wake and into the jet wake for R = 2.5.

For R = 0, the peak value and the spanwise coverage of S_w increases with downstream distance. The same trends are observed for the downwash flow regime (R = 0.5) but are generally smaller than when R = 0. The may be due to the effect of the weak jet flow that tends to counter the downwash from the free end. In the case of the crosswind-dominated flow regime, R = 1, the profiles at x/D = 10 (Figure 6.18(a)) and 15 (Figure 6.18(b)) are similar, while for R = 2.5 (jet-dominated flow regime), the profile at x/D = 15 is slightly different from the profile at x/D = 10, in that the peak value for R = 2.5 at x/D = 15 occurs at a relatively higher distance above the ground plane than

at x/D = 10. This is because the jet rises higher at x/D = 15 compared with the jet flow at x/D = 10.

6.5.2 Flatness Factor

The streamwise flatness factor, F_u, and the wall-normal flatness factor, F_w, profiles are shown in Figure 6.19 and Figure 6.20, respectively, at x/D = 10 and 15. For all values of R, a region with a flatness factor larger than 3 is observed. The largest values (> 3) of the flatness factor occur in a region mid-way between the negative and positive regions of the streamwise skewness factor (see Figure 6.19). The behaviour of both F_u and F_w indicate that there are strong intermittent turbulent events within the stack and jet wake.

For the downwash flow regime, R = 0, the large values of F_u and F_w which occur near the stack free end may be the result of the tip vortex structures (see e.g., Sumner *et al.*, 2004) and the downwash flow from the stack free end that gives rise to the strong intermittent behaviour. A similar behaviour is noted for R = 0.5, except that the numerical values of F_u and F_w are slightly greater near the stack free end compared with R = 0. This is due to the interaction between the cross-flow and weak jet flow. In the case of R = 1 (crosswind-dominated flow regime) and 2.5 (jet-dominated flow regime), this intermittency now occurs in the jet wake and is associated with the jet flow structures and mixing between the cross-flow and jet flow. The relative location of this region above the ground plane increases with R.

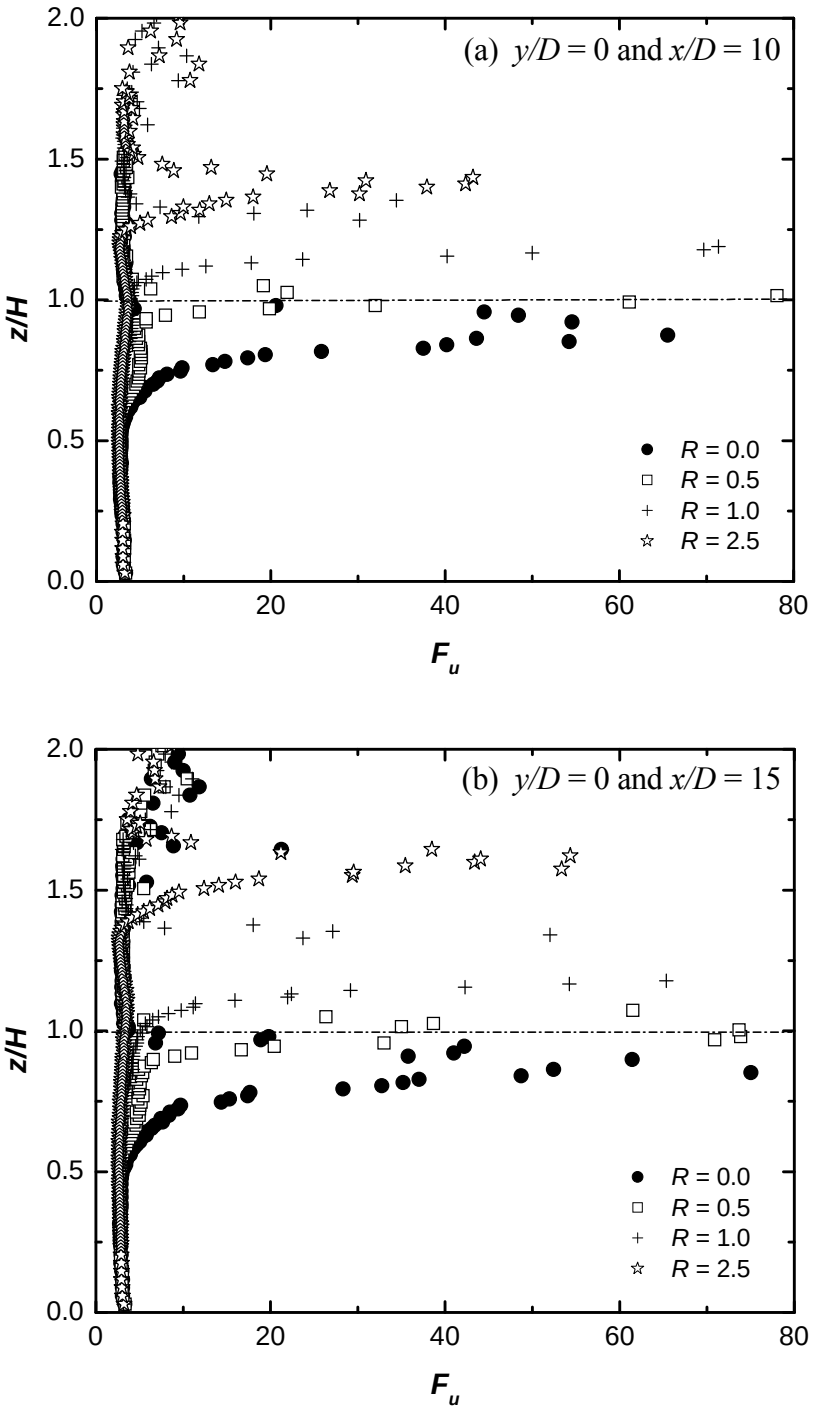

Figure 6.19: The streamwise flatness factor (F_u) profiles along the wake centreline ($y/D = 0$) at (a) $x/D = 10$ and (b) $x/D = 15$.

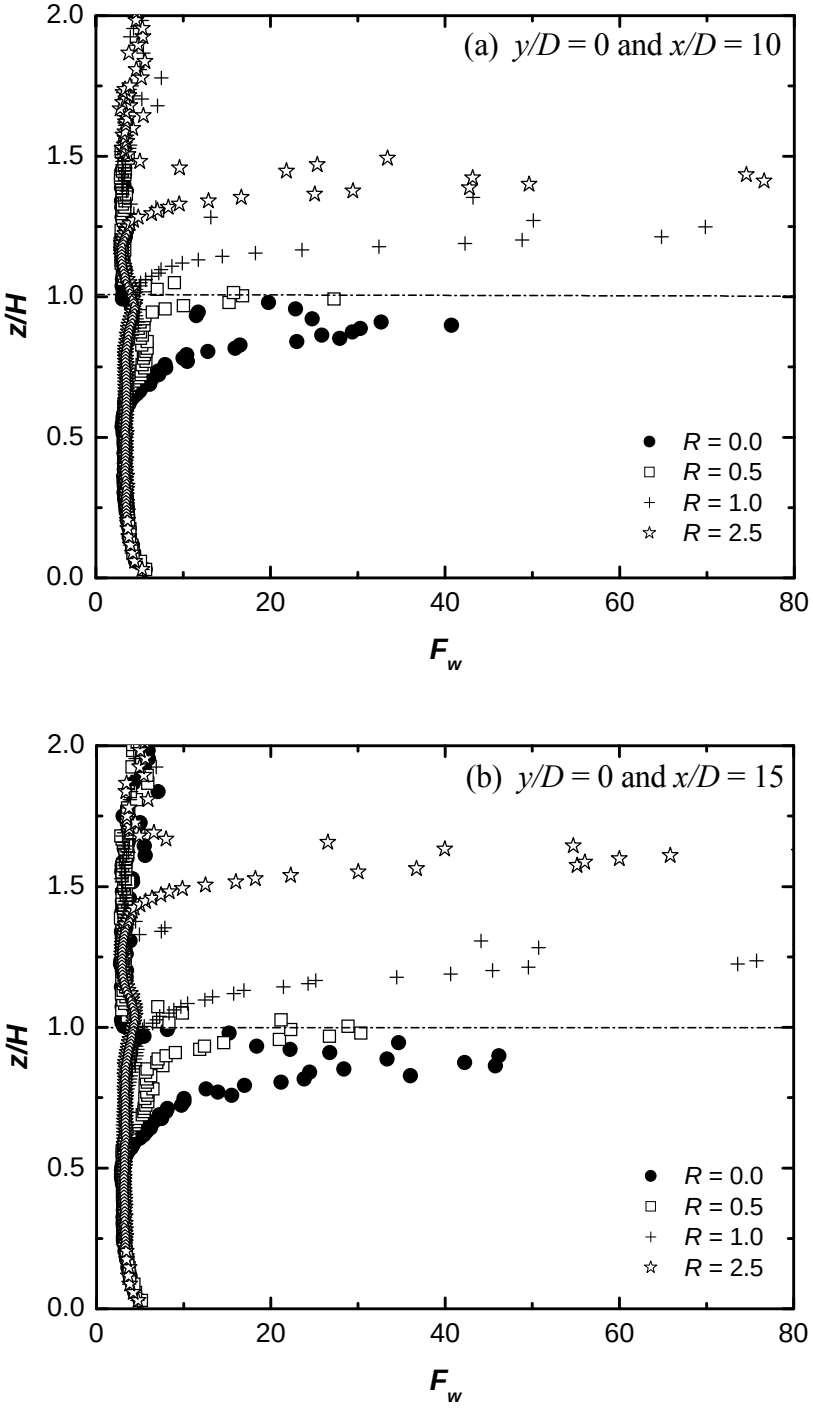

Figure 6.20: The wall-normal flatness factor (F_w) profiles along the wake centreline ($y/D = 0$) at (a) $x/D = 10$ and (b) $x/D = 15$.

6.6 Summary

In this Chapter, the effect of the velocity ratio on the turbulence field in the wake of a short stack was presented. Complex changes were observed in the streamwise and wall-normal directions within the stack and jet wakes. In general, the streamwise and wall-normal turbulence intensity fields are characterized by two regions of elevated turbulence, that coincide with regions of low streamwise time-averaged velocity in the stack and jet wakes. The Reynolds shear stress and the triple correlation were strongly influenced by the local velocity gradient, especially for lower values of R within the stack wake and within the jet wake for higher values of R. The skewness and flatness factors indicated a strong deviation from a Gaussian distribution, which is evidence of the complexity of the flow.

CHAPTER 7

VORTEX SHEDDING FROM A STACK

7.1 Introduction

In this chapter, the effect of the velocity ratio on the characteristics of the vortex shedding from the stack and the vortex formation length are examined, and their relationship with the time-averaged and turbulent parameters is presented and discussed. The measurements were made with a single-sensor hot-wire probe (Section 3.5). For the vortex shedding measurements, the probe was located at a fixed streamwise and cross-stream position, $x/D = 3$ and $y/D = 1.5$, respectively, and varied in the wall-normal direction, z/H. In the case of the vortex formation length measurements, the probe was fixed at $y/D = 0$ and $z/H = 0.5$, and the probe position was varied along the streamwise direction, x/D.

It was earlier shown (in Chapter 5 and Chapter 6) that the velocity ratio has a pronounced effect on the streamwise vortex structures and the turbulence characteristics within both the stack wake and jet wake. In particular, it was shown that the tip vortex structures reduce, while the jet wake vortex structures increase, in both size and strength as the velocity ratio increases from 0 to 3, with a slight reduction in the peak vorticity value when R is increased from 2.5 to 3. The significance of the behaviour of the

streamwise vortices is that they are basically a representation of the Kármán vortices and therefore, changes in streamwise vortex behaviour indicate potential changes in Kármán vortex shedding behaviour.

7.2 Strouhal Number and Vortex Formation Length at Mid-Height (z/H = 0.5)

The Strouhal number data measured in the wake at the mid-height of the stack (corresponding to z/H = 0.5) are summarized in Table 7.1 and Figure 7.1 for various values of R. The result for no flow from the stack (R = 0) compares favourably with the finite circular cylinder result of Sumner *et al*. (2004), which also involved a thick boundary layer on the ground plane (δ/H = 0.3) despite the differences in the Reynolds number between these studies.. The Strouhal number measured by Okamoto and Yagita (1973) is higher, but this was for the case of a very thin flat-plate boundary layer (δ/H = 0.02). This is due to the fact that the thicker boundary layer interferes with and weakens the Kármán vortex shedding from the stack. The results for R = 1.5 and 3 compare favourably with the data from Eiff and Keffer (1999).

The trend in the Strouhal number data at mid-height shows a gradual increase with velocity ratio, with the Strouhal number approaching the value of an "infinite" cylinder (St ≈ 0.2) with an increase in R. There is a more abrupt increase in St at R ≈ 0.7, which could indicate a change in the stack wake flow regime. The overall effect of the jet-to-cross-flow velocity ratio is to make the stack behave similar to a finite circular cylinder of higher aspect ratio. For sufficiently high aspect ratio, the finite circular cylinder attains the Strouhal number value of an infinite cylinder and the St number variation along the height assumes a cellular structure (Farivar, 1981; Lee and Wang,

Table 7.1: Selected Strouhal number data measured at mid-height ($z/H = 0.5$) for a finite circular cylinder or stack of AR = 9 (unless otherwise indicated).

	Re	δ/H	δ/D	St
Okamoto and Yagita (1973), $R = 0$	1.3×10^4	0.02	0.15	0.18
Sumner *et al*. (2004), $R = 0$	6.0×10^4	0.3	2.6	0.16
$R = 0$	2.3×10^4	0.5	4.6	0.167
$R = 0.5$	2.3×10^4	0.5	4.6	0.169
$R = 0.6$	2.3×10^4	0.5	4.6	0.176
$R = 0.7$	2.3×10^4	0.5	4.6	0.185
$R = 1$	2.3×10^4	0.5	4.6	0.185
$R = 1.5$	2.3×10^4	0.5	4.6	0.190
Eiff and Keffer (1999), $R = 1.5$, $AR = 8$	4.0×10^4			0.190
$R = 2$	2.3×10^4	0.5	4.6	0.193
$R = 2.5$	2.3×10^4	0.5	4.6	0.195
$R = 3$	2.3×10^4	0.5	4.6	0.192
Eiff and Keffer (1999), $R = 3$, $AR = 8$	2.2×10^4			0.191
Eiff and Keffer (1999), $R = 6$, $AR = 8$	1.0×10^4			0.203

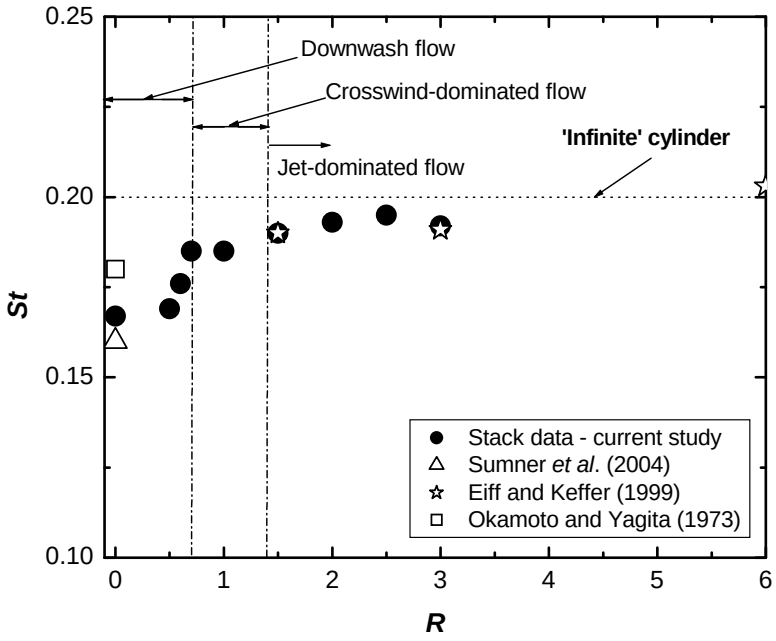

Figure 7.1: The Strouhal number at the stack mid-height.

1987). A similar result was noted by Eiff *et al.* (1995). The data in Table 7.1 and Figure 7.1 also suggest three different types of behaviour for the Strouhal number, with a

common low value of St obtained for R = 0, 0.5, and 0.6; an elevated intermediate value of St obtained for R = 0.7 and 1; and a higher common value of St for R = 1.5, 2, 2.5, and 3. From this Figure and Table 7.1, it is seen that the Strouhal number for R = 3 (St = 0.192) is slightly lower than when R = 2.5 (St = 0.195), but is similar to the data of Eiff and Keffer (1999) for R = 3 and AR = 8 (St = 0.191). These small differences may be partially attributed to the measurement uncertainty of the St data, which is estimated to be about ± 1%.

Figure 7.2 shows the vortex formation length, L_f, of the stack measured at mid-height (z/H = 0.5) for different jet-to-cross-flow velocity ratios, R = 0 to 3. As mentioned in Section 3.10, the vortex formation length was defined as the location of the local maximum value of the streamwise turbulence intensity on the wake centerline. It represents the distance from the stack where the separated shear layers eventually detached from the stack. For an "infinite" circular cylinder, the vortex formation length at $Re_D = 2.7\times10^4$ ranges from L_f/D = 1.3 to 1.5, depending on the freestream turbulence intensity (Norberg, 1986; Noca *et al*., 1998). Due to the downwash flow from the free end of the cylinder, the vortex formation length at mid-height for a finite circular cylinder is greater than that of an "infinite" cylinder and is a function of AR and δ/H. In this study, a value of L_f/D = 3.6 is obtained for a stack of AR = 9 and δ/H = 0.5, while L_f/D = 4.4 was obtained by Sumner *et al*. (2004) for δ/H = 0.3, and L_f/D = 3.8 for AR = 10 and δ/H = 0.01 by Park and Lee (2000). As shown in Figure 7.2, the vortex formation length of the stack decreases as the jet-to-cross-flow velocity ratio increases, and approaches the value for the "infinite" cylinder at high velocity ratios. The reduction in vortex formation length with increasing R is consistent with the behaviour

of the Strouhal number at mid-height, as described above and shown in Figure 7.1, where the jet acts as a bluff body and increases the effective aspect ratio of the stack. This is also related to the recirculation region behind the stack that reduces as *R* increases (see Chapter 5).

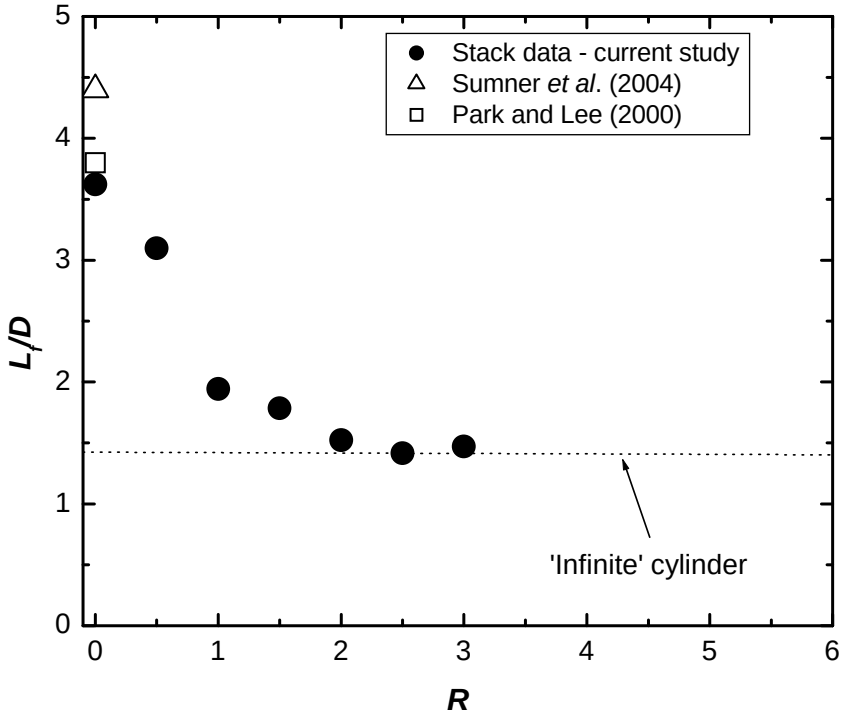

Figure 7.2: The vortex formation length at the stack mid-height.

These two figures (Figures 7.1 and 7.2) show that the Strouhal number and the vortex formation length are inversely related (Gerrard, 1966); as *St* increases, L_f/D decreases. Farivar (1981) argued that the higher vortex formation length and the lower *St* observed for the finite cylinder compared with the infinite cylinder is due to the effect of the downwash flow from the cylinder's free end, which prevents the interactions between the Kármán vortices from either side of the cylinder. The downwash flow also suppressed Kármán vortex shedding and gives a lower value of *St* for the finite circular

cylinder and this value reduces as the aspect ratio of the cylinder reduces. For a higher aspect ratio cylinder, the upwash flow from the ground plane also influences the Kármán vortex shedding frequency. It was shown in the Chapter 5 that as the value of R increases the recirculation region within the stack wake decreases (Section 5.3).

7.3 Strouhal Number Variations with Height

The variation of the Strouhal number along the height of the stack, z/H, for various jet-to-cross-flow velocity ratios, R, is shown in Figure 7.3. Three different types of Strouhal number patterns were observed. The changes in vortex shedding characteristics are an essential issue to be considered when designing a stack due to the likelihood of flow-induced vibration that could damage the structure. At a low jet-to-cross-flow velocity ratio of $R = 0.5$ (Figure 7.3(a)), the Strouhal number is nearly the same value as that for no jet flow ($R = 0$, or the finite cylinder case). Along the height of the stack, the same Strouhal number value is measured, and no cellular variation of St is observed. Similar behaviour is observed for $R = 0.6$, although the magnitude of the Strouhal number is slightly higher than for $R \leq 0.5$. This uniform shedding along the height corresponds to "one-cell antisymmetric shedding" behaviour (Lee, 1997) and is consistent with the finite-cylinder results for AR = 9 obtained by Sumner *et al.* (2004). The results from the present study, where $\delta/H = 0.5$, further support the view that a larger value of δ/H suppresses the cellular variation of St along the height for small aspect ratios (Sakamoto and Oiwake, 1984). This range of jet-to-cross-flow velocity ratio, $R < 0.7$, coincides with the downwash flow regime identified by Huang and Hsieh (2002, 2003) and discussed in Chapter 5 of this thesis.

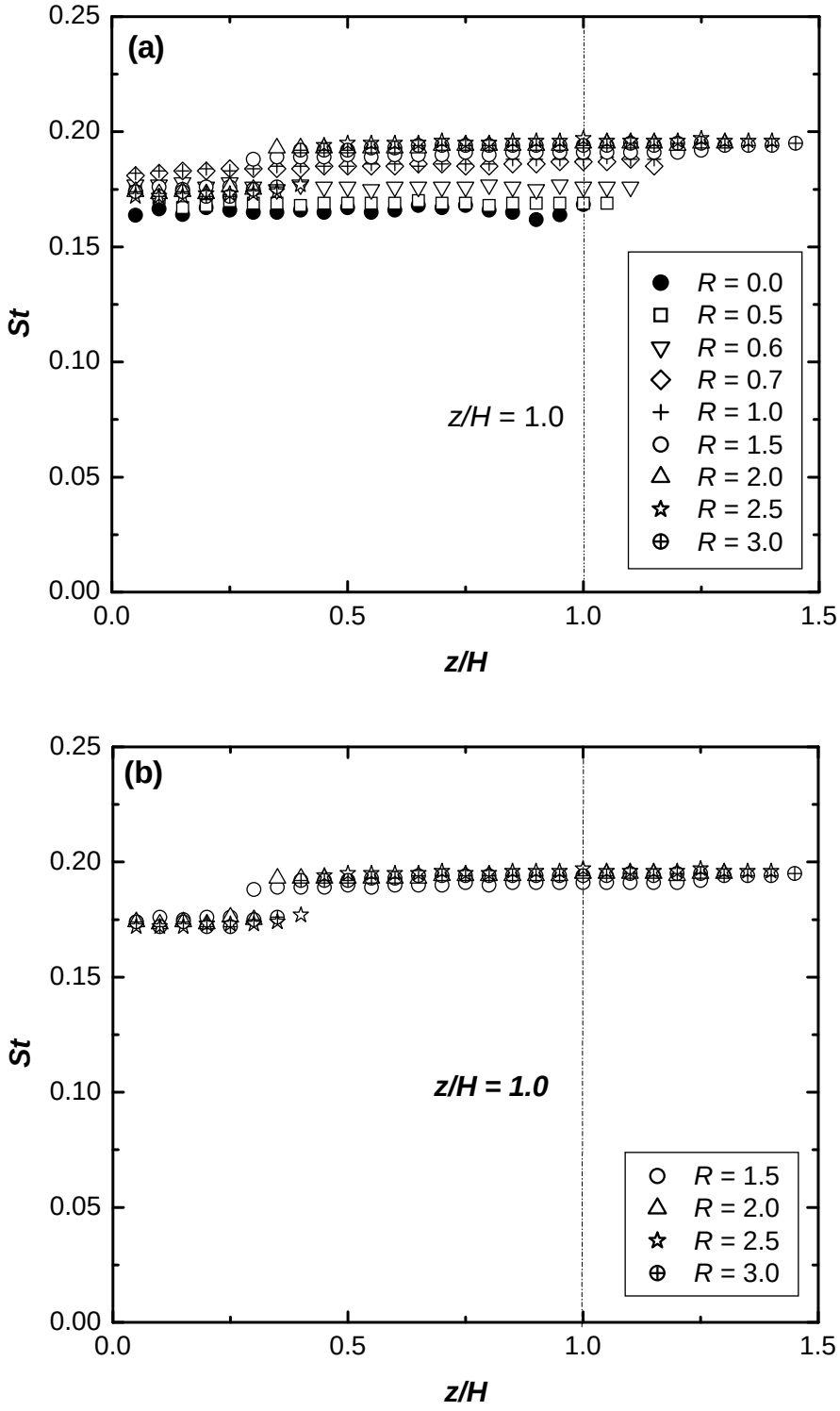

Figure 7.3: Strouhal number measured $y/D = 1.5$, $x/D = 3$ and along the height of the stack for (a) all the flow regimes, and (b) the jet-dominated flow regime.

For R = 0.7 and 1 (Figure 7.3(a)), the magnitude of the Strouhal number is greater than for R = 0, 0.5, and 0.6, but remains constant along the stack height. There continues to be no cellular variation of the Strouhal number along the stack height or reduction in the Strouhal number near the free end of the stack. For these values of R and also for R = 0.5 and 0.6, however, the vortex shedding is now detected above the end of the stack (i.e., for $z/H > 1$). This range of jet-to-cross-flow velocity ratio, $0.7 \leq R < 1.5$, coincides with the crosswind-dominated flow regime identified by Huang and Hsieh (2002, 2003) and in Chapter 5 of this thesis.

For $R \geq 1.5$ (Figure 7.3(a,b)), which falls within the jet-dominated flow regime (see Chapter 5), there is another change in the behaviour of the Strouhal number. A cellular structure is now observed, with a discontinuity or 'jump' in the Strouhal number along the height of the stack within the stack wake to give two cells of constant Strouhal number. Moving away from the ground plane, the 'jump' from a lower Strouhal number value near the ground plane to higher Strouhal number (e.g., from St = 0.176 to 0.193 for R = 2) occurs inside the ground plane boundary layer, between z/H = 0.2 and 0.5 depending on the value of R. This observed jump in the Strouhal number may be due to the presence of a longitudinal vortex in the uniform flow (Maull and Young, 1973), the change in velocity gradient within and outside the boundary layer thickness, as well as the reduced influence of downwash (with increasing R) on the separated shear layers from the stack. Within the jet-dominated flow regime and for each particular value of R, the Strouhal number is relatively constant for each cell. The higher Strouhal number value is measured along most of the stack height outside the boundary layer and into the jet wake. Its value is similar to that reported by Eiff and Keffer (1999) for a stack of AR = 8 (see Table 7.1). For R = 1.5, the higher value of the Strouhal number is slightly

reduced in magnitude than for R = 2 to 3, whereas the Strouhal number data for R = 2 and 2.5 overlap one another. Again, there is slight reduction in the Strouhal number data for R = 3 compared when R = 2.5. It is noted that R = 1.5 coincides with the transitional flow regime and R = 2 to 3 coincide with the transitional and jet-dominated flow regimes identified by Huang and Hsieh (2002, 2003).

For a finite cylinder, a two-cell structure would be expected for AR = 7 to 12 for a thin plane wall boundary layer (Lee, 1997). In a uniform flow, Maull and Young (1973) observed a similar cellular structure in the wake of an infinite-semi elliptic nose bluff body, but the higher Strouhal number was at the base region of the bluff body, unlike in the present study. However, for the same model immersed in a shear flow, Maull and Young (1973) found a different cellular frequency; with the lower Strouhal number cells occurring closer to the ground plane, similar to the result of the present work. For a circular cylinder of AR = 8, two cells of different Strouhal number were observed by Mair and Stansby (1975) with the lower value of St occurring closer to the ground plane similar to the observation of the present study. Fox and Apelt (1993(a)) made a similar observation for finite cylinders of AR < 13, subjected to a uniform flow.

The presence of a Strouhal number above the stack's free end (i.e., for z/H > 1) indicates that vortex shedding activity is also occurring in the jet wake. Since the value of the Strouhal number within the stack and jet wakes is the same (for a particular value of R), it suggests that similar vortices are being shed in both wakes. This result is in agreement with Moussa *et al.* (1977), who reported that when vortex shedding occurs from the jet, it is controlled by Kármán vortex shedding from the sides of the stack. It is also in an agreement with Eiff *et al.* (1995) and Eiff and Keffer (1999), who reported "lock-in" of the vortex structures between the stack and jet wakes when 0.63 < d/D <

0.83; the diameter ratio in the present study is $d/D = 0.67$, which falls within this range. But, for $0.42 < d/D < 0.63$, they did not observe this lock-in phenomenon.

7.4 Power Spectra

The individual power spectra of the streamwise velocity fluctuations are presented in Figures 7.4 to 7.8. Each spectrum represents 250 averages and the vertical logarithmic scale is arbitrary, but the same scale and off-set are used for each spectrum throughout these figures. It should be noted that a small shedding frequency ($St = 0.028$) is observed above the stack wake for $R < 1$, and above the jet wake for $R > 1$. This reason for the presence this frequency and its significant are not know. At $R = 0$ (Figure 7.4(a)), when there is no jet exiting the stack, considerable variation in the shape and strength of the vortex shedding peak along the height of the stack is observed. The behaviour of the vortex shedding peak at $R = 0$ is similar to the finite-cylinder behaviour observed by Okamoto and Yagita (1973), Okamoto and Sunabashiri (1992), and Sumner *et al.* (2004). Near the base of the stack and within the ground plane boundary layer, from $z/H = 0.05$ to about $z/H = 0.25$, weak and broad-banded peaks are observed, indicating a weak but still dominant vortex shedding frequency. Within the vicinity of the mid-height of the stack, from about $z/H = 0.5$ to $z/H = 0.75$, the vortex shedding frequency peak becomes stronger and sharper, indicating stronger and more dominant vortex shedding behaviour. However, at about $z/H = 0.85$ to 0.95, near the free end of the stack, weaker and more broad-banded peaks become evident. At the free end of the stack, the absence of a prominent peak shows that vortex shedding can no longer be detected.

Similar behaviour is observed for $R = 0.5$ (Figure 7.4(b)), within the downwash flow regime, but a stronger vortex shedding peak is now found over a wider range of

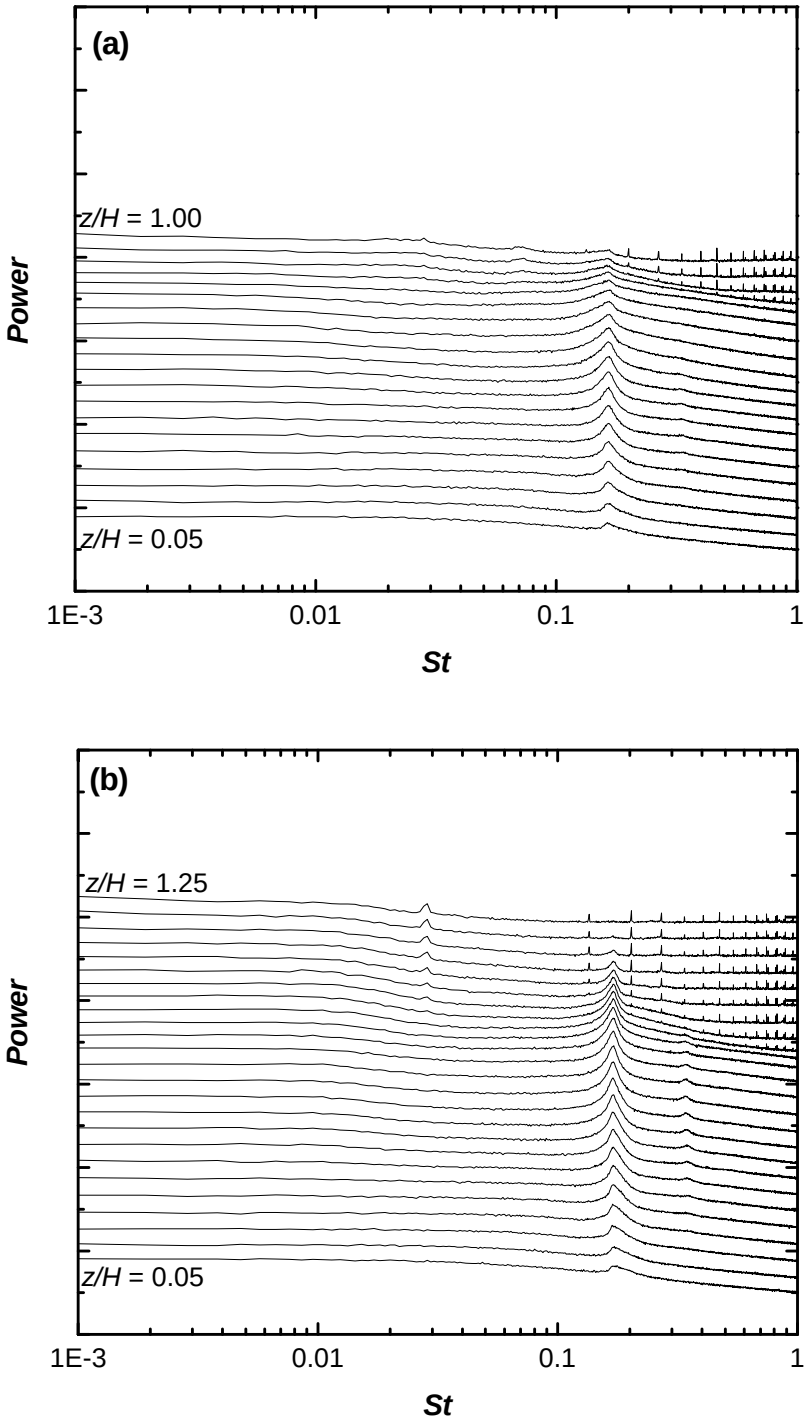

Figure 7.4: Power spectra along the height of the stack for the downwash flow regime, measured at $x/D = 3$ and $y/D = 1.5$, starting at $z/H = 0.05$, at an interval of $\Delta z/H = 0.05$: (a) $R = 0$; and (b) $R = 0.5$.

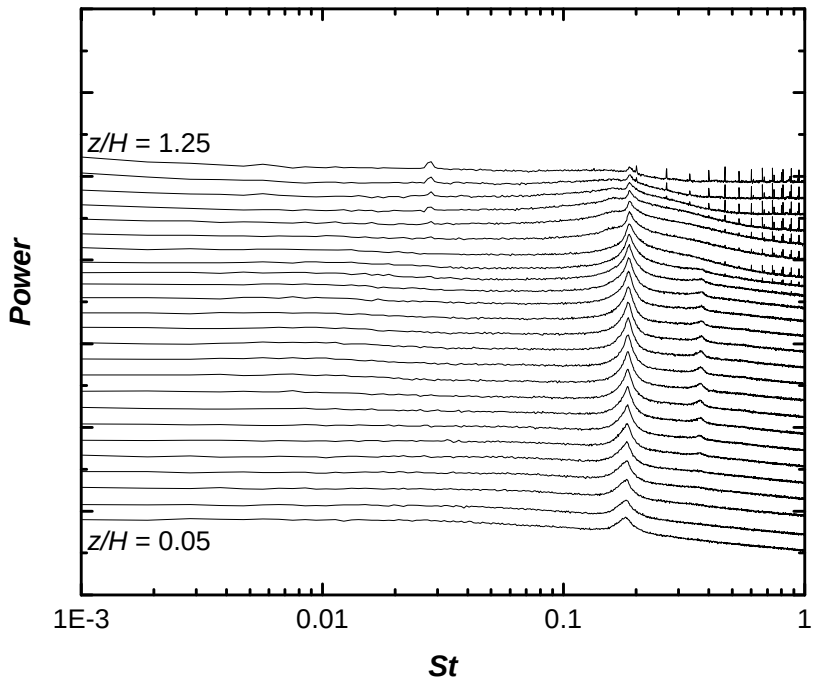

Figure 7.5: Power spectra along the height of the stack in the crosswind-dominated flow regime for $R = 1$. Measurements are at the same location as in Figure 7.4.

stack height including the top of the stack ($z/H = 1$). The results in Figure 7.4(b) show that the presence of the stack jet intensifies vortex shedding from a finite cylinder and makes it more uniform along the cylinder height.

The power spectra for $R = 1$ (Figure 7.5) are representative of the crosswind-dominated flow regime. The behaviour of the power spectra is similar to that of $R = 0.5$, but the peak occurs at a slightly higher Strouhal number. A weak vortex shedding peak can be identified above the end of the stack (it is still discernible at $z/H = 1.2$).

For $R = 1.5$ (Figure 7.6(a)), the power spectra close to the base of the stack ($z/H = 0.05$ to 0.15) have a short broad-banded peak. Moving upward from the base, but still within the flat-plate boundary layer, the 'jump' phenomenon noticed in the Strouhal number data in Figure 7.4 is seen instead as a gradual change in dominance between two closely spaced peaks (see Figure 7.7) which is similar to the observation of Maull and

Young (1973). The dual peaks are seen in the power spectra for $z/H \approx 0.2$ to 0.5. In the middle of the stack height and outside the flat-plate boundary layer, $z/H = 0.5$ to 0.85

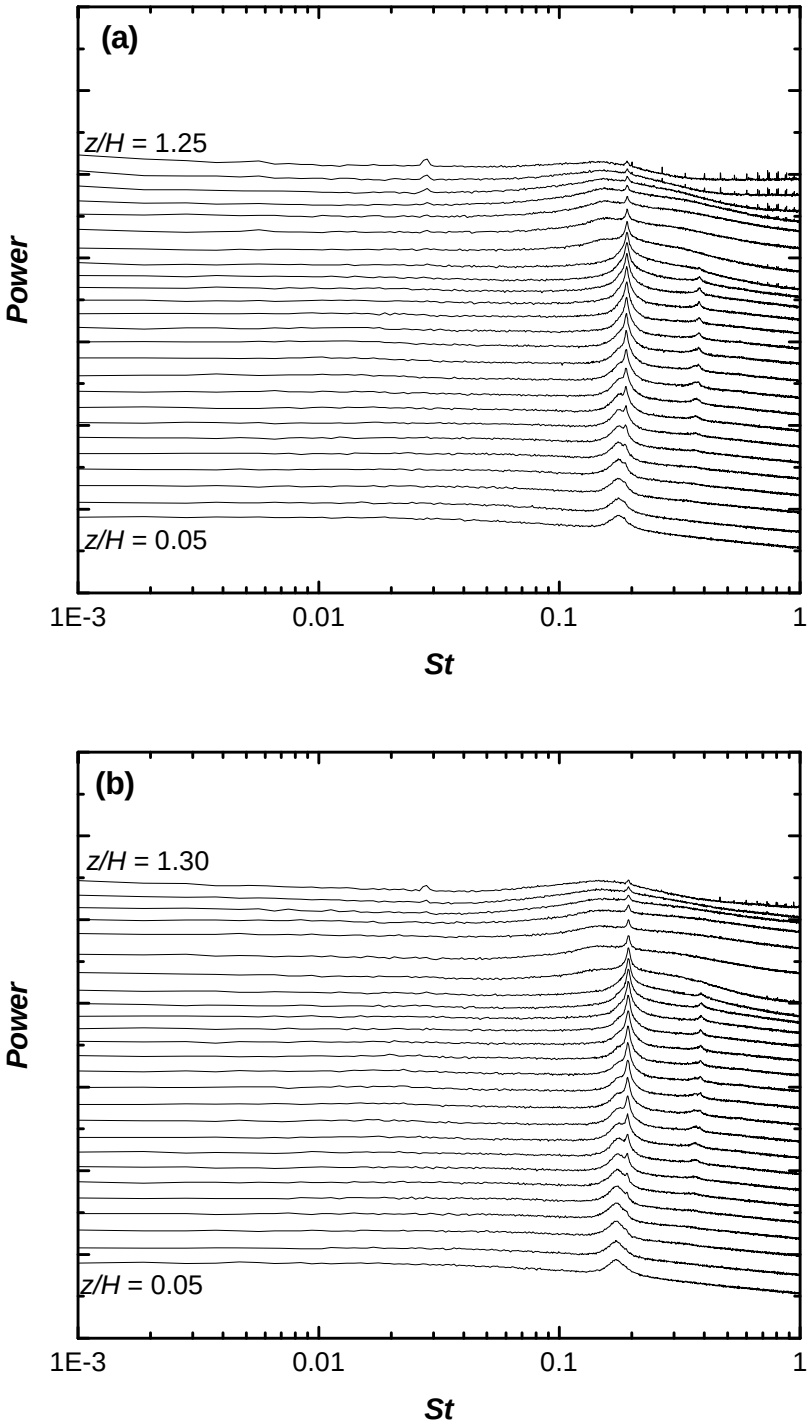

Figure 7.6: The power spectra along the height of the stack in the jet-dominated flow regime for (a) $R = 1.5$, (b) $R = 2$, (c) $R = 2.5$ and (d) $R = 3$. Measurements are at the same location as in Figure 7.4.

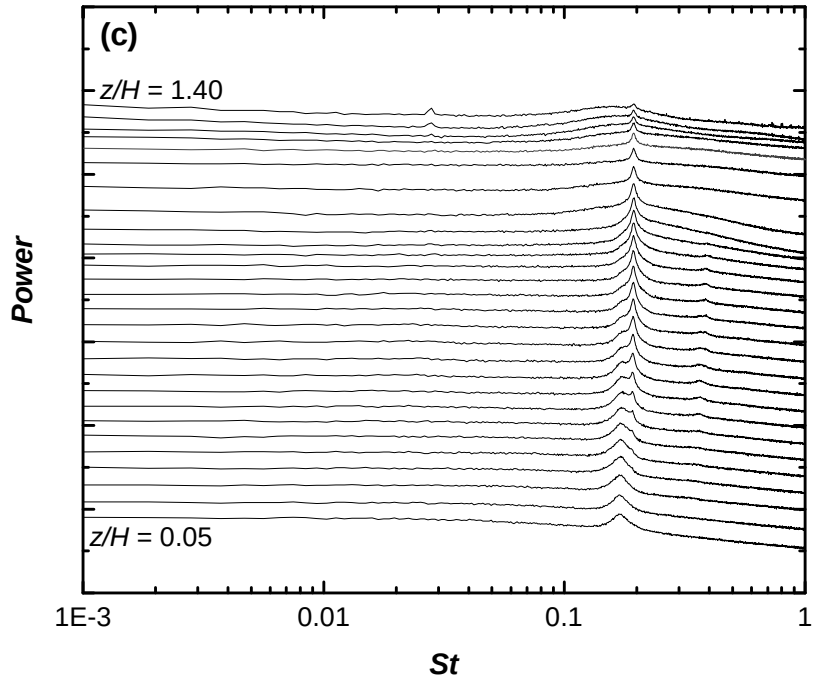

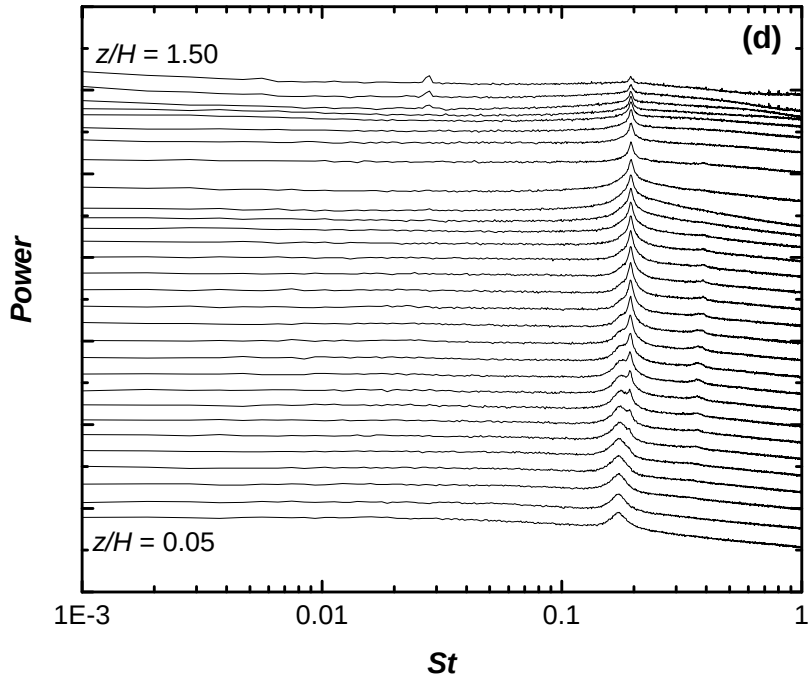

Figure 7.6 continued.

(Figure 7.6(a)), a strong, sharp vortex shedding peak is observed, signifying that strong vortex shedding occurs in this region. Above the free end of the stack and into the jet wake region, z/H = 1 to 1.5, the vortex shedding peak continues to be observed, but the peak strength is much lower.

For R = 2 to 3 (Figure 7.6(c-d)), the behaviour of the power spectra is similar to the case of R = 1.5 (Figure 7.6a), with the double-peak behaviour within the flat-plate boundary layer, and detection of a weakened vortex shedding signal in the jet wake region above the free end of the stack.

In order to further investigate the discontinuity observed in the Strouhal number for the jet-dominated flow regime, another set of measurements was taken along the stack height in the vicinity of the discontinuity. The range of values of z/H used in these measurements depends on the value of R, but a smaller interval of $\Delta(z/H) = 0.01$ was

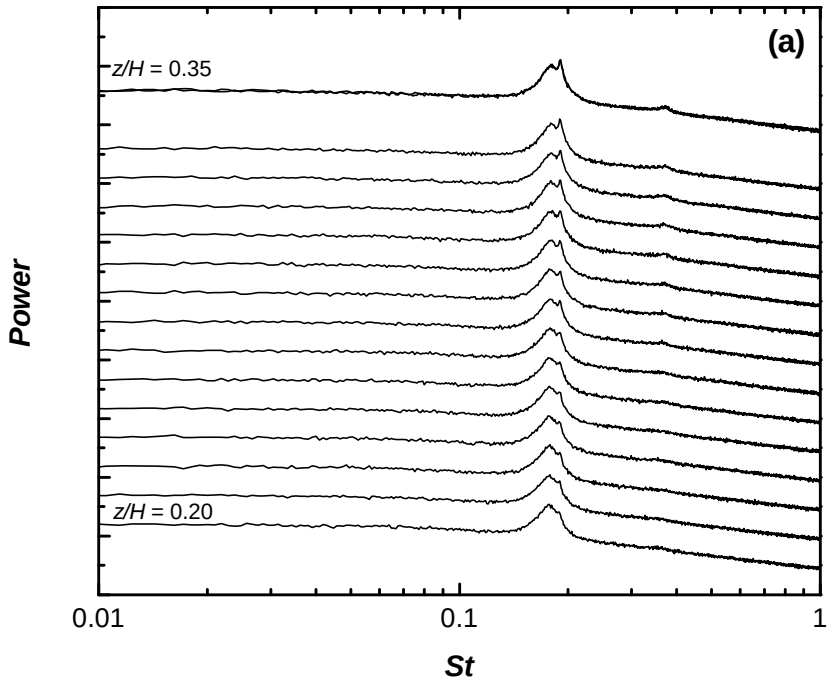

Figure 7.7: The power spectra in the jet-dominated flow regime for within the "jump" in Strouhal number along the stack height: (a) R = 1.5, (b) R = 2, (c) R = 2.5 and (d) R = 3.

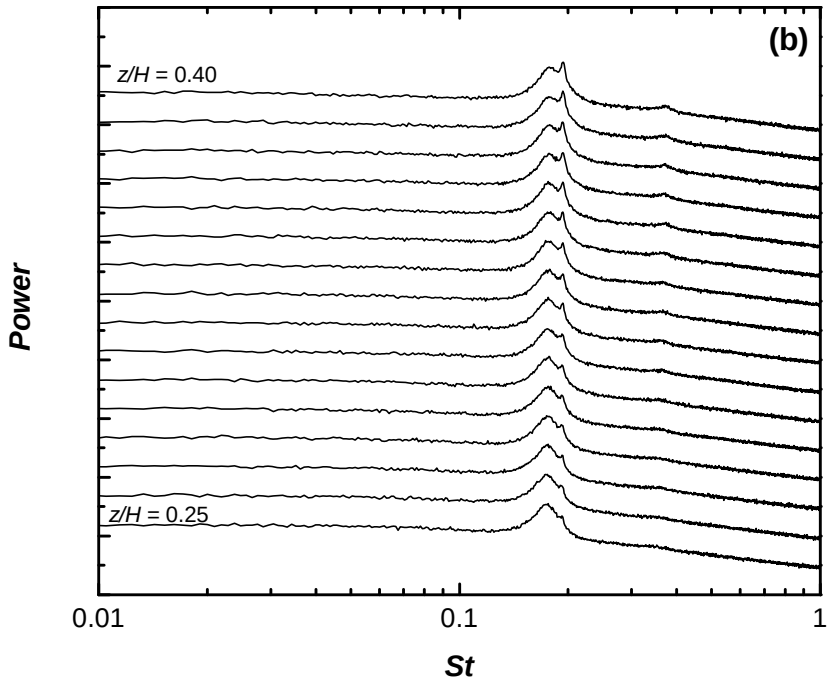

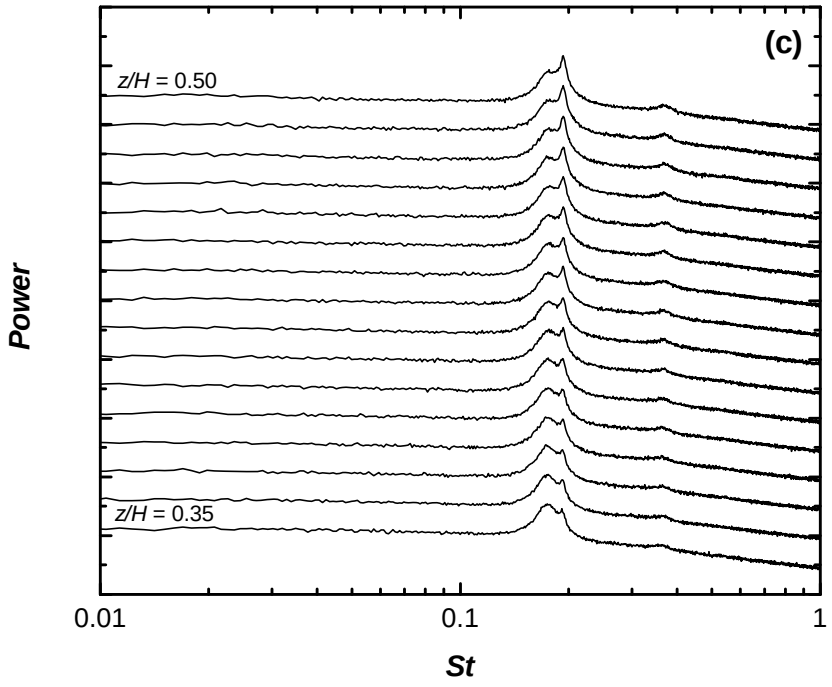

Figure 7.7 continued.

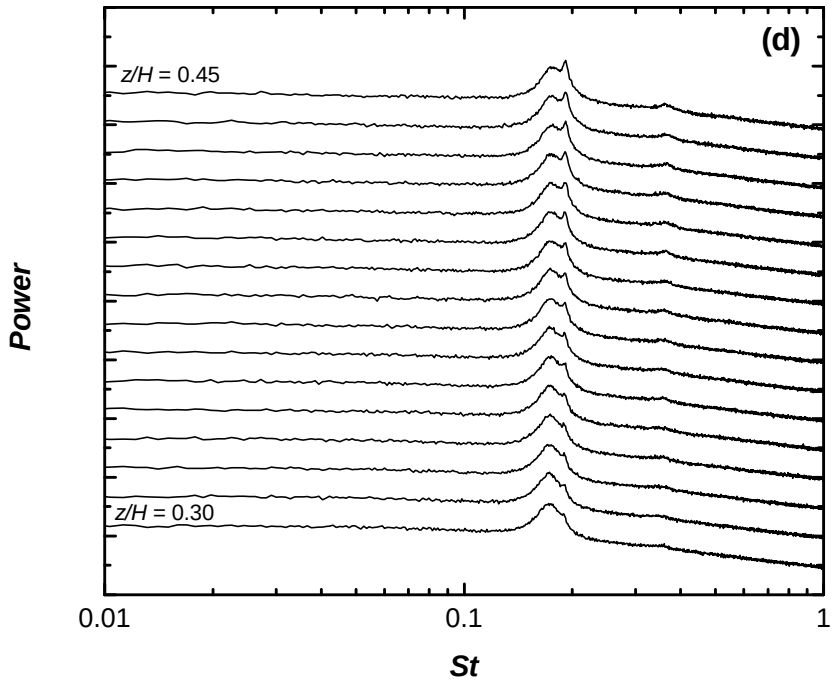

Figure 7.7 continued.

used. The power spectra for $R \geq 1.5$ showing the double-peak behaviour is presented in Figure 7.7. It is seen that the two peaks are very close together, with a sharp high-frequency peak and a wider low-frequency peak being observed. The lower-frequency peak is more prominent closer to the ground plane while the higher-frequency peak becomes dominant further from the ground plane and along the rest of the stack height.

The power spectra at three different locations along the stack height are shown in Figure 7.8. For varying R at a constant stack mid-height, $z/H = 0.5$ (Figure 7.8(a)), there are changes from a single and sharp peak when $R \leq 1$ to a dual peak region for $R \geq 1.5$. For varying R at $z/H = 0.75$ (Figure 7.8(b)) a low narrow broad-banded peak is observed for $R = 0$ and changed into a sharp long peak at $R \geq 0.5$, indicating a gradual increase in vortex shedding frequency as R increases. For varying R at $z/H = 1.0$ (Figure 7.8(c)), the same trend is found as for $z/H = 0.75$. The shape of the peak changes gradually from

near broad-banded for R = 0.5, moving towards a short narrow sharp peak and eventually changing to a long narrow sharp peak.

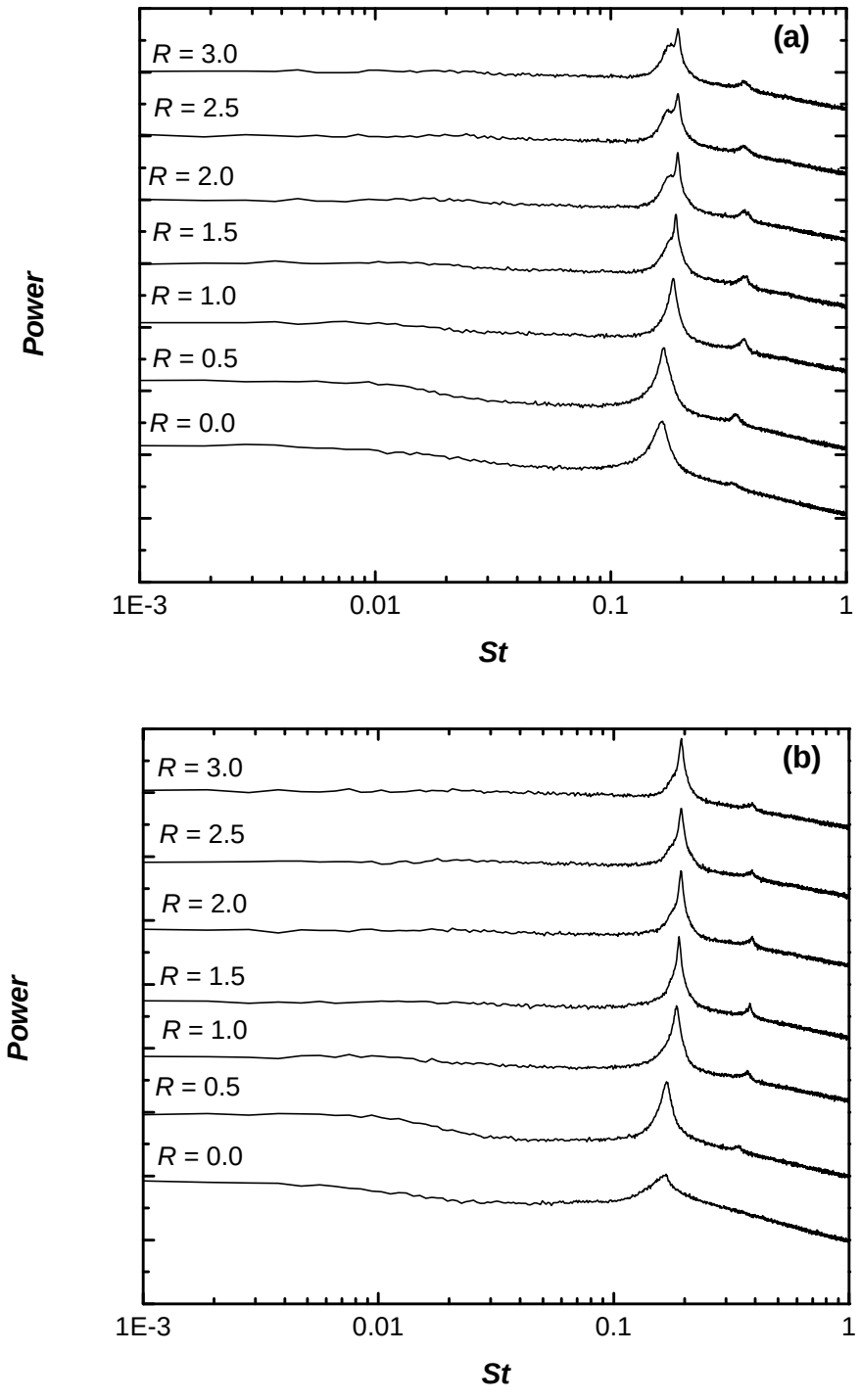

Figure 7.8: The power spectra at selected locations along the stack height: (a) z/H = 0.5; (b) z/H = 0.75; and (c) z/H = 1.

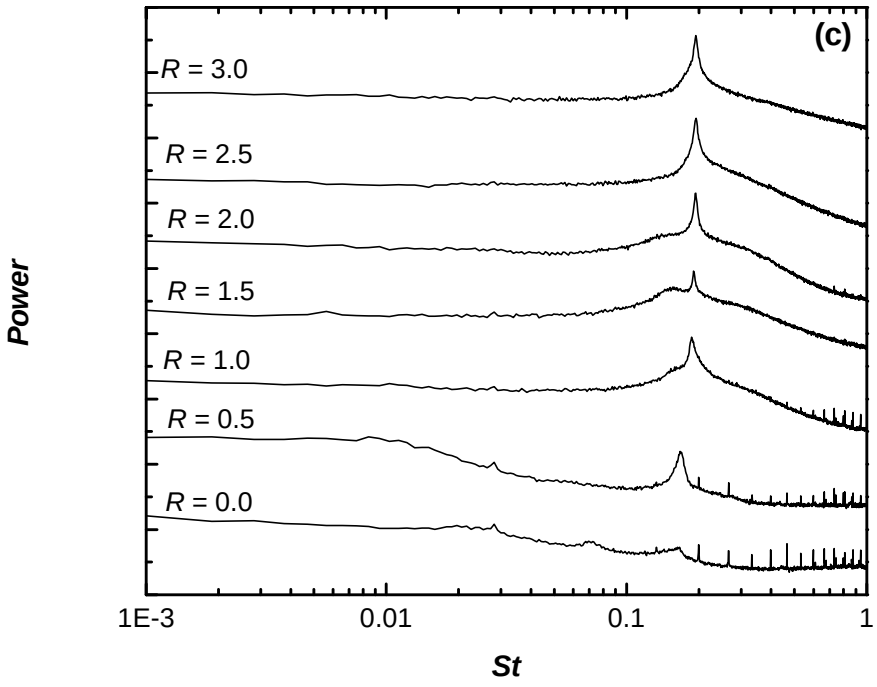

Figure 7.8 continued.

7.5 Summary

The effect of the velocity ratio on the characteristics of the vortex shedding from the stack, and the vortex formation length, were examined in this Chapter. The characteristics of the Strouhal number agreed with the three flow regimes identified in Chapter 5. In the downwash flow regime, a single Strouhal number was measured along the entire stack height. In the crosswind-dominated flow regime a higher Strouhal number, when compared with downwash flow regime, was obtained. In the jet-dominated flow regimes, a jump in Strouhal number occurred within the ground plane boundary layer.

CHAPTER 8

CONCLUSIONS, CONTRIBUTIONS, AND RECOMMENDATIONS

In this Chapter, conclusions of this study, contributions and recommendations for future work are presented.

8.1 Conclusions

8.1.1 Finite Circular Cylinder

The research reported in the thesis is divided into two different but related topics: finite circular cylinder and stack flow. In the first case, the wake characteristics of a finite circular cylinder of four different aspect ratios (3, 5, 7 and 9) were investigated experimentally using X-probe anemometry. Each cylinder was mounted normal to a ground plane and was partially immersed in a turbulent boundary layer, $\delta/D = 3$. It was found that the cylinders of $AR = 5$, 7, and 9 had a similar turbulent wake structure, with a localized region of low streamwise mean velocity and high turbulence intensity behind the cylinder, which was centred between four main streamwise vortex structures. A strong downwash velocity field was found between the tip vortex structures closer to the free end, and an upwash velocity field was found between the base vortex structures closer to the ground plane. The sign of the Reynolds shear stress changed near the mid-

height of the cylinder between the two pairs of vortex structures.

The time-averaged velocity, turbulence intensity, and Reynolds shear stress characteristics for the cylinder with AR = 3 indicated that it had a different turbulent wake structure. This is due to the absence of the base vortex structures and their associated upwash velocity field from the ground plane. Some of the data suggest that a transitional turbulent wake structure may exist for the cylinder with AR = 5. The triple correlation behaviour within the wake of the cylinder with AR = 3 also behaved differently compared with the other cylinders. This may be because the downwash flow from the free end reaches the vicinity of the ground plane and thereby suppresses the upwash flow.

The high values, irrespective of the value of AR, observed for the skewness and flatness factors around the free end of the cylinders may be attributed to the tip vortex structures and the interaction with downwash flow that dominates this region of the cylinder.

8.1.2 Short Stack

The wake characteristics of a short stack of AR = 9 were investigated using both the seven-hole pressure probe and X-probe. Both the seven-hole probe and the X-probe were used to measure the time-averaged velocity field and the two-component turbulent velocity field in the wake at various downstream locations from the stack. The stack was mounted normal to a ground plane and was partially immersed in a flat-plate turbulent boundary layer, δ/D = 6, and the jet-to-cross-flow velocity ratio was varied from R = 0 to 3. In addition, measurements of the vortex shedding frequency were made with a single-component hot-wire probe.

Based on these measurements, the flow around the stack could be classified into three regimes depending on the value of R: the downwash ($R < 0.7$), crosswind-dominated ($0.7 < R < 1.5$), and jet-dominated ($R \geq 1.5$) flow regimes. As R is varied, marked changes occur in the downwash and upwash velocity fields, and in the location, strength, and number of streamwise vortex structures. Also, the size and shape of the recirculation zone in the near wake of the stack is affected by the value of R. From the time-averaged wall-normal velocity field, the strength of the downwash velocity was found to decrease as R increased, and the upwash velocity field extended further above the ground plane. In the jet-dominated flow regime, there is an absence of appreciable downwash flow. There are two main regions of low time-averaged streamwise velocity within the combined wake of the stack and the jet flow. One is located behind the stack and the other is located in the jet wake region. The size of this second region within the jet wake increases with R.

In the downwash flow regime, the flow is similar to that of a finite circular cylinder, with two pairs of counter-rotating streamwise vortex structures, each of opposite sign, in the stack wake. The tip vortex pair is found near the free end of the stack and is associated with a strong downwash velocity field immediately behind the stack. The weaker base vortex pair is found within the flat-plate boundary layer on the ground plane and is associated with an upwash velocity field directed away from the ground plane. In addition, two elevated regions, one negative region within the ground plane boundary layer and another positive region just above the mid-height of the stack, are observed in the Reynolds shear stress profiles along the centreplane. The negative region is a result of the upwash flow from the ground plane, while the positive region coincides with the downwash flow region within the stack wake. In this flow regime, a

Strouhal number of St = 0.166 which is independent of the position along the height of the stack was observed.

In the crosswind-dominated flow regime, the tip vortex pair extends just above the free end of the stack, and the base vortex pair is stretched vertically towards the mid-height of the stack. The downwash and upwash velocity fields, and the vortex pairs, are weakened compared to the downwash flow regime. Also, in the Reynolds shear stress profiles, two negative peaks and one positive peak are observed within the stack wake, and another positive region is observed above the stack free end. The positive region above the stack free end is due to the presence of the jet flow. Also within this flow regime, a Strouhal number of St = 0.186, which is independent of the position along the stack height, was observed.

For the jet-dominated flow regime, three pairs of counter-rotating streamwise vortex structures are observed. In addition to the tip vortex and base vortex pairs observed for the other flow regimes, the jet-wake vortex pair appears in the jet wake region above the free end of the stack. The jet-wake vortex pair is associated with the jet rise and a strong upwash velocity on the jet wake centreline. The positive region in the Reynolds shear stress profile within the jet wake becomes stronger for the jet-dominated flow compared to the cross-wind dominated flow due to the stronger interaction between the jet flow and cross-flow. In this flow regime, a completely different Strouhal number characteristic was observed, compared with other flow regimes, with a 'jump' in Strouhal number from St = 0.176 to 0.193. The lower value of St = 0.176 occurs within the flat-plate turbulent boundary layer, while the higher value of St = 0.193, which is close to the value for an infinite circular cylinder, was measured in the jet-wake region. This was evidence of the "lock-in" of the Kármán-type vortex

structures between the stack and jet wakes, and showed that the higher-momentum jet acts in a similar manner to a bluff body, effectively extending the stack's aspect ratio and allowing the Kármán-type vortex structures to extend above the stack's free end.

The skewness and flatness factor profiles (in both the streamwise and wall-normal directions) show a deviation from the Gaussian distribution of 0 and 3, respectively, especially toward the stack free end for the downwash flow regime; above the stack free end for the crosswind-dominated flow regime; and within the jet wake for the jet-dominated flow regime. In the case of the downwash flow regime, this deviation is due to the interaction between the tip vortex structures and the downwash flow that gives rise to strong turbulent events. For the crosswind-dominated flow and the jet-dominated flow regimes, this deviation is as a result of the jet-wake vortex and the strong interaction between the jet flow and the crossflow within the jet wake.

The vortex formation length at the mid-height of the stack ($z/H = 0.5$) decreases with increasing R, indicating that the stack wake becomes more two-dimensional and similar to that observed behind an infinite (or higher-aspect-ratio) circular cylinder. This observation was supported by the Strouhal number data, which showed the Strouhal number for the stack approaches the value for an infinite circular cylinder with an increase in R. Again, the vortex formation length behaviour also supported the three flow regimes mentioned above.

8.2 Contributions of this Study

The results of this study have provided more insight into the turbulent wake characteristics of both the finite circular cylinder and a short stack, both partially immersed inside a turbulent boundary layer and subjected to a cross-flow. Also, the

detailed experimental data acquired can be used as verification information for future work that might involve computational fluid dynamics modeling.

The results of this study have improved the current state of knowledge on the wake of a finite circular cylinder, which is limited. For example, the time-averaged streamwise vorticity field and the turbulent kinetic energy distribution in a finite-cylinder wake were measured by Leder (2003), but the results were mostly restricted to the recirculation zone, and were made only for one cylinder aspect ratio, $AR = 2$. The wake studies of Tanaka and Murata (1999) and Sumner *et al.* (2004), while comprehensive, were limited to mean velocity and vorticity measurements. Okamoto and Sunabashiri (1992) measured the three turbulence intensity components in the wake of a finite cylinder, but their measurements were restricted to profiles at the mid-height position only. More detailed measurements were made by Park and Lee (2004), who used PIV to study the turbulent velocity field near the free end and in the recirculation zone of a finite cylinder. However, their study focused mostly on the effects of the shape of the free end and were made at only one cylinder aspect ratio, $AR = 6$. Some of the results of the current research on a finite circular cylinder have been published in a journal paper and appeared in various conference proceedings as listed below. These results addressed some of the shortcomings of the previous studies and provided detailed information about the turbulent wake structure of a finite circular cylinder.

1) M. S. Adaramola**,** O. G. Akinlade, D. Sumner, D. J. Bergstrom, and A. J. Schenstead (2006): Turbulent Wake of a Finite Circular Cylinder of Small Aspect Ratio, *Journal of Fluids and Structures* **22**, pp. 919-928.
2) M. S. Adaramola, D. J. Bergstrom, D. Sumner**,** "Effect of Aspect Ratio on the Triple Correlations in the Wake of a Finite Circular Cylinder", *Proceedings of the*

21st Canadian Congress of Applied Mechanics, Toronto, Canada, June 3-7, 2007, pp. 440 – 441.

3) M. S. Adaramola, O. G. Akinlade, D. Sumner, D. J. Bergstrom, and A. J. Schenstead (2005): "Turbulent wake of a finite circular cylinder", *Proceedings of the Fourth Symposium on Bluff Body Wakes and Vortex-Induced Vibrations* (BBVIV4), Santorini, Greece, pp. 207 – 210.
4) M. S. Adaramola, O. G. Akinlade, D. Sumner, D. J. Bergstrom, and A. J. Schenstead (2005): "Turbulent wake of a finite circular cylinder of small aspect ratio", *Proceedings of the 20th Canadian Congress of Applied Mechanics* , Montreal, Canada, pp. 305 – 306.

Few studies have appeared in the literatures which focus on the wake structure of an elevated jet in a cross-flow, and the wake characteristics of a stack are not yet fully understood. This study provides further insight into the structure of this complex flow. Some of the results of the current research on a short stack have been published in a journal paper and appeared in various conference proceedings as listed below. These results provided detailed information about the turbulent wake structure of a short stack in a cross-flow. Specific contributions include information about vortex shedding characteristics from a stack, turbulence statistics and the time-averaged velocity and streamwise vorticity fields.

1) M. S. Adaramola, D. Sumner, D. J. Bergstrom (2007), *"*Turbulent wake and vortex shedding for a stack partially immersed in a turbulent boundary layer" *Journal of Fluids and Structures* **23**, pp. 1189-1206.
2) M. S. Adaramola, D. J. Bergstrom, D. Sumner, "The turbulent statistics in the

wake of a short stack", *Proceedings of the Turbulence and Shear Flow Phenomena -5,* Munich, Germany, August 27-29, 2007, Vol. 2, pp. 643 – 648.

3) M. S. Adaramola, D. Sumner, D. J. Bergstrom, "Effect of velocity ratio on the vortex structures within the wake of a stack", *Proceedings of the IUTAM Symposium on Unsteady Separated Flows and their Control,* Kerhyra, Greece, June 18-22, 2007.
4) M. S. Adaramola, A. O. Oladeinde, D. Sumner, D. J. Bergstrom "Vortex shedding from a short stack", *Proceedings of the 6th International Symposium on Fluid-Structure Interactions, Aeroelasticity, Flow-Induced Vibration & Noise*, Vancouver, Canada, ASME Pressure Vessels and Piping Division, July 23-27, 2006, Paper No. PVP2006-ICPVT11-93121
5) M. S. Adaramola, D. Sumner, D. J. Bergstrom "Turbulent wake of a stack and the influence of velocity ratio", *Proceedings of the 6th International Symposium on Fluid-Structure Interactions, Aeroelasticity, Flow-Induced Vibration & Noise*, Vancouver, Canada, ASME Pressure Vessels and Piping Division, July 23-27, 2006, Paper No. PVP2006-ICPVT11-93629
6) M. S. Adaramola, D. Sumner, D. J. Bergstrom (2005): "Influence of velocity ratio on turbulent wake of a small stack", *Proceedings of the 20th Canadian Congress of Applied Mechanics,* Montreal, Canada, pp. 321 – 322.

In addition to the above listed papers, the following manuscripts on both the finite circular cylinder and short stack are in preparation and will be submitted for publication soon.

1) M. S. Adaramola, D. J. Bergstrom, D. Sumner, “The turbulent statistics in the wake of a short stack”.
2) M. S. Adaramola, D. Sumner, D. J. Bergstrom, “Effect of velocity ratio on the vortex structures within the wake of a stack”.
3) M. S. Adaramola, D. J. Bergstrom, D. Sumner, “Effect of aspect ratio on the turbulence characteristics in the wake of a finite circular cylinder”.

8.3 Recommendations for Future Work

This study has provided useful and detailed information about the characteristics of the flow around a finite circular cylinder and a short stack in a cross-flow. Due to the limitations of the available facilities and the complex nature of these flows, some issues still need to be addressed.

The X-probe provides information about the turbulent parameters within both the cylinder and stack wakes, but this information is limited to two velocity components. The seven-hole probe provides information about three-components of the time-averaged velocity fields within the stack wake, but in its current setup at the University of Saskatchewan cannot be used to measure the turbulence of the wake. In addition, the X-probe and the seven-hole probes cannot be used to measure the wake properties very near the cylinder and the stack (where the flow recirculates) due to the high flow angles. Therefore, there is a need for further study with instruments that can measure the three components of the turbulence velocity fields around these structures (e.g. triple-wire anemometry, laser Doppler velocimetry (LDV), and stereoscopic particle image velocimetry (SPIV)). These instruments can measure the three components of instantaneous velocity in the near wake from which other parameters such as Reynolds

stress tensor, turbulence production and turbulent kinetic energy distributions can be determined. The information from these measurements would make it possible to sketch the flow around a stack in a cross-flow as shown in Figure 2.3.

For stacks, the information provided in this study is limited to non-buoyant jet flow and further study is required to focus on the buoyant jet flow, and test the validity of the three flow regimes identified in this study. In addition, the influence of the ground plane boundary layer properties (smooth and rough surface) and the cross-flow Reynolds number on the wake of the stack are some of the other areas that need to be studied. For a ground-source jet flow, it has been shown that jet exit velocity profile and the shape of the ground source can significantly influence the penetration of the jet flow and the entrainment of the ambient cross-flow into the jet flow. For an elevated jet in cross-flow, the implications of the velocity profile and the shape of the stack (both internal and external dimensions) need to be investigated.

The effect of the jet flow on the wake structure of an inclined stack has not been investigated. In addition, in some practical applications of cylinders and stacks, more than one of these structures are employed and arranged in various ways, and there is also need to further study the implications of these arrangements on the rise of the jet flow as well as on wake structure.

REFERENCES

Afgan, I., Moulinec, C., Prosser, R., Laurence, D., 2007. Large eddy simulation of turbulent flow for wall mounted cantilever cylinders of aspect ratio 6 and 10. *International Journal of Heat and Fluid Flow* **28**, 561–574.

Agui, J.H., Andreopoulos, J., 1992. Experimental investigation of a three-dimensional boundary layer flow in the vicinity of an upright wall-mounted cylinder. *ASME Journal of Fluids Engineering* **114**, 566-576.

Akinlade, O.G., 2005. Effects of surface roughness on the flow characteristics in a turbulent boundary layer. Ph.D. Thesis, Department of Mechanical Engineering, University of Saskatchewan, Saskatoon, Canada.

Andreopoulos, J., Rodi, W., 1984. Experimental investigation of jets in a crossflow. *Journal of Fluid Mechanics* **138***,* 93-127.

Arya, S.P.S., Lape, J.F., 1990. A comparative study of the different criteria for the physical modeling of buoyant plume rise in a neutral atmosphere. *Atmospheric Environment* **24A**, 289-295.

ASHRAE, 1997. *Handbook-Fundamentals*, Chapter 15.10 Airflow around buildings, ASHRAE, Atlanta, USA.

ASHRAE, 1999. *Handbook of HVAC Operations*, Chapter 43: Building Air Intake and Exhaust Design, ASHRAE, Atlanta, USA.

ASHRAE, 2001. *Handbook of Fundamentals*, Chapter 16: Airflow around Buildings, ASHRAE, Atlanta, USA.

Baker, C.J., 1979. The laminar horseshoe vortex. *Journal of Fluid Mechanics* **95**, 347-367.

Baker, C.J., 1980. The turbulent horseshoe vortex. *Journal of Wind Engineering and Industrial Aerodynamics* **6**, 9-23.

Ballio, F., Bettoni, C., Franzetti, S., 1998. A survey of time-averaged characteristics of laminar and turbulent horseshoe vortices. *Journal of Fluids Engineering* **120**, 233-242.

Becker. S., Lienhart, H., Durst. F., 2002. Flow around three-dimensional obstacles in boundary layers. *Journal of Wind Engineering and Industrial Aerodynamics* **90**, 265-279.

Briggs, G.A., 1969. Plume rise. *U.S. Atomic Energy Commission*, TID-25075, 5-8.

Briggs, G.A., 1984. Plume rise and buoyancy effects, in *Atmospheric Science and Power Production*, Office of Scientific and Technical Information Centre, USDOE, DOE/TIC-27601 (DE 84005177), pp. 327-366.

Bruun, H.H., 1995. *Hot-Wire Anemometry, Principles and Signal Analysis*. New York, Oxford University Press.

Canepa, E., 2004. An overview about the study of downwash effects on dispersion of airborne pollutants. *Environmental Modelling and Software* **19**, pp. 1077-1087.

Cheung, J.C.K., Melbourne, W.H., 1995. Building downwash of plumes and plume interactions. *Journal of Wind Engineering and Industrial Aerodynamics* **54**/**55**, pp. 543-548.

Coleman, H.W., Steele, W.G., 1999. *Experimentation and Uncertainty Analysis for Engineers*. 2nd Edition, Wiley, New York.

Contini, D., Robins, A., 2001. Water tank measurements of buoyant plume rise and structure in neutral crossflows. *Atmospheric Environment* **35**, 6105-6115.

Contini, D., Robins, A., 2004. Experiments on the rise and mixing in neutral crossflow of plumes from two identical sources for different wind directions. *Atmospheric Environment* **38**, 3573-3583.

Coutanceau, M., Defaye, J.R., 1991. Circular cylinder wake configurations: a flow visualization study. *Applied Mechanics Reviews* **44**, 255-305.

Donnert G.D., Kappler, M., Rodi, W., 2007. Measurement of tracer concentration in the flow around finite-height cylinders. *Journal of Turbulence* **8**, 1-18.

Eiff, O.S., Kawall, J.G., Keffer, J.F., 1995. Lock-in of vortices in the wake of an elevated round turbulent jet in a crossflow. *Experiments in Fluids* **19**, 203-213.

Eiff, O.S., Keffer, J.F., 1997. On the structures in the near wake region of an elevated turbulent jet in a crossflow. *Journal of Fluid Mechanics* **333**, 161-195.

Eiff, O.S., Keffer, J.F., 1999. Parametric investigation of the wake-vortex lock-in for the turbulent jet discharging from a stack. *Experimental Thermal and Fluid Science* **19**, 57-66.

Etzold, F., Fiedler, H., 1976. The near-wake structure of a cantilevered cylinder in a cross-flow. *Zeitschrift Fuer Flugwissenschaften* **24**, 77-82.

Farivar, D.J., 1981. Turbulent uniform flow around cylinders of finite length. *AIAA Journal* **19**, 275-281.

Fox, R.W., McDonald, A.T., Pritchard, P.J., 2004. *Introduction to Fluid Mechanics*. 6th Edition, John Wiley and Sons Inc. New Jersey.

Fox, T.A., Apelt, C.J., 1993a. Fluid-induced loading on cantilevered circular cylinders in a low-turbulence uniform flow. Part 1: Fluctuating loads with aspect ratios 4 to 30. *Journal of Fluids and Structures* **7**, 1-14.

Fox, T.A., Apelt, C.J., 1993b. Fluid-induced loading on cantilevered circular cylinders in a low-turbulence uniform flow. Part 2: Fluctuating loads with aspect ratios 30. *Journal of Fluids and Structures* **7**, 15-28.

Fox, T.A., Apelt, C.J., 1993c. Fluid-induced loading on cantilevered circular cylinders in a low-turbulence uniform flow. Part 3: Fluctuating loads with aspect ratios 4 to 25. *Journal of Fluids and Structures* **7**, 375-386.

Fric, T.F., Roshko, A., 1994. Vortical structure in the wake of a transverse jet, *Journal of Fluid Mechanics* **279**, 1-47.

Fröhlich, J., Rodi, W., 2004. LES of the flow around a circular cylinder of finite height. *International Journal of Heat and Fluid Flow* **25**, 537–548.

Gad-el-Hak, M., Bandyopadhyay, P.R., 1994. Reynolds number effects in wall-bounded turbulent flows. *Applied Mechanics Review*, **47**, 307-365.

Gallington, R.W., 1980. Measurement of very large flow angles with non-nulling seven-hole probe. Aeronautics Digest, USAFA-TR-80-17, 60-88.

Gerner, A.A., Maurer, C.L., Gallington, R.W., 1984. Non-nulling seven-hole probes for high angle flow measurement. *Experiments in Fluids* **2**, 95-103.

Gerrard, J.H., 1966. The mechanics of the formation region of vortices behind bluff bodies. *Journal of Fluid Mechanics* **25**, 401- 413.

Graf, W.H., Yulistiyanto, B., 1998. Experiments on flow around a circular cylinder; the velocity and vorticity fields. *IAHR Journal of Hydraulic Research* **36**, 637-744.

Griffin, O.M., 1985. Vortex shedding from bluff bodies in a shear flow: a review. *ASME Journal of Fluids Engineering* **107**, 298-306.

Heseltine, J.L., 2003. Flow around a circular cylinder with free end. M.Sc. Thesis, Department of Mechanical Engineering, University of Saskatchewan, Saskatoon, Canada.

Hsieh, R.H., Huang, R.F., 2003. Tomographic flow structures of a round jet in a crossflow. *Journal of the Chinese Institute of Engineers* **26**, 71-80.

Huang, R.F., Hsieh, R.H., 2002. An experimental study of elevated round jets deflected in a crossflow. *Experimental Thermal and Fluid Science* **27**, 77-86.

Huang, R.F., Hsieh, R.H., 2003. Sectional flow structures in near wake of elevated jet in a crossflow. *AIAA Journal* **41**, 1490-1499.

Huang, R.F., Lan, J., 2005. Characteristic modes and evolution processes of shear-layer vortices in an elevated transverse jet. *Physics of Fluids* **17**, 034103.

Johnston, C.R., Wilson, D.J., 1997. A vortex pair model for plume downwash into stack wakes. *Atmospheric Environment* **31**, 13-20.

Kamotani, Y., Greber, I., 1972. Experiments on a turbulent jet in a cross flow. *AIAA J.* **10**, 1425-1429.

Kawamura, T., Hiwada, M., Hibino, T., Mabuchi, T., Kumada, M., 1984. Flow around a finite circular cylinder on a flat plate. *Bulletin of the JSME* **27**, 2142-2150.

Kiya, M., Matsumura, M., 1985. Turbulence structure in the intermediate wake of a circular cylinder. *Bulletin of the JSME* **28**, 2617-2624.

KÖnig, C.S., Mokhtarzadeh-Dehghan, M.R., 2002. Numerical study of buoyant plumes from a multi-flue chimney released into an atmospheric boundary. *Atmospheric Environment* **36**, 3951-3962.

Krogstad, P.-Å., Antonia, R.A., 1994. Structure of turbulent boundary layers on smooth and rough walls *Journal of Fluid Mechanics* **277**, 1-21.

Leder, A., 2003, 3D-flow structures behind truncated circular cylinders, *Proceedings of FEDSM'03, 4th ASME-JSME Joint Fluids Engineering Conference*, Honolulu, USA, Paper No. FEDSM2003-45083.

Lee, L.W., 1997. Wake structure behind a circular cylinder with a free end. *Proceedings of the Heat Transfer and Fluid Mechanics Institute*, pp. 241-251.

Lee, L.W., Wang, Y.L., 1987, Aerodynamics of a circular cylinder of finite length in cross-flow, *Proceedings of the ASME Applied Mechanics, Bioengineering, and Fluids Engineering Conference,* Cincinnati, USA, pp. 61-65.

Lim, T.T., New, T.H., Luo, S.C., 2001. On the development of large-scale structures of a jet normal to a cross flow. *Physics of Fluids* **13,** 770-775.

Luo, S.C., 1993, Flow past a finite length circular cylinder, *Proceedings of the Third (1993) International Offshore and Polar Engineering Conference, Singapore*, Vol. III, ISOPE: Golden, CO, USA, pp. 530-534.

Macdonald, R.W. Strom, R.K., Slawson, P.R., 2002. Water flume study of the enhancement of buoyant rise pairs of merging plumes. *Atmospheric Environment* **36**, 4603-5615.

Mahjoub Saïd, N., Habil, S., Mhiri, H., Bournot, H., Le Palec, G., 2007. Flow field measurement in a crossflowing elevated jet. *Journal of Fluids Engineering* **129**, 551-562.

Mahjoub Saïd, N., Mhiri, H., Le Palec, G., and Bournot, P., 2005. Experimental and numerical analysis of pollutant dispersion from a chimney. *Atmospheric Environment* **39**, 1727-1738.

Mair, W.A., Stansby, P.K., 1975. Vortex wakes of bluff cylinders in shear flow. SIAM *Journal on Applied Mathematics* **28**, 519-540.

Matsumura M. and Antonia, R., 1993. Momentum and heat transfer in the turbulent intermediate wake of a circular cylinder. *Journal of Fluid Mechanics* **250**, 651-668.

Maull, D.J., Young, R.A., 1973. Vortex shedding from bluff bodies in a shear flow. *Journal of Fluid Mechanics* **60**, 401-409.

Moussa, Z.M., Trischka, J.W., Eskinazi, S., 1977. The near field in the mixing of a round jet with a cross-stream. *Journal of Fluid Mechanics* **80,** 49-80.

New, T.H., Lim, T.T., Luo, S.C., 2006. Effects of jet velocity profiles on a ground jet in cross-flow. *Experiments in Fluids* **40,** 859-875.

Noca, F., Park, H.G., Gharib, M., 1998. Vortex formation length of a circular cylinder (300 < Re < 4,000) using PIV. *Proceedings of ASME FEDSM'98*, Washington, D.C., pp. 46-53, New York: ASME.

Norberg, C., 1986. Interaction between freestream turbulence and vortex shedding for a single tube in cross-flow. *Journal of Wind Engineering and Industrial Aerodynamics* **23**, 501-514.

Okamoto, S., 1991. Flow past circular cylinder of finite length placed on ground plane, *Transactions of the Japan Society for Aeronautical and Space Sciences* **33**, 234-246.

Okamoto, S., Sunabashiri, Y., 1992. Vortex shedding from a circular cylinder of finite length placed on a ground plane, *ASME Journal of Fluids Engineering* **144**, 512-521.

Okamoto, T., Yagita, M., 1973. The experimental investigation on the flow past a circular cylinder of finite length placed normal to the plane surface in a uniform stream. *Bulletin of the JSME* **16**, 805-814.

Onbaşıoğlu, S.U., 2001. On the simulation of the plume from stacks of buildings. *Building and Environment* **36**, 543-559.

Österlund, J.M, 1999.Experimental studies of zero pressure-gradient turbulent boundary layer flow. PhD Thesis, Royal Institute of Technology, Stockholm.

Overcamp, T. J., 2001. A review of the conditions leading to downwash in physical modeling experiments. *Atmospheric Environment* **35**, 3503-3508.

Overcamp, T.J., Ku, T., 1988. Plume rise from two or more adjacent stacks. *Atmospheric Environment* **22**, 625-637.

Park, C.-W., Lee, S.-J., 2000. Free end effects on the near wake flow structure behind a finite circular cylinder. *Journal of Wind Engineering and Industrial Aerodynamics* **88**, 231-246.

Park, C.-W., Lee S.-J., 2002. Flow structure around a finite circular cylinder embedded in various atmospheric boundary layers. *Fluid Dynamics Research* **30**, 197-215.

Park, C.-W., Lee S.-J., 2004. Effects of free-end corner shape on flow structure around a finite cylinder. *Journal of Fluids and Structures* **19**, 141-158.

Petersen, R.L., Cochran, B.C., Carter, J.J., 2002a. Specifying exhaust and intake systems. *ASHRAE Journal* **44**, 30-37.

Petersen, R.L., Cochran, B.C., LeCompte, J.W., 2002b. Specifying exhaust systems that avoid fume reentry and adverse health effects. *ASHRAE Transactions* **108**, 1039-1049.

Plesniak, M. W., Cusano, D. W., 2005. Scalar mixing in a confined rectangular jet in crossflow. *Journal of Fluid Mechanics* **524,** 1-45.

Raupach, M.R., Antonia, R.A., Rajagopalan, S., 1991. Rough-wall turbulent boundary layers. *Applied Mechanics Review* **44**, 1-25.

Rediniotis, D.K., Hoang, N.T., Telionis, D.P., 1993. The seven-hole probe: its application and use. In: Industrial Fluid Dynamics Experiments, FED-vol.152. ASME, New York, pp. 21–26.

Sakamoto, H., Arie, M., 1983, Vortex shedding from a rectangular prism and a circular cylinder placed vertically in a turbulent boundary layer. *Journal of Fluid Mechanics* **126**, 147-165.

Sakamoto, H., Oiwake, S., 1984, Fluctuating forces on a rectangular prism and a circular cylinder placed vertically in a turbulent boundary layer, *ASME Journal of Fluids Engineering,* **106**, 160-166.

Sarode, R. S., Gai, S. L., Ramesh, C.K., 1981. Flow around circular- and square- section models of finite height in a turbulent shear flow. *Journal of Wind Engineering and Industrial Aerodynamics* **8**, 223-230.

Schulman, L.L., Scire, J.S., 1991. The effect of stack height, exhaust speed, and wind direction on concentrations from a rooftop stack. *ASHRAE Transactions* **97**, 573-582.

Slawson, P.R., Csanady, G.T., 1971. The effect of atmospheric conditions on plume rise. *Journal of Fluid Mechanics* **47**, 33-49.

Snyder, W.H., Lawson, Jr., E.E., 1991. Fluid modeling simulation of stack-tip downwash for neutrally buoyant plumes. *Atmospheric Environment* **25A**, 2837-2850.

Smith, S.H., Mungal, M.G., 1998. Mixing, structure and scaling of the jet in crossflow. *Journal of Fluid Mechanics* **357**, 83-122.

Stathopoulos, T., Lazure, L., Saathoff. P., Gupta, A., 2004. The effect of stack height, stack location and rooftop structures on air intake contamination. Studies and Research Report*, R-392*, IRSST, Quebec, Canada.

Sumer, B.M., Fredsøe, J., 2002. *The Mechanics of Scour in the Marine Environment*, Vol 17, Advanced Series on Ocean Engineering. World Scientific, Singapore.

Sumner, D., 2002. A comparison of data-reduction methods for a seven-hole probe. *Journal of Fluid Eng.-T. ASME* **124,** 523-527.

Sumner, D., Heseltine, J.L., Dansereau, O.J.P., 2004. Wake structure of a finite circular cylinder of small aspect ratio. *Experiments in Fluids* **37**, 720-730.

Szepessy, S., 1991. On the three-dimensionality of vortex shedding from a circular cylinder. Ph.D. Thesis, School of Mechanical Engineering, Chalmers University of Technology, Gothenburg, Sweden.

Tanaka, S., Murata, S., 1999. An investigation of the wake structure and aerodynamic characteristics of a finite circular cylinder. *JSME International Journal Series B: Fluids and Thermal Engineering* **42**, 178-187.

Taniguchi, S., Sakamoto, H., Arie, M., 1981, Flow around circular cylinders of finite height placed vertically in turbulent boundary layers, *Bulletin of the JSME,* **24**, 37-44.

Tsang, G., 1972. Stack exit velocity distribution for higher effective stack height. *Atmospheric Environment* **6**, 815-828.

Uematsu, Y., Yamada, M., Ishii, K., 1990. Some effects of free-stream turbulence on the flow past a cantilevered circular cylinder. *Journal of Wind Engineering and Industrial Aerodynamics* **33**, 43-52.

Wang, H. F., Zhou, Y., Chan, C. K., Lam, K. S., 2006. Effect of initial conditions on interaction between a boundary layer and a wall-mounted finite-length-cylinder wake. *Physics of Fluids* **18**, 065106.

Wegner, B., Huai, Y., Sadiki, A., 2004. Comparative study of turbulent mixing in cross-flow configurations using LES. *Inter. J. of Heat and Fluid Flow* **25,** 767-775.

West, G. S., Apelt, C. J., 1982. The effects of tunnel blockage and aspect ratio on the mean flow past a circular cylinder with Reynolds numbers between 10^4 and 10^5. *Journal of Fluid Mechanics* **114**, 361–377.

White, F.M., 2003. *Fluid Mechanics*. 5th Edition, McGraw-Hill, New York.

Williamson, C.H.K., Miller, G.D., 1994. Three-dimensional phase dynamics in a cylinder wake. *Meccanica* 29, 411-429

Williamson, C.H.K., 1996. Vortex dynamics in the cylinder wake. *Annual Review of Fluid Mechanics* **28**, 477-539.

Wilson, D.J., 1979. Flow patterns over flat-roofed buildings and application to exhaust stack design. *ASHRAE Transactions* **85**, 284-295.

Zdravkovich, M.M., 1997. *Flow around Circular Cylinders. Vol. 1: Fundamentals.* Oxford University Press, Oxford.

Zdravkovich, M.M., 2003. *Flow around Circular Cylinders. Vol. 2: Applications.* Oxford University Press, Oxford.

Zilliac, G.G., 1993. Modelling, calibration, and error analysis of seven-hole pressure probes. *Experiments in Fluids* **14**, 104-120.

APPENDIX A

DESIGN OF A ROOFTOP STACK

Stack downwash occurs when the jet or plume does not rise but is drawn downward into the low pressure region in the near-wake of the stack. A similar phenomenon, called building downwash, occurs around buildings when a jet flow is released from a rooftop or downwind side of a building. The downwash has the effect of reducing the effective height of the jet thereby increasing the ground level concentration of any pollutants. Stack downwash typically occurs when the crosswind velocity is much higher than the stack exit velocity or at low velocity ratio. For economic, structural and aesthetic (architectural) reasons, short stacks are desired, but to prevent re-entry of exhaust from the stacks into the building fresh air intake system, taller stacks, higher volume flow rates (Q) and optimum locations on the rooftop are essential. To avoid the adverse effect of building downwash, the height of the stack should be more than 2 to 2.5 times the building height (Cheung and Melbourne, 1995) or the height of any nearby building whose wake can cause the jet flow downwash and its entrainment into the lee of the building. Some standards or recommendations regarding exhaust stack design are listed in Petersen *et al.* (2002a) and Petersen *et al.* (2002b). ASHRAE (1997) recommends a minimum stack height of 3 m above the rooftop and a minimum jet exit velocity of 10 m/s. The required scaling criteria for avoiding downwash in subcritical model experiments have been discussed by Overcamp (2001).

For non-buoyant elevated jets in a crosswind, Snyder and Lawson (1991) reported that downwash occurs if $R < 1.5$ in the subcritical Reynolds number regime (based on the stack external diameter D) and $R < 1.1$ in the supercritical Reynolds

number regime. These observations have not been verified for buoyant jet flow. For highly buoyant jet flow, downwash flow is less likely to occur when $R < 1.5$ (Briggs, 1969).

As mentioned above, in order to reduce the effect of pollutants on the rooftop and ground level, the stack effective height is recommended to be sufficiently above the three flow regions shown in the Figure 1.3. For a rectangular building, the dimensions shown in Figure 1.3 are expressed in terms of **R**, which is defined as

$$\mathbf{R} = B_s^{0.67} B_L^{0.33} \quad , \tag{A.1}$$

where B_s is the smaller of upwind building height or width and B_L is the larger of upwind building height or width. The dimensions of the different flow regions on the building are expressed as follows:

$$H_c = 0.22\mathbf{R}, \tag{A.2}$$

$$X_c = 0.50\mathbf{R}, \tag{A.3}$$

$$L_c = 0.90\mathbf{R}, \tag{A.4}$$

$$L_r = 1.00\mathbf{R}. \tag{A.5}$$

where H_c is the maximum height of the roof recirculation region, X_c is the distance from the leading edge to H_c, L_c is the length of the roof recirculation region, and L_r is the length of the building wake region.

This approach assumes that the boundary of the high turbulence region is defined by a line with a slope of 10.1 extending from the top of the leading edge separation bubble as shown in Figure 1.3. The location of the jet flow relative to the recirculation regions is determined by taking into consideration the jet rise due to its momentum and

assuming a conical jet flow with a gradient of 5:1. The effective stack height (the physical height of the stack and the jet rise) above the rooftop is defined as

$$h = H + \Delta h - h_d, \tag{A.6}$$

where H is the physical height of the stack, Δh is the jet rise, and h_d is the reduction in jet height due to entrainment of the jet into the stack wake if the crosswind velocity is sufficiently greater than the jet flow velocity. According to Briggs (1984) and Wilson *et al*. (1998), Δh and h_d are respectively, defined as follows:

$$\Delta h = 3\beta dR \text{ , and} \tag{A.7}$$

$$h_d = d(3.0 - \beta R) \tag{A.8}$$

where d is the internal diameter, U_e is the jet exit velocity, U_∞ is the crosswind velocity at the building height (or freestream velocity) and β is the stack capping factor (β = 1 and 0 for an uncapped and capped stack, respectively). The expression in equation 1.8 is based only on non-buoyant jet flow. Equation (A.8) is valid for $R < 3$, and for $R > 3$ when $h_d = 0$ (i.e. no stack downwash flow).

APPENDIX B

PERMISSIONS TO REPRINT FIGURES

Figure 1.2: Schematic illustration of the merging process for two buoyant plumes released from a pair of stacks arranged in a line perpendicular to the wind.

ELSEVIER LIMITED LICENSE
TERMS AND CONDITIONS

Jan 03, 2008

This is a License Agreement between Muyiwa S Adaramola ("You") and Elsevier Limited ("Elsevier Limited"). The license consists of your order details, the terms and conditions provided by Elsevier Limited, and the payment terms and conditions.

License Number	1861461121613
License date	Jan 03, 2008
Licensed content publisher	Elsevier Limited
Licensed content publication	Atmospheric Environment
Licensed content title	Water flume study of the enhancement of buoyant rise in pairs of merging plumes
Licensed content author	Macdonald R. W., Strom R. K. and Slawson P. R.
Licensed content date	October 2002
Volume number	36
Issue number	29
Pages	13
Type of Use	Thesis / Dissertation
Portion	Figures/table/illustration/abstracts
Quantity	1

Figure 1.3: The flow pattern on the roof of a rectangular building

Date: Sat, 08 Mar 2008
From: "Publication Permissions" <permissions@ashrae.org>
Subject: RE: Request for Permission to Use
To: "Muyiwa Adaramola" <msa097@mail.usask.ca>

Dear Sir,

I apologize for the delay in responding to your request. I can provide a license agreement for you. The royalty fee to use the figure is $25 U.S.

Sincerely,

Tony Giometti
Tony Giometti, Manager of Communications and Programs
American Society of Heating, Refrigerating and Air-Conditioning Engineers, Inc.
Direct Line: 678-539-1155 Fax: 678-539-2155 eMail:
Giometti@ashrae.org Web: www.ASHRAE.org

Figure 2.1: Flow around a finite-length circular cylinder

Date: Thu, 28 Feb 2008

From: Masahiro Suyama <suyama@jsme.or.jp>

To: msa097@mail.usask.ca

Subject: Request for Permission to Use

Dear Dr. Muyiwa Adaramola,

My name is Masahiro Suyama, a staff of the Japan Society of Mechanical Engineers. I (We) hereby grant permission for the use of the material requested above.
By: The Japan Society of Mechanical Engineers
Date: February 28,2008
Name: Masahiro Suyama
Manager, Publishing Department,
The Japan Society of Mechanical Engineers

Figure 2.2: The time-averaged velocity filed along the wake centreline (y/D = 0) (a) AR = 9, (b) AR = 7, (c) AR = 5 and (d) AR = 3.

Figure 2.3: The time-averaged streamwise vorticity at x/D = 6 for (a) AR = 9, (b) AR = 7, (c) AR = 5 and (d) AR = 3

Figure 2.4: The vortical structures of the ground-source jet in the crossflow

PERMISSION INVOICE

Inv. # P03J 14559

February 29, 2008

Muyiwa Adaramola
Division of Environmental Engineering
University of Saskatchewan
57 Campus Drive
Saskatoon, SK, S7N 5A9
Canada

CAMBRIDGE UNIVERSITY PRESS

32 Avenue of the Americas
New York, NY 10013-2473, USA

www.cambridge.org

Telephone 212 924 3900
Fax 212 691 3239

REFERENCE

Journal:	Journal of Fluid Mechanics, 279, 1-47, 1994
Author:	Fric, T.F., Roshko, A.
Title:	Vortical structure in the wake of a transverse jet
Selection/pp.:	figure 1

Additional

USE

Reprint Title:	(flow structure within the wake of a stack in cross-flow)
Publisher:	University of Saskatchewan, Saskatoon, Canada
Format:	dissertation / thesis
Quantity (Limit*):	20
Avail. Date:	2008

RIGHTS/ACKNOWLEDGEMENT

Permission is granted for nonexclusive rights throughout the World in the English language for interior text editorial use in the format described above only. Please fully acknowledge our material and indicate the copyright notice as it appears in our publication, followed by the phrase "Reprinted with the permission of Cambridge University Press."

All requests from third parties to reproduce this material must be forwarded to Cambridge University Press.

FEES/RESTRICTIONS

$0.00

*You must re-apply for permission if this print run is exceeded. This permission is restricted to the indicated format and excludes reproduction in any other medium; for additional use, you must apply for permission separately. This permission does not allow reprinting of any material copyrighted by or credited in our publication to another source; Cambridge disclaims all liability in connection with the use of such material without proper consent. A COPY OF THIS INVOICE MUST ACCOMPANY PAYMENT. Payment is due upon publication or within 12 months, whichever is sooner. Make check payable to Cambridge University Press, Attn: Rights and Permissions. (CUP Fed. I.D. #: 13-1599108.)

This permission does not supersede permission that may be required from the original source indicated in our publication.

This permission requires that you send zero (0) copies of your publication directly to our author and zero (0) copy of your publication to this office upon availability.

Authorization: Adam Hirschberg

Adam Hirschberg
Rights and Permissions Coordinator

Figure 2.5: The flow structures of downwash, crosswind-dominated, transitional and jet dominated flow for elevated jet in a cross-flow.

ELSEVIER LIMITED LICENSE
TERMS AND CONDITIONS

Jan 03, 2008

This is a License Agreement between Muyiwa S Adaramola ("You") and Elsevier Limited ("Elsevier Limited"). The license consists of your order details, the terms and conditions provided by Elsevier Limited, and the payment terms and conditions.

License Number	1861470021626
License date	Jan 03, 2008
Licensed content publisher	Elsevier Limited
Licensed content publication	Experimental Thermal and Fluid Science
Licensed content title	An experimental study of elevated round jets deflected in a crosswind
Licensed content author	Huang R. F. and Hsieh R. H.
Licensed content date	December 2002
Volume number	27
Issue number	1
Pages	10
Type of Use	Thesis / Dissertation
Portion	Figures/table/illustration/abstracts
Quantity	1

Figure 2.6: Different region of the plume evolution.

ELSEVIER LIMITED LICENSE
TERMS AND CONDITIONS

Jan 03, 2008

This is a License Agreement between Muyiwa S Adaramola ("You") and Elsevier Limited ("Elsevier Limited"). The license consists of your order details, the terms and conditions provided by Elsevier Limited, and the payment terms and conditions.

License Number	1861461382565
License date	Jan 03, 2008
Licensed content publisher	Elsevier Limited
Licensed content publication	Atmospheric Environment
Licensed content title	Experimental and numerical analysis of pollutant dispersion from a chimney
Licensed content author	Mahjoub Saïd Nejla, Mhiri Hatem, Le Palec Georges and Bournot Philippe
Licensed content date	March 2005
Volume number	39
Issue number	9
Pages	12
Type of Use	Thesis / Dissertation
Portion	Figures/table/illustration/abstracts
Quantity	1

Figure 3.2: Thermal anemometry probes (a) single sensor hot-wire, and (b) X-probe.

Thu, 28 Feb 2008
From: "Troolin, Dan" <dtroolin@tsi.com>
To: Muyiwa Adaramola <msa097@mail.usask.ca>
Subject: Request for Permission to Use

Muyiwa,

Yes, we are happy to have you use this figure. Please add the following to the caption:

Courtesy: TSI Incorporated

Thanks,

Dan Troolin
TEL: 651-490-3885
FAX: 651-490-3824
TSI Incorporated
500 Cardigan Rd
Shoreview, MN 55126

Figure 3.6: a) Flow angle nomenclature; (b) sectoring scheme based on hole numbers 1 through 7.

Date: Wed, 27 Feb 2008

From: Beth Darchi <DarchiB@asme.org>

To: muyiwa.adaramola@usask.ca Cc: Michelle DeBlasi <DeBlasiM@asme.org>

Subject: Re: ASME PUBLICATIONS PERMISSION REQUEST FORM SUBMISSION

Dear Mr. Adaramola,
It is our pleasure to grant you permission to publish the following ASME Figure 1 from "A comparison of Data-Reduction Methods for a Seven-Hole Probe," by David Sumner, Journal of Fluids Engineering, Vol. 124, 20023, p. 524, cited in your letter for inclusion in your dissertation entitled THE WAKE OF AN EXHAUST STACK IN A CROSS-FLOW to be published by College of Graduate Studies and Research, University of Saskatchewan, Saskatoon, Canada. As is customary, we request that you ensure proper acknowledgment of the exact sources of this material, the authors, and ASME as original publisher.

In accordance with ASME policy, this permission is contingent upon payment of a royalty fee of US$20 for 1 figure ($20.00 for the first figure/table, $10 thereafter). This is solely charged to non-authors of the requested ASME papers.
Thank you for your interest in ASME publications.

Sincerely,

Beth Darchi
Copyrights & Permissions
ASME International
Three Park Avenue
New York, NY 10016
P: 212-591-7700
F: 212-591-7292
E: darchib@asme.org

Figure 3.7: Flow over probe at high angle of attack.

SPRINGER LICENSE
TERMS AND CONDITIONS

Jan 03, 2008

This is a License Agreement between Muyiwa S Adaramola ("You") and Springer ("Springer"). Please note that you are liable to account for Value Added Tax (VAT). The license consists of your order details, the terms and conditions provided by Springer, and the payment terms and conditions.

License Number	1861470640263
License date	Jan 03, 2008
Licensed content publisher	Springer
Licensed content publication	Experiments in Fluids
Licensed content title	Non-nulling seven-hole probes for high angle flow measurement
Licensed content author	A. A. Gerner
Licensed content date	Nov 29, 2004
Volume number	2
Issue number	2
Pages	95 - 103
Type of Use	Thesis / Dissertation
Details of use	Print
Portion of the article	Figures
Title of your thesis / dissertation	WAKE OF AN EXHAUST STACK IN A CROSS-FLOW
Expected completion date	Apr 2008